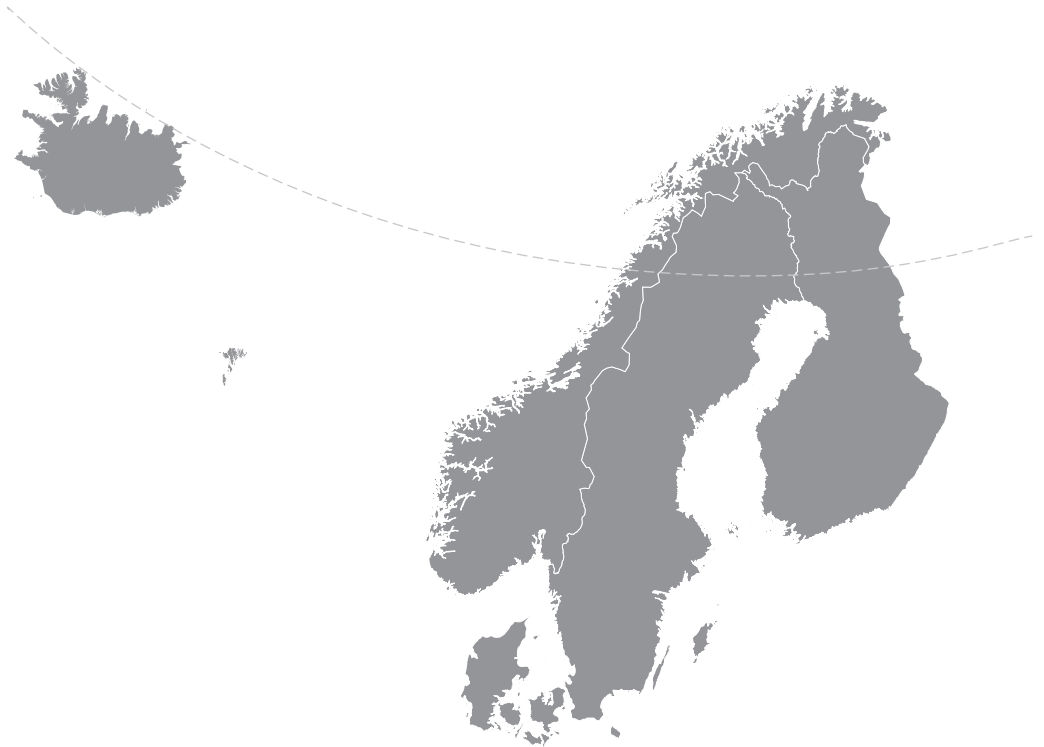


# Nordic Concrete Research



Nordic  
Concrete  
Federation

# **NORDIC CONCRETE RESEARCH**

**EDITED BY  
THE NORDIC CONCRETE FEDERATION**

**CONCRETE ASSOCIATIONS OF: DENMARK  
FINLAND  
ICELAND  
NORWAY  
SWEDEN**

**PUBLISHER: NORSK BETONGFORENING  
POSTBOKS 2312, SOLLI  
NO - 0201 OSLO  
NORWAY**

**STOCKHOLM/OSLO, JUNE 2019**



## **Preface**

The interest in publishing in Nordic Concrete Research (NCR) has increased substantially during recent years. In 2016, we only published ten papers in the spring and autumn issues together. The following two years, we published 15 and 18 papers, respectively. This issue contains nine papers and we have already a number of papers that are under review. Two times ten papers make the amount that we have anticipated when negotiating with our publishing company, De Gruyter. I guess that it is the decision to make NCR an Open Access paper that has played the main role in making our scientific journal more popular among authors. Most of these are young PhD students or young university researchers that conduct their research on projects with governmental support. The pressure from these governmental funding agencies in publishing the results open for everyone without cost increases. NCR fulfils that requirement.

In August next year, the Nordic Concrete Federation and the Norwegian Concrete Association are organizing the 24th Nordic Concrete Research Symposium in the lovely city Sandefjord on the Norwegian south coast. The call for papers is still open. However, the symposium proceedings allow only very short papers. What about combining a short summary paper to be presented at the symposium with a full paper submitted to NCR? The editor will be in Sandefjord during these days and you are most welcome to discuss these matters with me.

Stockholm in June 2019

Johan Silfwerbrand  
Editor of NCR



**CONTENTS**

1	Jukka Lahdensivu, Elina Lahdensivu & Arto Köliö <b>Case Study on the 20 Years Propagation of Carbonation in Existing Concrete Facades and Balconies</b>	1
2	Mette Rica Geiker & Emmanuel Gallucci <b>Clays as SCM – Reactivity of Uncalcined Kaolinite and Bentonite, and Impact on Phase Assemblage and Strength Development of PC Mortars</b>	13
3	Ingrid Lande Larsen, Otto Terjesen, Rein Terje Thorstensen & Terje Kanstad <b>Use of Concrete for Road Infrastructure: A SWOT Analysis Related to the three Catchwords Sustainability, Industrialisation and Digitalisation</b>	31
4	Jelena Zivkovic & Jan Arve Øverli <b>Failure of Lightweight Aggregate Concrete in Compression under Stress Gradients</b>	51
5	Faez Sayahi, Mats Emborg, Hans Hedlund & Andrzej Cwirzen <b>Plastic Shrinkage Cracking of Self-compacting Concrete: Influence of Capillary Pressure and Dormant Period</b>	67
6	Mikko Kuusela, Olli Asp & Anssi Laaksonen <b>Cracking of the End Diaphragm of a Post-tensioned Beam Bridge</b>	89
7	Rasoul Nilforoush <b>A Refined Model for Predicting Concrete-Related Failure Load of Tension Loaded Cast-in-Place Headed Anchors in Uncracked Concrete</b>	105
8	Tuomas Lehtonen, Matias Hirvikoski & Julius Rajamäki <b>Comparison of Punching Shear Design in Finland According to the Current and the Former Method</b>	131
9	Fahim Al-Neshawy, Teemu Ojala & Jouni Punkki <b>Stability of Air Content in Fresh Concretes with PCE-Based Superplasticizers</b>	145
	<b>Research Council &amp; Editorial Board of NCR</b>	159



	
© Article authors. This is an open access article distributed under the Creative Commons Attribution-NonCommercial-NoDerivs licens. ( <a href="http://creativecommons.org/licenses/by-nc-nd/3.0/">http://creativecommons.org/licenses/by-nc-nd/3.0/</a> ).	ISSN online 2545-2819 ISSN print 0800-6377
DOI: 10.2478/ncr-2019-0004	Received: March 26, 2019 Revision received: June 19, 2019 Accepted: June 25, 2019

## Case Study on the 20 Years Propagation of Carbonation in Existing Concrete Facades and Balconies



Jukka Lahdensivu, DSc.  
Adjunct Professor at Tampere University  
Faculty of Built Environment  
Korkeakoulunkatu 10  
FI-33720 Tampere, Finland  
[jukka.lahdensivu@tuni.fi](mailto:jukka.lahdensivu@tuni.fi)



Elina Lahdensivu  
MSc Student at Tampere University  
Faculty of Built Environment  
Korkeakoulunkatu 10,  
FI-33720 Tampere, Finland  
[elina.lahdensivu@tuni.fi](mailto:elina.lahdensivu@tuni.fi)



Arto Köliö, DSc.  
Postdoctoral researcher, Tampere University  
Faculty of Built Environment  
Korkeakoulunkatu 10  
FI-33720 Tampere, Finland  
[arto.kolio@tuni.fi](mailto:arto.kolio@tuni.fi)

## ABSTRACT

In the most service life models of reinforced concrete structures the initiation phase is the most crucial, because according to models, service life of the structure will end underestimation on conservative side when carbonation achieves the reinforcement for the first time. The square root model is widely used in predicting carbonation depth of reinforced concrete. The model is based on diffusion laws and thereby arguable for inhomogeneous concrete. The model was evaluated by field measurements from one existing concrete building by conducting condition investigation twice at a time interval of 20 years. Samples were taken from exposed aggregate concrete sandwich panels and balcony side panels. Compared to the data collected from large number of buildings, the measured carbonation rates were very common for Finnish concrete buildings made during the 1960s and 1970s. According to this study, in solid concrete the progress of carbonation of concrete can be predicted reliably with Fick's second law. This model, however, gives too pessimistic predictions for concrete suffering from freeze-thaw damage. Therefore, a new model has been presented for damaged concrete.

**Key words:** Concrete, carbonation, corrosion, field measurement, service life, modelling

## 1. INTRODUCTION

### 1.1 General

Carbonation induced corrosion of reinforcement together with freeze-thaw damage in concrete facades and balconies are the major degradation mechanisms causing repair need in Finland [1]. Corrosion of steel reinforcement in concrete is commonly regarded as an electrochemical phenomenon meaning that corroding reinforcement works as a mixed electrode where cathodic and anodic areas are formed on the steel surface [2]. The size of anodes and cathodes determine the nature of corrosion. Corrosion due to carbonation is general over the reinforcement surface with relatively evenly spaced cathode and anode areas. [3]. Because concrete protects steel from corrosion as a protective layer for the reinforcement, corrosion does not initiate immediately. This has been taken into account by depicting reinforcement corrosion as a process consisting of two or more consecutive phases [4, 5, 6] as shown in Figure 1.

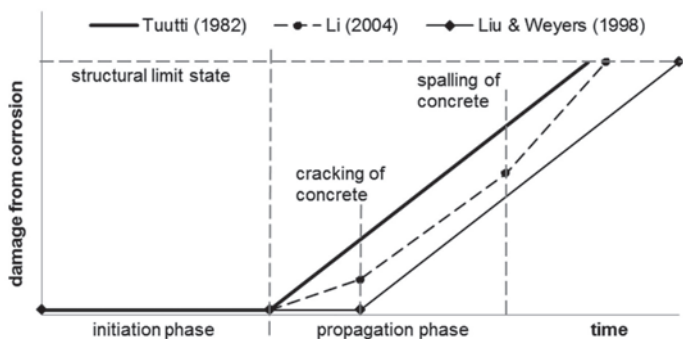


Figure 1 – Models for reinforcement corrosion utilizing the principle of initiation and propagation.

According to Finnish concrete codes [7, 8] the service life of reinforced concrete structure will end when carbonation of concrete achieves the steel bar first time. To determine the service life of the reinforced concrete structure it is important that the calculation of the initiation phase is correct.

This study analyses the actual observed progress of carbonation on concrete facades and balconies in one actual building situated in Helsinki suburban area by a survey of condition assessments made in 1994 [9] and repeated sampling in 2014 enabling a 20 years' time interval. This information is contrasted to the widely used square root model to evaluate its use in predicting the progression of carbonation in concrete structures exposed to Nordic climate.

## 1.2 Case study in Jakomäki

Jakomäki suburban area is situated in northern Helsinki, approximately 16 km northeast from the city centre. The area consists of 31 blocks of flats, which are built between 1967 and 1969. In general, those blocks of flats have 3 to 6 floors. About 5800 inhabitants live in the area. Tampere University of Technology (TUT) carried out large condition investigation program to the concrete facades and balconies of Jakomäki buildings in 1994. Several degradation mechanisms were found on concrete facades and balconies after 25 years' service life. Based on the condition assessment a large renovation program was launched in 1996 and it ended in 2014 to the demolition of two last buildings, while others were renovated.



*Figure 2 – Case building in 1994 during first condition investigation.*

The case study building was completed in 1968. It was a 5-storey block of flats with exposed aggregate concrete facades and suspended concrete balconies, see Figure 2. The structure of this building consist of prefabricated sandwich facade panels and balcony slab, frame and parapet elements. The surface of facades was exposed aggregate concrete and balconies were painted with non-permeable paint. The typical dimensions of precast panels of the case study building are shown in Table 1 based on the first condition assessment. The case study building was demolished

in the end of 2014 after being in service for 46 years. Before demolition several samples were taken from facades and balcony frames.

*Table 1 – Dimensions and reinforcement properties of prefabricated facades and balconies in the case study building.*

Structure/ unit	Dimensions	Reinforcement	Comments
Facade sandwich panel	Outer layer 61-82 mm, Inner layer 80 mm (non-bearing) or 150 mm (load bearing)	Outer layer: mesh 3 mm with 150 mm spacing, edge rebars 6 and 8 mm, trusses connecting outer and Inner layer spacing 600 mm, aux. reinforcement/lifting straps	Thickness of thermal insulation 78-99 mm, elastic element joints (polymer sealants), no ventilation gap = dries slowly
Balcony slab	thickness 130-160 mm (sloped upper surface)	Bearing reinforcement: 10 mm spacing 100-150 mm in the lower section of the slab upper section: tie rods, aux. reinforcement, lifting straps	Water drainage system: spout pipe through the parapet. No waterproofing.
Balcony side panel	Thickness 162-166 mm	8 mm mesh in both surfaces with 200 mm spacing edge rebars 10 mm, aux. reinforcement/lifting straps	The bottom side panel is suspended from the head of partition wall with six 18 mm rebars.
Balcony parapet	Thickness 95-98 mm	Heavy reinforcement near both surfaces, rebars 6 mm spacing 150 mm	Connected to side panel with steel plates and bolts.

## 2. CARBONATION OF CONCRETE

Carbonation of concrete is a chemical reaction between alkaline hydrates of concrete and carbon dioxide gas both dissolved in concrete pore water. The reaction product is calcium carbonate, which lowers the pH of the pore water (and concrete) gradually to a level where steel can corrode. As the alkaline hydroxide reservoir in concrete is limited, it is eventually completely consumed leading to the neutralization of concrete. Since carbon dioxide originates from the atmosphere the concrete structure is exposed to, carbonation advances inside concrete as a carbonation front and the diffusion of it inside concrete serves as a limiting factor for its progression. [10].

Factors that limit carbonation are (1) moisture content of concrete, (2) reserve of calcium hydroxide in cement, (3) impermeability of concrete, (4) low CO<sub>2</sub> concentrations in air and (5) outwards diffusion of OH<sup>-</sup> in water saturated concrete [5]. These factors are related to e.g. the thickness of concrete cover, high cement content and pore structure as well as the water-cement ratio of the concrete as actual properties of the structure [10, 11] and the amount of atmospheric CO<sub>2</sub> and precipitation (sources of moisture) as external environment properties.

Because carbonation is controlled by the diffusion of carbon dioxide inside concrete, it is commonly modelled with a square root relationship with time, see Eq. 1, [5] derived from the differential equation of diffusion [9]. The rate of carbonation, including the effect of both internal and external factors, is in this model denoted by the factor  $k$  (carbonation coefficient).

$$x = k \cdot \sqrt{t} \quad (1)$$

where,

$x$  = carbonation depth

$k$  = carbonation coefficient [ $\text{mm} \cdot \text{a}^{-1/2}$ ]

$t$  = time [a].

Extensive research has been conducted since late 1950s on relating carbonation depth in laboratory environment to such concrete properties as water-cement ratio, compressive strength and curing as well as controlled levels of carbon dioxide or relative humidity [11].

Many models have been proposed for depicting carbonation all utilizing the square root relationship [10]. Although, it is mentioned that empirical measurements indicate that, especially in the cases of concrete exposed to rain, the exponent for time is less than 0.5 [5, 12]. Therefore, the square root equation should be regarded as an upper limit for carbonation in these cases. The square root equation has also been developed to separate the influence of different individual internal and external factors to carbonation [13] and further on to isolate the influence of specific factors [14] opposed to the one parameter in Eq. 1.

### **3. CONDITION INVESTIGATIONS MADE FOR THE BUILDING**

#### **3.1 Condition investigation**

In Finland concrete facades have been subjected to condition assessments since late 1980s and data measured by standardised procedures [15] have been produced in majority of these assessments. The condition assessments consist of preliminary desk top studies, visual observation and rating in situ, measurements and sampling in situ and laboratory tests [16].

Carbonation depth has been measured from core samples taken during the field investigation by spraying freshly cut surface with a phenolphthalein pH indicator. The carbonation depth is measured from a single sample as the average and the maximum depth of the carbonation front. By average 12 samples have been taken from one building during a single condition assessment in general [16].

#### **3.2 First condition investigation**

First condition assessment was carried out to the case study building during the summer 1994. Totally 44 concrete samples were taken from facades and balconies. According to original construction plans concrete grade was C25/30 both in facades and balconies.

Concrete samples with the diameter of 50 mm were extracted from the outer concrete layer of the façade and from balcony panels by a diamond core drill. The samples were marked on site and

stored for further studies and analyses. All of the samples were subjected to a thorough visual inspection for the concrete quality (e.g. pores, capillaries, and any damage visible to the naked eye). Also the carbonation depth was recorded during the visual inspection.

Part of the samples were then prepared for the microscopic study from a thin section and part of the samples were tested for the pore structure (capillary porosity and protective porosity) by the standard SFS 4475 and tensile strength by the standard SFS 5445. In standard SFS 4475 the weight of concrete samples is measured as oven dry ( $+ 105 \pm 2$  °C), capillary saturated and pressure saturated (all pores forced to saturate high pressure). Protective pore ratio  $p_r$  is calculated as follows:

$$p_r = (p_p - p_c) / (p_c - p_d) \quad (2)$$

where,

$p_r$  = protective pore ratio [-]

$p_p$  = weight of the totally saturated sample [g]

$p_c$  = weight of the capillary saturated sample [g]

$p_d$  = weight of the oven dry sample [g].

All of the analyses carried out with the samples aimed at determining the quality, durability properties and evident degradation in the façade concrete.

### 3.3 Sampling 2014

After the initial condition investigation in 1994, a decision was made concerning the case study building that no repairs were carried out. Instead the case study building, and its neighbouring building were meant to serve as long as possible and then be demolished. Before the demolishing of the building in the late autumn 2014, a repeated sampling was carried out.

Core samples were extracted from the outer concrete layer of the façade and from balcony frame panels in the same way as in the first condition investigation. The sampling was focused on the south-eastern façade to enable the collection of as many samples as possible in limited time. 14 samples with the diameter of 75 mm and three samples with the diameter of 100 mm were taken from the exposed aggregate facades and four samples with the diameter of 75 mm were taken from the balcony panels. The samples were inspected visually in the same way, but by a different person than in the first time. The inspection is standardized so that error caused by different assessor should be minimised. The carbonation depth was recorded during the visual inspection from all samples.

The samples were then tested for the pore structure (capillary porosity and protective porosity) by the standard SFS 4475. The larger samples (diameter of 100 mm) were subjected to compressive strength tests.

Before demolishing the building, sampling was carried out during late autumn 2014. Totally 21 samples were drilled from balcony frames and facades.

## 4. RESULTS AND DISCUSSION

### 4.1 Carbonation of concrete

Carbonation of concrete was measured with phenolphthalein pH indicator on the surface of drilled sample. All measurements are shown in Table 2.

In 1994 condition investigation carbonation of concrete was 12 mm in average with 3.8 mm standard deviation in exposed aggregate concrete facades. This mean  $2.28 \text{ mm a}^{-1/2}$  average carbonation coefficient. Only some single corrosion damage was seen. 13 % of measured cover depths were less than 5 mm. On the other hand, exposed aggregate concrete facades were found non-freeze-thaw resistant and some incipient freeze-thaw damage was detected in thin-section analyses. The cracking caused by the freeze-thaw damage may also slightly have increased the carbonation rate of the façade concrete. For this reason, also the freeze-thaw resistance and damage are briefly discussed in next chapter.

*Table 2 – Carbonation depth of concrete and carbonation coefficient of all samples measured in 1994 and 2014.*

1994			2014		
Sample number	Carbonation depth av. [mm]	Carbonation coefficient, $k$ [mm/a <sup>0.5</sup> ]	Sample number	Carbonation depth av. [mm]	Carbonation coefficient, $k$ [mm/a <sup>0.5</sup> ]
6a2 sw	4	0,78	J1 sw	12	1.77
6a5 sw	17	3.33	J2 sw	10	1.47
6a7 sw	20	3.92	J3 sw	8	1.18
6a8 sw	16	3.14	J4 sw	11	1.62
6a9 sw	6	1.18	J5 sw	11	1.62
6a14 sw	10	1.96	J6 sw	13	1.92
6a15 sw	9	1.77	J7 sw	14	2.06
6a16 sw	11	2.16	J8 sw	11	1.62
6a17 sw	12	2.35	J9 sw	12	1.77
6a19 sw	5	0.98	J10 sw	11	1.62
6a20 sw	14	2.75	J11 sw	8	1.18
6a21 sw	8	1.57	J12 sw	9	1.33
6a22 sw	10	1.96	J13 sw	10	1.47
6a23 sw	12	2.35	J14 sw	9	1.33
6a26 sw	11	2.16	J15 sw	11	1.62
6a35 sw	9	1.77	J16 sw	12	1.77
6a36 sw	14	2.75	J17 sw	11	1.62
6a37 sw	16	3.14	average	10.8	1.59
6a38 sw	13	2.55			
6a39 sw	12	2.35	PP2 sp	22	3.24
6a41 sw	6	1.18	PP3 sp	26	3.83
6a44 sw	15	2.94	PP4 sp	19	2.80
average	12,0	2,28	PP5 sp	15	2.21
			average	20.5	3.02
6a27 sp	17	3.33			
6a28 sp	13	2.55			
average	15.0	2.94			

sw = Exposed aggregate concrete sandwich panel

sp = Balcony side panel

In balcony frames carbonation of concrete was 15 mm in average (only two samples), which mean  $2.94 \text{ mm a}^{-1/2}$  average carbonation coefficient. Cover depths were too small in general, 70 % of reinforcement was in the depth of 15 mm or less. There were several visually seen corrosion damages in balcony frames.

In 2014 average carbonation in balcony frames was 21 mm with 4.0 mm standard deviation. In facades average carbonation depth was 11 mm with 1.6 mm standard deviation.

#### 4.2 Freeze-thaw resistance and capillary porosity of concrete

Façade panels were not freeze-thaw resistant in the first place. Protective pore ratio was approximately 0.05 (std. dev. 0.02). According to Finnish national concrete guideline in force during construction of this building, the protective pore ratio should be 0.20 at least for freeze-thaw resistant concrete [16]. Serious and wide spread freeze-thaw damage was detected in thin-section analyses during the first condition investigation. Capillary porosity of concrete was 6.5 vol-% (std. dev. 0.9), which is the most typical value for exposed aggregate concrete made in 1960s and 1970s [1].

From balcony structures, only two samples were taken. Protective pore ratio was 0.12 and 0.14, which is the most common value for balconies in that era. Concrete was not freeze-thaw resistant in balconies either, but no damage was detected.

#### 4.3 Progress of carbonation during last 20 years

The first condition investigation was carried out in 1994 with 38 samples in total from different kinds of concrete panels and from all the facades, but only 7 of them were comparable to the second investigations samples. The second investigation took place in 2014 with 21 samples but only from south-eastern facade. Results can be seen in table 3.

Table 3 – Average and standard deviation of measured carbonation coefficient.

	1994			2014		
	Outer surface av. [mm]	Carbonation coefficient, $k$ [mm/a <sup>0.5</sup> ]	Standard deviation	Outer surface av. [mm]	Carbonation coefficient, $k$ [mm/a <sup>0.5</sup> ]	Standard deviation
Sandwich panels to South-East	10 (n=5)	2.04	0.53	11 (n=17)	1.59	0.24
Balcony side panels to South-East	15 (n=2)	2.94	-	21 (n=4)	3.02	0.69

On the balcony side panels, the carbonation coefficient is approximately the same in both investigations. The standard deviation is also approximately the same, and carbonation curve follows Eq. (1) nicely, see Figure 3. On the other hand, in sandwich panels, the carbonation

coefficient is very different between 1994 and 2014. Results from 2014 investigation do not follow the equation based on the first condition investigation, see blue dots in Figure 3.

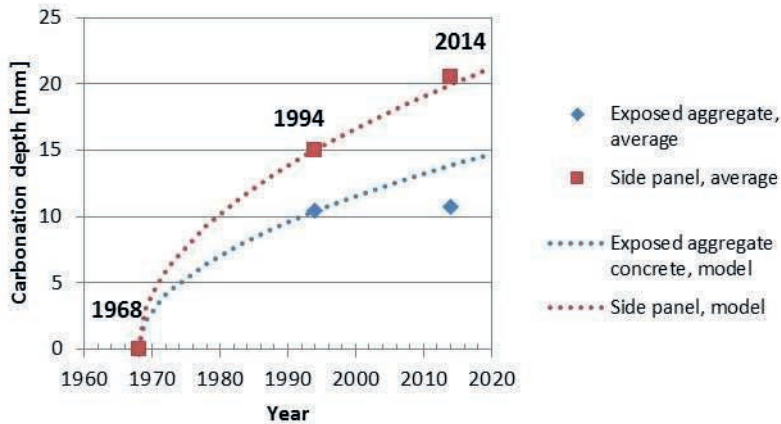


Figure 3 – Average carbonation of concrete in 1994 and 2014 and computational progress of carbonation based on the first condition investigation.

In balcony side panels the carbonation coefficient in 1994 was  $2.94 \text{ mm/a}^{0.5}$  and in 2014  $3.02 \text{ mm/a}^{0.5}$  (std. dev. 0.69). The side panels' carbonation coefficient was approximately same in both condition investigations and the difference is caused by inaccuracy in measurement of carbonation depth and inhomogeneity of concrete.

In sandwich panels in 1994 the carbonation coefficient was  $2.04 \text{ mm/a}^{0.5}$  (std. dev. 0.53) and in 2014 it was  $1.59 \text{ mm/a}^{0.5}$  (std. dev. 0.24) which is significantly lower. Lahdensivu [1] has analysed the carbonation of concrete facades and balconies under real outside environment in a study of 947 concrete buildings built between 1960 and 1996. The average carbonation coefficient for exposed aggregate concrete panels was  $1.96 \text{ mm/a}^{0.5}$  in concrete panels made in 1960s and 1970s. Compared to this average carbonation coefficient of  $2.04 \text{ mm/a}^{0.5}$  from 1994 made condition investigation, it gives an impression on very common concrete for that era. However, freeze-thaw damage was detected in exposed aggregate concrete as early as 1994. Freeze-thaw damage has caused small cracking to concrete surface and, therefore, diffusion of carbon dioxide into concrete pore structure is faster than in solid concrete. Therefore, the calculated carbonation coefficient does not illustrate the progress of carbonation deeper in the concrete.

In Figure 4 is presented different carbonation curves for sandwich panels to illustrate the progress of the carbonation.

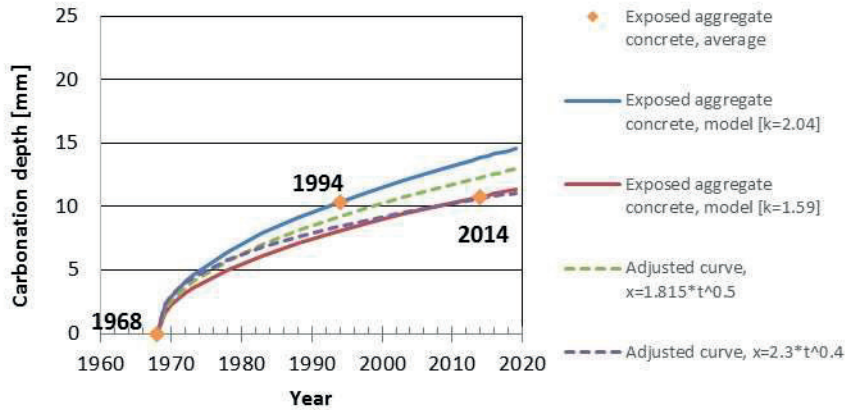


Figure 4 – Average carbonation of concrete in sandwich panels in 1994 and 2014 and computational progress of carbonation based on two different models.

In Figure 4 the progress of carbonation has been adjusted with square root model (Eq. (1)), too. Three different curves have been drawn: carbonation coefficient  $k = 2.04$  (first condition investigation),  $k = 1.59$  (second condition investigation) and  $k = 1.815$  (average of both condition investigations). The fourth curve in the Figure is adjusted based on Eq. (3).

If Eq. (1) and the uppermost curve are used for freeze-thaw damaged concrete, it gives too pessimistic estimation on the condition of the reinforcement's state of corrosion. In 2014 it gives 4 mm deeper carbonation depth than it actually is. Therefore, more reinforcement will be exposed and repaired than actually needed. This could lead to too heavy repair, e.g. overlapping instead of patch repair.

If Eq. (1) is used in this case together with the curve based on the latter carbonation measurements ( $k = 1.59$ ) it gives a too positive estimation of what has happened in the early age of the façade. This may lead to the underestimation of the time that certain depth of the concrete has been carbonated. This may lead to underestimation of the corrosion propagation of rebars and the underestimation of rebar diameter loss or the need of patch repair.

The Eq. (1) together with the adjusted average curve work adequately in describing both early and later phases but any prediction made using this trend line will overestimate the further progression of carbonation.

Eq. (1) gives too pessimistic values for carbonation in freeze-thaw damaged concrete as can be seen in Figure 4. For freeze-thaw damaged concrete the adjusted 4 curve follows Eq. (3):

$$x = k t^{0.4} \quad (3)$$

where,

$x$  = carbonation depth

$k$  = carbonation coefficient [ $\text{mm} \cdot \text{a}^{-0.4}$ ]

$t$  = time [a].

## 5. CONCLUSIONS

In this case study several samples were taken from one building only. Samples were taken from exposed aggregate concrete sandwich panels and balcony side panels. Compared to the data collected from large number of buildings, the measured carbonation rates were very common, as well as the large deviation of carbonation rates.

In the most service life models of reinforced concrete structures the initiation phase is the most crucial, because according to models, service life of the structure will end when carbonation achieves the reinforcement for the first time. Initiation phase is usually modelled after simplified solution of Fick's second law. In solid concrete the progress of carbonation can be predicted reliably with usually used square root model. This model, however, gives too pessimistic predictions for concrete suffering from freeze-thaw damage.

Freeze-thaw damaged concrete (in this case exposed aggregate concrete) may alter the progression of carbonation from the conventional model. Carbonation is slowed down due to more moisture being able to penetrate the freeze-thaw cracked concrete and the concrete stays wet for longer time. The slowing down can be described by altering the time-exponent in the common square root relationship Eq. (3) instead of Eq. (1).

## REFERENCES

1. Lahdensivu J: "Durability properties and actual deterioration of Finnish concrete facades and balconies". Tampere, Tampere University of Technology, Publication 1028, 2012, 117 p + app. 37 p.
2. Page C. L: "Basic Principles of Corrosion". In: Schiessl P (editor): Corrosion of Steel in Concrete, London, Chapman and Hall, 1988, pp. 3–21.
3. Schiessl P: "Corrosion of Steel in Concrete". London, Chapman and Hall, 1988, 101 p.
4. Liu Y & Weyers R E: "Modelling the Time-to-Corrosion Cracking in Chloride Contaminated Reinforced Concrete Structures". *ACI Materials Journal*, Vol. 95, No. 6, 1998, pp. 675 – 681.
5. Tuutti K: "Corrosion of steel in concrete". Stockholm, Swedish Cement and Concrete Research Institute, CBI Research 4:82, 1982, 304 p.
6. Li C Q: "Reliability service life prediction of corrosion affected concrete structures". *ASCE Journal of Structural Engineering*, Vol. 130(10), 2004, pp. 1570–1577.
7. Concrete Association of Finland: "Concrete codes". Helsinki, The Concrete Association of Finland, BY 65, 2016, 164 p. (in Finnish)
8. Concrete Association of Finland: "Selection of concrete and service life design – guideline for construction designers". Helsinki, The Concrete Association of Finland, BY 68, 2016, 95 p. (in Finnish)
9. Pentti, M., Huopainen, J., Lahdensivu J., Mäkelä, K. "Condition investigation of concrete facades and balconies in Jakomäki". Tampere University of Technology, Research report 274, 1994, 93 p. (in Finnish)
10. Parrott L J: "A review of carbonation in reinforced concrete". Cement and Concrete Association, Slough, UK, 1987, 42 p.
11. Huopainen J: "Carbonation of concrete facades – a field study". Tampere University of Technology, MSc thesis, 1997. (in Finnish)
12. Neves R, Branco F A & de Brito J: "A method for the use of accelerated carbonation tests in durability design". *Construction and Building Materials*, Vol. 36, 2012, pp. 585-591.

13. fib Bulletin No. 34. “Model Code for Service Life Design”. International Federation for Structural Concrete, Lausanne, 2006, 116 p.
14. Concrete Association of Finland: “Condition assessment manual of concrete facades and balconies”. Helsinki, The Concrete Association of Finland, BY 42, 2013, 163 p. (in Finnish)
15. Lahdensivu J, Varjonen S, Pakkala T & Köliö A: „Systematic condition assessment of concrete facades and balconies exposed to outdoor climate”. *International Journal of Sustainable Building Technology and Urban Development*, Vol. 4:3, 2013, pp. 199-209.
16. Concrete Association of Finland: “Durability of concrete structures”. Helsinki, The Concrete Association of Finland, BY 9, 1976, 44 p. (in Finnish)

	
© Article authors. This is an open access article distributed under the Creative Commons Attribution-NonCommercial-NoDerivs licens. ( <a href="http://creativecommons.org/licenses/by-nc-nd/3.0/">http://creativecommons.org/licenses/by-nc-nd/3.0/</a> ).	ISSN online 2545-2819 ISSN print 0800-6377
DOI: 10.2478/ncr-2019-0006	Received: March 31, 2019 Revision received: June 16, 2019 Accepted: June 18, 2019

### Clays as SCM – Reactivity of Uncalcined Kaolinite and Bentonite, and Impact on Phase Assemblage and Strength Development of PC Mortars



Mette Rica Geiker, Dr.  
Professor, Department of Structural Engineering  
Norwegian University of Science and Technology (NTNU)  
NO-7491 Trondheim, Norway  
[mette.geiker@ntnu.no](mailto:mette.geiker@ntnu.no)



Emmanuel Gallucci, Dr.  
Principle Scientist, Sika Technology AG  
Tüffenwies 16  
CH-8048 Zürich, Switzerland  
[gallucci.emmanuel@ch.sika.com](mailto:gallucci.emmanuel@ch.sika.com)

#### ABSTRACT

The impact of substitution of cement paste with uncalcined clay (bentonite and kaolinite) in the range of 5% by volume of paste on the development of hydration and properties of mortar was investigated. Two issues were addressed, the expected filler effect of the dispersed sub-micron clay particles, and the possible chemical reactivity of the clay.

The study indicated that Portland cement paste may be modified by addition of well dispersed clay and that the impact includes accelerated cement hydration as well as altered distribution of products. Compressive strength development was accelerated, but later age strength was reduced, especially for the bentonite mixes. In contrast, microscopic porosity measurements indicated no detrimental impact on the coarse capillary porosity.

The investigation indicates that for durability related engineering properties, the application of uncalcined clay might be a potential means for reduction of the clinker factor in concrete in support of sustainability.

**Key words:** Uncalcined clay, cement hydration,

## 1. INTRODUCTION

By mass, cement is the largest manufactured product on Earth. Because of the increased demand, the emissions due to cement production are increasing. It was in 2016 estimated by some sources to be around 10% of the total anthropogenic CO<sub>2</sub> or about 6% of the total anthropogenic greenhouse gasses [1]. Thus, even relatively small improvements may have a measurable impact. Alternative materials, so-called supplementary cementitious materials (SCMs), have for many years been used to improve and engineer the properties of concrete. During the last decades, SCMs are in addition increasingly used to reduce the amount of Portland clinker in concrete [1, 2].

Lothenbach et al. summarized the impact of SCMs on cement hydration [3]. At early ages, the so-called “filler effect” increases the rate and/or prolongs the Portland clinker reaction. There seems to be two mechanisms of the filler effect: a) apparent higher water-to-cement ratios (w/c): in case of the same water-to-solid ratio, the space for early cement hydration is relatively larger if part of the solid is none or slowly reacting, and b) enhanced nucleation: especially fine filler brings extra surfaces for nucleation. Examples of the mechanisms can e.g. be found in [4, 5]. SCMs react later; their reaction depends on composition, fineness and glassy phases and increases with pH and temperature [3]. Reactive SCMs affects the amount and kind of hydrates formed and thus the engineering properties of the concrete. At normal levels of substitution of silica rich SCMs, the major changes are reduced portlandite and reduced Ca/Si ratio of the calcium-silicate hydrates (C-S-H) [3]. Alumina-rich SCMs increase the aluminates containing hydrates and the aluminium-uptake in C-S-H [3].

Clay particles may increase the cement’s reaction rate. The effect of selected layer silicates (kaolinite and bentonite) on the rate of reaction of cement was investigated by Krøyer et al. [6] using <sup>29</sup>Si magic-angle spinning (MAS) nuclear magnetic resonance (NMR) on cement pastes (white Portland cement, 10% bentonite or 20% kaolinite by weight of cement, w/c = 0.5) hydrated between 1 and 90 days at 20°C. They found that the clays increased the rate of cement hydration. The clay addition affected the SiO<sub>4</sub>-chains in the C-S-H gel. In average kaolinite caused longer SiO<sub>4</sub>-chains to form, whereas bentonite resulted in slightly shorter SiO<sub>4</sub>-chains, which at later age increased in length. Using <sup>27</sup>Al MAS NMR Krøyer et al. [6] observed similar rate of ettringite formation in pastes with and without kaolinite and that kaolinite was not consumed. The increased rate of cement hydration in pastes with clay was explained by clay particles acting as nucleation sites for the cement hydrates.

Lindgreen et al. [7] focusing on the dispersion of the clay particles in the mix found that addition of micro and nanosized particles to cementitious mixtures may result in a more homogeneous and finer pore structure. This seems mainly to be due to the growth of C-S-H on the clay particle surfaces, where the nanostructure of the C-S-H seems to depend on the size, shape and charge of the clay particles. Based on the observations, they argued that the cement paste structure and porosity can e.g. be engineered by addition of non-pozzolanic layer silicates having specific particle shapes and surface properties (e.g. surface charge and specific surface area).

In addition, both bentonite and kaolinite have finer grain size than cement (mean grain size at  $300 \cdot 50 \cdot 3$  nm, and  $0.1\text{-}1$   $\mu\text{m}$ , respectively, compared to cement with a typical main grain size of  $10$   $\mu\text{m}$ ), they will, when well dispersed, affect the packing of the solid particles of the paste in areas where the packing is restricted, i.e. in interfacial zones (ITZ) towards larger particles as coarse aggregates and reinforcement. Some clays adsorb water, the amount depending on the structure of and the ionic layer on the clay. Possible adsorbed water may also affect the final pore structure.

The purpose of the present study was to investigate the effect of uncalcined bentonite and kaolinite clays on the microstructure of Portland cement mortar. Bentonite clay adsorbs water, whereas kaolinite clay according to Lindgreen et al. [7] does not. Two issues were addressed, the expected filler effect of the dispersed sub-micron clay particles, and the possible chemical reactivity of the clay.

## 2. EXPERIMENTAL

The impact of uncalcined clay was investigated on mortars with 20% or 40% sand by volume and target  $w/c = 0.50$  (Series 1) and  $w/c = 0.48$  (Series 2a) and on pastes with target  $w/c=0.48$  (Series 2b). The clay substituted approximately 5% by volume of cement paste. The bentonite used was found to adsorb 37% water by weight. This was taken into account in Series 1 (by adding a comparable amount of additional water to the bentonite mix), but not in Series 2. Series 1 focused on microstructure and phase assemblage in well hydrated specimens, whereas Series 2 focused on property development.

### 2.1 Raw materials

The cement was an CEM I 52,5 R - SR5 (according to EN 197-1:2011) white Portland cement from Aalborg Portland A/S, Denmark. The chemical composition of the cement is given in Table 1. The phase composition of the cement is given in Table 2. Selected physical properties are given in Table 3. Due to time difference between undertaking Series 1 and Series 2, two different batches of cement with slightly different properties were used.

The clays were kaolinite and bentonite from English China Clay and Leca, respectively. The chemical composition of the bentonite and the kaolinite is given in Table 1. Bentonite was microcrystalline (60% illite/smectite, 18% illite and 22% kaolinite); the phase composition is given in Table 3. The illite/smectite component had an average thickness of 3 nm with net negative charge and pronounced colloidal properties. Kaolinite is crystalline, almost neutral sized  $0.1\text{-}1$   $\mu\text{m}$  particles with slight colloidal properties. [7] Based on water sorption and suction measurements on the bentonite in artificial pore solution the amount of water adsorbed by the clay in a cement paste was estimated to 37% [8], see Figure 1. The absorption of the kaolinite was according to Lindgreen et al. 0% [7].

The sand was sea sand (Søsand 0-2, kl. E, SA-Storebæltsand). The grading of the sand is given in Table 5.

For Series 2, Sika® Viscocrete PC2 was used as superplasticizer and Sika® Stabilizer-4R was used as stabilizer.

*Table 1 - Oxide composition and loss on ignition (LOI) of cement (Series 1 (S1) [4], Series 2 (S2) own measurements) and the bentonite and kaolinite clays [6], LOI Series 2 own measurements.*

Raw material	SiO <sub>2</sub>	Al <sub>2</sub> O <sub>3</sub>	Fe <sub>2</sub> O <sub>3</sub>	CaO	MgO	SO <sub>3</sub>	TiO <sub>2</sub>	K <sub>2</sub> O	Na <sub>2</sub> O	MnO	P <sub>2</sub> O <sub>5</sub>	LOI <sup>a</sup>
Cement (S1)	24.7	2.1	0.4	68.7	0.6	1.8	0.1	0.1	0.2	0.0	0.5	1.0
Cement (S2)	24.1	2.6	0.5	68.9	0.7	2.2	0.1	0.1	0.2	0.0	0.3	1.0
Bentonite	55.2	19.3	8.3	0.9	2.8	0.9	0	0.9	3.7	-	-	8.0 (11.5)
Kaolinite	68.8	18.6	1.6	0.3	0.7	-	1.2	2.1	0.2	-	-	6.7 (6.3)

Note a: Series 2 in brackets

*Table 2 - Phase composition of cement. Series 1 [4]; Series 2 own measurements.*

	C <sub>3</sub> S	C <sub>2</sub> S	C <sub>3</sub> A	C <sub>4</sub> AF	C $\bar{S}$ ·2H	C $\bar{S}$ ·½H	C $\bar{S}$	CH
Series 1	68.1	23.6	3.6	0	0	0.5	2.9	0.5
Series 2	70.6	20.3	3.1	0.3	2.1	1.0	0.2	1.2

Note: No traces of lime C, periclase M, arcanite K $\bar{S}$  or calcite C $\bar{C}$

*Table 3 - Selected physical properties of cement and clays [7].*

Property	Unit	Cement	Bentonite	Kaolinite
Mean grain size	µm	d50=10	Laths, thickness 0.003 width ~0.1 length 0.1 – 0.5	Platy; thickness 0.005-0.05 width 0.005-0.05
Specific surface	m <sup>2</sup> /kg	397	79.000	19.000
Density	kg/m <sup>3</sup>	3135	2600	2600
Absorption	%	-	37	0

*Table 4 - Phase composition of clays.*

	Quartz	Muscovite 2M	Muscovite 3T	Dickite	Illite	Amorphous
Kaolinite	52.1	19.1	0.3	24.1	-	4.5
Bentonite	3.8	39.0	-	11.5	2.0	43.7

*Table 5 - Grading of sand (% passing).*

Sieve size, mm	0.075	0.125	0.25	0.5	1	2
Series 1 and 2	0.2	0.5	14.4	74.7	97.3	100

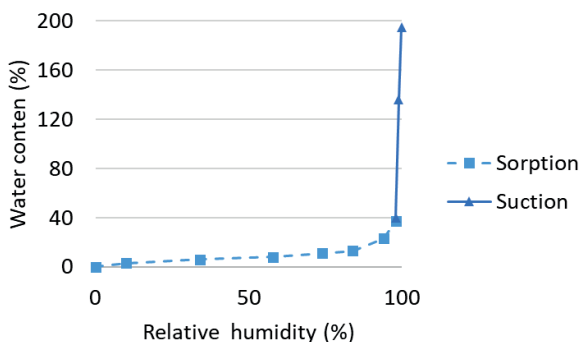


Figure 1 – Sorption and suction isotherm for bentonite in artificial pore fluid, after [8].

## 2.2 Mix designs, casting and curing

Mortars with the compositions given in Table 6 and Table 7 (Series 1 by volume and weight), and Table 8 (Series 2 by weight), and pastes with the compositions given in Table 9 were prepared. The mix id includes abbreviations of the binder (R: Cement (reference); K: Cement plus kaolinite, B: Cement plus bentonite) and the volume fraction of sand. In the preparation of the specimens, the dispersion of the layer silicates in the mixtures was carefully considered. The clays were added as suspensions, premixing the clay with water for 24 hours to facilitate dispersion [9]. The free water includes the LOI of the clays, but excludes water adsorbed in bentonite (37%). For Series 1, the free water content by weight of cement is comparable, while for Series 2, the total water content by weight of cement is comparable.

### Series 1

Series 1 was prepared with target  $w/c = 0.50$ , the actual  $w/c$  includes unexpected water (LOI, Table 1) in the clays. Mixing of Series 1 was undertaken in a custom-made 2 litres container by means of custom-made mixer. The clays were dispersed by premixing the clays with mixing water; the ratio was either 1:2.5 or 1:4. Bleeding was not observed except a faint bleeding for the reference. Specimens were stored in closed plastic containers, which were kept in a water saturated atmosphere at room temperature to limit long-term evaporation and carbonation reactions.

Table 6 - Mortar compositions, Series 1 (volume fractions).

Mix	Cement	Kaolinite	Bentonite incl. ads. water	Sand	Ads. water in clay	Free water	Total water
R_20	0.310	0.000	0.000	0.20	0.000	0.490	0.490
B_20	0.293	0.000	0.037	0.20	0.025	0.468	0.493
K_20	0.294	0.037	0.000	0.20	0.000	0.470	0.470
R_40	0.233	0.000	0.000	0.40	0.000	0.368	0.368
B_40	0.219	0.000	0.028	0.40	0.018	0.350	0.369
K_40	0.220	0.028	0.000	0.40	0.000	0.353	0.353

Table 7 - Mortar compositions, Series 1 (weight per kg cement).

Mix	Cement	Kaolinite	Bentonite incl. ads. water	Sand	Ads. water in clay	Free water	Total water
R_20	1.000	0.000	0.000	0.536	0.000	0.500	0.500
B_20	1.000	0.000	0.099	0.575	0.027	0.506	0.533
K_20	1.000	0.104	0.000	0.564	0.000	0.507	0.507
R_40	1.000	0.000	0.000	1.430	0.000	0.500	0.500
B_40	1.000	0.000	0.099	1.533	0.027	0.506	0.533
K_40	1.000	0.104	0.000	1.505	0.000	0.507	0.507

*Series 2*

Mortars were mixed according to EN 196-1 [10]. The batch size corresponded to approximately 2.5 kg cement. The clays were dispersed by premixing the clays with mixing water; bentonite with all mixing water, kaolinite with half. Table spread flow was measured immediately after mixing and 100 g of mortar were used for isothermal calorimetry. For each of those mix designs, 12 40·40·160 mm<sup>3</sup> prisms were cast according to EN 196-1 for compressive strength testing, two per testing age. The prisms were kept in moulds during the first 24 hrs, 2 prisms were immediately tested after demoulding for the 1 day properties, and the others were stored in climatic chamber at 23°C under 95% relative humidity (RH).

Pastes were mixed using a Heidolph mixer at 2000 rpm for 2 min. The batch size corresponded to approximately 100 g cement.

Table 8 - Mortar compositions, Series 2a (weight per kg cement).

Mix	Cement	Kaolinite	Bentonite incl. ads. water	Sand	Stabilizer 1)	Super- plasticizer 1)	Ads. water	Free water 2)	Total water
R_40	1.000	0.000	0.000	1.430	0.001		0.000	0.480	0.480
B_40	1.000	0.000	0.098	1.533		0.002	0.026	0.464	0.490
K_40	1.000	0.104	0.000	1.505		0.001	0.000	0.488	0.488

1) Excluding water

2) Including water in admixtures

Table 9 - Paste compositions, Series 2b (weight per kg cement).

Mix	Cement	Kaolinite	Bentonite incl. ads. water	Stabilizer 1)	Super- plasticizer 1)	Ads. water	Free water 2)	Total water
R_40	1.000	0.000	0.000	0.001	-	0.000	0.480	0.480
B_40	1.000	0.000	0.098	-	0.002	0.026	0.464	0.490
K_40	1.000	0.104	0.000	-	0.001	0.000	0.488	0.488

1) Excluding water

2) Including water in admixtures

### 2.3 Methods

An overview of the investigations undertaken on the hardening and hardened specimens is given in Table 10. In addition, the workability of mortars in Series 2 was characterized. The development of hydration was determined by calorimetry up to 2 days and X-ray diffraction (XRD), thermogravimetry (TGA) and scanning electron microscopy (SEM) at later age. The microstructure was investigated using SEM and low temperature calorimetry (thermoporometry, LTC). Strength development was determined on mortar prisms.

SEM of the paste and mortar specimens prepared in Series 1 showed that only the mortars with 40 % sand had an acceptable homogeneity for quantitative analysis, indicating an inefficient mixing of pastes and of mortars with 20 % sand. The pastes and the mortars with 20 % sand were therefore only used for determination of the chemical composition.

#### *Fresh concrete properties, spread*

The consistency of the mortars in Series 2 was determined using an automated shocking spread flow table according to EN 1015-03 [11].

*Table 10 - Overview of investigations on hardening and hardened specimens. S1 and S2 refer to Series 1 and Series 2. XRD: X-ray diffraction, TGA: thermogravimetry, SEM: scanning electron microscopy; LTC: low temperature calorimetry.*

Binder	Material	Id	Calorimetry 0-2 days	XRD 1, 3, 7, 21, 35, 70 days	TGA 7 days	SEM 35 days	120 days	LTC 120 days	Strength 1, 3, 7, 21, 35, 113 days
Cement (R)	Paste	R_0		S2	S2	S1	S1		
	Mortar, 20% sand	R_20				S1	S1	S1	
	Mortar 40% sand	R_40	S2				S1	S1	S2
Cement plus bentonite (B)	Paste	B_0		S2	S2	S1	S1		
	Mortar, 20% sand	B_20				S1	S1	S1	
	Mortar 40% sand	B_40	S2				S1	S1	S2
Cement plus kaolinite (K)	Paste	K_0		S2	S2	S1	S1		
	Mortar, 20% sand	K_20				S1	S1	S1	
	Mortar 40% sand	K_40	S2				S1	S1	S2

#### *Calorimetry*

Development of hydration was measured by isothermal calorimetry on 100 g mortar specimens (Series 2) using and ICal 8000 device from Calmetrix. Hydration kinetics were followed continuously from right after mixing until 48 hours.

#### *X-ray diffraction (XRD)*

Phase assemblage of raw materials and hydrated specimens was measured using X-ray diffraction XRD D8 advance device from Bruker, and calculated through Rietveld analysis using Bruker Topas 5.0. Amorphous content was always back calculated using an external standard strategy

and pure metallic silicon as standard. Raw materials were measured as received while hydrated specimen were measured on hardened pastes which hydration was stopped at desired ages through solvent exchange in isopropyl alcohol, then dried at low temperature and ground.

#### *Thermogravimetry (TGA)*

TGA diagrams were acquired using a Netzsch TG209 F1 Libra device at a heating rate of 10°K/mn and under constant flow of pure nitrogen. For each measurement, 15 to 20 mg of specimen were used and measurements were run in alumina crucibles. Raw materials were processed as provided while hydrated paste specimens were evaluated after isopropanol exchange and oven drying as described in the XRD section.

#### *Scanning electron microscopy (SEM)*

Prior to scanning electron microscopy (SEM) investigation, vertical slices of around 5 mm thickness were cut in the specimens at given ages (Table 10) and dried by solvent exchange in isopropyl alcohol for one week. The slices were then epoxy impregnated (epotek 301) and softly polished with decreasing grades of diamond crystallites. Backscattered Electron Imaging was done at 15 kV with FEI Quanta 200 SEM. EDS elemental characterisation was done with a PGT SiLi detector using pure standard minerals.

#### *Low temperature calorimetry (LTC)*

Cylindrical specimens of mortar (40% sand, Series 1) with diameter of 15 mm and a length of 70 mm were used. The specimens were vacuum saturated prior to testing according to NT Build 492 [12]. Excess liquid was removed with a damp cloth. After low temperature calorimetry (LTC) the specimens were dried at 105°C ± 5°C until constant weight was achieved (± 0.1°C) to determine the total water content of the specimens.

The LTC measurements were performed in a low temperature Calvet Micro Calorimeter, model “-196°C to 200°C”, from Setaram [13,14]. Temperature cycles were made between +20°C and minimum -48°C. The cooling and heating rates were -3.3°C/h and +4.1°C/h, respectively. No nucleation agent was used. The measured temperatures were registered in the reference block. The heat flow is given as the apparent heat capacity; calculated using the method of Sellevold and Bager [15].

#### *Mechanical testing*

Compressive strength testing was undertaken on mortar prisms with 40% sand (Series 2) according to EN 196-1 [10], two prisms were tested for flexural strength and the obtained four half prisms were tested for compressive strength and testing was undertaken after 1, 3, 7, 21, 35 and 113 days in a high humidity climate chamber.

The air content of mortars was determined in accordance with [16] on the basis of the density of theoretically air void free mortar and the weight at testing. The compressive strength was normalized to an air content of 2 vol % using Bolomey’s equation, e.g. [16].

### **3. RESULTS AND DISCUSSION**

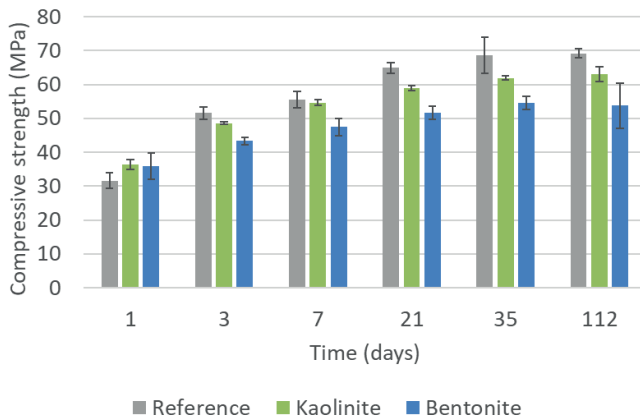
Addition of kaolinite and bentonite changed the colour of the white Portland paste and mortar from white/light grey to brownish and dark, respectively. The clay addition also affected the consistency of the fresh mortars, which is illustrated by the need for superplasticizer to obtain

comparable spread (Table 8). Furthermore, despite similar spread right after mixing, the spread 30 min after mixing was significantly lower in the case of the kaolinite mix compared to the reference, see Figure 2. The reduced consistency of the clay mixes is expected to have affected the degree of compaction of the mortars, which is indicated in the air content calculated based on the difference between theoretical and measured densities of the prisms cast in Series 2 (average calculated air content 1.3%, 3.8% and 2.8% for the reference, bentonite and kaolinite mortar prisms).



Figure 2 - Spread of mortar (Series 2) 30 min after mixing; left: reference; right: kaolinite.

Compressive strength development of mortars with 40 % sand (Series 2) is shown in Figure 3; both as measured and when calculated to constant (2%) air content. The coefficient of variation was 1-7%. Both kaolinite and bentonite are observed to enhance the early age strength development, whereas the strength at later age appears compromised, especially when substituting cement paste with the bentonite. It should be noted that the bentonite used was found to adsorb 37% water by weight. This was not taken into account in Series 2, see Table 8.



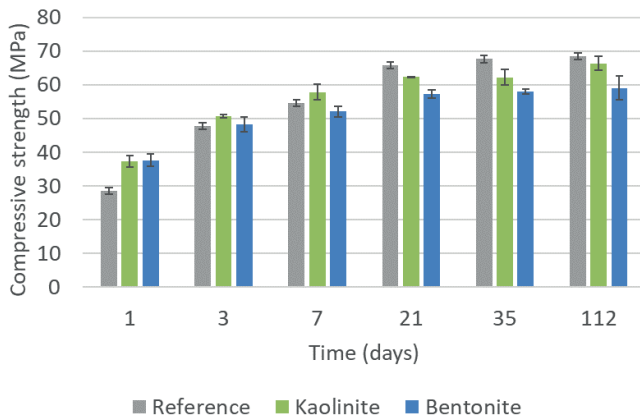


Figure 3 - Development of compressive strength of mortar prisms (Series 2); top) as measured, bottom: recalculated to 2% air content in mortars. The error bars mark the standard deviation.

The impact of the clay addition on the early hydration is illustrated in Figure 4. Both clays are observed to cause an earlier start of the acceleration period and a higher maximum heat flow of the aluminates peak (second peak in the acceleration period, bentonite slightly more than kaolinite). Considering the two mechanisms for filler effects described in [3]: a) increased space causing prolonged hydration and b) increased nucleation sites causing acceleration, the effect of the clays are in these mixes enhanced nucleation. This is according to expectations considering the large surface area of the clays.

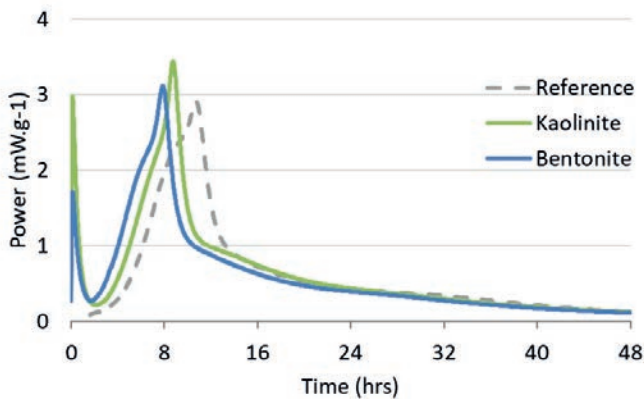


Figure 4 - Development of early hydration as a function of time determined by calorimetry of mortars (Series 2) hydrated sealed at 20°C. The data are normalized to weight of mortar.

Two issues are addressed: the expected filler effect of the clay particles and the possible chemical reactivity of the clay.

### Filler effect of bentonite and kaolinite

Both bentonite and kaolinite had a filler effect on the hydration of the cement. A shorter induction period and an increased reaction rate in the acceleration period (nucleation rate) were observed by calorimetry (Figure 4).

The observations were confirmed by XRD. Figure 5 shows the degree of hydration (DoH) measured from normalized content of  $C_3S$ ,  $C_2S$ ,  $C_3A$  and calcium sulphate. ( $C_4AF$  not taken into account since present in very little amount and probably not reactive). The impact of clays at early age is clearly visible with a lower DoH for cement and higher DoH for bentonite, in agreement with hydration kinetics measured by calorimetry. At later ages the differences level out. Most probably, higher DoH of bentonite at 70 days is mainly due to a sudden drop of belite content as measured by XRD and is most likely caused by an artefact.

The observed filler effect of the clays is in agreement with  $^{29}Si$  MAS NMR data [6]. They found that bentonite and kaolinite accelerated the hydration of alite and belite. However, using  $^{27}Al$  MAS NMR Krøyer et al. [6] did not observe a corresponding filler effect of kaolinite clay on the reactions of the aluminate phases (bentonite clay was not investigated due to the impact of iron on the aluminium spectrum).

The accelerating effect of the clays might be explained by either a) higher ionic concentrations due to reduction of available water upon adsorption by the clays or b) more surface available for nucleation of hydrates.

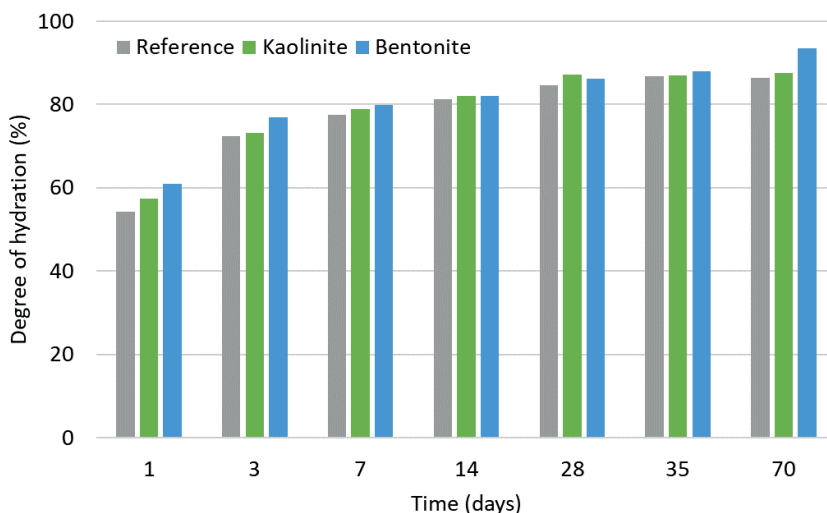


Figure 5 - Development of hydration as a function of time of pastes hydrated at 23°C and 95% RH (remains of  $C_3S$ ,  $C_2S$ ,  $C_3A$ , and calcium sulphate determined by XRD and Rietveld analysis).

A qualitative microstructural description is obtained from micrographs of the 120 days old specimens (Figure 6). The systems were highly hydrated as only belite and large alite grains remained unhydrated. At the used resolution, the microstructure of the hydrated systems was not much affected by the clays: same patterns for calcium hydroxide (CH) precipitates, same

morphology of C-S-H “blobs”, and similar pore morphology are observed. Also, the ITZ was apparently not affected as much CH was observed.

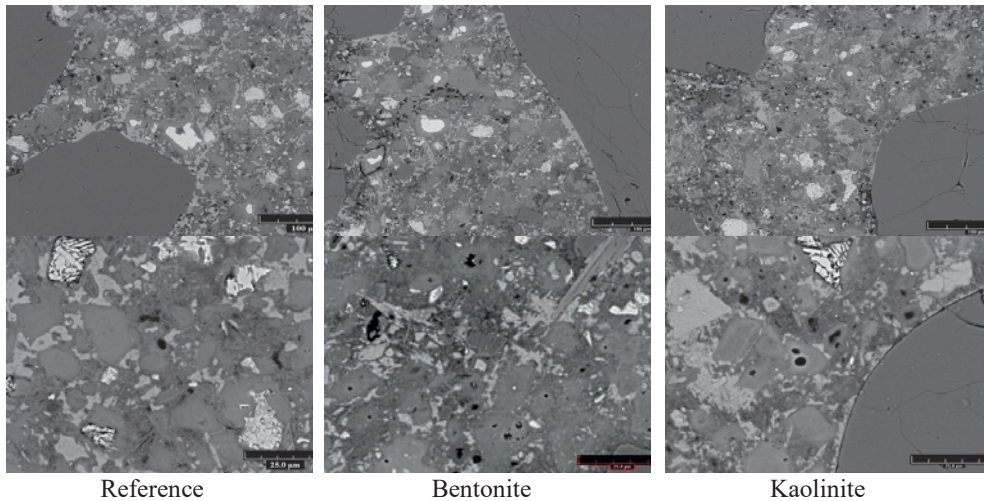


Figure 6 - Micrographs of highly hydrated systems (120 days old mortars, 40% sand, Series 1). Width: Upper 0.5 mm, lower 0.1 mm.

Figure 7 shows that the substitution of cement paste by bentonite and kaolinite clays had nearly no impact on the long-term coarse capillary porosity, whereas the presence of clay appears beneficial at early age. Capillary pores were measured by image analysis down to a size of 350 nm. The data given in Figure 7 are normalised to the content of paste and the error bars indicate  $\pm$  one standard deviation. Also, the substitution of cement paste by bentonite and kaolinite clays had limited impact on ice formation (threshold pores and percolated pore volume) in well hydrated systems, see Figure 8. The measured differences in total freezable water are within observed variations between similar samples [17]. Freezing in the clay samples started at relatively higher temperature, indicating less super-cooling (facilitated ice nucleation). The apparent higher amount of freezable water detected in the high temperature range might indicate larger volumes of percolated pores and possibly larger volumes of coarser pore sizes. The microscopic observations (Figure 6) appears to be in contradiction to the lower compressive strength observed for the Series 2 mortars containing clay (see Figure 3); the low temperature calorimetry data are non-conclusive. It should be noted that the measured water adsorption by bentonite (37% water by weight) was taken into account in the mix design for Series 1, but not for Series 2, which should favour the performance of the bentonite mix in Series 2 compared to Series 1.

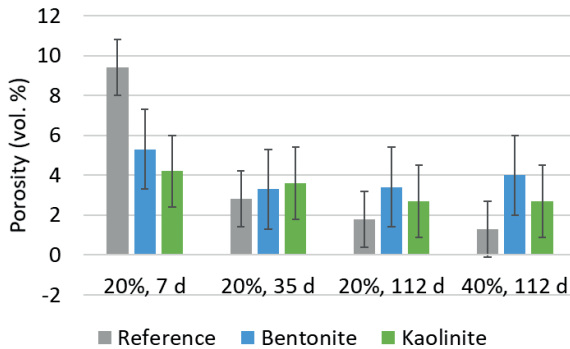
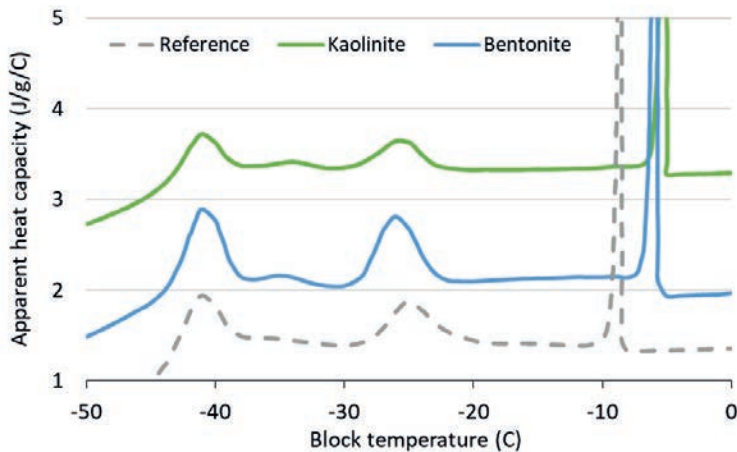


Figure 7 - Capillary porosity (> 350 nm) measured by image analysis on mortars (Series 1). The standard deviation was 0.5-2 vol. %. The error bars mark the standard deviation.

#### Pozzolanic reactivity of bentonite and kaolinite

Krøyer et al. [6] found by  $^{29}\text{Si}$  MAS NMR that the bentonite and the kaolinite clays were not consumed during cement hydration. In contrast to this, we observed at 35 days, the assemblage of phases in equilibrium differs between pure Portland cement (PC) mortar or blend with bentonite and kaolinite clays (Figure 9). In the pure PC mortar, the matrix is mainly a mixture of calcium hydroxide (CH), C-S-H (C-S-H and CH are not marked on the plot but are theoretically at the origin position (no sulphur and no aluminium) and ettringite (Aft) (trend of the grey EDS spot analysis along the line C-S-H / Aft) while in the case of the presence of clay systems, the aluminate phase in equilibrium with C-S-H and CH is calcium monosulfoaluminate (AFm) (scattered blue and green points along the line C-S-H / AFm). This difference in the stability of the AFt vs AFm is probably due to excess aluminate ions brought in the system by the clays and which thermodynamically stabilise the AFm.



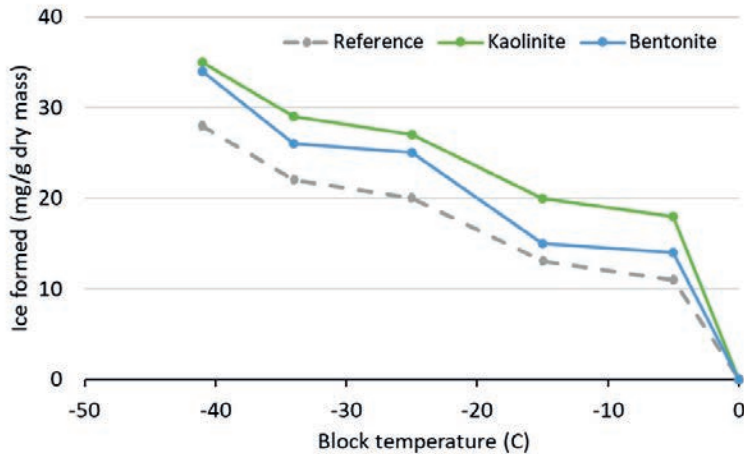


Figure 8 - Threshold pores (upper graph) and ice formation (lower graph) determined by low temperature calorimetry on 120 days old mortars (40% sand, Series 1).

Figure 10 shows that while the pure PC mortar (grey points) had equilibrium between C-S-H, CH and eventually a bit of AFm/AFt, the clay systems had a strong dispersion of the data towards Al and Si rich regions. This is explained by a fine intermixing between C-S-H and the clays at the micron level. In agreement with the composition of the two clays, the trends of the blue and green points vary slightly from each other with the bentonite system tending towards Si richer assemblages while the kaolinite system tends towards an Al richer phase.

The composition of the inner-C-S-H was measured in thick homogeneous rims around unreacted cement grains (or in the place of totally reacted grains) to avoid the intermixing with other phases. The Ca/Si or Ca/(Si+Al) ratios as well as the level of substitution of Si by Al are not affected at all by the presence of the clays in the concerned mixes compared to the reference mortar (Figure 11). This shows that a) if a pozzolanic reaction of the clays has started, it is not developed enough to affect the composition of the so-called inner-C-S-H (or HD-C-S-H); and b) that even if the clays have slightly decomposed (which is supported by observations of Al brought by the clays to the phase assemblage of the matrices, see Figure 9), this does not affect the inner-C-S-H (no change in the Al content).

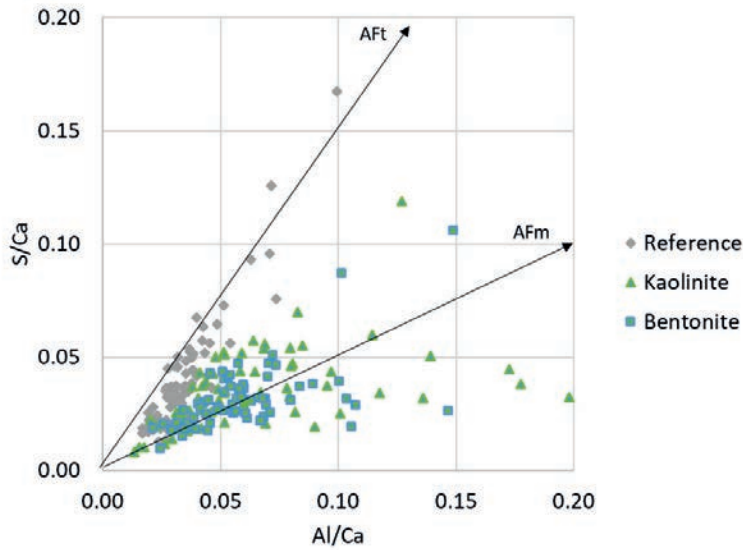


Figure 9 - S/Ca ratio versus Al/Ca ratio of the outer products in 35 days old systems (mortar 20% sand, Series 1). The lower graph is a zoom of the upper.

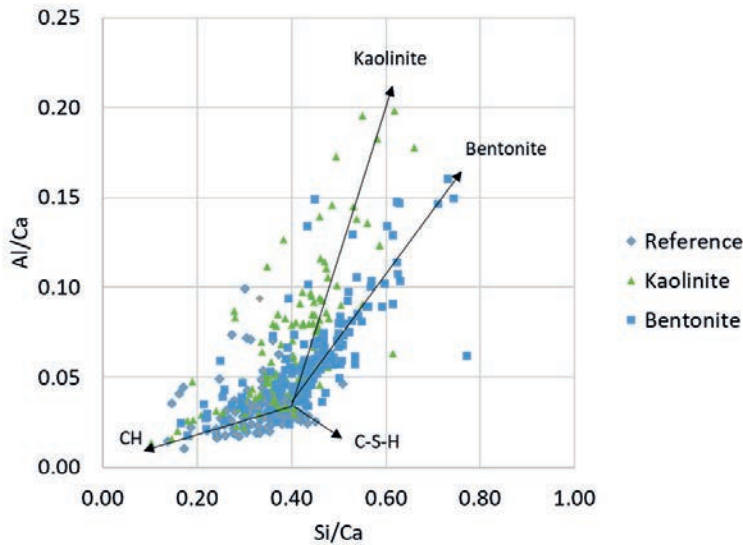


Figure 10 - Al/Ca ratio versus Si/Ca ratio of outer products in 35 days old mortars (20 % sand, Series 1).

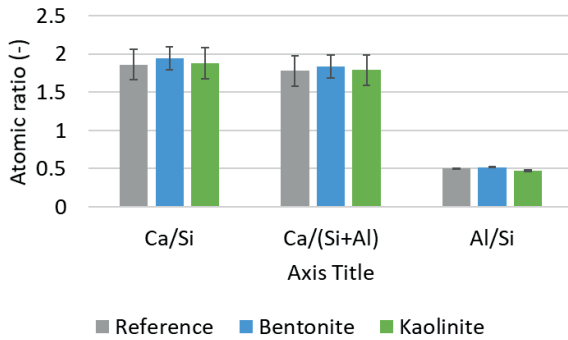


Figure 11 - Composition of inner-C-S-H measured in thick homogeneous rims around unreacted cement grains (112 old mortar specimens with 40% sand, Series 1). The standard deviation was approx. 0.05 for Ca/Si and Ca/(Si+Al); approx. 0.02 for Al/Si.

The pozzolanic activity of the clays has been roughly assessed with the evolution of the CH content in each system (Figure 12). The results given in Figure 12 were renormalized to 140 g of paste (those are not percent). The TGA data for the clay specimens at 35 and 70 days were affected by minor carbonation, which was corrected for assuming all carbonation came from CH. The CH content in the clay specimens appears at later age slightly lower than the CH content in the reference. This might indicate pozzolanic reactivity of the uncalcined clays.

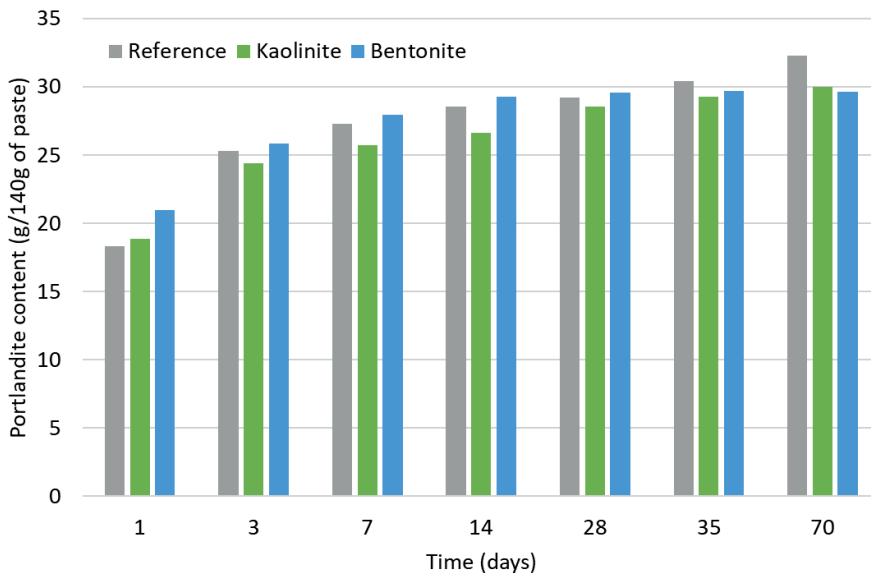


Figure 12 - Portlandite content determined by TGA, paste specimens (Series 2).

#### 4. CONCLUSIONS

The impact of substitution of cement paste with uncalcined clay in the range of 5% by volume of paste on the development of hydration and properties of mortar was investigated. Two issues were addressed, the expected filler effect of the dispersed sub-micron clay particles, and the possible chemical reactivity of the clay.

Well dispersed uncalcined bentonite and kaolinite clays were observed by calorimetry and XRD to have a filler effect increasing early cement reactions; this explains a measured higher early strength development mortars with clay. In combination with observations of clay intermixed with outer C-S-H this indicates that the clays act as nucleation sites; i.e. have a filler effect.

SEM-EDS indicated a fine intermixing of clay and outer hydration products, the inner products were unaltered. Observations of phase assemblages in the clay systems towards AFm instead of AFt indicated some decomposition of the clays. Measurement of portlandite consumption by TGA also indicated potential pozzolanic reactivity of the uncalcined clays.

Replacement of cement paste by clay keeping the free water-to-cement ratio (w/c) constant (Series 1) appeared to lead to unaltered large capillary porosity in the well hydrated systems. In contrast, replacement of cement paste by clay keeping the total water-to-cement constant (Series 2) led to reduction of later strength, especially for the mortar with bentonite. This indicates that the addition of uncalcined alters the porosity reducing compressive strength, but not necessarily durability related properties. The investigations calls for more detailed porosity and durability studies.

#### 5. ACKNOWLEDGEMENTS

The first author would like to thank the Danish Technical Research Council (STVF project 2020-00-0005) and Professor Karen Scrivener, EPFL, Switzerland, for financial support. Also Senior Scientist Holger Lindgreen, GEUS, and Associate Professor Jørgen Skibsted, iNANO, NMR Centret, Aarhus Universitet, are thanked for the collaboration.

#### 6. REFERENCES

1. Scrivener KL, John VM, Gartner EM: “Eco-efficient cements. Potential, economically viable solutions for a low-CO<sub>2</sub>, cement-based materials industry.” In United Nations Environment Program, Paris, France, 2016, 64 pp.
2. Damtoft JS, Lukasiak J, Herfort D, Sorrentino D, Gartner EM: ”Sustainable development and climate change initiatives”. *Cement and Concrete Research*, Vol. 38, No. 2, 2008, pp. 115-127.
3. Lothenbach B, Scrivener K and Hooton RD: “Supplementary cementitious materials”. *Cement and Concrete Research*, Vol. 41, No. 12, 2011, pp. 1244-1256.
4. Kocaba V: “Development and evaluation of methods to follow microstructural development of cementitious systems including slags”, PhD thesis, EPFL-TH4523, EPFL, Laboratoire des Matériaux de Construction, Lausanne, Switzerland, 2009, 263 pp.
5. Fernandez Lopez R: “Calcined clayey soils as a potential replacement for cement in developing countries”. PhD thesis, EPFL-TH4302, EPFL, Laboratoire des Matériaux de Construction, Lausanne, Switzerland, 2009, 178 pp.

6. Krøyer H, Lindgreen H, Jakobsen HJ, Skibsted J: “Hydration of Portland cement in the presence of clay minerals studied by  $^{29}\text{Si}$  and  $^{27}\text{Al}$  MAS NMR spectroscopy”. *Advances in Cement Research*, Vol. 15, No. 3, 2003, pp. 103-112.
7. Lindgreen H, Geiker M, Krøyer H, Springer N, Skibsted J H: “Microstructure engineering of Portland cement pastes and mortars through addition of ultrafine layer silicates”. *Cement and Concrete Composites*, Vol. 30, No. 8, 2008, pp. 686-699.
8. Kjeldsen AM: “New Concretes through addition of layer silicates. Bentonite clay soprtion.” *Personal communication*, 2003.
9. Lindgreen HB, Jakobsen HJ, Geiker MR, Stang H, Krøyer H, Skibsted JB: “*Suspension of clays in water for addition to e.g. concrete*”. Patent WO2008052554A1, 2008-05-08.
10. EN 196-1. Methods of testing cement - Part 1: Determination of strength, 2005.
11. EN 1015-03. Determination of consistence of fresh mortar (by flow table), 2004
12. NordTest, NT Build 492, “Concrete, mortar and cement-based repair materials: chloride migration coefficient from non-steady-state migration experiments”, approved 1999-11.
13. Fontenay le Sage de C, Sellevold EJ: “Ice formation in hardened cement pastes – I. Mature water-saturated pastes”, *Durability of building materials and components*, ASTM STP 691, 1980.
14. Bager D & Sellevold EJ: “Ice formation in hardened cement paste, Part I – Room temperature cured pastes”, *Cement and Concrete Research*, Vol. 16, 1986, pp. 709–20.
15. Sellevold EJ & Bager D: “Low temperature calorimetry as a pore structure probe”, *Proceedings, 7<sup>th</sup> International Congress on the Chemistry of Cement*, Paris, vol. 4; 1981.
16. Osbæk B: “The influence of air content by assessing the pozzolanic activity of fly ash by strength testing”. *Cement and Concrete Research*, Vol. 15, No. 1, 1985. pp. 53-64.
17. Wu, M, Fridh K, Johannesson B & Geiker M: "Impact of sample crushing on porosity characterization of hardened cement pastes by low temperature calorimetry: Comparison of powder and cylinder samples." *Thermochimica Acta*, Vol. 665, 2018, pp. 11-19.

	
© Article authors. This is an open access article distributed under the Creative Commons Attribution-NonCommercial-NoDerivs license. ( <a href="http://creativecommons.org/licenses/by-nc-nd/3.0/">http://creativecommons.org/licenses/by-nc-nd/3.0/</a> ).	ISSN online 2545-2819 ISSN print 0800-6377
DOI: 10.2478/ncr-2019-0007	Received: March 31, 2019 Revision received: June 14, 2019 Accepted: June 18, 2019

## Use of Concrete for Road Infrastructure: A SWOT Analysis Related to the three Catchwords Sustainability, Industrialisation and Digitalisation



Ingrid Lande Larsen, M.Sc.  
PhD Research Fellow, University of Agder  
Jon Lilletuns vei 9,  
4879 Grimstad  
[ingrid.larsen@uia.no](mailto:ingrid.larsen@uia.no)



Otto Terjesen, M.Sc.  
PhD Research Fellow, University of Agder  
Jon Lilletuns vei 9,  
4879 Grimstad  
[otto.terjesen@uia.no](mailto:otto.terjesen@uia.no)



Rein Terje Thorstensen, M.Sc.  
Professor, University of Agder  
Jon Lilletuns vei 9,  
4879 Grimstad  
[rein.t.thorstensen@uia.no](mailto:rein.t.thorstensen@uia.no)



Terje Kanstad, Ph.D.  
Professor, Norwegian University of Science and Technology  
Richard Birkelands vei 1A,  
7491 Trondheim  
[terje.kanstand@ntnu.no](mailto:terje.kanstand@ntnu.no)

## ABSTRACT

This paper aims at identifying the direction for more sustainable development of the use of concrete in road infrastructure in an industrialised context.

The increase in the global mean temperature is one of the most severe challenges today. The concrete industry is responsible for significant emissions of greenhouse gases, most attributable to cement production. However, concrete is one of the most important building materials in the world and indispensable for the societal development in countries at all development stages. Thus, the concrete industry needs to take measures for reducing emissions.

This paper investigates possible directions for the development of the concrete industry, to reduce climatic impact and accommodate positive societal growth. The investigation is carried out as a SWOT analysis, focusing on three terms dominating the present discussion on any development within the construction industry; sustainability, industrialisation and digitalisation. The result is a thorough discussion and a set of recommendations for the direction of future research and innovation on sustainable use of concrete in the construction of road infrastructure. The major opportunities and threats are summarised in the conclusions, and future research to be carried out in two of the authors' PhD-projects are described.

**Keywords:** Concrete infrastructure, Sustainability, Digitalisation, Industrialisation, SWOT analysis

## 1. INTRODUCTION

In a world striving towards sustainable development, economic, societal and environmental perspectives have to be implemented simultaneously. All these issues are challenging to the construction industry. The development of road infrastructure is fundamental to the growth of the economy and welfare.

The increase in the global mean temperature is currently one of the most severe sustainability issues [1]. According to the Intergovernmental Panel on Climate Change (IPCC), the global mean temperature has increased rapidly during the last 50 years and is projected to rise [2], clearly influenced by anthropogenic emissions of greenhouse gases. The prospects of continued emission are further global warming and long-lasting changes in climate systems, increasing the severe, negative effects for people and ecosystems [2]. In order to limit these climate change risks, substantial reductions in greenhouse gas emissions are required. Consequently, IPCC has established global reduction goals on CO<sub>2</sub> emissions for all nations. Norway has committed to reduce the greenhouse gas emissions of at least 40% compared to 1990 levels within 2030 [3]. Other authoritative sources define different goals and different deadlines for when these goals are to be met. Accommodating different time span requires implementation of different strategies. Some of these strategies might even be conflicting [4].

Concrete is indispensable for the development of countries at all development stages. The annual growth in consumption of concrete in highly developed countries has diminished. However, densely populated countries are still rapidly evolving, consequently experiencing rapid growth in the use of concrete. Hence, the world's demand for concrete is growing. The development of societies and climatic changes lay premises for the development and use of concrete. Three topics

are presently dominating most discussions on industrial and societal development; i) sustainability, ii) industrialisation and iii) digitalisation. These terms are widely used, and each user tends to define the contents slightly differently.

In this article, a functional definition of the three catchwords is stated, and SWOT analysis is executed for each of them to help identify the direction of sustainable development for the use of concrete in road infrastructure in an industrialised context. The main opportunities and threats are summarised and used as a basis for future research in the first and second authors' PhD-projects.

### 3. RESEARCH METHODOLOGY

A SWOT analysis is executed to investigate premises for sustainable growth in the use of concrete in road infrastructure, and to identify research needs. SWOT is an abbreviation for the four terms Strength, Weaknesses, Opportunities and Threats, and is a well-known tool in economic and strategic management. The usage is not equally widespread in the construction industry. However, successful implementation is emerging. Jiang et al. [5] applied a SWOT analysis to study off-site construction in China. Yuan [6] correspondingly investigated successful construction waste management. Both gathered data for the SWOT analysis through interviews or meetings with experts, combined with literature reviews including research, regulations, and government reports [5, 6]. Inspired by these researchers, we applied a model for research methods, as illustrated in Figure 1. In this study, SWOT analysis is executed on the three topics; i) sustainability, ii) industrialisation and iii) digitalisation.

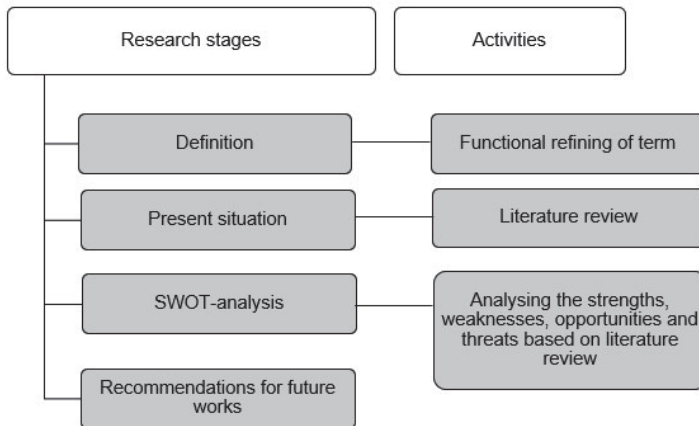


Figure 1 – Applied research methodology, similar to Yuan [6].

## 4. RESULTS AND DISCUSSION

### 4.1 Sustainable use of concrete

#### *Functional refinement of the term*

Sustainability is a broad term, often defined as “development that meets the needs of the present without compromising the ability of future generations to meet their own needs”. This definition originates from *Report of the World Commission on Environment and Development: Our Common Future* from 1987 [7]. Different professions tend to define sustainability in either economic, societal or environmental terms. All of these are necessary preconditions to support the needs of future generations. In the book *Concrete and Sustainability*, Jahren and Sui [4] define sustainability as the overlapping field between economy, social development and environment. This definition is applied in the following discussion. However, “environment” is in this paper limited to climate issues only.



Figure 2 – Sustainable development, according to [4].

#### *Present situation*

According to the European Cement Association CEMBUREAU, the total cement production in the world was 4.65 billion tonnes in 2016 [8]. Anticipating an average world consumption of 300 kg cement per cubic meter concrete, the present cement production corresponds to almost 2 cubic meters of concrete per capita in the world is built into new structures every year. Scrivener et al. [9] illustrate the consumption of concrete relative to other conventional building materials (Figure 3, left part), according to a report based on the efforts from the UN Environmental Program Sustainable Building and Climate Initiative. Without even arguing on the mechanical and durability properties, price or geographic availability of various materials, it is evident from a pure volume perspective that no other material can fully substitute concrete.

According to Jahren and Sui [4], Asia is responsible for approximately 80% of the world’s cement production. The major part of the growth is due to countries outside China, India and Japan [4], mostly in low-income countries with strong growth in population and economy. In 2017 the world population was 7.6 billion, expected to grow to nearly 10 billion within 2050 [10]. Assuming cement consumption per capita remaining at today’s level, the production of cement will have to grow to 6 billion tonnes in 2050, only considering the population growth. This result corresponds to an estimate made by the International Energy Agency [9].

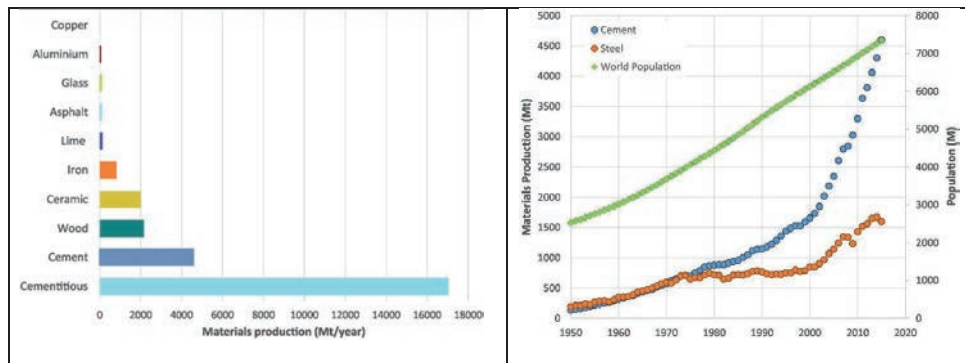


Figure 3 – Left part: Estimated consumption of common materials 2002-2005 [9]. Right part: Correlation on growth in world population and cement production 1950-2015 [9].

The World Bank estimates that around 40% of the world's population lives in low-income countries and that more than 60% of those living in slums without access to simple infrastructure like sanitation [9]. To accommodate the needs for a decent level of societal infrastructure for both the existing world population and the expected growth, the above estimate for cement consumption seems conservative. Scrivener et al. [9] showed that while the world population grew by 15% during the period 2000-2015, the cement production grew by 150% (Figure 3, right part). This unproportional growth in cement production probably illustrates welfare growth exceeding population growth.

According to CEMBUREAU [8], the cement and concrete industry generated more than 380 000 direct jobs within the EU in 2012. Also estimating indirect effects, this number grows to more than 1 million. EU is far more industrialised than most low-income countries, where concrete consumption is expected to grow. Hence, the importance of employment and economic growth is huge.

The social and economic impact stemming from the consumption of concrete seems indispensable, both due to material properties for creating necessary infrastructure and for the role of the related industry to generate personal employment, security and welfare for the citizens. Additionally, the structures being built through the concrete consumption constitute infrastructure and arenas necessary for future growth in industrial and social activities, economy and welfare.

#### *SWOT analysis*

As argued above, cement and concrete are indispensable for sustainable development of society. Consumption will grow substantially, especially in low-industrialised countries. Cementitious materials are favourable for availability, cost-effective and flexible design, simplicity of use, high strength/cost ratio and high durability. However, the concrete industry is responsible for a considerable demand for resources and greenhouse gas emissions. Production of cement is most significant, accountable for approximately 5-7% of the global anthropogenic CO<sub>2</sub> emissions [11-13].

A major measure to reduce CO<sub>2</sub> emissions would be carbon capture and storage (CCS) or even better than storage; use (CCU). A project on CCS is under development in Norway, including a full-scale pilot on Norcem's factory in Brevik expected to be realised in 2020-21. However, CCS is expensive, and unless disruptive technology is emerging, CCS/CCU is not expected to solve

the climatic challenges of the cement industry worldwide. This was the origin of a UN initiative to find alternative solutions on CO<sub>2</sub> reduction from the use of cementitious materials, recently reported by Scrivener et al. [9]. Mehta [1] proposes three tools for making the concrete industry more sustainable; i) consume less concrete for new structures, ii) consume less cement in concrete mixtures and iii) consume less clinker for making cement. Scrivener et al.'s conclusions are in harmony with Mehta's approach, and this logic is followed in the discussion below. Several measures are essential for global solutions, without being central to development in highly industrialised societies. A fourth tool – spanning wider than just within the cement and concrete industry is related to utilising resources that are waste from other industrial processes (often referred to as by-products) –; iv) circular economy.

#### i) Consume less concrete for new structures

Improved durability – reducing the need for replacement of structures – is unarguably an effective mean to reduce consumption of resources in a long-time perspective. The designed service life of infrastructure members such as bridges and tunnels in Norway is 100 years [14, 15]. The designed service life is the period a structure is expected to be in use fulfilling its intended purpose with predicted maintenance, without extensive repairs [14]. Jähren and Sui [4] emphasise that designing structures for enhanced durability has a significant positive effect on emissions when considering long-time span, but might conflict towards short time focus.

Several strategies support durability enhancement. Two of those are careful design of structures to reduce degrading loads (e.g. avoiding surface water accumulation) and careful execution of construction work (e.g. avoiding reinforcement corrosion due to lack of cover). A third measure is careful inspections and maintenance, to stop degradation before it has propagated to a level where replacement is favourable to repair.

A fourth measure – emphasised by Mehta – is using highly durable concrete materials. Ultra High Performance Concrete (UHPC) is an emerging material presently being subject to massive research efforts. In addition to having higher strength than standard concrete, UHPC is also defined by having enhanced durability. This eliminates reinforcement corrosion caused by carbonation or chloride migration [16, 17], within any service life expectancy. Pilot projects are being built worldwide, and some early design codes have even been introduced [18, 19]. Using UHPC in the rehabilitation of existing concrete bridges is also investigated by several researchers [12, 20]. Habert et al. [12] showed that it is possible to lower the impact over the life cycle by using UHPC solutions rather than traditional methods.

Design optimisation offers several strategies to reduce concrete consumption. One is designing structures with flexibility for future changes in use. Another is the optimisation of cross sections. Prefabrication might support this, e.g. by offering slender beams with optimised cross sections, that would not be economically favourable for on-site production. Traditionally, concrete design utilises the lower part of the strength span allowed by design codes such as EN 1992 (EC2) [21]. Traditional use of concrete in structural design has rarely aimed at reducing CO<sub>2</sub> emissions. Investigating potential in the exploitation of high strength concrete and concrete having high targeted performance in other areas, might be fruitful.

Utilising the unique mechanical properties and the possible enhanced service-life of UHPC can drastically reduce the material consumption of concrete for some types of structural members [22]. Several studies [23-25] have shown that using high and ultra high performance concrete for construction can give more environmentally friendly solutions. A study aiming at innovation in

traditional building design, focused on the utilisation of high strength concrete still within the limitation of EC2, in combination with biaxial hollow decks [26]. Potential for 60% reduction of CO<sub>2</sub> and at the same time 20% reduction of the cost was indicated, utilising today's formal regulations and commercially available products. Scrivener et al. [9] also concluded that using high strength concretes in suitable applications can be more efficient and decrease the total material consumption.

#### ii) Consume less cement in concrete mixtures

It is known that the amount of cement used to produce concretes of given strength and workability, varies enormously. Utilising pozzolans or other supplementary cementitious materials (SCM) to partly substitute cement in ready-mix production, is a well-implemented measure to use less cement. A drawback is the extended hardening time. Utilising 56- or 90-days strength instead of 28-days strength in structural design makes it possible to exploit the potential of these concretes [1]. However, this practice is often conflicting with design standards. According to the preliminary version of EC2 (2021), it will be possible to utilise 91-day compressive strength.

Another possibility to use less cement is to minimise the amount of water needed for obtaining the required consistency of fresh concrete. When keeping w/c-ratio constant, reduction of water consequently reduces the amount of cement. Superplasticisers can be utilised to reduce the amount of water required, still maintaining workability [1]. However, this strategy is well utilised in industrialised countries.

Further development to reduce water content is related to the functions of paste in concrete. The primary function is to fill the voids between aggregate particles; to envelope each particle in “glue” to obtain the required strength and durability of hardened concrete. The volume of voids is a function of particle packing. Scrivener et al. [9] claim that packing the particles of aggregate by carefully selecting the dosages of different fractions is an effective measure to reduce water and cement content in concrete. Mehta [1] also mentions the possibilities lying in optimised aggregate size and grading, without in this connection making an issue of the extra resources this would request. A secondary function of the paste in concrete is to reduce friction between aggregate particles to enhance the workability of fresh concrete. This is obtained by adding a surplus of paste exceeding the volume of voids to separate aggregate particles from each other, and hence increasing the consumption of cement. The shape of the particles also rules the friction within aggregates, as the content of flaky shaped particles creates more friction. Consequently, reducing the share of flaky shaped particles reduces the need for paste in the concrete.

Additionally, there is an emerging focus on the effect of small particles in concrete; the fillers. Scrivener et al. [9] claim that “engineering particle size distribution combined with the use of dispersants allow a binder replacement of up to 70% by inert fillers without the negative effects of dilution.” Properties and grading of aggregates vary with location, which might explain variations in cement consumption. The consumption of cement, and hence also the price, can effectively be reduced by increasing focus on the composition of aggregates and the use of fillers. These measures are also location independent.

#### iii) Consume less clinker for making cement

Consume less clinker for making cement can be obtained by utilising other cementitious materials for partly substituting Portland clinker [1]. Depending on properties, these materials can be added into the cement production prior to, or after the calcination process – thus ending up as SCMs. Some examples are fly ash, silica fume, ground granulated blast furnace slag, rice husk ash, lime

filler and several other natural pozzolans [9, 24]. This is considered to be one of the key strategies to reduce greenhouse gas emissions from concrete production [9] having an effect both on a short time horizon and lifetime perspective [4]. The availability of these materials depends on other productions, as they are often by-products from industrial processes. Some SCMs have shown to mutually affect each other positively. These synergetic mechanisms of ternary and quaternary binder blends are not yet fully investigated. If the particle size distribution and combinations of cement, fillers and SCMs are fully optimised, an average clinker substitution level of above 40% is realistic worldwide [9].

Often, SCMs have slower strength development than cement clinker, and resistance towards migration develops correspondingly. This slower development might require intermediate measures towards the migration of harmful components into unmaturing concrete. Additionally, the availability of SCMs differ locally, and some require costly processing to obtain acceptable quality [9].

#### iv) Circular economy

Circular economy is gaining increased attention. The aim is to improve utilisation of resources, decrease waste and improve sustainability. This philosophy has several applications within the concrete industry. The most obvious would be the reuse of structures or elements for other purposes than they were designed for. Use of SCMs stemming from industrial processes to substitute cement is another example.

The construction industry produces large amounts of materials that are presently deposited or used for landfill; some from construction works and demolition of old structures, others from excavation or blasted rock. Xuan et al. [13] suggest one way of making the concrete industry more sustainable by increasing the use of waste from ready-mix concrete plants. Another study showed that it is possible to produce UHPC with reduced cement content [27] by utilising a by-product from the production of gravel. Often, these surplus masses are produced on-site, where aggregate for concrete is required. However, they fail to fulfil quality requirements according to concrete standards. For some materials, the quality requirements can be obtained by simple processing. However, tests also show that it is possible to produce high-quality concrete from aggregates that fail to meet some standardised quality requirements.

The concrete industry is ruled by formal regulations. Severe efforts are put into harmonising standards internationally, to simplify execution and to take advantage of existing competence. The existence of clear, authoritative guidelines are guarantors for quality and safety. However, standardised solutions might prevent innovation. Scrivener et al. [9] emphasise that avoiding the prescriptive regulations in traditional standards and instead allowing for flexibility to exploit local opportunities for raw materials can only be achieved with performance standards specifying properties that must be met (like strength, E-modulus and durability).

The above findings are organised by strength, weaknesses, opportunities and threats (SWOT) and presented in Table 1.

Table 1 – SWOT sustainable use of concrete

<p><b>Strengths</b></p> <ul style="list-style-type: none"> <li>• The demand is increasing and will remain so due to population growth.</li> <li>• No material can replace concrete, due to required volume and availability.</li> <li>• Several advantages, like the simplicity of use, local part materials, flexible in design, cost-effectiveness and durability.</li> </ul>	<p><b>Weaknesses</b></p> <ul style="list-style-type: none"> <li>• Resource demanding locally and globally.</li> <li>• Causes substantial CO<sub>2</sub>-emissions.</li> <li>• Conflicting timespan considerations for varying environmental goals.</li> </ul>
<p><b>Opportunities</b></p> <p>Reduction of environmental loads through</p> <ul style="list-style-type: none"> <li>• Reduced material consumption through innovative design, prefabrication and use of HPC and UHPC.</li> <li>• Clinker reduction by use of SCMs and fillers.</li> <li>• Cement reduction by optimising grading and shape of aggregate particles.</li> <li>• Utilising potential in extended maturity considerations (91 days hardening time, and innovative hardening technology).</li> <li>• Increase the use of waste and recycled materials.</li> <li>• Enhancement of durability.</li> <li>• CCS/CCU.</li> </ul>	<p><b>Threats</b></p> <ul style="list-style-type: none"> <li>• Climatic changes.</li> <li>• Resource demanding.</li> <li>• Rigid regulations.</li> <li>• Availability of SCMs.</li> </ul>

## 4.2 Industrialisation of the construction process

### *Functional refinement of the term*

The term “industrialisation” is traditionally used to characterise the transition of economies from being dominated by agriculture, towards being dominated by manufacturing. Development of new technology, including the steam engine, was the vital driving force for the European transition. The term is still frequently used even in highly developed economies, now to describe the transition of industrial sectors away from craftsmanship and one-of-a-kind solutions, towards standardised and automated production. The gaining is efficiency; a higher volume of production per time and at a lower cost. Once again, new technology is a major driving force. However, the organisation of processes and data to promote human interaction is considered equally important.

### *The present situation*

The construction industry is still dominated by one-of-a-kind design and low level of automation in management, design and production. Although changes as increased use of innovative formwork technology, self-compacting concrete, fibre reinforcement, grinding- and surface treatment machinery, and sprayed concrete robots are emerging, it is widely accepted that construction lags behind manufacturing industry on productivity. The Norwegian construction industry and the government have established a joint effort to improve productivity and sustainability, named Bygg21. In a recent report from Bygg21, the following definition is given: “Industrialising construction projects is to plan and execute processes; maximising repeated use of standardised solutions, industrial methods and digital tools” [28].

The well-known “Lean Construction” (LC) philosophy, adapted from Toyota’s “Lean Production”, has inspired this definition. Most major contractors have been struggling to

implement LC for many years already, often adopting company-specific names like Veidekke’s “involverende planlegging” (participative planning). LC-implementation has often originated on-site to manage logistics and fabrication, but efforts are now spanning the entire process from planning and design, throughout deliverances that support operation and maintenance. Several “models” or “schools” have been developed to support these processes; like “Integrated Project Delivery” (IPD) and “Virtual Design and Construction” (VDC).

#### *SWOT analysis*

Three basic principles central to LC are: i) to improve flow in processes, ii) to reduce waste and iii) to continuously learn from experiences. These three principles are used for facilitating the SWOT analysis below.

##### i) Improve flow in processes

The most important “flow” in construction processes, is the flow of information relevant for each actor to execute his/her part as efficient as possible. All actors in the construction process must be involved early enough to influence actions laying premises for their own deliverance. All must also have access to correct and required information prior to executing any action, and uncertainty must be adequately handled. IPD is developed as a method utilising early involvement to focus on producing maximum value for the customer through building alliances between all people and “systems” vital for production, avoiding individual stakeholders to sub-optimize own gaining.

Though theoretical approaches to LC emphasise manual tools like “PostIt-technique”, the industry soon called for computer-based LC implementations, due to the amount of information to be handled and the number of actions necessary for keeping the system updated [29]. IPD clearly defines seven sequences in a construction project, identifying vital actors in each sequence. This clear structure facilitates the use of digital solutions. Building Information Model/Modelling (BIM) is emphasized as “one of the most powerful tools supporting IPD” [30]. This is argued by BIM being able to combine all information and support all phases in a construction process, from design through the entire life-span. This is correctly the idea of BIM. However, there are still some shortcomings in the present use of BIM. Some of these are discussed in the section “Digitalisation” further down in this paper.

Another important “flow” in construction processes is the fabrication. Traditional thresholds include uncertainty; related to logistics, lack of drawings or staffing, unwanted events, etc. Prefabrication might be a strategy to reduce uncertainty. A state-of-the-art report by the Fédération Internationale du Béton (fib) from 2004 [31] reports that there are significant differences in the development and application of precast bridges in various countries. In the report, it is claimed that “Especially in the Scandinavian countries, there are few precast bridges, although the climatic conditions would logically incite to an opposite attitude”. According to an investigation amongst practitioners on the use of precast bridge elements [32], there seems to be a widespread opinion that precast bridges are more prone to damage due to degradation mechanisms. These problems are recognised for bridges dated before 1990. However, in an investigation based on the NPRA database “Brutus”, it was found that this is not correct – at least for bridges designed according to standards dated after 1990 [33].

Figure 4 (left part) shows the results of an investigation mapping the bridges related to four-lane national highways in the south of Norway [32]. As shown in the figure, there is a tendency that highway bridges are limited to a low number of typical lengths, clearly indicating a large potential for standardisation. NPRA has recently initiated two projects to use more prefabricated elements

in road construction. One of them has resulted in standardised solutions for prefabricated concrete culverts. The other project aims to develop new pre-accepted precast bridge solutions utilising up to 40 meter long beams [34].

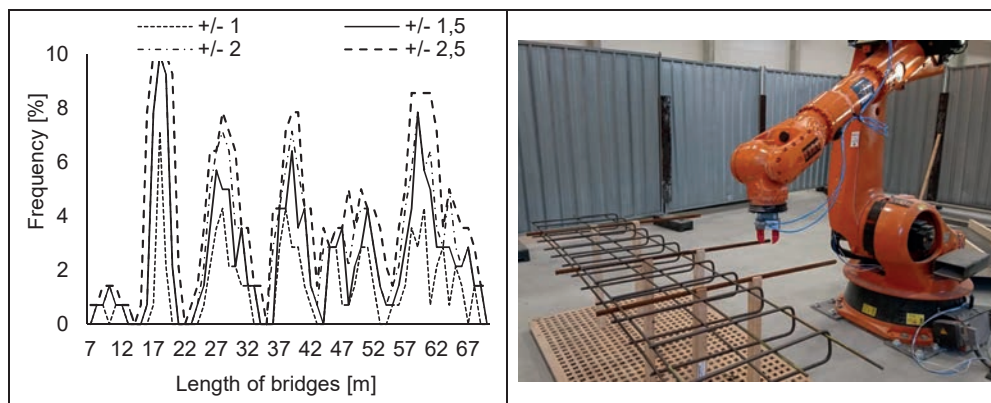


Figure 4 - Left part: Frequency of length of bridges on four-lane national highways in the south of Norway (a total of 140 bridges were included) [32].

Right part: Robotised placement and welding of prefabricated reinforcement.

Photo: Rebartek – Maximilian Trommer.

According to [32], some interviewed experts highlighted that there are challenges for precast bridges related to requirements in the regulation for bridge constructions by NPRA [14]. The Norwegian topography can also limit the use of straight precast elements. Transport on Norwegian roads can limit the span length both due to regulations and due to the road geometry (roundabouts define the maximum bridge lengths). Additionally, prefabricated (standard) elements are straight, limiting the road geometry, horizontal and vertical curvature, transverse inclination and inclining abutments. However, most agreed on the benefits of prefabrication regarding Health, Safety and Environment (HSE). Higher production speed, improved quality, reduction of traffic interrupts and potential reduction of production cost were other benefits emphasized in the interviews. These are major indicators of higher efficiency.

#### ii) Reduce waste

Improving flow inevitably leads to reduction of waste, as time is saved for involved personnel and equipment. Time is valuable both to business (personnel and equipment) and to the social economy (e.g. reducing traffic interruption).

Waste can also be reduced by implementing new technology like automated production of reinforcement cages (Figure 4, right part). In addition to the reduction of production time and material consumption it opens for more advanced design, e.g. by welding the minimum required the amount of reinforcement, omitting lap joints and reinforcement design optimised for production rather than structural needs. VDC is another process model heavily focusing on BIM and visualisation; including 3D models and further dimensions (time, cost, progress, risks, etc.). Once again, the primary driving force is to secure interaction and information access through organisation and the use of technology creating a work zone where all construction activities take place.

Standardisation is expected to promote industrialisation in road construction by reducing the number of alternative solutions, e.g. for fixation of railings. Reduction of the alternative solutions increases reuse of formwork, scaffolding and production techniques. Learning by repeated doing is a consequence of standardisation of production, resulting in reduction of process time, increased predictability and reduction of errors. Also, the reduction of work hours related to design processes and quality control are positive outcomes.

Standardisation inevitably leads to repetitive use of structural solutions, which might be perceived as aesthetically monotonous, limiting architectural expression. Traditionally, aesthetics is considered vital for Norwegian road infrastructure governed by an NPRA report [35]. Another drawback is that standardisation may act to conserve today's solutions. The regime of standardisation offered by today's formal regulations is frequently criticised for being conservative and counteracting new solutions and cost reductions. The urge to standardise for promoting leaner production today might prevent innovation and be a threshold to cost-efficient changes in the future. Additionally, the basic purpose is to ensure solutions that have proven their durability in practice. If opening the rigidity of standards to promote innovation, measures must be taken to make sure that the durability aspect is still attended.

### iii) Continuously learning from experiences

Seen in the light of hindsight, some parts of a construction process could always have been improved. Individuals often claim to learn from experiences, however organisations like companies are known to struggle to avoid repeating mistakes. Explicit measures for organisations to learn from experiences calls for systematic registration, analysis, alternative investigation, storing and active education. Formal initiatives, processes and systems to promote this kind of organisational learning, are not always well developed. Digitalisation provides powerful tools supporting this development, but still the organisation of humans and processes is needed. One obvious reason why this is still often lacking is that these processes are time-consuming. However, the overall goal is to reduce time consumption by learning systematically from experiences.

Another measure to promote learning is the use of formerly approved solutions and practices. This might be formal standardisation through legal regulations and design codes, or restrictions given by building client (like the above-mentioned restrictions for fixation of railings along highways). However, it might also be the reuse of former design, proven to be successful. Once again, the use of digital solutions like BIM supports this kind of “standardisation” through easy access and reuse. However, also this kind of standardisation might prevent innovation.

Table 2 – SWOT industrialisation of the construction process

<p><b>Strengths</b></p> <ul style="list-style-type: none"> <li>• Improved productivity by reducing the time for design and production.</li> <li>• Consequently, reduced cost (per unit).</li> <li>• Reduce climate impact (by reducing waste).</li> </ul>	<p><b>Weaknesses</b></p> <ul style="list-style-type: none"> <li>• Depending on successful implementation of interaction between numerous actors.</li> </ul>
<p><b>Opportunities</b></p> <ul style="list-style-type: none"> <li>• Early involvement improves the possibility to influence at early stages, avoiding changes at later stages when the cost of changes rises.</li> <li>• Correct information required for prerequisite available for all – at any time.</li> <li>• Consequences of choices understood through analysis including all existing prerequisites, and easily available through visualisation.</li> <li>• Advanced/automated production methods open for design optimised for structural performance rather than for easy manual production.</li> <li>• Standardisation allows for reuse of design, equipment and production techniques.</li> <li>• Prefabrication allows for cost reduction, sustainable solutions and improvements on HSE.</li> <li>• Improved quality through systems for continuously learning.</li> </ul>	<p><b>Threats</b></p> <ul style="list-style-type: none"> <li>• Aesthetics – promotes monotony.</li> <li>• Standard prefabricated elements limit road geometry and adaptation to terrain.</li> <li>• Complicated and demanding handling processes (lifting, transport and assembly).</li> </ul>

### 4.3 Digitalisation of construction and management processes

#### *Functional refinement of the term*

Digitalisation is the process of using digital methods to achieve results that would not be available without these methods. The enablers are high capacity for accessing, storing, processing and presenting data. In this paper, digitalisation refers to digital information of the structure that is applied in all stages throughout the life cycle of the structure, from design until the end of service life. Digital information in the form of models including metadata may be used at the design stage, for structural analysis and dimensioning, for construction at the building site, for operation, maintenance and management and finally for demolishing, recycling and deposition of waste materials at the end of service life.

#### *Present situation*

There is an emerging interest in the opportunities related to a more digitalised construction industry. The most used development within digitalisation is BIM. By using BIM, it is possible to replace structural drawings with virtual, 3-dimensional digital models of the structure and construction site, and assign more information to the different parts than just the geometry [36]. In addition to the description of the structure and the applied materials, this may include information needed for technical and quality control, and extraction of quantities necessary for pricing. Digitalisation and BIM-models can be used throughout the life cycle of a structure. However, presently the information is often modelled in different ways and by various software tools and platforms from phase to phase, which is a serious hindrance for future development.

According to Azhar [37], BIM can be used for 3-D visualisation, fabrication of drawings, estimation of cost, automatic extraction and updates of material quantities, construction sequencing (coordinate material ordering, fabrication, and delivery schedules for all building components), conflict situations, and collision detection, to mention some. The same author also mentions that BIM may give benefits in terms of faster and more effective processes, better design (as the design of the buildings can easily be analysed and changed in the digital model), control of the lifetime costs and environmental data, and improved production quality. It is possible to achieve substantial reductions in time consumption related to generating cost estimates and utilise lifecycle data for facility management. More recently there has been increased interest in using BIM to achieve more sustainable solutions by including EPDs (Environmental Product Declaration) in the BIM-model and carry out optimum design [36].

An important part of digitalisation in the construction industry is to use modelling tools and software for structural analysis and dimensioning. Direct application of BIM and the growing sophistication of computer programs, increasing computer capacity and decreasing costs, give great possibilities for better design. Table 3 presents today's practice and two possible future scenarios for structural analyses and design, which both may facilitate more efficient material use and therefore more sustainable solutions.

*Table 3 The structural design process*

Solution	Date	Drawings/Design	Structural Analysis	Dimensioning/Design
I	Today	Drawings or BIM	Linear elastic methods, Finite Element Analysis (FEA) occasionally. Supported by human competence and special purpose program accounting for cracking, creep, shrinkage, relaxation and temperature effects, and construction history. Nonlinear analysis rarely used in practice.	Manually in critical sections, often using special purpose programs.
II	Future scenario, alt I	BIM	Linear elastic FEA based on the BIM, occasionally nonlinear and time-dependent. Modification of linear FEA to account for cracking, creep, shrinkage, relaxation and temperature effects, and construction history.	Computerised checks of all sections.
III	Future scenario, alt II	BIM	Numerical simulation of structural behaviour based on BIM-model. Nonlinearities and time-dependent behaviour well accounted for. Probabilistic safety-formats. Structural analysis and dimensioning fully integrated.	

In today's structural design, it is most common that the design of each structural member is done manually in critical sections using special purpose programs. This is time-consuming, and in a market with great competition and economy focus for both designers and contractors, the approach does not always give the optimal solutions and sustainable design.

Compared to today's practice, future scenario I will utilise BIM to make more accurate linear finite element analysis (FEA) of structural systems. Still, care must be taken to distribute stress concentrations, account for time-dependent effects, and in some cases also nonlinear behaviour. This, together with computerised design of all sections in a member, may contribute to more optimal and sustainable solutions. For instance, industrialising the process of prefabricating beams by placing the exact amount of shear reinforcement required by the design code, precisely fixed in position by robots. Hence, industrialising open for flexible production by standardising processes, not products.

Future scenario II assumes frequent use of advanced numerical simulations of the structural behaviour based on the BIM. The preferred method will be Non-linear Finite Element Analysis (NLFEA), including accurate material models. These tasks are challenging and require development of guidelines and regulations to be able to achieve the right structural safety concerning design resistance and robustness, and quality control of the results. NLFEA is used already today, but only in special cases, e.g. for existing structures (remaining/rest-capacity), or when there has been a structural collapse (accident) and investigations to explore the causes are required.

To fully utilise the advancement in digitalisation, to achieve future scenario II, should be one goal to achieve more sustainable solutions but, as mentioned above, further research and development of regulations and guidelines are required.

#### *SWOT analysis*

As illustrated in Figure 5, digitalisation may facilitate communication, information sharing, innovative thinking, design adjustments and construction planning. The different sub-processes work together towards a better and sustainable design.

First sub-process, denoted building opportunities (Gear 1), is constantly moving and must be checked with preliminary and advanced models to obtain the best design. This sub-process also requires feedback from the other sub-processes to improve. If one process works alone and does not communicate, it will hinder the abilities for the other sub-processes to work together.

The authors agree with the statement from Azhar [37] that BIM contributes to a better design, but the authors would like to address this broad term. Among the conclusion for a better design, one is that the building proposals can be rigorously analysed, and simulations performed quickly.

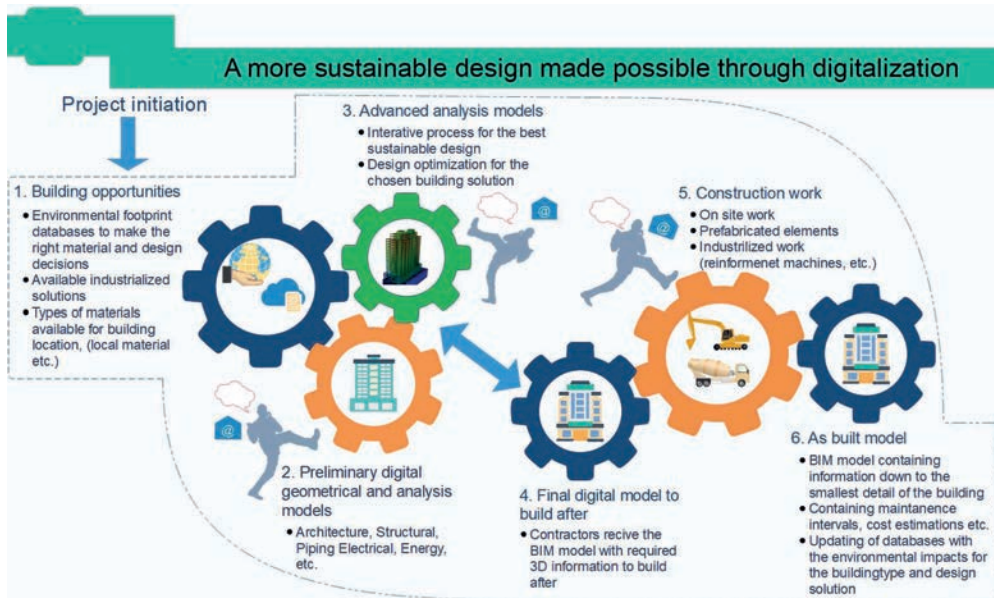


Figure 5 – A more sustainable design made possible through digitalisation (own design of illustration).

A risk when using more advanced software is that complex structures may become too simple to handle in the software’s environment. In worst-case, this can lead to serious faults, and also structural failures with large consequences. Therefore, it is of vital importance that engineers understand and maintain competence within their field. Some of the advanced structural analysis programs now available for the industry were previously only available in the academic environments.

Table 4 shows the results from the SWOT analysis in digitalisation of construction and management processes.

Table 4 – SWOT Digitalisation of construction and management processes

<b>Strengths</b>	<b>Weaknesses</b>
<ul style="list-style-type: none"> <li>• Faster and more effective processes.</li> <li>• More efficient design process and better quality of the design.</li> <li>• Faster and more correct cost estimates.</li> <li>• More accurate geometry and material modelling for structural analysis.</li> <li>• More accurate descriptions of the construction history.</li> </ul>	<ul style="list-style-type: none"> <li>• Information may be modelled in different ways and using different software tools and platforms from phase to phase.</li> <li>• The computer programs may use different theory and algorithms than those known to the designer, which may lead to misunderstandings and faults.</li> <li>• Too large amount of information creates unnecessary complexity.</li> </ul>

<b>Opportunities</b>	<b>Threats</b>
<ul style="list-style-type: none"> <li>• More efficient (economic and sustainable) use of materials.</li> <li>• Interaction of BIM and LCA-software/EPDs.</li> <li>• More optimal design (easier to improve the design of a structure).</li> <li>• More optimal and sustainable solutions.</li> </ul>	<ul style="list-style-type: none"> <li>• Changes in data-formats and platforms over time.</li> <li>• Robustness of systems (data storage, hacking, etc.).</li> <li>• Loss of competence due to phasing out valuable computer programs.</li> <li>• Lack of understanding of how the structural systems work – may lead to possible faults.</li> <li>• Import of geometrical 3D models for structural analysis– possibly wrong connections between elements due to different formats.</li> <li>• Too much information in the models related to the necessary task at hand.</li> </ul>

## 5. DISCUSSION

The aim of this paper is to identify and discuss directions for more sustainable development of the use of concrete for road infrastructure, in an industrialised context. The term “sustainable” is defined to embrace not only environmental issues, however also the economy and social development. Hence, issues regarding HSE and productivity are included. The term “industrialised context” reflects that the discussion regards highly industrialised societies, where advancements in digitalisation and automation are natural traces of development.

Substantial growth in the use of concrete is inevitable. Consequently, measures must be taken to avoid a corresponding growth in CO<sub>2</sub> emissions, and to reduce the anthropogenic influence on climate change. Future solutions might involve CCS/CCU, however widespread use of these solutions requires disruptive technology that substantially reduces cost. Hence, CCS/CCU is not further discussed in this article.

The three terms sustainability (in a threefold understanding), industrialisation and digitalisation are separately discussed in SWOT analysis above. No cross-disciplinary conflicts have been identified. On the contrary, synergies are described, and simultaneous utilisation of the three considerations is necessary for realising the full potential in each. A fundamental approach to reduce the use of natural resources, emissions, time and money, is to secure flow in all processes. Flow is pursued by taking all preconditions into account in all processes and choices, including design and production. This calls for sharing information and evaluating each choice real-time, enlightened by all relevant information in the project.

Concepts like “flow”, “early involvement” and “sharing information” are all vital in different approaches towards industrialisation, e.g. LC, IPD and VDC. The use of digital methods is another important measure in industrialisation; to achieve results that would not be available without these methods. Hence, further industrialisation requires both organisation of processes and the use of digital methods. Digitalisation on the other hand, will only produce gaining if all relevant information is available. Hence digitalisation requires industrialisation.

## 6. CONCLUSIONS AND RECOMMENDATIONS FOR FUTURE WORK

The paper considers the three frequently used catchwords; sustainability, industrialisation and digitalisation, and gives a functional refinement of them related to their application within the

construction industry. As a contribution towards more sustainable solutions within the road infrastructure a SWOT analysis is carried for each term. Several opportunities for sustainable development of the use of concrete have been identified. A prerequisite for taking advantages of these opportunities is that processes for further industrialisation and digitalisation are carefully implemented. Some of these identified opportunities are:

- More efficient use of materials through innovative design, utilisation of advanced and automated production, prefabrication and investigation into smart use of HPC/UHPC.
- More optimal design made possible by early involvement of stakeholders, the interaction of BIM and LCA software, and digital visualisation, allowing for better informed decision processes.
- Improved quality in processes, decisions and products, supported by operational systems for continuous learning; including both explicit actions and knowledge tacit in the reuse and standardisation of solutions.

Several important threats to the sustainable development of road infrastructure have also been identified:

- The main threats towards future sustainable development of the concrete infrastructure are the lack of natural resources, too rigid regulations and availability of SCMs.
- Concerning industrialisation, a threat to be avoided is making solutions that are rational when implemented but may act preservative in the longer run, preventing future innovations.
- Related to digitalisation the major threats are due to changes in data-formats and platforms over time, the robustness of systems (data storage, hacking, etc.), loss of competence due to phasing out valuable computer programs, and finally lack of understanding of how the structural systems work – which may lead to possible faults.

The paper is a part of two ongoing PhD-projects, and the findings in this paper will be followed up. One of these will focus on the development of production of Ultra High Performance Concrete (UHPC) from local constituents and investigate the structural behaviour of this material. The other one will study industrialised sustainable concrete bridges in Service Limit State (SLS). The objective is to improve structural analysis and design of concrete bridges in SLS that are adapted to new sustainability-requirements, industrialisation and digitalisation.

## ACKNOWLEDGEMENTS

Two funding bodies supported this work: The Research Council of Norway (NFR) and Sørlandets Kompetansesfond, through the project More Efficient and Environmental friendly Road Construction (MEERC).

## REFERENCES

1. Mehta P K, "Global concrete industry sustainability," *Concrete international*, vol. 31, no. 2, pp. 45-48, 2009.
2. Pachauri R and Meyer L, "Climate change 2014 Synthesis Report-Summary for Policymakers," ed: Intergovernmental Panel on Climate Change (IPCC), 2014.

3. Samferdselsdepartement, "Meld. St. 33 Nasjonal Transportplan 2018-2029 (in Norwegian) (National Transport Plan 2018-2029)," Oslo, Norway 2017.
4. Jahren P and Sui T, *Concrete and sustainability*. CRC Press, 2013.
5. Jiang R, Mao C, Hou L, Wu C, and Tan J, "A SWOT analysis for promoting off-site construction under the backdrop of China's new urbanisation," *Journal of Cleaner Production*, vol. 173, pp. 225-234, 2018/02/01/ 2018.
6. Yuan H, "A SWOT analysis of successful construction waste management," *Journal of Cleaner Production*, vol. 39, pp. 1-8, 2013/01/01/ 2013.
7. Brundtland G H, *Our common future*, Oxford: Oxford University Press, 1987. [Online]. Available.
8. CEMBUREAU The European Cement Association. (2016, 17.03). *Key figures*. Available: <https://cembureau.eu/cement-101/key-facts-figures/>
9. Scrivener K L, John V M, and Gartner E M, "Eco-efficient cements: Potential economically viable solutions for a low-CO<sub>2</sub> cement-based materials industry," *Cement and Concrete Research*, vol. 114, pp. 2-26, 2018/12/01/ 2018.
10. United Nations. (2017, 22.03). *World Population Prospects: The 2017 Revision*. Available: <https://www.un.org/development/desa/publications/world-population-prospects-the-2017-revision.html>
11. Benhelal E, Zahedi G, Shamsaei E, and Bahadori A, "Global strategies and potentials to curb CO<sub>2</sub> emissions in cement industry," *Journal of Cleaner Production*, vol. 51, pp. 142-161, 2013/07/15/ 2013.
12. Habert G, Denarié E, Šajna A, and Rossi P, "Lowering the global warming impact of bridge rehabilitations by using Ultra High Performance Fibre Reinforced Concretes," *Cement and Concrete Composites*, vol. 38, pp. 1-11, 2013/04/01/ 2013.
13. Xuan D, Poon C S, and Zheng W, "Management and sustainable utilization of processing wastes from ready-mixed concrete plants in construction: A review," *Resources, Conservation and Recycling*, vol. 136, pp. 238-247, 2018/09/01/ 2018.
14. Norwegian Public Road Administration, *Håndbok N400 Bruprosjektering (in Norwegian) (Manual N400 Bridge design)*. Oslo: Directorate of Public Roads, 2015.
15. Norwegian Public Road Administration, *Håndbok N500 Vegtunneler (in Norwegian) (Manual N500 Road Tunnel design)*. Oslo: Directorate of Public Roads, 2016.
16. Russell H G and Graybeal B A, "Ultra-high performance concrete: A state-of-the-art report for the bridge community," 2013.
17. Thorstensen R, Larsen I, Heimdal A, and Hansen H, "LCC and carbon footprint of bridge made from locally produced UHPC, compared to standard concrete," in *Proceedings of HiPerMat 2016 4th International Symposium on Ultra-High Performance Concrete and High Performance Materials*, 2016.
18. *National addition to Eurocode 2–Design of concrete structures: Specific rules for ultra-high performance fiber-reinforced concrete (UHPRFC)*, NF P18-710, 2016.
19. *Recommendation: Ultra High Fibre Reinforced Cement-Based composites (UHPRFC): Construction material, dimensioning and application*, SIA 2052, 2016.
20. Brühwiler E, "Structural UHPRFC": Welcome to the post-concrete era," in *First International Interactive Symposium on UHPC*, 2016.
21. *Eurocode 2: design of concrete structures–part 1-1: general rules and rules for buildings*, EN 1992-1-1:2004, 2004.
22. Randl N, Steiner T, Ofner S, Baumgartner E, and Mészöly T, "Development of UHPC mixtures from an ecological point of view," *Construction and Building Materials*, vol. 67, pp. 373-378, 2014/09/30/ 2014.

23. Habert G, Arribe D, Dehove T, Espinasse L, and Le Roy R, "Reducing environmental impact by increasing the strength of concrete: quantification of the improvement to concrete bridges," *Journal of Cleaner Production*, vol. 35, pp. 250-262, 2012/11/01/ 2012.
24. Liew K M, Sojobi A O, and Zhang L W, "Green concrete: Prospects and challenges," *Construction and Building Materials*, vol. 156, pp. 1063-1095, 2017/12/15/ 2017.
25. Larsen I L, Aasbakken I G, O’Born R, Vertes K, and Thorstensen R T, "Determining the Environmental Benefits of Ultra High Performance Concrete as a Bridge Construction Material," in *IOP Conference Series: Materials Science and Engineering*, 2017, vol. 245, no. 5, p. 052096: IOP Publishing.
26. Fidjestol P and Thorstensen R T, "Improving sustainability of concrete construction - the role of high strength high performance concrete," presented at the 37th Conference on Our World in Concrete and Structures, Singapore, 2012.
27. Larsen I L, Thorstensen R T, and Vertes K, "Lowering environmental impact from UHPC, utilizing industrial by-products," in *12th fib International PhD-Symposium in Civil Engineering*, Prague, 2018, pp. 93 - 101: Federation internationale du beton (fib).
28. Bygg21, "Tenk nytt – bruk kjente løsninger (in Norwegian) (Think New - Use Known Solutions)," 2019, Available: <https://www.bygg21.no/rapporter-og-veiledere/tenk-nytt-bruk-kjente-losninger/>.
29. Thorstensen R T, Kalsaas B T, Skaar J, and Jensen S, "Last planner system innovation efforts on requirements for digital management system," in *Annual conference of the international group for lean construction*, 2013, vol. 21.
30. The American Institute of Architects (AIA National & AIA California Council), "Integrated Project Delivery: A guide," 2007.
31. Fédération internationale du béton (fib), *Precast Concrete Bridges: State-of-the-art report*. International Federation for Structural Concrete (fib), 2004.
32. Heimdal A, Larsen I L, and Norheim T, "Standardisering av brokonstruksjoner for nasjonale hovedveier (in Norwegian) (Standardization of bridge structures for national highways)," Engineering science, University of Agder, Grimstad, 2017.
33. Bårseth E and Birkeland K, "Bestandighet og holdninger til flerspenns prefabrikkerte brokonstruksjoner (in Norwegian) (Durability and attitudes towards multi-span prefabricated bridge structures)," BSc thesis, University of Agder, 2018.
34. Persson S, "«Brubjelkeprosjektet» (in Norwegian) ("The bridge beam project")," presented at the Brukonferansen 2017, Oslo 2017. Available: [https://www.vegvesen.no/\\_attachment/2069373/binary/1218553?fast\\_title=Betongelementer.+Stian+Persson+%285+MB%29.pdf](https://www.vegvesen.no/_attachment/2069373/binary/1218553?fast_title=Betongelementer.+Stian+Persson+%285+MB%29.pdf)
35. Amundsen I, "Vegen i landskapet, om vakre veger (in Norwegian) (The road in the landscape, about beautiful roads)," in "Norwegian Public Roads Administration reports," No. 300, 2014.
36. Sandvik C and Fougner F, "BIM as a tool for sustainable design," in *The International Federation for Structural Concrete 5th International fib Congress, Better - Smarter - Stronger, 7 – 11 October 2018*, Melbourne, Australia, 2018, pp. 786-791: fib (Fédération internationale du béton).
37. Azhar S, "Building Information Modeling (BIM): Trends, Benefits, Risks, and Challenges for the AEC Industry," *Leadership and Management in Engineering*, vol. 11, no. 3, pp. 241-252, 2011.

	
© Article authors. This is an open access article distributed under the Creative Commons Attribution-NonCommercial-NoDerivs licens. ( <a href="http://creativecommons.org/licenses/by-nc-nd/3.0/">http://creativecommons.org/licenses/by-nc-nd/3.0/</a> ).	ISSN online 2545-2819 ISSN print 0800-6377
DOI: 10.2478/ncr-2019-0011	Received: April 1, 2019 Revision received: June 21, 2019 Accepted: June 25, 2019

## Failure of Lightweight Aggregate Concrete in Compression under Stress Gradients



Jelena Zivkovic  
M.Sc. PhD-candidate  
Department of Structural Engineering  
Faculty of Engineering Science  
Norwegian University of Science and Technology  
N-7491 Trondheim, Norway  
e-mail: jelena.zivkovic@ntnu.no



Jan Arve Øverli  
PhD, Professor  
Department of Structural Engineering  
Faculty of Engineering Science  
Norwegian University of Science and Technology  
N-7491 Trondheim, Norway  
e-mail: jan.overli@ntnu.no

### ABSTRACT

The objective of this experiment is to investigate the behaviour of lightweight aggregate concrete (LWAC) under compression and with stress gradients. Experimental program contained three sets of LWAC which were used for production of 21 prisms. Lightweight aggregate argillite slate, called Stalite, from North Carolina had been used. The sets differed in using dry (0.10% moisture content) or saturated (7.9% moisture content) aggregate. The third set included a small amount of polyvinyl alcohol fibres (PVA). The geometry of the prisms were 100 × 140 × 480 mm (width × length × height). Prismatic samples were loaded centrally and eccentrically in compression.

From the achieved experimental results, it is visible that the lateral deformation of the most stressed fibre is counteracted by the less stressed fibres that confine compressive stress and increase strains. The obtained strain level was much higher than expected, especially for the third set of concrete samples with PVA fibres. Recorded strains in prisms test was in range from 3.08‰ to 6.82‰. In general, LWAC with Stalite showed ductile behaviour followed with very high strains. The third set of samples included a small amount of polyvinyl alcohol fibres (0.5% of volume fractions) was even more ductile and non-brittle.

**Key words:** Lightweight Aggregate Concrete, Testing in Compression, Strain level, Centric and Eccentric Loading, Stress Gradients

## 1. INTRODUCTION

### 1.1 General

This investigation is part of the ongoing research program “Durable advanced concrete structures (DaCS)”. The part of this program is to investigate structural behaviour of lightweight aggregate concretes (LWAC), concretes with an oven dry density below 2000 kg/m<sup>3</sup>. The use of lightweight aggregate concrete (LWAC) is limited as a mainstream construction material in structural applications. A reason for that is related to the steepness of the descending branch of the stress-strain curve in compression [1-3]. Material models for compressive failure of concrete are normally based on a uniaxial compressive stress-strain curve obtained from tests, where the main assumption is uniform deformation of the concrete specimens. This assumption is reasonable for the ascending branch of the stress-strain curve, while for the descending branch it is not realistic as it is always accompanied by significant lateral deformations. The lateral deformations are mainly caused by splitting cracks, which are formed and expand during the test. LWAC is characterized by more brittle post-peak material behaviour and uncontrolled crack propagation compared to normal weight concrete (NWC).

In order to describe more in detail, the compressive behaviour and to measure compressive strains, the effect of a stress gradient was introduced and varied in an experimental program. Stress gradients influence both the strength and the ductility [4]. Beam experiments tested in the DACS-project had shown that high strength LWAC with Stalite as aggregate obtained much higher compressive strain levels than expected [1]. The raw material mined by STALITE is an argillite slate located in a geological area known as the Tillery Formation in North Carolina. It is a thinly laminated, grey, fine-grained siltstone, composed of clastic (transported) rock fragments. The Tillery Formation is a complex system that must be selectively mined in order to separate the desirable product from the non-desirable to manufacture a high quality expanded slate aggregate. Raw material is latter expanded in a rotary kiln to produce porous structural lightweight aggregate. The cooled, expanded slate is later conveyed to the classification area, where it is crushed and screened into different size fractions. After crushing, the different size fractions are stored in separate silos until they are blended into standard or custom gradation blends. Due to the higher material strength of STALITE slate aggregate, higher strength concretes can be achieved with lower cement contents allowing for more economical concrete mixes [5].

Three sets of test specimens were produced using lightweight aggregate Stalite fraction size ½ inch (12.7 mm), from the same batch, where the water content in aggregate varied between 0.1%

and 7.9%. The present experimental program included three LWACs for the production of 21 prisms. From each concrete, a total of 2x9 + 1x3 prisms and small samples (i.e. cubes and cylinders) were produced. The third set of samples included a small amount of polyvinyl alcohol fibres (0.5% of volume fractions). The geometry of the prisms were 100×140×480 mm (width × length × height). All samples were loaded both, centrally and eccentrically in compression.

The experimental setup of the prisms and the eccentricities were the same as in an earlier experiment and are therefore comparable [4]. The earlier studies looked at the lightweight concrete Liapor 8 and different types of normal weight concrete.

## 2. EXPERIMENTAL PROGRAMME

### 2.1 Test specimens

The experimental program consisted of 21 prisms, dimensions 100 × 140 × 480 mm (width × length × height), of plain LWAC which were loaded both centrally and eccentrically in compression. This study looks at the differences of using dry-DLWAC (0.10 % moisture content) or saturated – WLWAC (7.9 % moisture content) aggregate and the influence of adding 0.5% at volume fractions of polyvinyl alcohol fibres – FLWAC. In FLWAC the fibres were combined with the saturated aggregate concrete. The main test variables were the moisture of aggregate and the eccentricity of the loading. For each investigated combination, there were tested 3 samples. The complete test programme is shown in the Table 1.

Table 1-Test program for centrally and eccentrically loaded specimens

Prism No.	Type of concrete	Aggregate moisture [%]	Eccentricity / Number of the specimens		
			$e=0$	$e=h/18$ (140/18 =7.8 mm)	$e=h/6$ (140/6 =23.3 mm)
D1-3 D4-6 D7-9	DLWAC	0.1	3	3	3
W1-3 W4-6 W7-9	WLWAC	7.9	3	3	3
F1 F2 F3	FLWAC	7.9	1	1	1

All prisms had the same geometry that was limited due to capacity of the actuator. The geometry and forms for the prisms are shown in Figure 1. All the specimens were cast vertically in three layers. Each layer was compacted first by stamping by hand and, when the form was filled, by additional compaction using an internal vibrator. The prisms were unmoulded 24 hours after casting and immediately stored in water with the intention of preserving their natural content of moisture to the largest possible extent. The specimens were afterwards stored in the laboratory in water, at the temperature of approximately 20°C. The bottom of the specimens were prepared for testing by grinding and top of the specimens by sawing (see Figure 1.) and grinding at an age of 28 days.



Figure 1 – Geometry of the prisms (left), Forms for the prisms (centre), Preparation of the prisms (right).

Two days before the testing prisms were taken out from water and prepared for instrumentation. Two sides of the prisms were painted white and highlighted with a black marker for digital correlation method. The strain gauges and Linear Variable Differential Transformers were attached at the two other sides. The test age of the prisms varied from 32 to 60 days.

To establish the mechanical properties of each LWAC, cubes (with dimensions 100×100×100 mm), cylinders (Ø100×200mm) and small beams (100×100×1200mm) were cast to find the stress-strain diagram, the compressive strength for cube and cylinder [6] the tensile strength [7], Young's module of elasticity [8,9], and the fracture energy [10]. All these small specimens were demoulded after 24 hours and kept in water until the testing day. In order to follow material characteristics compression tests on cubes and cylinders were carried out simultaneously with the prisms testing. All the prisms and small samples, cubes and cylinders, were cast from the same concrete batch.

## 2.2 Material and mix properties

The concrete mixture for each mix DLWAC, WLWAC and FLWAC was prepared from one batch of the aggregate with varying moisture of the aggregate from 0.1% (DLWAC) to 7.9% (WLWAC and FLWAC). The lightweight aggregate was ½" (12.7mm) fraction from Stalite [11]. The moisture content and the absorbed water in the Stalite were measured to be able to design the concrete mix [12]. The moisture content varied from 0.1% to 7.9%, while the absorption for this batch was stable and after 24 hours and 100 hours was 6.58% and 7.72%, respectively. Table 2 gives the concrete mixtures. The mixing was done using two laboratory mixers with capacity of 250 liters and 50 liters. Two different mixing procedures were used. First procedure, called dry, was used for dry-DLWAC mixture, where all dry particles (cement, silica fume and sand) were placed in mixer and mixed for approximately 1 minute. Mixing was constant and aggregate Stalite was added to the rest of dry particles and mixed for 1 min more. Water and superplasticizer were continuously added and adjusted during mixing, until the desired workability of the concrete was achieved. Second procedure, called wet, was used for the wet-WLWAC and fibers-FLWAC mixtures. In the mixer first dry particles cement, silica fume and sand were added and mixed for approximately 30 seconds. Later approximately 70% of water and superplasticizer were added and after 1.5 minute, nice mortar was made. With continuously mixing presaturated aggregate Stalite were added and at the end rest of water and superplasticizer. After 2 minutes, resting and observation of the mixture and workability, additional water were added and superplasticizer until the desired workability of the concrete was achieved.

*Table 2 – Concrete mixtures for DLWAC, WLWAC and FLWAC*

Constituent weight (1000 liters)	DLWAC Weight [kg/m <sup>3</sup> ]	WLWAC Weight [kg/m <sup>3</sup> ]	FLWAC Weight [kg/m <sup>3</sup> ]
Moisture of the aggregate [%]	0.1	7.9	7.9
Cement ( Norcem Anlegg FA)	442.2	440.3	397.5
Silica fume (Elkem Microsilica)	23.3	23.2	20.9
Water (free)	146	180.8	163.2
Absorbed water in Stalite+sand (24 hours)	6.1	38.8	35.9
Water* (added in mixer)	139.9	142	127.3
Sand (Ramlo 0-2 mm)	230	231	377.3
Sand (Årdal (NSBR) 0-8 mm)	536.8	539	531
Aggregate (Stalite 1/2"(12.7mm))	515.4	517.5	493
Superplasticiser (Mapei Dynamon SR-N)	3.3	3.9	6.2
Fibers (Kuralon PVA 8mm)	-	-	6.5
Water*/cement ratio [w/c]	0.32	0.32	0.32

For fiber-FLWAC it was used the same wet mixing procedure with just one additional step. Polyvinyl alcohol fibers (PVA) were added first in nice mortar in order to provide good distribution of the fibers in the concrete. Later procedure was the same.

Polyvinyl alcohol fibres is mostly use to improve the inherent brittleness of cementitious materials and to control cracking. They have very little effect on the flexural strength and deflection capacity. The compressive capacity is slightly reduced while concrete surface of the elements become extremely ductile [13]. In this test the main concern was to deal with brittleness, explosive failure and to improve ductility of LWAC. Because of that PVA fibres were introduced in range 0.5 % at volume fractions. PVA was type “Kuralon RSC15”, 8 mm long with E-modul of 36 MPa [14].

For all prepared concrete mixtures, the fresh concrete characteristics like fresh density [15], air content [16] and slump [16] were followed. Results are given in Table 3.

*Table 3 – Fresh concrete characteristics for DLWAC, WLWAC and FLWAC*

	DLWAC	WLWAC	FLWAC
Fresh density [kg/m <sup>3</sup> ]	1989	2015	2011
Air content [%]	2.5	1.9	2.5
Slump [mm]	170	190	250
Matrix volume [l/m <sup>3</sup> ]	360	360	360

### 2.3 Test Setup and the procedure

All the prisms were loaded in an electro-hydraulic, servo-controlled actuator with a maximum compressive load capacity of 1000 kN. Prisms were first preloaded with 100 kN and later the load was constantly applied with a loading rate of 0.3 mm/minute until failure. This is displacement control test and load was applied centrally and eccentrically, which was provided by varying

stress gradients. Test set and the stress diagrams for the applied eccentricities, based on the assumption of linear stress-strain relationship, are shown in Figure 2.

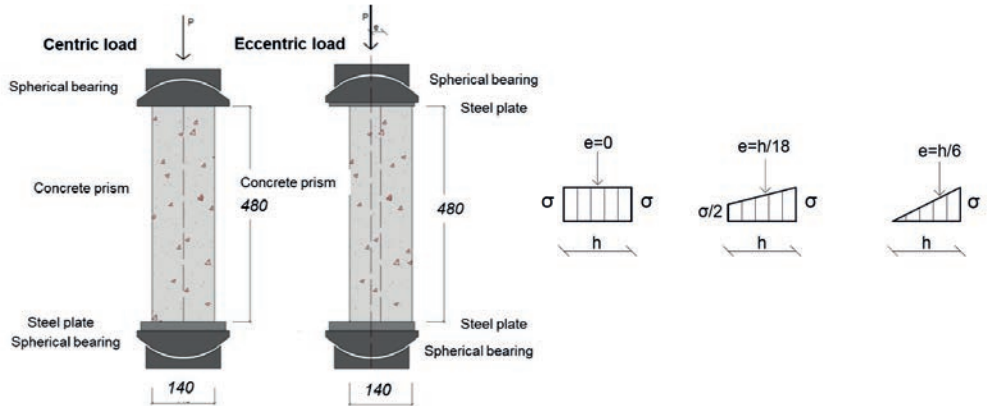


Figure 2 – Test setup for centrically and eccentrically loading. Stress distribution based upon linear theory for the different eccentricities ( $h$  is the height of the cross section).

The loading system was equipped with spherical ball bearings in direct connection to the top and the bottom surface of the prisms to ensure free rotation. The ball bearings were arranged in such a way that their rotation center lay on the surface of the specimens. Control lines were drawn on the contact plates of the bearings to ensure correct placement of the prisms. The contact surface between the ball and the concave ring of the bearings was lubricated prior to each test so as to reduce the friction at the sliding surface as much as possible [4]. Photos of the prism in the testing machine is shown in Figure 3.



Figure 3 – Prism in the 1000 kN testing machine. Wide side-140mm (left) and short side-100 mm (right).

## 2.4 Instrumentation

All the tested prisms were instrumented with the same measuring devices. Strain levels at the concrete area were recorded with strain gauges (SG) and Linear Variable Differential Transformers (LVDT) at two sides of the prism, called LVDT short and LVDT wide. On the other

two sides, called DIC short and DIC wide, Digital Image Correlation (DIC) was used [17]. The location of the measuring devices is shown in Figure 4.

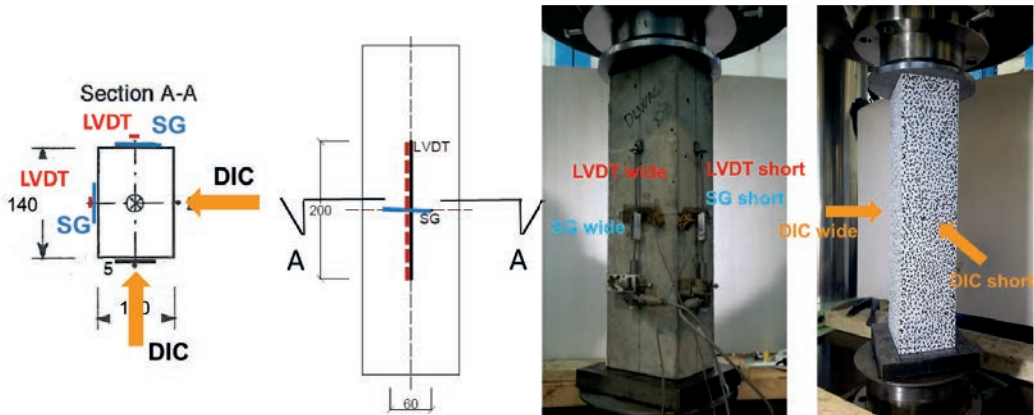


Figure 4 – Position of measuring devices for centric and eccentric loading.

The measuring length of the LVDT for observation of longitudinal direction of middle section was 200 mm. In addition, strain gauges with length 60 mm (type FLA-6-11-5L with gauge resistance of  $119.5 \pm 0.5 \Omega$ ) were inserted in the middle section for observation of transversal direction. DIC was used on other two sides of the prism where the complete strain field was registered. In the eccentric load situation the DIC side was chosen as the one with the maximum stress and where the highest strains were expected. For DIC was used set of two cameras and each were placed orthogonally in relation to the area of observation. That represent 2D DIC, see Figure 5.

All measuring devices (LVDTs and SGs) together with the load cell were connected to HBM eight channel spider to record the data. From here, data were sent to the computer using a specific software program, where the data were processed and stored in a text file. The deflection and load measurements were carried out as a control during the whole test. The output data were recorded by the data acquisition system. Pictures were taken at failure.

Since this was a compressive test and it is known that lightweight aggregate concrete can have very explosive failure special safety precautions were required during testing. Consequently, a plexiglass chamber around the concrete sample was used. It ensured that all parts of the concrete would stay inside of chamber when failure happened.

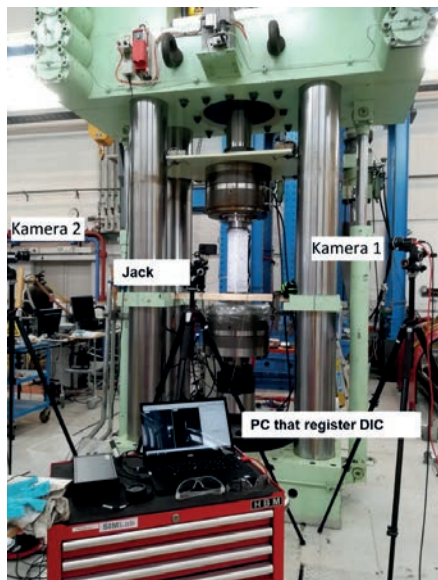


Figure 5 – Setup of the registration equipment.

### 3. EXPERIMENTAL RESULTS

#### 3.1 Results for small specimens

Small specimens were tested after 28 days for determination of compressive strength, tensile strength and Young’s modulus. Small beams for fracture energy for DLWAC were tested after 60 days and for WLWAC after 36 days. The fracture energy is determined on small  $100 \times 100 \times 1200$  mm beams according to SINTEF procedure [18]. This procedure is quite similar to the Hillerborg [10] proposed RILEM method. Small beams are just for 200 mm longer and notch is 0.4 instead of the 0.5 of the beam heights. Beams were first prenotched with notch depth 40 mm and tested in three-point bending test. Fracture energy is calculated when work or energy from the positive part of load-deformation curve observed during test is divided with fracture area. The aggregate type and content affect the result of fracture energy of concrete much stronger than the size of aggregates due to transition from the interfacial fracture to the trans-aggregate fracture. A brief summary of the small-scale test results is given in Table 4.

Table 4 – Mechanical properties for DLWAC, WLWAC and FLWAC

	DLWAC	WLWAC	FLWAC
Saturated density $\rho_{cs}$ [kg/m <sup>3</sup> ]	1997.9	2008.4	2019.2
Oven dry density $\rho_{cv}$ [kg/m <sup>3</sup> ]	1979.9	1864.6	1899.5
Compression strength for cube after 7 days $f_{icm,7}$ [N/mm <sup>2</sup> ]	51.1	58.1	48.8
Compression strength for cube after 28 days $f_{icm,28}$ [N/mm <sup>2</sup> ]	71.6	77.5	71.
Compression strength for cylinder after 28 days $f_{icm,28}$ [N/mm <sup>2</sup> ]	67	72.9	63.7
Tensile strength after 28 days $f_{icm,28}$ [N/mm <sup>2</sup> ]	4.7	4.9	4.5
Modulus of elasticity after 28 days $E_{icm,28}$ [N/mm <sup>2</sup> ]	23653	21701	22549
Fracture energy after 32 days $G_F$ [Nm/m <sup>2</sup> ]	79.7	82	74.9

Concrete class measured from all small samples was LC65 and higher which represents a high strength lightweight concrete. The compressive failures of cubes and cylinders were very explosive which is typical for high strength and lightweight concrete [1].

### 3.2 Results for prisms

Figures 6 and 7 show the experimental results registered with LVDTs and SGs for the centrally and eccentrically loaded prisms.

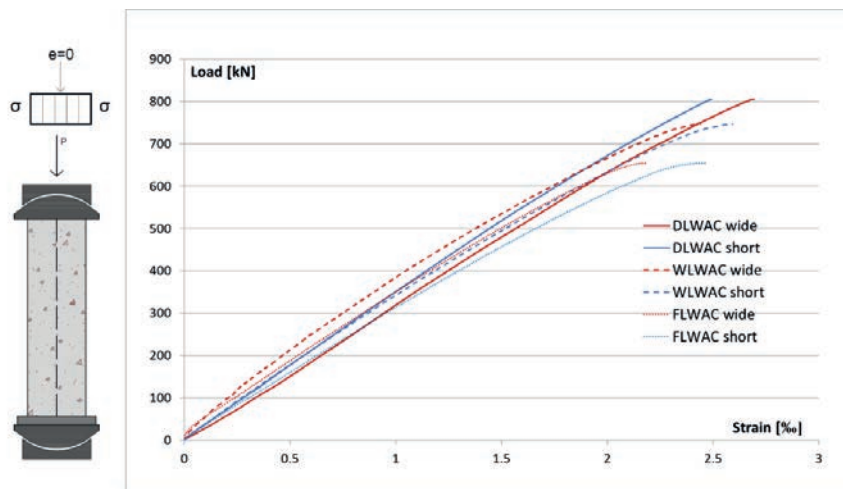


Figure 6 – Load-strain relationship for centric loading.

The load-strain relationship at centricity and eccentricity  $h/18$  and  $h/6$  are shown in Figure 6 and 7. The strains recorded with LVDTs represent lower strains that were registered during testing. For each loading case 3 prisms were tested. The curves are mean values from three tests, except FLWAC.

Table 5 - Test results

Prism Nr.	Type of concrete	Aggreg. moist. [%]	$f_{c,cube}$ [MPa]	$f_{c,prism}$ [MPa]	Eccentricity [mm]	$P_{max}$ [kN]	$P_{calc}$ [kN]	$\epsilon_{c,LVDT}$ [‰]	$\epsilon_{c,DIC}$ [‰]
1-3	DLWAC	0.1	77.9	57.5	e=0	804	763	2.69	3.12
4-6					e=7.77	668	513	2.51	3.47
7-9					e=23.33	495	382	2.70	3.81
1-3	WLWAC	7.9	80.7	53.5	e=0	746	791	2.59	3.40
4-6					e=7.77	648	531	2.19	3.69
7-9					e=23.33	541	395	2.96	4.53
1	FLWAC	7.9	77.6	46.7	e=0	653	760	2.46	2.94
2					e=7.77	669.9	511	2.18	4.54
3					e=23.33	577.8	380	3.38	6.82

Where  $f_{c,cube}$  is compressive cube strength;  $f_{c,prism}$  is compressive prism strength ( $P_{max}$  divided with prism cross section  $100 \times 140 \text{ mm}$ );  $P_{max}$  – load level of maximum load;  $P_{calc}$  – hand calculation of maximum load;  $\epsilon_{c,LVDT}$  – maximum concrete compressive strain recorded with LVDT;  $\epsilon_{c,DIC}$  – maximum concrete compressive strain recorded with DIC.

In addition to this results Table 5 shows summary of all registered results. In the case of eccentrically loaded prisms, the compressive strain registered with LVDT presents the side that was less stressed, see Figure 7, while strains registered by DIC were at the most stressed side. In the case of centrally loaded prisms we can notice very good agreement between LVDTs (see Figure 6) and DIC measuring method. Average compressive strain levels recorded in all the prisms were between 3.08‰ and 6.82‰.

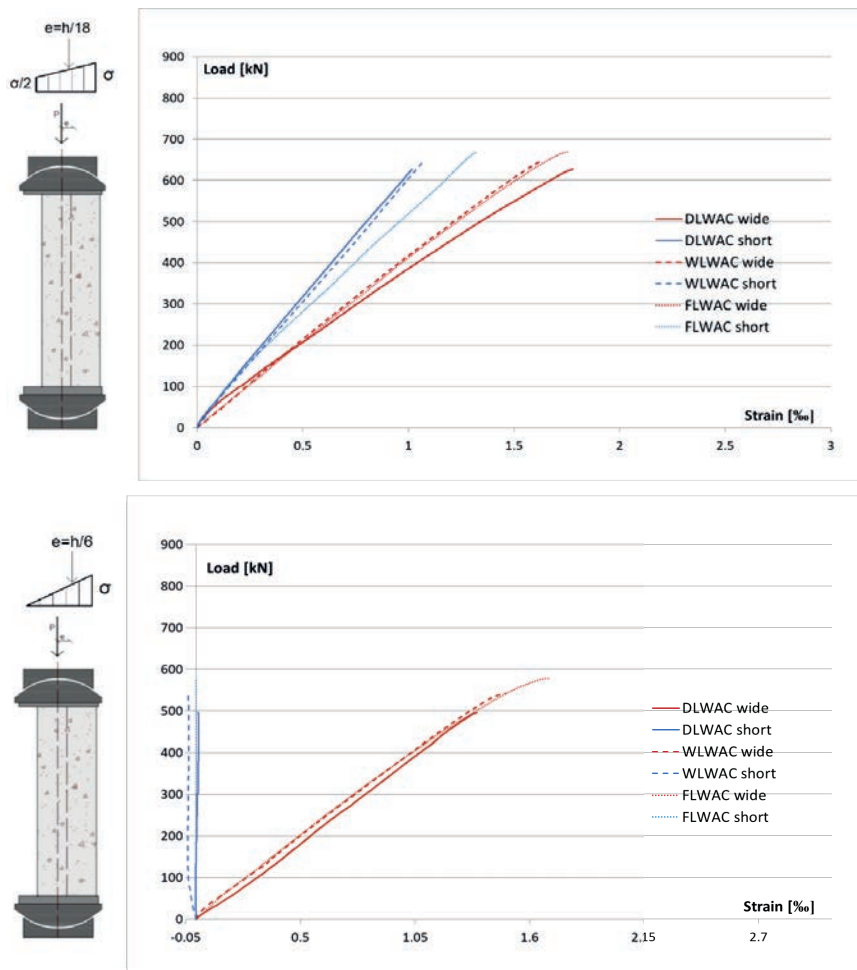


Figure 7 – Load-strain relationship at eccentricities  $e=h/18$  (top) and  $e=h/6$  (bottom).

### 3.3 Failure mode and crack patterns of the prisms

For a concrete specimen loaded in compression the fundamental failure mode is a combination of both axial splitting and sliding. However, the influence of each failure mode depends on concrete material factors such as concrete composition, type of aggregate and maximum aggregate size.

For LWAC it is well known that the weakest part in matrix is aggregate itself and cracking line goes usually through the aggregate [4].

For centrally loaded prisms two types of failure happened: shear, sliding mode of failure (when micro-cracks coalesce to inclined localized shear bands) and longitudinal failure (axial splitting happened when a critical lateral deformation is exceeded), see Figure 8.

At eccentrically loaded prisms longitudinal failure occurred, opening of longitudinal tensile cracks led to the final failure, cracks proceeded within the damage zone. The typical mode of failure for the eccentrically loaded prisms is illustrated in Figure 8. For all samples, the breaking length  $l_b$  and breaking depth  $d_b$  of the fracture were recorded. Table 6 shows the fracture size. In final fase the centrally loaded prisms had longitudinal breaks that went in center of the sample and therefore it was not possible to measure the breaking length  $l_b$  and breaking depth  $d_b$  of the fracture.

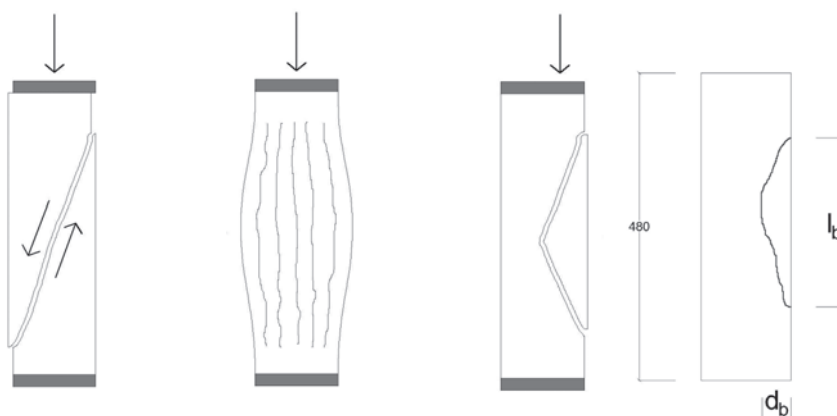


Figure 8 – Sketch of oblique shear fracture (left), longitudinal break (centre) and longitudinal tensile break at eccentric load (right). Typical mode of failure for the eccentrically loaded prisms (right).

Table 6 – Fracture size for eccentrically loaded prisms for DLWAC, WLWAC and FLWAC

<b>e=7.77 mm</b>	<b>DLWAC</b>	<b>WLWAC</b>	<b>FLWAC</b>
$l_b$ [mm]	440	470	340
$d_b$ [mm]	110	110	60
$l_b / d_b$	4	4.3	5.6
<b>e=23.33 mm</b>	<b>DLWAC</b>	<b>WLWAC</b>	<b>FLWAC</b>
$l_b$ [mm]	370	410	290
$d_b$ [mm]	40	280	50
$l_b / d_b$	9.2	5.1	5.8



Figure 9 – Cracking pattern for centrally and eccentrically  $h/18$  and  $h/6$  loaded samples.

Crack propagation depended on the loading conditions. Prisms subjected to centrally loading cracked from the centre of the sample and experienced large cracks and the lowest ultimate compressive strain was registered. Prisms that were loaded eccentrically only cracked at the most stressed part with higher strains. Prisms that were loaded under larger eccentricity experienced just small cracking, see Figure 9.

Through qualitative visual inspection of the fracture, it was discovered that in the concrete with dry Stalite, the fractures both penetrated and travelled around the aggregate particles (approximately 60% aggregate cracked), while in the concrete with saturated Stalite, the fracture to a much larger degree only penetrated the particles (almost 95% aggregate cracked). The concrete with the saturated Stalite had the most explosive fractures. By introducing a small amount of fibers (0,5% of the cement mass) the concrete became significantly more ductile and did not have brittle behaviour. The fracture was not explosive, and the prisms kept together afterwards. In general measured breaking length and depth were significantly smaller for FLAC than for DLWAC and WLWAC.

#### 4. DISCUSSION AND CONCLUSION

A stress gradient test has been used to investigate strains and ductility. The test was done by loading prisms centrally or with two different eccentricities. The proportions of the prisms and eccentricities were the same as in an earlier experiment and are therefore comparable. This study investigates differences using dry (0.10 % moisture content) or saturated (7.9 % moisture content) aggregate Stalite, and the effect of polyvinyl alcohol fibres on the compressive behaviour of LWAC. Crack propagation depended on the loading conditions. Prisms subjected to centrally loading experienced large cracks and the lowest ultimate compressive strain, while prisms loaded eccentrically only cracked at the most stressed part with higher strains. By using DIC, detailed strain fields of the observed compressive zones have been recorded, see Figure 10.

From the achieved experimental results, it is visible that the lateral deformation of the most stressed fibre is counteracted by the less stressed fibres that confine compressive stress. Close to the peak load the lateral deformations near the free surface become pronounced. Finally, in the post-peak region two different fractures developed and ultimate strains increased. In general, larger eccentricity lead to increased strains (recorded strains in prisms test was in range from 3.08‰ to 6.82‰).

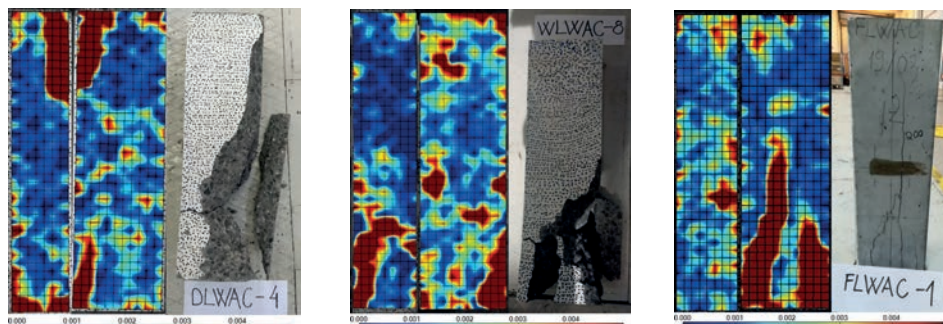


Figure 10 – Strain field for DLWAC (left), WLWAC (centre) and FLWAC (right) just before the final failure. Strain range from 0‰ till 5‰.

In general, measuring devices were in a good agreement, but close to failure, larger strains and localization were measured using DIC, compared to the strain values measured with the SGs and LVDTs. The concrete with the water saturated aggregate had somewhat higher strains and ductility than the concrete with dry aggregate. Through qualitative visual inspection of the fractures, it was observed that the concrete with the saturated aggregate had the most explosive fractures. By introducing a small amount of fibers (0.5% of volume fractions) the concrete became significantly more ductile, with a maximum compressive strain of 6.82 ‰, and the fracture was not explosive. FLWAC samples in final phase kept together afterwards. Eurocode 2 [19] does not differ between lightweight concrete with different types of aggregates and underestimated the largest strains in this experiment by 75-88 ‰.

#### 4.1 Comparison with previous experimental work

The experimental setup of the prisms and the eccentricities were the same as in an earlier experiment and are therefore comparable [4]. The earlier studies looked at the lightweight concrete Liapor 8 and different types of normal weight concrete. Table 7 compares new and old experiments. A ductility index  $D$  is calculated as:

$$D = \frac{\varepsilon_{cu} - \varepsilon_{el}}{\varepsilon_{el}} \cdot 100\% \quad (1)$$

where  $\varepsilon_{cu}$  is maximum compressive strain and  $\varepsilon_{el}$  is strain corresponding to elastic state. In elastic state strains are reversible which recovers while applied stresses are being removed. Plastic strains yield in the specimen before reaching peak point (maximum compressive strains before failure). Elastic and plastic zone of specimen depends on the stiffness, brittleness and ductility of specimen. Concrete is more ductile if difference between elastic and maximum strain is larger. In that case ductility index  $D$  is larger as well. Specimen having higher strength will lead to smaller strains and elastic portion in this case will be more. Concrete is a brittle material and it shows smaller value of strains before failure.

Table 7 - Comparison with experimental work from 1993 [2]

Type of concrete	Eccentricity [mm]	$f_{lc,prism}$ [MPa]	$f_{lc,cube}$ [MPa]	$\mathcal{E}_{cu}$ [%]	$D_{LVDT}$ [%]	$D_{DIC}$ [%]
DLWAC	e=0			3.12		
	e=7.77	57.5	77.9	3.47	11.2	13.3
	e=23.33			3.81		
WLWAC	e=0			3.40		
	e=7.77	53.5	80.7	3.69	15.1	14.9
	e=23.33			4.53		
FLWAC	e=0			2.94		
	e=7.77	46.7	77.6	4.54	37.2	37.6
	e=23.33			6.82		
Liapor 8	e=0			3.12		
	e=7.77	86.8	93.8	3.41	9.6	
	e=23.33			3.55		
Gneiss/ Granite	e=0			2.61		
	e=7.77	81.4	104.1	2.97	14.5	
	e=23.33			3.16		
Basalt	e=0			2.72		
	e=7.77	89.0	105.1	3.31	31.7	
	e=23.33			3.45		
Quartzite	e=0			2.47		
	e=7.77	86.5	106.7	2.81	14.8	
	e=23.33			2.84		

Where  $f_{lc,prism}$  is compressive prism strength;  $f_{lc,cube}$  is compressive cube strength;  $\mathcal{E}_{cu}$  – maximum concrete compressive strain;  $D_{LVDT}$  – ductility index calculated from maximum concrete compressive strain recorded with LVDT;  $D_{DIC}$  – ductility index calculated from maximum concrete compressive strain recorded with DIC.

It is clear that LWAC with Stalite showed more ductile behaviour than LWAC with Liapor 8. Compared to normal density concretes the ductility is similar while registered strains are much higher. When adding just small amount of polyvinyl alcohol fibers, the ductility increase, ductility index is doubled.

The results from this experiment are promising for increased use of high strength lightweight aggregate concrete with Stalite as aggregate for concrete structures. High strains and ductility show that concrete with Stalite can be considered as a product in between lightweight aggregate concrete and normal weight concrete. It combines the ductility from normal weight concrete with the low density from lightweight aggregate concrete. In general, based on this experimental results the use of high strength concrete with Stalite as aggregate should be increased because of the favourable combination of high strength with low density.

## 5. ACKNOWLEDGEMENT

The work presented in this paper is part of ongoing PhD study in scope of the DACS project (Durable Advanced Concrete Solutions). The DACS partners are Kværner AS (project owner), Norwegian Research Council, Axion AS (Stalite), AF Gruppen Norge AS, Concrete Structures AS, Mapei AS, Multiconsult AS, NorBetong AS, Norcem AS, NPR A (Statens vegvesen), Norwegian University of Science and Technology (NTNU), SINTEF Byggforsk, Skanska Norge

AS, Unicon AS and Veidekke Entreprenør AS. Jelena Zivkovic would like to express her outmost gratitude to the supervisors and all the project partners for contributions and making this PhD study possible. J. Zivkovic would like to thank to Master students Aleksander Hammer and Håvard Lauvsland for the help during experimental work.

## REFERENCES

1. Zivkovic J & Øverli J A: “Ultimate compressive strain in lightweight aggregate concrete beams”. *Proceedings*, 12<sup>th</sup> fib International PhD Symposium in Civil Engineering, Prague, Czech Republic, August 2018, pp. 829–836.
2. Nedreliid H: “Towards a better understanding of the ultimate behavior of lightweight aggregate concrete in compression and bending”. *Bulletin* No.123 (PhD Thesis), Norwegian University of Science and Technology, Department of Structural Engineering, Trondheim, Norway, 2012, 214 pp.
3. Øverli J A: “Towards a better understanding of the ultimate behavior of LWAC in compression and bending”. *Engineering Structures*, No. 151, 2018, pp. 821–838.
4. Markeset G: “Failure of concrete under compressive strain gradients”. *Bulletin* No.110 (PhD Thesis), Norwegian Institute of Technology, Department of Structural Engineering, University of Trondheim, Trondheim, Norway, 1993, 168 pp.
5. Carolina Stalite Company: “Production of Stalite”. Salisbury, North Carolina, USA available: <https://www.stalite.com/production>.
6. Standard Norge: “Testing hardened concrete - Compressive strength of test specimens”. Part 3, NS-EN 12390-3:2009, Lysaker, Norway, 2009, 24 pp.
7. Standard Norge: “Testing hardened concrete – Tensile strength of test specimens”. Part 6, NS-EN 12390-6:2009, Lysaker, Norway, 2009, 16 pp.
8. Skjølvold O, Bakken N & Johansen E : “Bestemmelse av E-modul iht NS3676 Losenhausen 5000kN trykkpresse”. Betong og natursteinslaboratoriene, KS 14-05-04 122, SINTEF Byggforsk, Trondheim, Norge, 2007. (in Norwegian)
9. Standard Norge: “Concrete testing - Hardened concrete - Modules of elasticity in compression”. NS 3676, Norway, 1987, 20 pp.
10. Hillerborg A: “The theoretical basis of a method to determine the fracture energy  $G_f$  of concrete”. RILEM Technical Committees, *Materials and Structures*, Vol. 18, Issue 4 2005, pp. 291-296.
11. Carolina Stalite Company: “Benefits of using Stalite”. North Carolina, USA , accessed October 21. 2009. <http://www.stalite.com/why-use-stalite.php?cat=138.html>.
12. American Concrete Institute: “Guide for structural lightweight aggregate concrete”. ACI213R–03, Farmington Hills, MI, United States, 2003, 38 pp.
13. Savija B, Lukovic M, Kotteman G, Chaves F S, de Mendoca Filho F F & Schlangen E: “Development of ductile cementitious composites incorporating microencapsulated phase change materials”. *International Journal of Advances in Engineering Sciences and Applied Mathematics*, Vol. 9, Issue 3, 2017, pp. 169-180.
14. Kuraray Co: “Characteristics of KURALON (PVA fibres), PVA fibres-application”. Japan, available: <http://kuralon-frc.kuraray.com/product-application>
15. Standard Norge: “Testing hardened concrete - Density of hardened concrete”. Part 7,

- NS-EN 12390-7:2009, Lysaker, Norway, 2009, 16 pp.
16. European Union – Brite EuRam III: “Methods for Testing Fresh Lightweight Aggregate Concrete”. BE96-3942/R4, December 1999, 51 pp.
  17. McCormick N & Lord J: “Digital Image Correlation for Structural Measurements”. ICE institution, *Civil Engineering*, 165 (CE4), 2012, pp. 185–190.
  18. SINTEF procedure: “Fracture energy of prisms with notch in three point bending test”. KS14-05-04123, September 2007, 3pp.
  19. European committee for standardization: “Eurocode 2: Design of concrete structures – General rules and rules for buildings”. Part 1-1, EN 1992-1-1 (2004), 2004, 225 pp.

	
© Article authors. This is an open access article distributed under the Creative Commons Attribution-NonCommercial-NoDerivs licens. ( <a href="http://creativecommons.org/licenses/by-nc-nd/3.0/">http://creativecommons.org/licenses/by-nc-nd/3.0/</a> ).	ISSN online 2545-2819 ISSN print 0800-6377
DOI: 10.2478/ncr-2019-0012	Received: April 22, 2019 Revision received: June 7, 2019 Accepted: June 18, 2019

## Plastic Shrinkage Cracking of Self-compacting Concrete: Influence of Capillary Pressure and Dormant Period



Faez Sayahi  
Ph.D.  
Div. of Building Materials  
Luleå University of Technology, LTU  
971 87 Luleå, Sweden.  
[faez.sayahi@ltu.se](mailto:faez.sayahi@ltu.se)



Mats Emborg  
Professor LTU/Head R&D Betongindustri AB  
971 87 Luleå, Sweden. /Betongindustri AB, 100 74 Stockholm.  
[mats.emborg@betongindustri.se](mailto:mats.emborg@betongindustri.se)  
[mats.emborg@ltu.se](mailto:mats.emborg@ltu.se)



Hans Hedlund  
Adjunct Professor LTU/Skanska Teknik AB  
971 87 Luleå, Sweden/Skanska AB, 405 18 Göteborg, Sweden  
[hans.hedlund@ltu.se](mailto:hans.hedlund@ltu.se)  
[hans.hedlund@skanska.se](mailto:hans.hedlund@skanska.se)



Andrzej Cwirzen  
Professor  
Div. of Building Materials  
Luleå University of Technology, LTU  
971 87 Luleå, Sweden  
Andrzej.cwirzen@ltu.se

## ABSTRACT

This research investigates the effect of capillary pressure and the length of the hydration dormant period on the plastic shrinkage cracking tendency of SCC by studying specimens produced with different w/c ratios, cement types and SP dosages. A relationship between the capillary pressure rate and the length of the hydration dormant period is defined, which can explain the cracking severity of the concrete when the volumetric deformation is unknown.

The results show, that the cracking tendency of SCC was the lowest in case of w/c ratio between 0.45 and 0.55, finer and more rapid hardening cement, and lower dosage of SP. The dormant period was prolonged by increasing the w/c ratio, using coarser cement, and higher SP dosage. It was concluded that the cracking tendency of concrete is a function of the capillary pressure build-up rate and the length of the dormant period.

**Keywords:** plastic shrinkage, cracking, evaporation, capillary pressure, dormant period.

## 1. INTRODUCTION

Plastic shrinkage cracks in concrete may form at the surface shortly after casting and before the concrete gain enough tensile strain capacity [1, 2]. The aesthetics, durability and serviceability of a structure may be dramatically impaired, as cracks facilitate ingress of harmful materials into the concrete that may cause damage in a long term. The physical aspect of plastic shrinkage is manifested in evaporation of the capillary water and the consequent build-up of a hydraulic pressure, i.e. capillary pressure, in the liquid phase of the material [3]. Autogenous shrinkage, during which the pore liquid is consumed by self-desiccation, does not play a decisive role in plastic shrinkage cracking, when water/cement ratio (w/c) is more than 0.5 [4, 5]. However, for concretes with low w/c ratio and/or high cement content, the effect of autogenous shrinkage in early-age cracking should be considered [6]. In this paper, the term "plastic shrinkage" refers to the contraction induced by drying, i.e. evaporation.

After placing the concrete in the mould, its solid particles settle due to gravity, forcing the pore water to move upwards to the surface, i.e. *bleeding* regime [7]. This surface water eventually

evaporates, after which menisci start to form inside the pores, i.e. *drying* regime [7]. At this point, a negative capillary pressure begins to build-up in the pore network, which in turn creates tensile forces applying on the solid particles. If the accumulated tensile stresses exceed the tensile strength of the young concrete, cracks will form [3].

Rapid and excessive moisture loss, mainly due to evaporation, is the main cause behind plastic shrinkage cracking. However, with constant w/c ratio, self-compacting concrete (SCC) is characterised by a higher risk of early-age cracking in comparison to a vibrated concrete (VC) [8, 9]. The reason lies in the lower water/binder ratio (w/b) and higher cement content of SCC which lowers the bleeding capacity.

The influence of different parameters on the risk of plastic shrinkage cracking has been investigated by a number of researchers. For example, Löfgren and Esping [10] found that the optimum w/c ratio for decreasing the plastic shrinkage cracking tendency of SCC is 0.55. Same authors also observed that increasing the cement content or decreasing w/c ratio increases the autogenous shrinkage [4]. They concluded that SCC with a w/c ratio lower than 0.4, most probably, cracks due to autogenous shrinkage, rather than plastic shrinkage. Other experiments also showed that the risk of plastic shrinkage cracking of SCC significantly decreases when w/b ratio is below 0.44 [11].

Furthermore, it has been observed that a normal hardening cement boosts the cracking tendency of SCC in comparison to a rapid hardening cement [4]. Finer cement particles, on the other hand, increase the cracking severity [12, 13], most probably due to autogenous shrinkage. However, coarser cements cause wider cracks, despite of lower cracking intensity [13]. Another study shows that superplasticizers (SP) increase the evaporation, delay the hydration, and lead to higher cracking risk [14].

Despite all the research done so far, the mechanism of plastic shrinkage is not yet fully understood, especially when considering the evaporation as the only driving force [13]. The main aim of this paper is to determine a relationship between capillary pressure and the hydration dormant period, which may explain the cracking mechanism. The findings of this research may then be utilized in developing new models to explain the phenomenon of plastic shrinkage.

## **2. MATERIALS AND METHODS**

### **2.1 Materials and mixing process**

The mix design of the concretes and composition of the cements are shown in Tables 1 and 2, respectively. A reference concrete (REF), with w/c ratio of 0.67 was produced using a Portland composite cement, (CEM II/A-LL 42.5R according to EN 197-1 [15]) known as Byggcement in Sweden and containing 11% of limestone. The reference mixture contained 60% of total aggregate mass of natural aggregates (0-4 mm and 0-8 mm) and 40% of total aggregate mass of mixed natural/crushed 8-16 mm aggregates. Limestone filler (Limus 40) with density of 2700 kg/m<sup>3</sup> and

SP (Sikament 56) based on polycarboxylate ether, with density of 1100 kg/m<sup>3</sup> and 37% of dry content were used.

Four mixtures with different w/c ratios (0.38, 0.45, 0.55 and 0.67) were produced and tested. The effect of SP dosage was investigated by changing its portion from 0.8% of cement weight in the REF mix, to 0.6% and 1.0% of cement weight in SP0.6 and SP1, respectively.

*Table 1 - Mix design of the tested SCCs, in kg/m<sup>3</sup>.*

Name	REF	REFS	REFA	W/C38	W/C45	W/C55	SP0.6	SP1
Cement	300	300	300	420	380	340	300	300
Cem. type*	Byggcement	SH-cement	Anläggningscement.	Byggcement	Byggcement	Byggcement	Byggcement	Byggcement
Water	200	200	200	160	171	187	200	200
Agg. 0-4	155	155	155	0	0	81	155	155
Agg. 0-8	771	771	771	1021	998	879	771	771
Agg. 8-16	628	628	628	694	678	651	628	628
Filler	220	220	220	40	100	160	220	220
SP	2.4	2.4	2.4	4.6	5.7	4.1	1.8	3
W/C	0.67	0.67	0.67	0.38	0.45	0.55	0.67	0.67

\* According to Table 2.

All components were stored at the temperature at which the concrete mixing took place (20 ± 1 °C). The aggregates, filler and cement were premixed in a pan type Zyklos mixer for one minute before the solution of water and the SP was added. The mixing process then continued for further five minutes. All the concrete mixtures were produced and tested twice to ensure the repeatability.

*Table 2 - Composition of the cements (produced by Cementa AB, Sweden).*

Name	CEM II/A-LL 42.5R (Byggcement)	CEM I 42.5N (Anläggningscement)	CEM I 52.5R (SH-cement)
CaO (%)	61.7	63.9	62.9
SiO <sub>2</sub> (%)	18.4	21.3	19.3
Al <sub>2</sub> O <sub>3</sub> (%)	5.0	3.6	5.2
Fe <sub>2</sub> O <sub>3</sub> (%)	2.9	4.5	3.1
MgO (%)	1.2	1.0	1.3
Na <sub>2</sub> O (%)	0.15	0.12	0.16
K <sub>2</sub> O (%)	1.3	0.66	1.3
SO <sub>3</sub> (%)	3.8	2.8	3.9
Cl (%)	0.03	0.01	0.04
C <sub>2</sub> S (%)	7.6	12.8	8.6
C <sub>3</sub> S (%)	55.4	64.1	62.2
C <sub>3</sub> A (%)	7.7	2.1	8.6
C <sub>4</sub> AF (%)	8.4	13.6	9.4
Density (kg/m <sup>3</sup> )	3080	3189	3125
Blaine (m <sup>2</sup> /kg)	430	310	550

## 2.2 Method

The cracking tendency was measured according to the NORDTEST-method (NT BUILD 433) [16], also known as the ring test method. The test set-up included three identical moulds, each consisted of two concentric steel rings. Steel ribs (stress raisers), welded to the rings, provided crack initiation points, see Figure 1.

After casting, the moulds were covered with a transparent air funnel attached to a suction fan, generating a wind of 4.5 m/s velocity across the specimen surface. The ambient temperature and the relative humidity were  $20 \pm 1^\circ\text{C}$  and  $35 \pm 3\%$ , respectively.

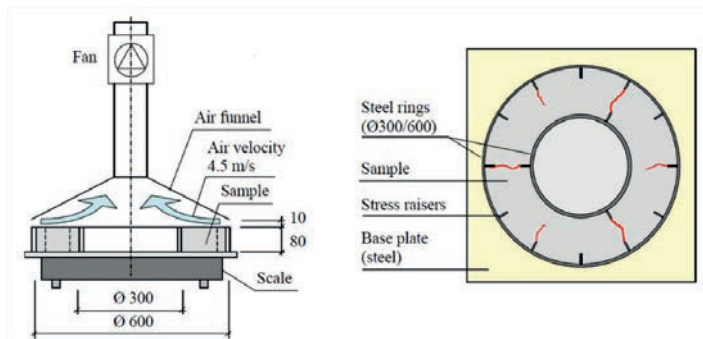


Figure 1 - The ring test set-up used to determine the plastic shrinkage cracking tendency, based on [10] (the dimensions are in mm).

One of the moulds was placed on three load cells (scales) in order to measure the weight loss (i.e. water evaporation), at 1 s intervals. The capillary pressure was measured every 15 s by two wireless pressure sensors (CPSS, manufactured by FTZ, HTWK Leipzig) filled with degassed water, see Figure 2. The sensors were inserted vertically, down to 4 cm from the concrete surface. The internal temperature was recorded at 1 s intervals with a thermo thread located 2 cm from the bottom of the mould. The measurements started 60 minutes after casting and ended 18 hours later.

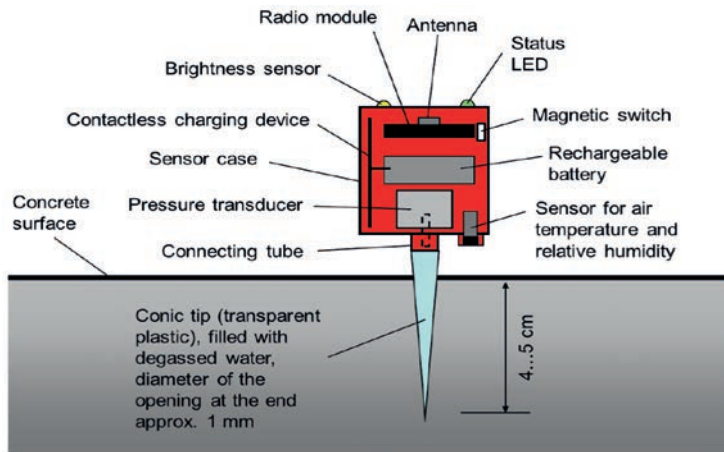


Figure 2 - Schematics of a wireless capillary pressure sensor, from [17].

The surface of the specimens was visually inspected every 30 minutes in order to determine the crack initiation time. The crack width and the crack length were measured by a digital microscope (Dino Lite AM-413T Pro) to an accuracy of 0.001 mm and a digital measuring wheel (Scale Master Pro) to an accuracy of  $\pm 1$  mm, respectively. The average crack area of the three moulds was calculated, according to [14].

### 3. RESULTS

#### 3.1 Concrete properties

Results of the slump flow test (according to EN 12350-2 [18]), associated with the density and air content, are presented in Table 3. Increasing the w/c ratio and SP dosage, increased the concrete flow, while no variation was detected by changing the cement type.

Table 3 - Concrete properties.

Name	REF	REFS	REFA	W/C38	W/C45	W/C55	SP0.6	SP1
Slump flow (mm)	760	760	760	650	700	730	710	800
T <sub>500</sub> (sec)	2	2	2	3	2.5	2	2.5	2
Density (kg/m <sup>3</sup> )	2348	2380	2423	2146	2226	2292	2336	2350
Air content (%)	1.7	1.8	2	1.5	1.5	1.6	1.6	1.8

#### 3.2 Effects of the w/c ratio

Figure 3 shows the influence of the w/c ratio on the average crack area and the crack initiation time. By increasing the w/c ratio from 0.38 to 0.45, the average crack area decreased from 34.3 to

9.2 mm<sup>2</sup>. However, further increase of the w/c ratio, exhibited an opposite effect, as the average crack area started to increase, especially above the w/c of 0.55, where the crack area, eventually, reached 91.4 mm<sup>2</sup> in REF. On the other hand, the crack initiation time gradually decreased from 7 hours in W/C38 to 3 hours in REF, see Figure 3.

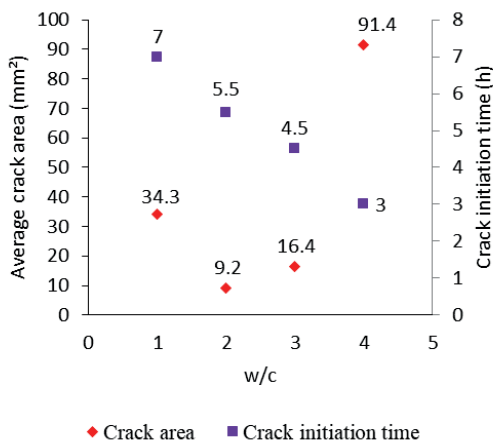


Figure 3 - Effect of w/c ratio on the average crack area and the crack initiation time (from mixing) of SCC.

Note that in this paper, the crack initiation time is the only parameter that was quantified from the concrete placement, while all the other measurements started 60 minutes after casting.

The total cumulative evaporation was raised by increasing the w/c ratio, see Figure 4. However, a notable difference was detected between the total evaporation of W/C38 and those of the other mixtures, where the evaporation of the former ceased after around 13 h, while the others exhibited ongoing evaporation, despite the falling rate.

With the exception of REF, increasing the w/c ratio did not significantly affect the capillary pressure build-up rate, see Figure 5. The onset time of the pressure evolution was not affected by the w/c ratio, as its absolute value started to increase simultaneously in all the specimens.

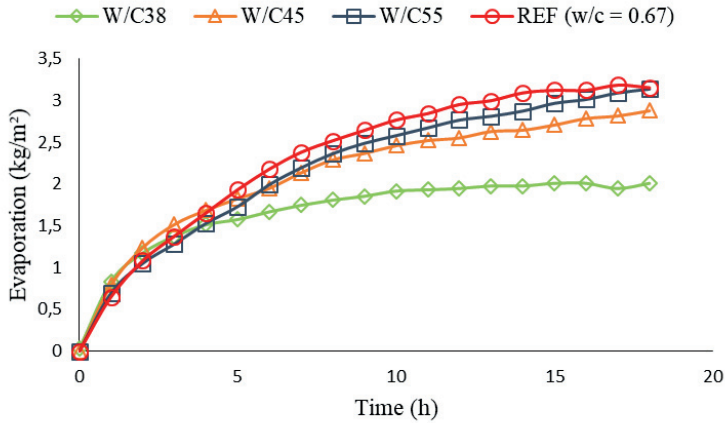


Figure 4 - Influence of w/c ratio on the cumulative evaporation (time after starting the measurement).

A gradual prolongation of the dormant period was observed, as the w/c ratio increased from 0.38 to 0.55 (see Figure 5 and Table 4). However, REF showed slightly shorter dormant period, compared to W/C55.

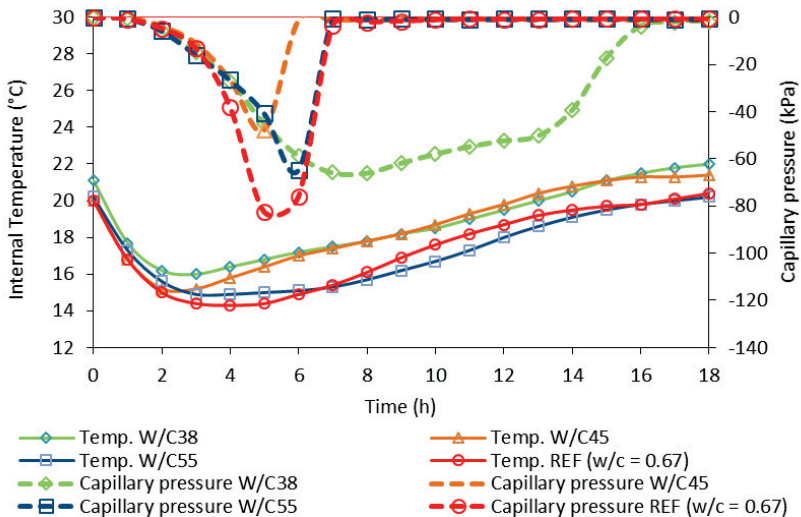


Figure 5 - Influence of w/c ratio on internal temperature and capillary pressure (time after starting the measurement).

### 3.3 Effects of the cement type

Crack areas of concretes produced with CEM II/A-LL 42.5R (REF) and CEM I 52.5R (REFS), were very close, see Figure 6. However, the crack area of REFA, produced with CEM I 42.5N, was around 50% larger in contrast to the other two mixes. The time of crack initiation was 3 hours after casting in the case of REF and REFA, whereas REFS showed the first crack after 7 hours.

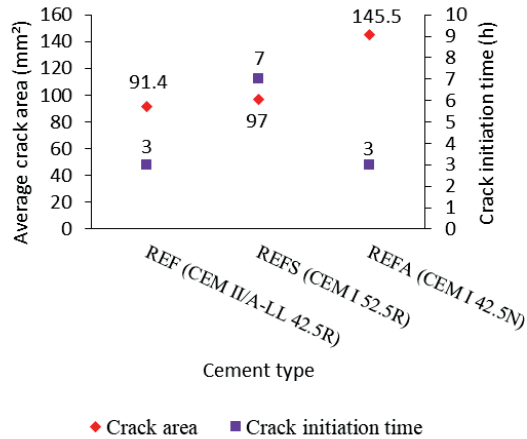


Figure 6 - Effect of cement type on the average crack area and the crack initiation time (from mixing) of SCC.

REFS showed a slightly less cumulative evaporation, compared to the reference concrete, see Figure 7. On the other hand, REFA had nearly 60% higher evaporation than that of REF. The difference was evident, even during the first hour. Figure 8 plots the maximum cumulative evaporation at the end of the test versus the blain size of the cements. The amount of the evaporated water, clearly increased when cements with coarser particles were used.

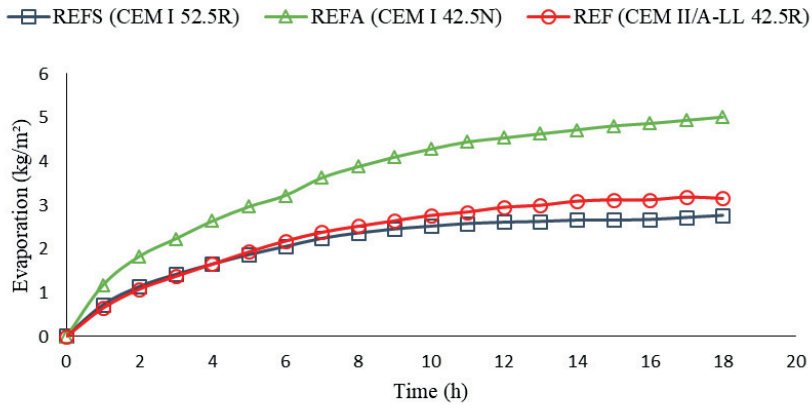


Figure 7 - Influence of the cement type on the cumulative evaporation (time after starting the measurement).

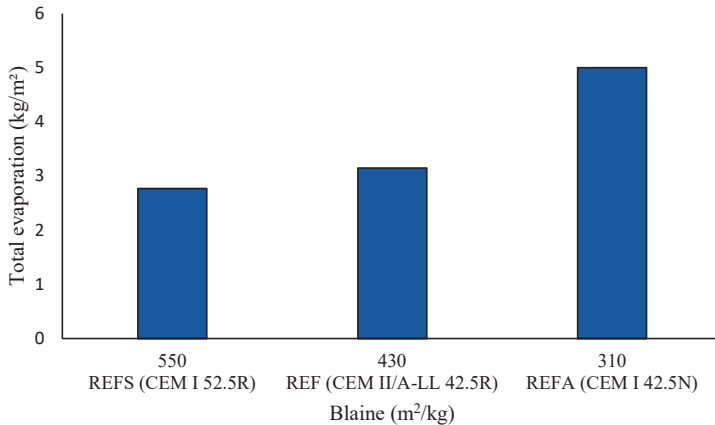


Figure 8 - Effect of cement fineness on the total evaporation.

The cement type did not have any noteworthy impact on neither the capillary pressure build-up rate nor its onset time, see Figure 9. On the contrary, significant difference was found in the internal temperature measurements, as the dormant periods of REFS and REFA were, respectively, shorter and longer than the one in the reference concrete. REFS was the only mixture to reach a maximum value of the internal temperature, among all specimens in this study, see Figures 5, 9 and 12.

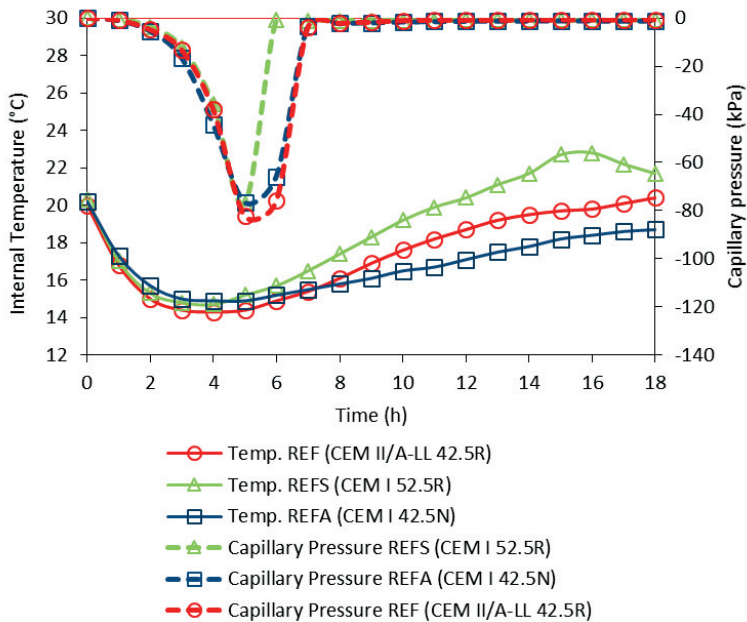


Figure 9 - Influence of cement type on the internal temperature and the capillary pressure (time after starting the measurement).

### 3.4 Effects of SP dosage

Increasing the SP dosage, increased the crack area almost at a constant rate, see Figure 10. The measured crack areas were 56.8, 91.4 and 112.4 mm<sup>2</sup> in SP0.6, REF (0.8%) and SP1, respectively. However, the amount of SP appeared to have no influence on the crack initiation time, as all the three specimens cracked at around 3 h after casting.

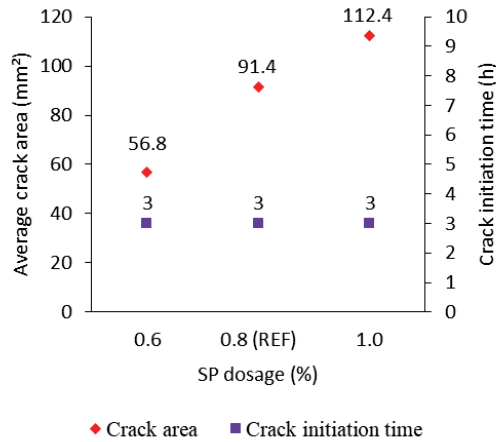


Figure 10 - Effect of the SP dosage on the average crack area and the crack initiation time (from mixing) of SCC.

Decreasing the SP dosage resulted in both lower evaporation rate and total amount of the lost water in SP0.6, compared to the reference mixture, see Figure 11. The opposite effect was observed when the SP content was increased to 1.0% of cement weight in SP1.

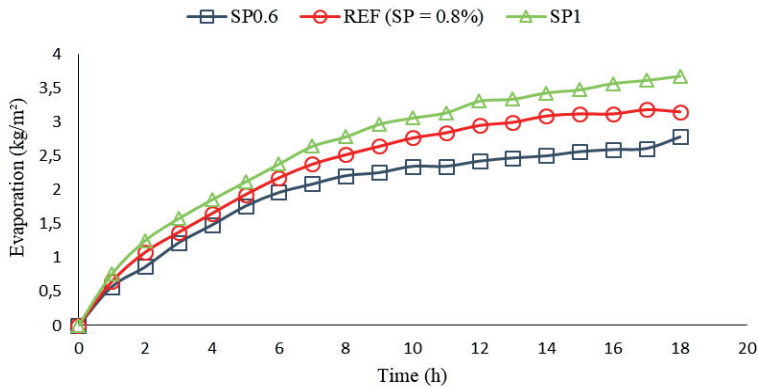


Figure 11 - Influence of SP on the cumulative evaporation (time after starting the measurement).

On the other hand, decreasing the SP content, caused higher capillary pressure build-up rate, see Figure 12. However, the pressure value in all the specimens started to increase almost simultaneously, regardless the SP dosage.

The amount of SP also affected the hydration rate, where SP0.6 and SP1, respectively, shortened and prolonged the dormant period, compared to the REF mix.

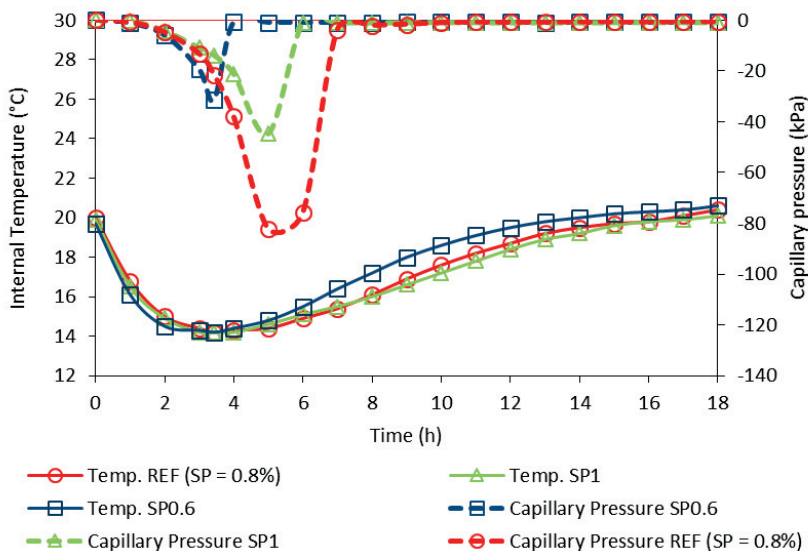


Figure 12 - Influence of SP dosage on the internal temperature and capillary pressure (time after starting the measurement).

### 3.5 Capillary pressure and dormant period characteristics

Table 4 gives the length of the dormant period (from the time of mixing), in addition to the rate and the onset time of the capillary pressure build-up, for all mixtures. The end of the dormant period was determined by calculating the inflection point of the internal temperature curve. In order to quantify the rate of the capillary pressure evolution, the lowest maximum absolute pressure value among all specimens, i.e. -31.56 kPa in SP0.6, was set as the upper limit. Then, for all mixtures, the pressure rate was calculated between the onset time, i.e. 1 h after starting the measurements (see Table 4), and the time at which the pressure reached the limit of -31.56 kPa.

Table 4 - Dormant period, capillary pressure build-up rate, and pressure build-up onset time of the tested mixtures.

Name	REF	REFS	REFA	W/C38	W/C45	W/C55	SP0.6	SP1
Dormant period* (h)	6.9	5.9	7.9	3.9	4.1	8.1	5.5	8.2
Pressure rate (kPa/h)	10.97	11.62	10.77	9.63	9.77	9.23	12.5	8.89
Pressure onset time* (h)	2	2	2	2	2	2	2	2

\* time from mixing which was almost equal to the casting time.

## 4. DISCUSSION

The effects of w/c ratio, cement type and SP dosage on the plastic shrinkage cracking of fresh concrete, have been studied previously [4]. However, the present research focuses on the effects of these variables on the capillary pressure build-up and on the hydration rate. The results were used to define a relationship between the pressure evolution rate and the duration of the hydration dormant period. The determined relationship can contribute to explanation of the cracking mechanism, even without knowing the actual volumetric deformation. Thus, the vertical and horizontal deformations of the specimens are not reported in this paper.

### 4.1 Capillary pressure

After the concrete enters the drying regime, the progressive evaporation gradually reduces the radii of the water menisci, and leads to further increase of the capillary pressure absolute value, which in turn, increases the tension level in the concrete bulk [3]. These tensile forces act on the solid particles and shrink the concrete mass. In case the concrete member is restrained (internally and/or externally), the shrinkage can lead to accumulation of tensile stresses, which may cause cracking, if they exceed the low early age tensile strength of the concrete [19]. Thus, assuming constant restraint degree, higher capillary pressure increases the tensile stresses in the concrete bulk, which may accelerate and facilitate surpassing of the still low tensile strength in the plastic state.

The maximum absolute pressure value in the concrete, however, differs by location, which can be attributed to the difference in the air penetration occurrence [3]. Accordingly, the maximum absolute value of the capillary pressure cannot be considered as a material property [19]. However, at a given depth, the rate at which the pore pressure increases (i.e. slope of the ascending part of the pressure-time curve) is the same, regardless the location [20], see Figure 13. Thus, the capillary pressure build-up rate may indicate the amount of the tension, applied on the solid particles of the mixture, and accordingly, the deformation of the concrete mass.

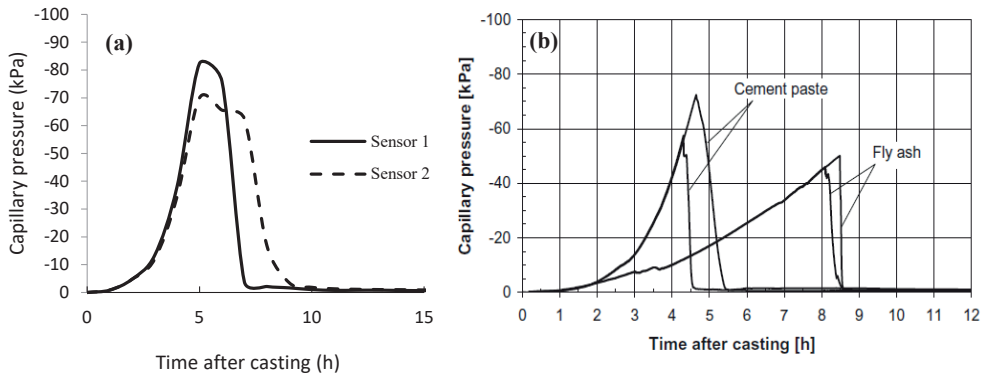


Figure 13 - Capillary pressure measured at 4 cm from the surface in two locations of one specimen: a) from [21]; b) from [19].

#### 4.2 Tensile strength development

As stated before, the cracking potential should be evaluated based on a comparison between the tensile stresses and the concrete tensile strength, since cracking does not occur, unless this limit is passed. Earlier studies show that the tensile strain capacity of concrete gradually decreases after mixing, and reaches its lowest value at around the initial setting time [22], i.e. shortly after the end of the hydration dormant period. On the other hand, development of early-age concrete tensile strength is consistent with the hydration degree [23, 24]. During the dormant period, when the hydration is at its lowest level, the concrete possesses poor tensile strength [25], see Figure 14. However, it rapidly increases, as soon as the dormant period is over, when the hydration rate increases. Hence, the length of the dormant period may be assumed equal to the timespan at which the concrete is highly vulnerable to tensile stresses.

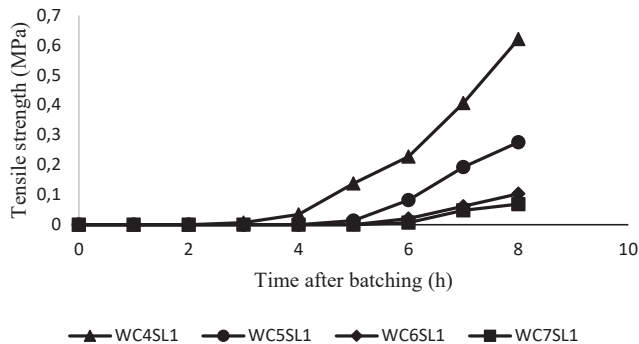


Figure 14 - Tensile strength development of concretes with  $194 \text{ kg/m}^3$  water content (in the legend, the numbers after WC and SL denote the w/c ratio and the intended slump in inches, respectively), from [25].

In the following sections, an effort is made to explain the observed effects of w/c ratio, cement type, and SP dosage on plastic shrinkage cracking. The measured crack areas are then related to the capillary pressure build-up rate and the duration of the dormant period.

### 4.3 Influence of w/c ratio

According to the results, the total evaporation increased with a higher w/c ratio, see Figure 4. However, the largest average crack area was measured in REF, with w/c ratio of 0.67, followed by W/C38, W/C55 and W/C45, respectively, see Figure 3. Evidently, this is not consistent with the evaporation trend. Subsequently, the substantial increase of the average crack area in REF cannot be explained, solely, based on the evaporation. Instead, it can possibly be related to the capillary pressure build-up rate and the length of the dormant period.

As mentioned, the tensile strength of the concrete is meagre during the hydration dormant period [23-25]. Increasing the w/c ratio, which in turn prolongs the dormant period, also delays the onset of the rapid increase of the tensile strength and decreases its rate [25], see Figure 14. Thus, SCC with high w/c ratio, such as REF in this case, has lower tensile strength for a longer period of time which can be easily exceeded by the tensile stresses.

Higher filler volume in SCC increases the risk of plastic shrinkage cracking [12]. Similarly, in the case of REF, a higher evaporation rate combined with presumably narrower pores rapidly increased the rate of capillary pressure development in comparison to the other mixtures, having lower fines content, see Figure 5. This implies that at any time, the amount of shrinkage in REF is higher than that in the other mixtures. For instance, the capillary pressure value at 4 hours after starting the measurement was -38 kPa in REF, versus -26.5 kPa in the other three, see Figure 5. The higher tensile stresses, induced by the faster pressure evolution, together with the concrete's lower tensile strength (i.e. longer dormant period), can explain the considerably higher average crack area of the REF mix. The crack width measurements complied with these results, where the cracks in REF (0.402 mm) were about 10 times wider than those in W/C45 (0.045 mm).

Since the cracking occurred before the end of the dormant period, see Figure 5 and Figure 3, it can be assumed that the plastic shrinkage was induced mainly by the drying contraction. This corresponds well to the general assumption that in a concrete having a w/c ratio exceeding 0.5, the evaporation is the governing mechanism of cracking [5, 6]. Moreover, higher amount of limestone filler, as in case of REF, decreases the autogenous shrinkage [26-28].

The lower evaporation measured in the W/C38 mix, presumably caused slower decrease of the radii of the menisci in the pores, which led to a somewhat lower capillary pressure build-up rate. However, the shorter dormant period was an indication of a faster hydration, which in turn reduced the intrinsic permeability of the mixture and blocked the pathways through which water was transported to the surface. Consequently, the menisci curvature decreased faster, and increased the capillary pressure build-up rate to be almost the same as W/C45 and W/C55. Moreover, taking the late crack initiation time of W/C38 into account, it seems that the shrinkage and cracking of

the SCCs with low w/c ratios was mostly related to the autogenous deformation, which agrees well with the conclusions made by other researchers [5, 29, 30].

Note that in order to maintain the integrity of the mixture and avoiding any segregation, in addition to the w/c ratio, the mix design of the specimens tested here was modified by changing the cement, filler, aggregate, and SP content, see Table 1. This was made due to the broad range of the tested w/c ratios, i.e. 0.38 to 0.67. Thus, the reported results cannot be attributed to the effect of w/c ratio solely, and therefore, should be further investigated in future.

#### 4.4 Influence of cement type

Evaporation rate decreases by increasing the specific surface area of the cement particles [13]. A finer cement makes the pore structure denser, which in turn, reduces the permeability [31], and impedes the transportation of the capillary water to the surface. Cement composition, is another important factor that may explain the evaporation results. It has been observed that higher amount of C<sub>3</sub>A in cement, reduces the bleeding of the concrete [32], due to the accelerated hydration and the consequent reduction of the intrinsic permeability of the matrix [33]. Hence, the significant increase in the evaporation of REFA, compared to REF (Figure 7), can be attributed to its presumably higher permeability due to the lower C<sub>3</sub>A content and coarser particles, see Table 2. Same argument can be used to explain the lower evaporation of REFS, as its finer particles and higher portion of C<sub>3</sub>A decrease the permeability.

Finer pores, according to the Laplace equation [34, 35], may increase the absolute pore pressure value. However, in these particular tests, changing the cement type had a minor effect on the capillary pressure build-up rate, see Figure 9 and Table 4. Hence, it seems that all mixtures should develop more or less equal ultimate shrinkage, assuming constant dormant period. However, this is not the case here, as REFS had a faster hydration and shorter dormant period, compared to REF, while REFA hydrated considerably slower. Higher specific area of the cement particles, i.e. finer cement, helps the dispersion of the particles which increases both the hydration rate and the hydration degree [13]. In addition, the presence of the higher amount of C<sub>3</sub>A, which liberates a significant amount of heat when it comes into contact with water, is another reason behind the faster hydration of REFS [32]. Thus, the difference in the length of the dormant period is the key parameter here, as it reveals the lower tensile strength of REFA.

The cracking in REFA occurs before the end of the dormant period, compare Figure 6 and Table 4. The relatively longer dormant period in REFA, means that the rate at which the concrete gains stiffness is lower. In other words, the specimen will be subjected to higher tension, induced by the capillary pressure, while at the same time the tensile strength develops at a lower rate. This indicates that, in REFA, the concrete cracks mainly due to plastic, rather than autogenous shrinkage.

REFS cracked around the end of the dormant period. It has been observed that the accelerated hydration rate of finer cements leads to larger chemical shrinkage at early ages [36]. Moreover, the higher C<sub>3</sub>A content of CEM I 52.5R also facilitates a more rapid early age chemical shrinkage.

Therefore, the cracks in the REFS seem to be partly autogenous, which complies well with the results of Esping and Löfgren [10].

Based on the discussion mentioned above, it can be concluded that when the capillary pressure build-up rates of different concretes are identical, the one with a longer dormant period is the most prone to plastic shrinkage cracking.

#### 4.5 Influence of SP

The prolongation of the dormant period in SP1 (see Figure 12), can be attributed to the retarding effect of the polycarboxylate ether based SP [37]. The slower hydration, facilitates more upwards transportation of the pore water, which in turn results in a higher cumulative evaporation, see Figure 11. It ought to be remarked, that the measured initial evaporation rate was almost the same for all specimens, which indicates that the later difference in the evaporation rate occurs, most probably, due to the change of the intrinsic permeability.

As it can be seen in Figure 12, the capillary pressure build-up rate decreased by raising the SP dosage. The trend can be explained based on the impact of SP on the concrete porosity, i.e. intrinsic permeability. As the initial porosity of the mix decreases because of the formation of hydration products, especially C-S-H, the lower hydration rate - in this case induced by the retarding effect of the SP - causes slower reduction of the initial porosity [37]. Consequently, the pore pressure increases at a lower rate.

However, lower hydration rate of SP1 prolongs the dormant period, which means that the specimen's tensile strength is very low and may easily be exceeded by the induced tensile stresses. On the contrary, despite of the faster capillary pressure build-up in SP0.6, its tensile strength develops fast enough - due to its shorter dormant period - to withstand the rapidly increasing tensile stresses. Similar results have been observed previously by Esping and Löfgren [4].

#### 4.6 Relationship of capillary pressure and dormant period

According to the results of this research, it is not possible to explain the cracking severity of the tested mixtures, only based on the evaporation. Instead, it seems that the risk of plastic shrinkage cracking tendency of concrete is a function of the capillary pressure rate and the length of the dormant period. Accordingly, the cracking tendency of concrete, or in this case the measured crack area, can be described as:

$$CA \propto \frac{dP}{dt} \times t_d \quad (1)$$

Where  $CA$  is the crack area,  $P$  is the capillary pressure, and  $t_d$  is the length of the hydration dormant period.

By plotting the crack area (Figures 3, 6 and 10) versus the product of the multiplication of the capillary pressure build-up rate and the length of dormant period (Table 4), a general similarity may be observed (i.e. both the crack area and the multiplication product increase or decrease simultaneously), see Figure 15. The only exception is W/C55, which is still in the range of 0.45 to 0.55 w/c ratio, at which the plastic shrinkage cracking risk does not change significantly [20]. Hence, for assessing the cracking severity of plastic concrete, without knowing its volumetric deformation, the combined effect of capillary pressure- and hydration rate should be considered.

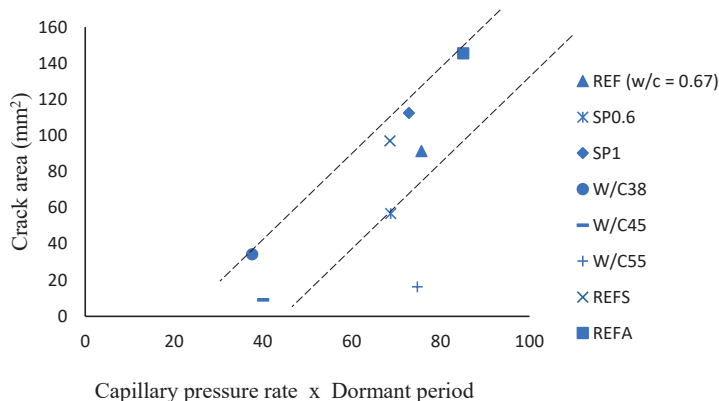


Figure 15 - Crack area versus capillary pressure build-up rate multiplied by the length of the dormant period.

Note that in all specimens, the capillary pressure started to increase around 1 hour after the beginning of the measurements (2 hours after the time of mixing), see Table 4, and thus, the effect of the pressure onset time can be disregarded. Otherwise, assuming constant capillary pressure build-up rate, the sooner the pressure starts to increase, the higher the cracking tendency, as the period between the tensile stress accumulation and the rapid tensile strength development - once the dormant period is ended - will be prolonged.

## 5. CONCLUSIONS

Plastic shrinkage cracking is a complex interaction of several variables that may change under different circumstances and conditions at early ages. These variables may influence the evaporation, in addition to the capillary pressure- and hydration rate. Based on the results of this study, the following concluding remarks can be listed:

- Plastic shrinkage cracking tendency of concrete, in this study, is assumed to be directly proportional to the product of the capillary pressure build-up rate multiplied by the length of the dormant period.

- SCC with high w/c ratio (higher than 0.55), cracks mainly due to plastic shrinkage, while autogenous shrinkage is the main cause of cracking in SCCs with low w/c ratio (lower than 0.45).
- Cracks in SCC, produced by using fine rapid hardening cements are caused by plastic and partly autogenous shrinkage. On the other hand, coarser normal hardening cements result in cracking, induced mainly by plastic shrinkage.
- Higher SP dosage decreases the capillary pressure build-up rate, delays the hydration and increases the evaporation. Concretes with higher SP dosage are more prone to plastic shrinkage cracking, despite the slower capillary pressure development.
- Assuming constant length of the hydration dormant period, the rate of capillary pressure evolution must be reduced by decreasing the evaporation. This can be done, among others, by fogging and/or covering the concrete surface.

## 6. FUTURE WORK

The findings of this research gives a clearer picture about the role of capillary pressure and hydration rate in plastic shrinkage cracking. In future, the relationship discussed here can be used to develop new models to explain the phenomenon.

## ACKNOWLEDGMENT

The authors would like to gratefully appreciate the financial support they received from the Development Fund of the Swedish Construction Industry, SBUF. Special thanks are also due to M.Sc. students and staff of the MCE and Thysell lab at Luleå University of Technology.

## REFERENCES

1. Lerch, W: "Plastic Shrinkage". *ACI Materials*. Vol. 53, 1957, pp. 797-802.
2. Ravina, D & Shalon, R: "Plastic shrinkage cracking". *ACI Materials*, Vol. 65, 1968, pp. 282-291.
3. Slowik, V, Schmidt, M & Fritzsche, R: "Capillary pressure in fresh cement-based materials and identification of the air entry value". *Cement and concrete composites*, Vol. 30, 2008, pp. 557-565.
4. Esping, O & Löfgren, I: "Cracking due to plastic and autogenous shrinkage-investigation of early age deformation of self-compacting concrete-experimental study". Technical report, Chalmers University of Technology, Sweden, 2005.
5. Turcry, P & Loukili, A: Evaluation of plastic shrinkage cracking of self-consolidating concrete. *ACI Materials*, Vol. 10, 2006, pp. 272-279.
6. Esping, O: "Early age properties of self-compacting concrete- Effects of fine aggregate and limestone filler". Doctoral thesis, Chalmers University of Technology, Göteborg, Sweden, 2007.

7. Lura, P, Pease, B, Mazzotta, G.B, Rajabipour, F & Weiss, J: “Influence of shrinkage-reducing admixtures on development of plastic shrinkage cracks”. *ACI Materials*, Vol. 104, 2007, pp. 187-194.
8. . Persson, B: “Plastic shrinkage of self-compacting concrete”. In: Jensen, O.M., Geiker, M., Stang, H. (eds.) *Proceedings of the Knud Hojgaard Conference*, Lyngby, Report R-155 DTU, 2005, pp. 43-57.
9. Gram, H.E & Piiparinen, P: "Properties of SCC: Especially early age and long term shrinkage and salt frost resistance". In: Skarendahl, Å., Petersson, Ö. (eds.) *Proceedings of the 1st International RILEM Symposium on Self-compacting Concrete*, Stockholm, RILEM Publications S.A.R.L., Bagnaux, 1999, pp. 211-225.
10. Löfgren, I, Esping, O, Jensen, O, Lura, P & Kovler, K: “Early age cracking of self-compacting concrete”. *International RILEM Conference on Volume Changes of Hardening Concrete: Testing and Mitigation*, Lyngby, Denmark, 2006, pp. 251-260.
11. Leemann, A & Lura, P: “Creep and Shrinkage of SCC”. In *Mechanical Properties of Self-Compacting Concrete*, edited by K. H. Khayat and G. DeSchutter, New York, 2014, pp. 73–94
12. Hammer, T.A: “Cracking susceptibility due to volume changes of self-compacting concrete (SCC)”. In: Wallevik, O., Nielsson, I. (eds.) *Proceedings of the 3rd International RILEM Symposium on SCC*, Reykjavik, RILEM Publications S.A.R.L., Bagnaux, 2003, pp. 553-557
13. Yang, K, Zhong, M, Magee, B, Yang, C, Wang, C, Zhu, X & Zhang, Z: “Investigation of effects of Portland cement fineness and alkali content on concrete plastic shrinkage cracking”, *Construction and Building Materials*, Vol. 144, 2017, pp. 279-290.
14. Esping, O, Löfgren, I, Marchand, J, Bissonnette, B, Gagné, R & Jolin, M: “Investigation of early age deformation in self-compacting concrete”. *Proceedings of the 2nd International Symposium on Advances in Concrete Science*, Quebec, 2006.
15. EN 197-1, Cement: Composition, Specifications and Conformity Criteria for Common Cements, Br. Stand. Inst. London. 2000.
16. Johansen, R & Dahl, P: “Control of plastic shrinkage of cement”. *Proceedings of the 18th Conference on Our World in Concrete and Structures*, Singapore, 1993.
17. CPSS - User Manual, manufactured by Research and Transfer Centre (FTZ) at the Leipzig University of Applied Science (HTWK Leipzig).
18. EN 12350e12352, Testing Fresh Concrete: Slump Test, Br. Stand. Inst, London. 2000.
19. Slowik, V & Schmidt, M: “Early age cracking and capillary pressure controlled concrete curing”. *Advance in Cement-Based Materials*, Vol. 126, 2010, pp. 229-234.
20. Sayahi, F: “Plastic Shrinkage Cracking in Concrete”, Licentiate thesis, Luleå University of Technology, 2016.
21. Sayahi, F., Emborg, M., Hedlund, H & Löfgren, L: “Plastic Shrinkage Cracking in Self-Compacting Concrete: A Parametric Study”, *Proceedings*, International RILEM conference on Materials, Systems and Structures in Civil Engineering, MSSCE, 2016, pp. 609-619
22. Boshoff, W.P & Combrinck, R: "Modelling the severity of plastic shrinkage cracking in concrete". *Cement and Concrete Research*. Vol.48, 2013, pp.34-39.
23. Dao, V.T.N, Dux, P.F & Horris, P.H: “Tensile properties of early-age concrete”. *ACI Materials*, Vol. 106, 2009, pp. 483–492.
24. Hammer T.A & Fosså, K.T: “Cracking tendency of HSE: Tensile strength and self-generated stress in the period of setting and early hardening”. *Materials and Structures*, Vol. 40, 2007, pp. 319-324.

25. Abel, J & Hover, K: “Effect of water/cement ration the early age tensile strength of concrete”. *Transportation Research Record: Transport Research Board*, Vol. 1610, 1998, pp. 33-38.
26. Poppe, A.M & De Schutter, G: “Creep and shrinkage of self-compacting concrete”. In: Yu, Z, Shi C, Khayat KH, Xie Y (eds) *Proceedings of the 1st International RILEM Symposium on SCC*. RILEM Publications S.A.R.L, Bagneux, 2005, pp. 329-336
27. Rozière, E, Granger, S, Turcry, P & Loukili, A: “Influence of paste volume on shrinkage cracking and fracture properties of self-compacting concrete”. *Cement and Concrete Composites*, Vol. 29, 2007, pp. 626-636.
28. Pons, G., Proust, E & Assié, S: “Creep and shrinkage of self-compacting concrete: a different behaviour compared with vibrated concrete”. In: Wallevik, Ó, Nielsson, I. (eds) *Proceedings of the 3rd International RILEM Symposium on SCC*, Reykjavik. RILEM Publications S.A.R.L., Bagneux, 2003, pp. 645-654
29. Darquennes, M.I.A, Khokhar, E & Rozière, A: “Loukili, F. Grondin, S. Staquet, Early age deformations of concrete with high content of mineral additions”. *Construction and Building Materials*, Vol. 25, 2011, pp. 1836-1847.
30. Mora-Ruacho, J, Gettu, R & Aguado, A: “Influence of shrinkage-reducing admixtures on the reduction of plastic shrinkage cracking in concrete”. *Cement and Concrete Research*, Vol. 39 2009, pp. 141-146
31. Ghourchian, S, Wyrzykowski, M, Baquerizo, L & Lura, P: “Susceptibility of Portland cement and blended cement concretes to plastic shrinkage cracking”. *Cement and Concrete Composites*, Vol. 85, 2018, pp. 44-55.
32. Neville, A.M & Brooks, J.J: “Concrete Technology”. Longman, London. 1990.
33. Ghourchian, S, Wyrzykowski, M, Baquerizo, L & Lura, P: “A poromechanics model for plastic shrinkage of fresh cementitious materials”. *Cement and Concrete Research*, Vol. 31 2018, pp. 120-32.
34. Wittmann, F.H: “On the action of capillary pressure on fresh concrete”. *Cement and Concrete Research*, Vol. 6, 1976, pp. 49-56.
35. Sayahi, F., Emborg, M., Hedlund, H: “Plastic shrinkage cracking in concrete: State of the art”. *Nordic Concrete Research*, Vol. 51, 2014, pp. 95-16.
36. Dellinghausen, L.M., Gastaldini, A.L.G., Vanzin, F.J & Veiga, K.K: “Total shrinkage, oxygen permeability, and chloride ion penetration in concrete made with white Portland cement and blast-furnace slag”, *Construction and Building Materials*, Vol. 37, 2012, pp. 652-659.
37. Gu, P, Xie. P, Beaudoin, J.J & Jolicoeur, C: “Investigation of the Retarding Effect of Superplasticizers on Cement Hydration by Impedence Spectroscopy and Other Methods”. *Cement and Concrete Research*, Vol. 24, 1994, pp. 433-442.

	
© Article authors. This is an open access article distributed under the Creative Commons Attribution-NonCommercial-NoDerivs licens. ( <a href="http://creativecommons.org/licenses/by-nc-nd/3.0/">http://creativecommons.org/licenses/by-nc-nd/3.0/</a> ).	ISSN online 2545-2819 ISSN print 0800-6377
DOI: 10.2478/ncr-2019-0001	Received: January 22, 2019 Revision received: June 26, 2019 Accepted: June 26, 2019

## Cracking of the End Diaphragm of a Post-tensioned Beam Bridge



Mikko Kuusela, MSc.  
Bridge Engineer, A-Insinöörit Civil Oy, Tampere, Finland  
mikko.kuusela@ains.fi



Olli Asp, MSc.  
Research Scientist, Tampere University, Tampere, Finland  
olli.asp@tuni.fi



Anssi Laaksonen, PhD.  
Professor, Tampere University, Tampere, Finland  
anssi.laaksonen@tuni.fi

### ABSTRACT

In concrete beam bridges, the end diaphragm at the end of the bridge is a common structural component that connects the main beams and transfers the beam loads to the bridge bearings. In integral bridges the end diaphragm also retains the soil of embankments due to the absence of abutments. Cracking of the front surface on the end diaphragm has been detected in post-tensioned

beam bridges in Finland and Sweden. Presumably the post-tensioning of the bridge and the shaping and detailing of the connection of the end diaphragm and main beam have an effect on cracking tendency. The aim of this study is to examine the structural behaviour and the cracking potential of end diaphragms using linear analysis of the post-tensioned bridge and to find measures to prevent the cracking.

The observations collected through field surveys are compared to results of linear FE analysis to clarify the cause of the cracking. The verification of model is performed by comparison of patterns of cracking observed in field surveys and the distribution of maximum tensile stresses in the FE model. With model variations, the effectiveness of measures for the prevention of cracking are observed.

**Key words:** Bridge, post-tensioning, end diaphragm, concrete, cracking.

## 1. INTRODUCTION AND BACKGROUND

It has been detected that cracking after post-tensioning occurs in the front surface on the end diaphragm of beam bridges. This problem has been detected in Finland and Sweden [1, 2]. Post-tensioned beam bridges are very common bridge structures in Finland. For example, in 2015 some 23% of all bridges built were post-tensioned beam bridges [3].

The aim of this study was to find out the causes of the cracking and ways to prevent it. The causes of cracking were examined using FEM analysis. The main purpose was to examine the structure rather than to improve modelling. In addition, this study examines what kind of cracking typically appears on the end diaphragm of post-tensioned bridges (described in the Field Surveys section). At Chalmers University of Technology (Sweden), a master's thesis on the same subject was written using nonlinear FE analysis. In the thesis, it was found that cracking only occurs due to prestressing force and vertical loads do not have an effect on cracking. According to the thesis, the most efficient way to limit the cracks is to insert more horizontal reinforcement on the front surface of the end diaphragm [1].

### 1.1 Field Surveys

The field surveys were performed on 16 bridges. The cracking of the end diaphragms was detected on inspections of these bridges. The surveys included several types of post-tensioned bridges. However, the end diaphragms were basically the same type, connected directly to the main girder by an indirect support, which means the main beam of the bridge is connected on the side of the supporting end diaphragm. The number of main girders varied between one and three. The height of the end diaphragm and the main girder varied between 1.3 and 2.3 metres and the width of the web varied from 1.2 to 5.4 metres.

Three of the examined bridges are continuous and with a short cantilever (overhang), while the others are supported from the ends with piles or bearings. The end spans vary between 16.5 and 42.5 metres. The amount of horizontal reinforcement in the front surface of the end diaphragm varies between 1005mm<sup>2</sup>/m and 4909 mm<sup>2</sup>/m. General information about the observed bridges is presented in the annexes in Table 1.

The surveys show that there are typically two kinds of cracking caused by post-tensioning. The first type of crack is inclined cracks between the main girder and the bearing (showed in Figure 1a). The second type is vertical cracks following the connection to the main girder web (showed in Figure 1b). The cracking below the flanges is also noted. On integral bridges with a higher end diaphragm, the cracking also occurs below the wedge of the girder (showed in Figure 1c).

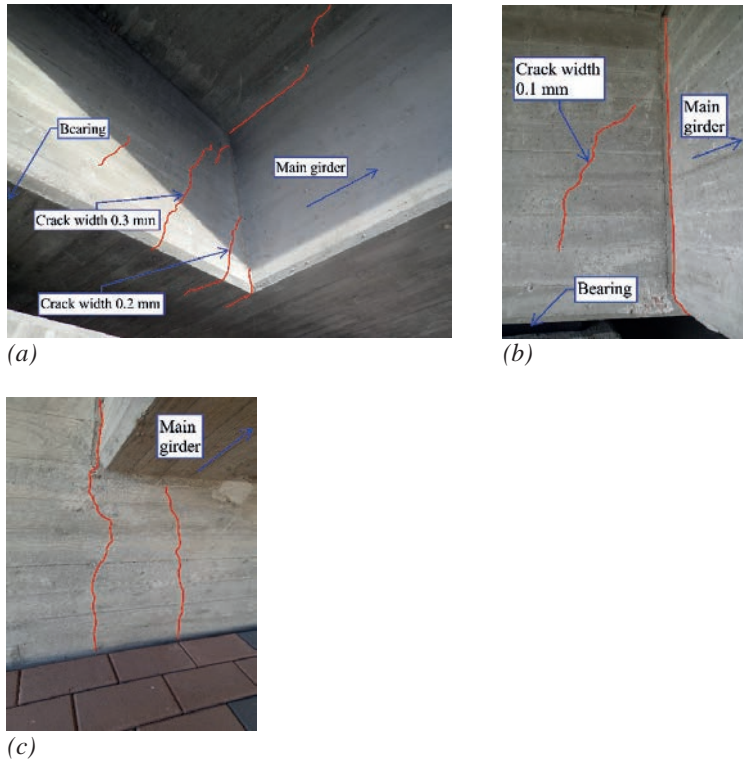


Figure 1 – Cracking on the front surface of the end diaphragm a) Sähköseman risteysilta (first case bridge), b) Skägbyntien risteysilta (second case bridge), c) Pyhtään risteysilta

The measured crack width varies between 0.1...0.5 mm. Cracking seems to be a common problem. For example, the cracking is detected on eight out of a total of 24 post-tensioned bridges in the E18 Koskenkylä-Kotka project. This type of behaviour is also discovered at the end diaphragms of bridges in other projects: Tampereen Rantatunneli, Kehä III VT4-VT7 and Kehä III Lentoasemantie [2].

## 1.2 Case Bridges

Finite-element analysis included two flyover bridges: Sähköseman risteysilta (Vantaa) and Skägbyntien risteysilta (Loviisa). FE analysis was limited to bridges which have one main girder and bearings on the end support. The observed cracking was similar in the bridges of the same type. The first of the case bridges was chosen for the analysis because its prestressing force is

high, which requires a lot of post-tensioning anchors. A significant amount of cracking on the front surface of the end diaphragm is observed.

The second case bridge was chosen because it has almost the same dimensions on the end diaphragm as the first case bridge, but much less prestressing force. The bearings are located closer to each other than in the first case bridge. The second case bridge is also an integral bridge while the first one is not. The case bridges represent typical Finnish post-tensioned beam bridges. The crack pattern and geometry of the case bridges are shown in Figures 2 and 3.

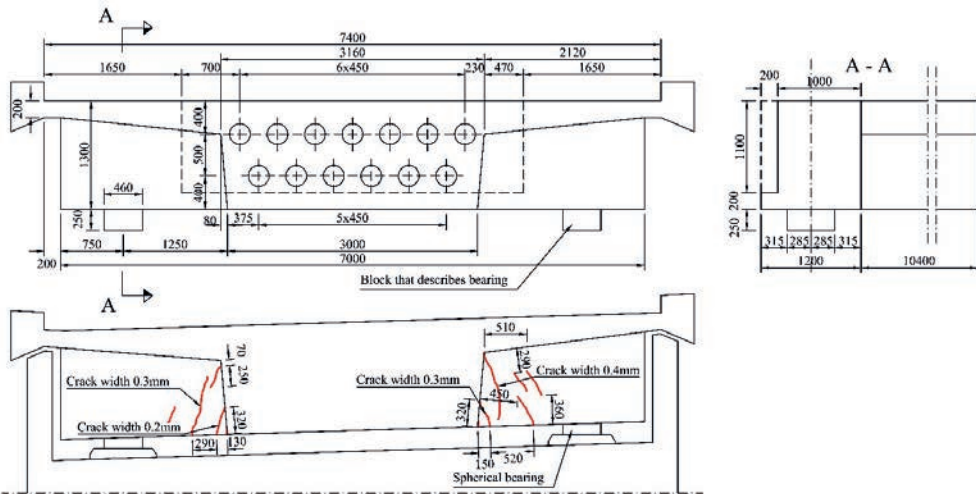


Figure 2 – Geometry of the volume model (upper) and the crack pattern of the first case bridge (lower), span length 28.2+47.0+28.2 m

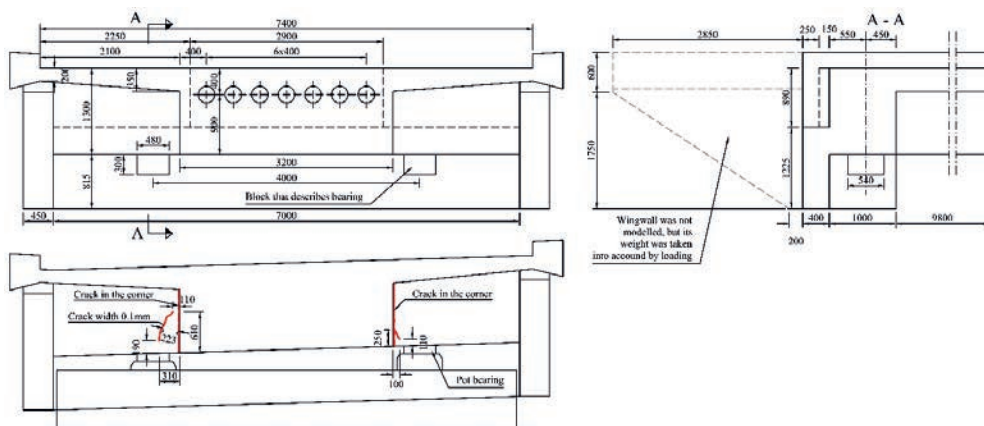


Figure 3 - Geometry of the volume model (upper) and the crack pattern of the second case bridge (lower), span length 26.0+26.0 m

## 2. FINITE ELEMENT ANALYSIS

### 2.1 Modelling

FE analysis is performed by using solid elements and linear calculations. The cracking studied is located in a discontinuity area and therefore it is a three-dimensional problem. That is why the slab or shell elements were not suitable for analysis. A cross section of the volumetric model included only concrete and reinforcement was not considered. The study is performed by examining tensile stresses and comparing them to concrete tensile strength. The use of non-linear analysis with various parameters would have been too time consuming and the verification of results would have been difficult. Using linear modelling is considered to be more reliable.

The material model is linear elastic ( $E=34$  GPa,  $\nu=0.2$ ,  $\gamma=25$  kN/m<sup>3</sup>). In the calculation, the cracking is not taken into account, as the calculation is linear. Therefore, during the combination of results the superposition principle can be used. The elements mainly used in modelling are 3D hexagonal solid elements with 20 nodes (HX20 in [4]) and pentagonal solid elements with 15 nodes (PN15 in [4]). Both used elements are with quadratic interpolation order. The size of the mesh was 100 mm in the area in which the highest tensile stresses are assumed, and 200 mm in other areas in order to keep the calculation time reasonable. The element size was identified by starting with a coarse mesh and refining it, until the calculation time was approximately 30–45 minutes [2].

Only the end area of the bridge is modelled with solid elements; including the end diaphragm and approximately 11 metres of the main girder. This corresponds to 39% of the first span of the first case bridge and 42% of the span of the second case bridge. The main girder is intercepted in a rigid zone, where the rigid nodal support is attached. The bearings are modelled with the same material parameters as the bridge girder and the same size as the bearing plate. Rigid plates are attached under bearing. The stiff beam, with a length of 100 mm, is used to connect the rigid plate to the nodal support under the bearing. The nodal support at the lower end of the stiff beam is fixed in the Z-direction. The friction of the bearing is not included in the analysis. The solid model of the first case bridge is shown in Figure 4a.

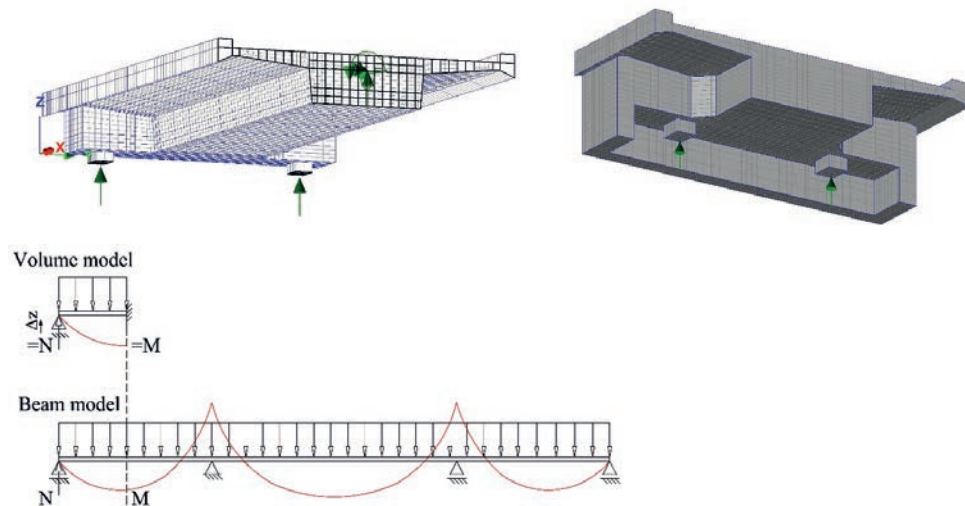


Figure 4 - a) Solid model of the first case bridge b) Solid model of the second case bridge with smaller wedges (the full model is not shown) c) The schematic presentation of the volume model in relation to the beam model

The beam model of the full bridge is used to solve the support reactions of the bearings. Due to loading, the support reactions in the volume model were not as depicted in the beam model at first because it had different support conditions and a different span length to the case bridges. Support reactions in volume model were fitted by modelling additional vertical support displacement, which matches the support reaction to the beam model. The support reactions and forces used are shown in the annexes (Table 2). The beam model is used for comparing bending moments and shear forces to the volume model in order to check the suitability of the solid model.

In the analysis, some simplifications are made. In the model geometry, the longitudinal and horizontal slopes and the inclination, curvature and obliqueness of the end diaphragm, accessories and chamfers are not taken into account. The post-grouting of tendon anchors is neglected because it does not contribute to structural behaviour during post-tensioning. The main girder in the first case bridge is a haunched girder, which is assumed to be constant in height in the volume model. The structure was modelled as symmetrical.

## 2.2 Loads

The selection of loads is made based on observations during mould removal, when the cracking end diaphragm is noticed at an early stage. The significant sources of loads effecting new structures are selected.

The loads in the model are the self-weight of structures, post-tension force, traffic load and internal temperature gradient due to hydration of concrete and ambient air temperature fluctuations. The volumetric model is constructed by modelling rigid plates above bearings and pinned supports under plates, and a rigid plate at the location at which the bridge model is cut according to Fig. 4c. The application of loads is performed by using equivalent support

displacement at bearing locations which the bearing forces with beam model corresponds with. Because the geometry of the model is symmetric and there is no horizontal support on the bearing, all the loads are also modelled symmetrically. Due to this simplification of the model, the torsion of the main girder on the support reaction is not included. Also, the effects caused by asymmetrical traffic (causes torsion) or the effects of asymmetrical temperature gradients are neglected. Because volume models are symmetrical, the stress field has to be symmetrical to verify the model. Influence of creep is not examined. The values of the loads are shown in the annexes (Table 2).

Self-weight included the volumetric weight of the concrete, which was added with gravitation force. The weight of the parapets is included (0.8kN/m) with the weight of layers of tarmac (2.64kN/m<sup>2</sup>). On the case bridge, two wing walls, which are connected to the bridge and supports, were only modelled by equivalent loading of their self-weight. Earth pressure at rest is modelled on the end screen of the bridge from case 2. The effect of passive earth pressure is not considered.

Traffic load is modelled by Load Model 1 (EC1991-2, NCCI1). The axle load is 300kN and one tyre has an effect on a 400x400mm area. It was assumed that a tyre load distributes at an angle of 1:1 in tarmac and it affects the bridge deck over an area of 620x620 mm<sup>2</sup>. According to the Finnish national annex to Eurocode, the first UDL lane has a load of 9 kN/m<sup>2</sup> and the second 6 kN/m<sup>2</sup>, and outside the lanes 3 kN/m<sup>2</sup>.

Both bridges have an effective width of 7.5 metres, so a maximum of two lanes fit on the bridge deck. The traffic load is modelled with two combinations. The first combination is single lane loaded in the middle of the bridge deck. The second combination is two lanes loaded central to the bridge deck and for the symmetric loading both of them should have UDL 7.5 kN/m<sup>2</sup>. It has to be pointed out that the described traffic load attempts to represent the real maximum characteristic loading and it is made for design purposes.

The force used for post-tensioning is post-tension force after immediate losses. The post-tension anchor used in the bridges has three planes that transfer the prestress force to the concrete. Longitudinal post-tension force is modelled on three layers, which were approximately 100 mm apart from each other. The area on which prestress force affects is simplified to a square, which has the same area as the real anchor (220x220 mm<sup>2</sup>). The equivalent load on the anchor is modelled on the same area as the horizontal force. The vertical load component of the post-tensioning is modelled by an equivalent line load to a line which lies in the middle of the anchor area.

The temperature gradient is only modelled on the web of the girder (shown in Figure 5) for simplification. The hydration temperatures of the end diaphragm and the flanges of the main beam are neglected. The web is the most massive part of the girder and it was assumed to have an effect. In the middle of the girder the temperature difference is  $-\Delta T$  °C (blue) and on the edge 0 °C (red). The used temperature gradient  $\Delta T$  was 20.0 °C at the moment of tensioning due to hydration. The modelling temperature gradient is based on measurements of the Myllypuron risteysilta made by Tampere University of Technology [5] [6]. A creep effect is considered by reducing the temperature gradient by a factor  $k = \frac{1}{1+0.85*\varphi} = \frac{1}{1+0.85*0.39} = 0.75$ . The resulting value on the gradient in model is 15.0 °C.

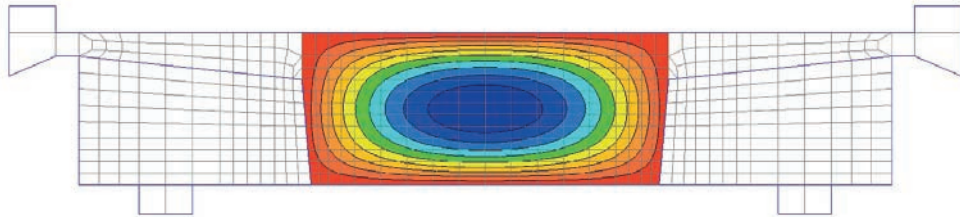


Figure 5 – Modelling of the temperature gradient

The effects of different loads are combined using the superposition principle. All the results were combined with full values.

### 2.3 Variations of the structure

The geometry of the end diaphragm was changed in order to find out how the observed cracking could be reduced. The following variations of structure were studied on the first case bridge:

- the end diaphragm height was extended (downwards) by 400mm
- the thickness was increased symmetrically by 400mm (both sides by 200mm)
- the positions of the bearings were each moved 700mm closer to the centre of the end diaphragm

On the second case bridge:

- the end diaphragm height was extended (downwards) by 815 mm
- the thickness was raised from the front side by 400 mm and 800 mm
- setting only one bearing in the middle of the end diaphragm
- two different sizes of wedges ( $400 \times 400 \text{ mm}^2$ ,  $640 \times 800 \text{ mm}^2$ , shape is shown in Figure 4b).

On both case bridges, the effect of the anchor positioning on the cracking of the diaphragm is examined. The modifications to the model are made one at the time in order to notice the effect of the alteration.

## 3. RESULTS AND ANALYSIS

As the result of FE analysis, it was found that a crack does not open from a single loading but a combination of them. The magnitude of principal tensile stress is quite the same due to the self-weight, post-tension force, traffic load and temperature gradient of the main girder. Under different types of loads, the stress field is different and the maximum stress is not found at the same point. The schematic stress field at the front surface of the end diaphragm and the location of maximum stresses due to different load cases is shown in Figure 6.

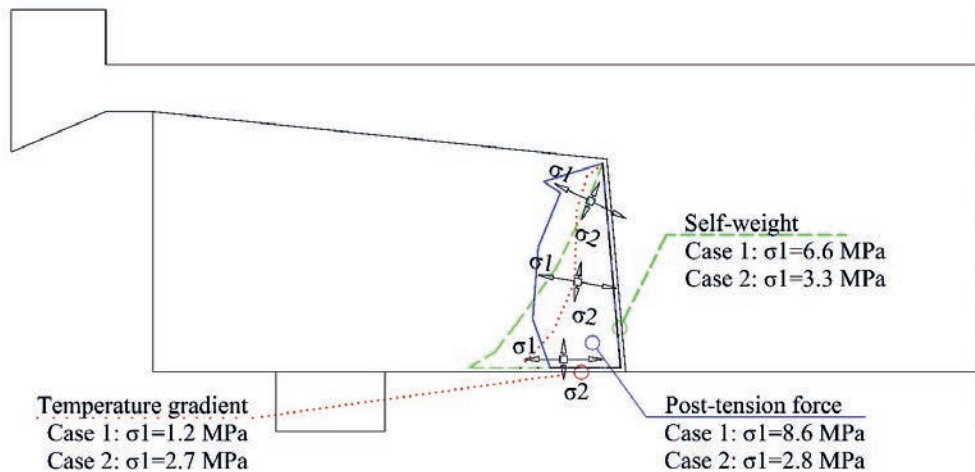


Figure 6 – Schematic stress field due to different load cases and maximum tensile stress values with location, corresponding colours and line types in leader(lines) and stress fields

After post-tensioning, the forces added to the structure were self-weight, post-tension force and temperature difference due to hydration temperature. After post-tensioning, the maximum observed principle tensile stress ( $\sigma_1$  in Fig. 6) in the model is 10.7 MPa on the first case bridge and 7.6 MPa on the second. This shows that it is most likely that the cracking occurs after post-tensioning because a tensile strength  $f_{ctk,0.95}$  of the C35/45 concrete is 4.2 MPa [7]. It should also be noted that concrete has not reached its full strength before post-tensioning.

The cracks in concrete are assumed to form in a perpendicular direction to the principal tension stress [8]. In Figure 7 the vectors of principal stresses are shown (blue: compression, red: tension) in the front of the end diaphragm (case 1) after post-tensioning. The perpendicular direction of principal tensile stress matches the observed cracks in the real structure.

In the corner area, the direction of principal tension stresses is almost the same in vertical loads, post-tension force and temperature difference. From the direction of principal stresses, it can be noted that the majority of the tension stress occurs horizontally in the lower part of the end diaphragm. In the upper part of the end diaphragm, the direction inclines and so do the cracks. At the upper part of diaphragm, the horizontal stress component becomes smaller and is not so dominant in comparison to other components. In addition, the highest tensile stresses are detected to be in the same area as the observed cracking in the real structure.

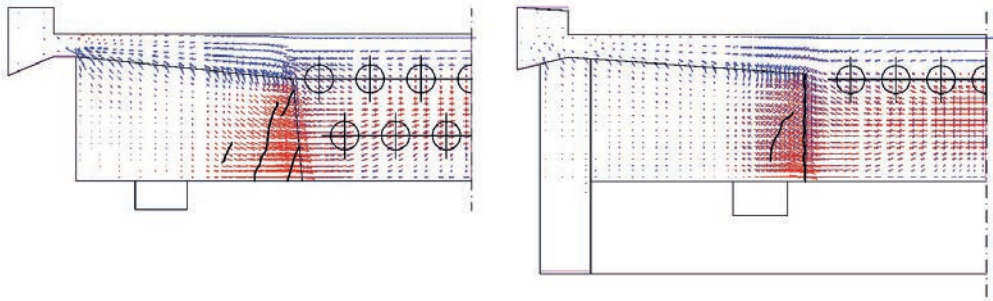


Figure 7 – Direction of cracking compared to principal tensile stress direction (left: first case bridge, right: second case bridge)

Because the maximum stresses do not occur at the same location in each load case and do not have same principal direction, they cannot be summed directly. In Figure 8, the principal stresses are shown in the location in which the highest tensile stresses occur after combining all loads. Because the principal stresses are not in same direction, each component is calculated with a weighting so that the resulting stress is correct in the chart. The result is not the same at all points because the contribution of different loads on the total effect is different.

It is significant that making the end diaphragm thicker does not have a great influence on the highest tensile stress. The end diaphragm is not a normal beam loaded with a constant load. Making the end diaphragm thicker also raises the stiffness and consequently the total influence on tensile stress is minor. The highest tensile stresses after post-tensioning on the first case bridge reduced by 11% by increasing the end diaphragm thickness by 400mm. On the second case bridge the reduction is 7%. Increasing the thickness of the end diaphragm does not have an influence on the stress pattern and the highest tensile stress gathers in the same area as in the original structure.

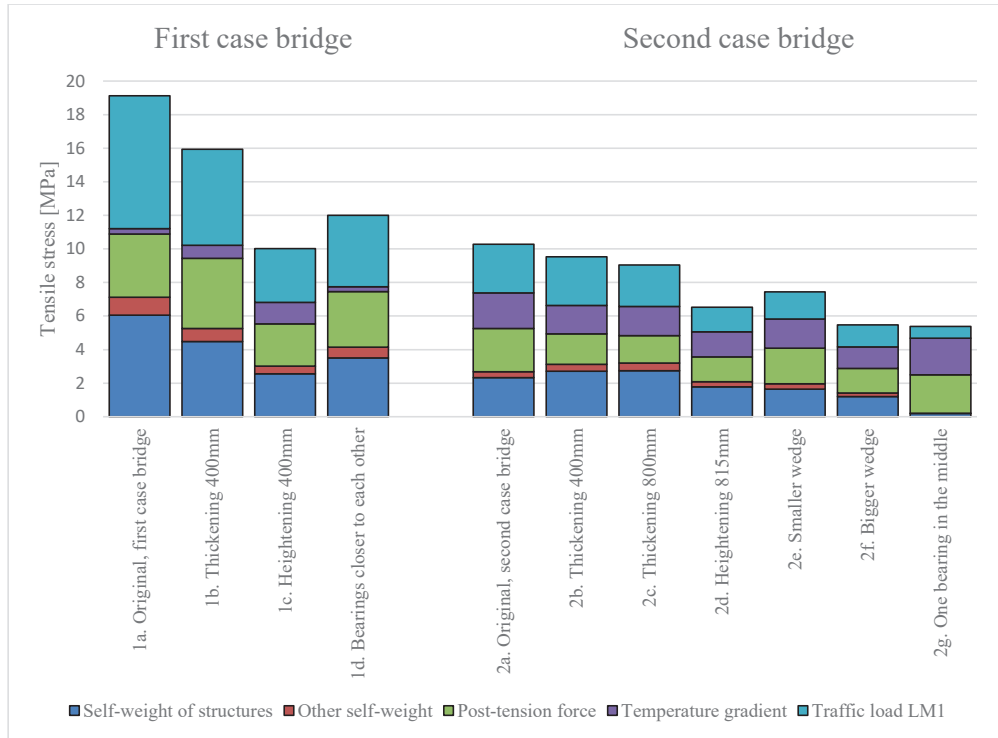


Figure 8 – Combination of stresses on the location with highest total tensile stress

Increasing the height of the end diaphragm has a greater influence on tensile stress than increasing the thickness. It was noted that the stress pattern changed when the end diaphragm was higher. In the original structure the highest stresses occur at the bottom corner of the end diaphragm (shown in Figure 9). In the case with the higher end diaphragm, the highest stresses occur in the upper section in the corner area of the main girder and the end diaphragm. The highest tensile stress was reduced by 38% on the first case bridge and by 34% on the second case bridge in the situation after tensioning.

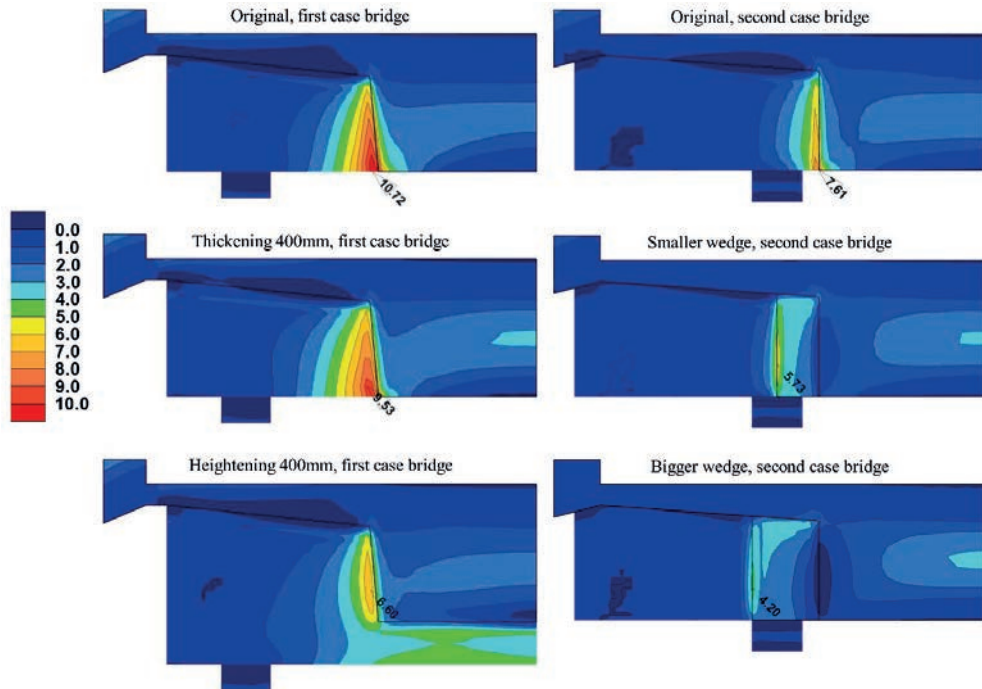


Figure 9 – Comparing stress patterns with structure variations

The wedging of the corner reduced the tensile stress significantly (with the smaller wedge by 25% and the bigger wedge by 45% after tensioning). Major tensile stresses by prestressing force and horizontal loads occur in different locations on the wedged structure: in the front corner with horizontal loads; and in the back corner with prestressing force. This is why their combination value is not so significant.

In the analysis, it was noted that the position of the post-tension anchors has an effect on the stress values. The upper post-tension anchors cause tension stresses to the entire height of the end diaphragm. The lower anchors cause more tensile stress in the bottom area of the end diaphragm. The schematic tensile stress pattern is shown in Figure 10. Anchors located on the edge of the main girder causes wider tensile stresses in a horizontal direction than those located more closely to the centre of the girder. The anchors on the edge also cause higher tensile stresses than the inner ones.

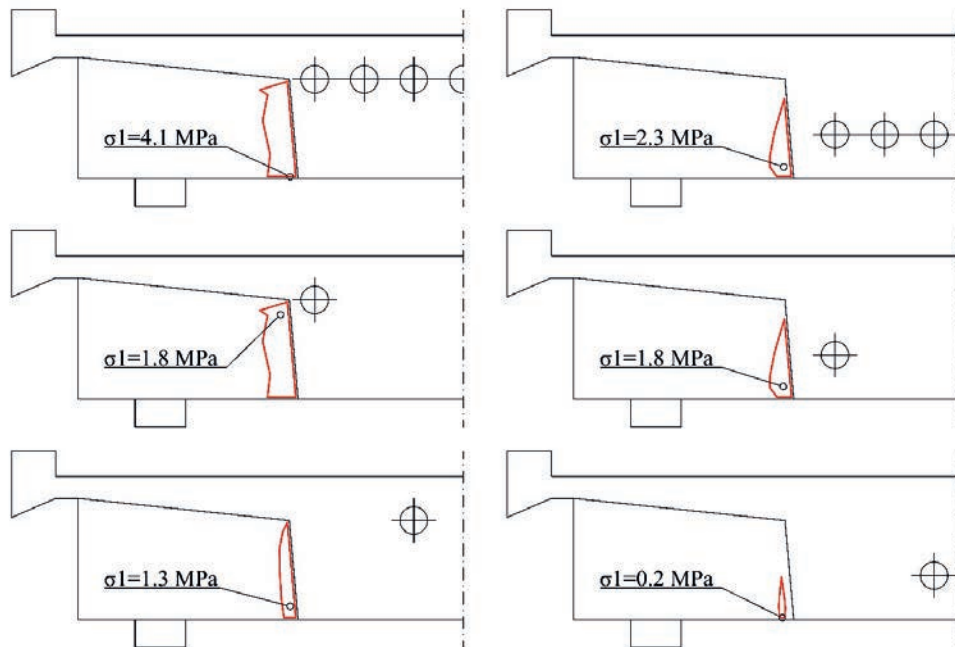


Figure 10 - Schematic tensile pattern by location of anchors, first case bridge

Compression due to post-tension force spreads out to the stresses in the end diaphragm at an angle of about 45° and becomes narrower when transmitting towards the web of the girder. This presumably causes bursting stresses to the front surface of the end diaphragm, which is why the outer anchors cause higher tensile stresses. On the inner anchors, post-tension force cannot spread to the end diaphragm. Due to the post-tension force, the flanges of the girder also try to bend the end diaphragm.

#### 4. CONCLUSIONS

The cracking on the end diaphragms of post-tensioned beam bridges is caused by the combination of loads, not by a single load. The tensile stresses caused by vertical loads, post-tension force and temperature difference occur in the same area at the corner of the end diaphragm and the main girder. The corner is a discontinuity area. Tensile force is mainly horizontal and it should be considered in the design of horizontal reinforcement on the front surface of the end diaphragm.

A linear model was sufficiently accurate to respond to the real structure despite the non-cracking behaviour. The cracks, which would have appeared according to the FE model, were in the same area as those detected in field surveys. The direction of the cracks would also have been the same. Presumably, a non-linear model would not have added more value to this study.

Adequate measures to reduce tensile stresses on the front surface of the end diaphragm were found, which would reduce cracking. Increasing the thickness of the end diaphragm does not have

a significant reducing effect on cracking, whereas increasing the height of the end diaphragm and adding wedges on the corners of the end diaphragm and the main beam have a more beneficial effect. By placing the post-tension anchors more centrally, a reduction in cracking could be achieved. With small changes, it would be possible to achieve a clearly more functional structure.

For further research, the analysis of different case bridges is recommended, such as bridges with multiple main girders. This study does not include analysis of the post-cracking behaviour of the structure. In addition, the mechanism that leads to cracking could have been identified, so that cracking due to indirect support can be excluded. For that to be the case, structures should be analysed with a non-linear model including reinforcement bars.

## ACKNOWLEDGEMENTS

The research presented in this paper was financially supported by A-Insinööri Oy and the Finnish Transport Agency.

## REFERENCES

1. Fredriksson H & Yhlen H: “FE-analysis of cracking in transversal support beams of concrete bridges”. *Master Thesis* No. 2010:6, Chalmers University of Technology, Department of Civil and Environmental Engineering, Division of Structural Engineering, Göteborg, Sweden, 2010.
2. Kuusela M: “FEM analysis of causes of cracking in the end diaphragm of post-tensioned beam bridge”. *Report*, Tampere University of Technology, Department of Civil Engineering, Tampere, Finland. 2016.
3. Finnish Transport Agency: “Liikenneviraston sillat”. (“Bridges of the Finnish Transport Agency”). 1.1.2016. Finnish Transport Agency, Helsinki, Finland, 2016. (In Finnish.)
4. LUSAS. Element reference manual. Version 15.2 Issue 1, 2016.
5. Vilonen H: “Soil-structure interaction of skewed integral abutment bridge”. *Report*, Tampere University of Technology, Department of Civil Engineering, Tampere, Finland. 2007.
6. Mäntyranta L & Laaksonen A: “Sillan ja maan yhteistoiminta, SIMA.” (“Soil - Bridge Interaction”). *Unpublished report*, Tampere University of Technology, Department of Civil Engineering, Tampere, Finland. 2014.(In Finnish.)
7. SFS-EN-1992-1-1. (2004). Eurocode 2: Design of concrete structure. Part 1-1: General rules and rules for buildings. Brussels: CEN.
8. Leskelä M: ”Betonirakenteiden suunnittelu ja mitoitus”. (“Design of Concrete Structures”). Suomen Betoniyhdistys r.y. (Finnish Concrete Association), Helsinki, Finland, 2006. (In Finnish.)

ANNEXES

Table 1 - General information on field surveys, case bridges highlighted in blue/bold

Project	Kostenkylä-Juvissa-Kotka						Kehä III V4-V7						Lentosemantti			
	S108	S114 A	S114 B	S121 B	S122	S127	S136	S152	S1	S6	S5	S6	S7	S9	S11	S103
Bridge name and effective width [m]	7.5	12	12	12	13.5	8.5	13.5	4	24	12.7	7.5	4.5	10	7.5	7.5	10
Integral bridge	x				x			x	x						x	
Number of main beams	1	2	2	2	2	1	2	1	3	2	1	1	1	1	1	1
Span <sub>n</sub> (cantilever) [m]	<u>26 + 26</u>	42.5 + 4x85 + 37.8	32.2 + 36 + 3x85 + 37.2	19.5 + 32 + 20.5	(2.5) + 2x27 + (2.5)	22.5 + 4x28.5 + 22.5	23.5 + 29.5 + 26 + 16.0	19.5 + 32.0 + 20.5	16.5 + 2x25 + 32.8	(3.2) + 30.3 + 27.7 + (3.0)	<u>28.2 + 47</u> <u>+ 28.2</u>	20 + 25 + 30 + 20 + 20	17 + 22 + 24 + 3x28 + 22 + 27 + 21 + 26 + 2x31 + 23	17 + 20 + 27	(2.5) + 34 + 23 + 2x26 + 31 + 25 + (2.5) + 26	5.4
Width of main girder wedge [m]	<u>3.2</u>	1.2	1.2	1.6	1.8	3.5	1.9	1.4	2.3	1.8	<u>3</u>	1.5	5.4	2.5	2.5	5.4
Height of girder [m]	<u>1.3</u>	2.3	2.3	1.6	1.3	1.3	1.3	1.3	1.3...1.39	1.55	<u>1.3...2.6</u>	1.56	1.5		1.5	1.5
Height of end diaphragm [m]	<u>1.3</u>	2.3	2.3	1.6	2.4...2.9	1.3	1.45	2.7/1.3	3	1.6	<u>1.3</u>	1.56	1.5		1.5	1.5
Thickness of end diaphragm [m]	<u>1.15</u>	1	1	1	0.5 (3)	1	1.15	1.6/0.9	1.5	0.55	<u>1.2</u>	1.1			3.4	1.05
Number of tendons	7	8 + 8	8 + 8	7 + 7	6 + 6	11	6 + 6	5	8 + 5 + 10	6 + 6	<u>13</u>	5	10	5	8	20
Post-tension force per girder after immediate losses [MN]	<u>18.3</u>	21.8	21.7	15	15.9	23.4	16.5	10.8	22.9 / 14.3 / 26.2	16	<u>35.2</u>	13.2	26	16.8	20.7	39.4
Support reaction per bearing [MN]	<u>3.3</u>	5.8	4.9	4.4	4.8	2.3	4.3				<u>2.4</u>	0.8	3.6	3.1		3.5
Amount of vertical reinforcement [mm <sup>2</sup> /m]	<u>T16K200 (1005)</u>	T16K150 (1340)	T16K150 (1340)	T25K200 (2454)	T16K200 (1005)	T16K200 (1005)	T16K200 (1005)	T16K200 (1005)	T25K100 (4909)	T25K100 (4909)	<u>T20K150 (2094)</u>	T16K150 (1340)		T25K150 (3272)	T25K200 (2454)	T20K160 (1963)
Amount of shear links in end diaphragm [mm <sup>2</sup> /m]	<u>T16K120 (1670)</u>	T16K200 (1005)	T16K200 (1005)	T16K200 (1005)	T16K200 (1005)	T16K200 (1005)	T16K200 (1005)	T16K200 (1005)	T16K100 (2011)	T16K100 (2011)	<u>T16K200 (1005)</u>	T16K200 (1005)		T16K200 (1005)	T16K200 (1005)	T16K200 (1005)
Measured crack width [mm]	<u>0.1</u>	0.3...0.5	0.3...0.5	x	0.3	0.5	x	0.2	0.1	0.2	<u>0.4</u>	0.3	x	x	0.2	x
x: not measured																

Table 2 - Used post-tension force, restrain forces and support reactions

<b>Post-tension force, after immediate losses</b>	Unit	1st case bridge		2nd case bridge	
		Per tendon	Total	Per tendon	Total
Longitudinal post-tension force	MN	2.7	35.2	2.6	18.3
Equivalent load at anchor, upper tendons	kN	-87.4	-611.8	-330.3	-2312.1
Equivalent load at anchor, lower tendons	kN	-1.3	-7.7		
Equivalent line load, upper tendons	kN/m	12.5	87.8	29.0	203.2
Equivalent line load, lower tendons	kN/m	8.0	47.9		
<b>Support reaction per bearing</b>	Unit	1st case bridge		2nd case bridge	
Self-weight of structures	kN	630.4		939.2	
Deadload of surface structures etc.	kN	104.2		148.9	
Upper tendons	kN	18.5		93.1	
Lower tendons	kN	74.5			
Traffic load, total	kN	924.0		876.7	

	
© Article authors. This is an open access article distributed under the Creative Commons Attribution-NonCommercial-NoDerivs licens. ( <a href="http://creativecommons.org/licenses/by-nc-nd/3.0/">http://creativecommons.org/licenses/by-nc-nd/3.0/</a> ).	ISSN online 2545-2819 ISSN print 0800-6377
DOI: 10.2478/ncr-2019-0091	Received: March 15, 2018 Revision received: March 15, 2019 Accepted: June 18, 2019

## A Refined Model for Predicting Concrete-Related Failure Load of Tension Loaded Cast-in-Place Headed Anchors in Uncracked Concrete



Rasoul Nilforoush  
Ph.D., Associate senior lecturer  
Div. of Structural and Fire Engineering  
Luleå University of Technology, LTU  
SE-971 87 Luleå, Sweden.  
Email: [rasoul.nilforoush@ltu.se](mailto:rasoul.nilforoush@ltu.se)

### ABSTRACT

Current theoretical models for predicting the concrete cone breakout capacity of tension loaded headed anchors do not consider the influence of member thickness, size of anchor head, and orthogonal surface reinforcement. In the present study, the influence of the aforementioned parameters was studied both numerically and experimentally. Both the numerical and experimental results showed that the tensile resistance of headed anchors increases by increasing the member thickness or if orthogonal surface reinforcement is present. In addition, the anchorage capacity further increases with increase of the anchor head size.

The current model for predicting the concrete cone failure load of tension loaded headed anchors were refined and extended by incorporating three modification factors to account for the influence of the member thickness, size of anchor head, and orthogonal surface reinforcement. The accuracy of the proposed model was verified based on the results of 124 tests on single headed anchors from literature.

**Keywords:** Concrete Cone Breakout, Concrete Splitting, Anchor Bolt, Headed Anchor, Fastening System, Member Thickness, Anchor Head Size, Surface Reinforcement.

## 1. INTRODUCTION

Fasteners of different kinds, including cast-in-place and post-installed anchors, are often used to anchor loads in concrete structures. An overview of various anchorage systems is given in Eligehausen et al. [1]. The cast-in-place anchors have been used ever since reinforced concrete was introduced around 1900. The post-installed anchors started to be used in the 1960s with the advances in drilling technology of concrete structures. Over the past few decades, numerous experimental and numerical studies were carried out on anchors of different kinds which led to the development of various theoretical and empirical models for designing anchorage systems to concrete. The capacity and performance of anchors were studied under particular test setups, limited boundary conditions, and certain loading circumstances. The development of such models involved many limitations and uncertainties and, hence, various simplifying assumptions were adopted. For instance, it is assumed that the thickness of concrete member, size of anchor head, and presence of orthogonal surface reinforcement have negligible influence on the tensile resistance of anchors.

In a sustainable society, buildings and structures must, from time to time, be adjusted to meet new demands. The capacity and/or service life of structures typically must be increased to comply with the new requirements, and this increase requires upgrading of both the structural components and the structural connections. Therefore, the structural connections can also be subjected to an increased service load or needed for extended service life. From the structural point of view, the adequacy of existing fastenings for the intended increased load or service life must be determined, and inadequate fastenings must either be replaced or upgraded. On the other hand, the current design methods for fastening systems are generally believed to be conservative. However, it is not very clear to what extent they are conservative. As the development of such models involved many limitations and uncertainties, their reliability should be evaluated particularly for other possible geometrical, loading, and boundary conditions than those considered previously.

The overall objective of the research presented in this paper is to form a background for developing improved methods for the design and assessment of cast-in-place headed anchors. The research scope is limited to single headed anchors under tension loads in uncracked concrete. As tension loaded headed anchors often fail via concrete cone breakout or concrete splitting/bending, the research focus is exclusively on these failure modes. The anchorage failure load in these cases depends strongly on the fracture properties of concrete, the geometry of concrete component, the amount and configuration of reinforcements in the anchoring zone, the type and magnitude of load on the anchor, and the position of anchor in respect to concrete free edges and adjacent anchors. In the present paper, the influences of member thickness, size of anchor head, and amount of orthogonal surface reinforcement on the capacity and performance of headed anchors are evaluated both numerically and experimentally.

## 2. BACKGROUND

The literature contains numerous analytical and theoretical approaches, based on various assumptions, for calculating the concrete cone breakout. The first theoretical model proposed for the concrete cone breakout failure was the 45-degree cone model, which was incorporated into ACI 349 [2]. This model assumes a cone angle of  $45^\circ$  with respect to concrete surface and constant tensile stress of ( $f_{ct} = 0.3\sqrt{f_{cc}}$  N/mm<sup>2</sup>) acting over the projected cone surface (see Fig. 1). Based on this model, the tensile breakout capacity of a single anchor is calculated as follows:

$$N_{u,m} = 0.3\sqrt{f_{cc}}\pi \cdot h_{ef}^{2.0} \cdot \left(1 + \frac{d_h}{h_{ef}}\right) \quad (1)$$

where  $N_{u,m}$  is the mean concrete cone breakout failure load of a single anchor unaffected by concrete member edge/s and adjacent anchor/s [N],  $f_{cc}$  is the concrete cube compressive strength [N/mm<sup>2</sup>],  $h_{ef}$  is the anchor embedment depth [mm], and  $d_h$  is the diameter of anchor head [mm].

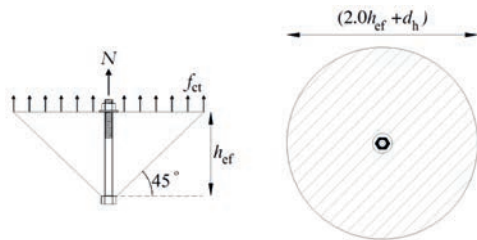


Figure 1 – Shape of concrete cone failure and the projected cone surface per 45-degree cone model [1].

This model was derived based on the results of pullout tests on headed anchors with a limited range of embedment depths (i.e.  $h_{ef}$  up to 150 mm) and therefore it does not account for a so-called size effect. The size effect on anchorage capacity exists because, at the ultimate load, the average tensile stress over the fracture surface decreases as the fracture area increases [1]. Moreover, subsequent experimental observations revealed that the slope of concrete cone surface is not constant over the embedment depth, which varies between 30° and 40° and is on average about 35° [1]. Therefore, Eq. (1) tends to overestimate the capacity of deep anchors because the assumptions of the constant tensile stress over the projected fracture surface and the cone angle of 45° deviate significantly from reality.

Fuchs et al. [3] later analyzed experimental results from a large database of European and American tests on various anchors at different embedment depths, and proposed a user-friendly method known as the Concrete Capacity (CC) method (i.e., known as Concrete Capacity Design CCD in the US). The CC method is an empirical model which takes the concrete’s size effect into account. According to the CC method, the concrete cone failure load of a single cast-in-place anchor is estimated by assuming a concrete cone angle of  $\sim 35^\circ$  with respect to the concrete surface. This assumption was reasonably supported by widespread observations that the horizontal extent of the concrete cone fracture on the surface of the concrete component is around  $3.0 \cdot h_{ef}$  (see Fig. 2).

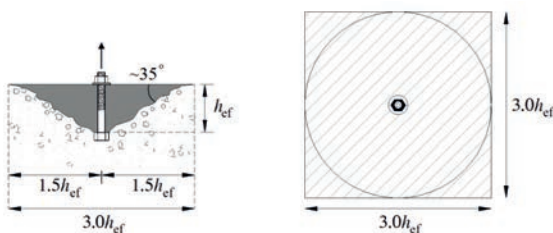


Figure 2 – Shape of concrete cone failure and the idealized cone surface per CC method [3].

The general form of the CC method for estimating the concrete cone failure load of a single anchor in uncracked concrete is as follows:

$$N_{u,m} = k_1 f_c^{0.5} \cdot k_2 h_{ef}^2 \cdot k_3 h_{ef}^{-0.5} = K \sqrt{f_c} h_{ef}^{1.5} \quad (2)$$

where  $f_c$  is the concrete cylinder compressive strength [N/mm<sup>2</sup>],  $k_1$ ,  $k_2$  and  $k_3$  are calibration factors;  $K$  is an empirical factor ( $K = k_1 \cdot k_2 \cdot k_3$ ) which has a dimensional unit of [N<sup>0.5</sup>/mm<sup>0.5</sup>];  $k_1 f_c^{0.5}$  represents the nominal concrete tensile stress at failure over a failure area given by  $k_2 h_{ef}^2$ ; and  $k_3 h_{ef}^{-0.5}$  accounts for the concrete size effect which was derived based on the fracture mechanics theory.

Based on evaluation of results of various tests, Fuchs et al. [3] proposed the following equation for concrete cone failure of a single-headed anchor under concentric tension that is positioned far from the concrete free edge/s and adjacent anchor/s in an uncracked concrete member:

$$N_{u,m} = 16.8 \sqrt{f_c} h_{ef}^{1.5} \quad (3)$$

According to Eligehausen et al. [1] and Fuchs et al. [3], the concrete cube and cylinder strengths are related as ( $f_c \approx 0.84 \cdot f_{cc}$ ). Therefore, if the concrete cube compressive strength ( $f_{cc}$ ) is given instead of the concrete cylinder compressive strength ( $f_c$ ), the leading coefficient of Eq. (3) is 15.5 rather than 16.8. Equation 3 was incorporated into several design-oriented documents and standards in Europe such as the CEB Design Guide [4] and CEN/TS 1992-4 [5], internationally in the *fib* Bulletin 58 [6], and in several US design standards (e.g., ACI 349 [7] and ACI 318 [8]).

Based on the CC method, the mean tensile breakout capacity of a single anchor is proportional to  $h_{ef}^{1.5}$ . However, subsequent numerical and experimental studies [9-13] showed that Eq. (3) may result in conservative capacities for deep embedment depths. For deep anchors (where  $h_{ef} \geq 280$  mm), American standards [7,8] allow the use of a modified CC method as below:

$$N_{u,m} = 16.8 \sqrt{f_c} h_{ef}^{1.5} \quad \text{for } h_{ef} < 280 \text{ mm} \quad (4.a)$$

$$N_{u,m} = 6.585 \sqrt{f_c} h_{ef}^{5/3} \quad \text{for } 280 \text{ mm} \leq h_{ef} \leq 635 \text{ mm} \quad (4.b)$$

The modified CC method uses an exponent of 5/3 (=1.667) rather than 1.5 for the effective embedment depth of deep anchors ( $h_{ef} \geq 280$  mm) and appropriately changes the leading coefficient of the CC method. Equations (3) and (4) were developed based on the results of numerous pullout tests on headed anchors at various embedment depths. The concrete cylinder compressive strength was in the range of 13 to 50 [N/mm<sup>2</sup>]. The ratios of measured concrete cone breakout capacities to the values predicted by the CC method ( $N_{test}/N_{CC \text{ method}}$ ) as a function of anchor embedment depth are presented in Fig. (3a). The figure shows the experimental results of 320 pullout tests on single-headed anchors reported in the literature [10-12]. The tested anchors had various head sizes and were embedded in un-reinforced and reinforced concrete members of various thicknesses, leading to a wide scatter in the obtained capacities. As the tested headed anchors had different head sizes, the concrete in the vicinity of the anchor heads experienced various bearing pressures. According to ACI 349 [7] and ACI 318 [8], to prevent a pullout failure and ensure a concrete cone breakout failure for cast-in-place headed anchors, the mean concrete pressure ( $\sigma_b$ ) under the head of anchors in uncracked concrete is limited to ( $15 \cdot f_c$ ). This indicates that, at anchor's peak load ( $N_u$ ), a minimum bearing area of ( $A_{b,min} = N_u / 15 \cdot f_c$ ) is required to prevent a pullout failure and allow the formation of a concrete cone failure. Fig. (3b) presents the ratios of bearing areas of anchor heads to their corresponding minimum required bearing areas ( $A_b / A_{b,min}$ ) as a function of anchor embedment depth, for the tested headed anchors (test data in Fig. 3(b) corresponds to those presented in Fig. (3a)).

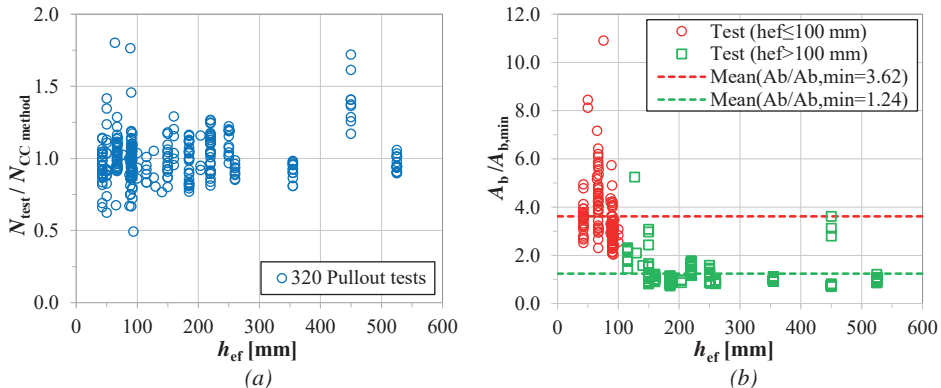


Figure 3 – (a) ratio of measured concrete cone failure loads to values predicted by CC-method (Eq. 3) as a function of anchor embedment depth for 320 pullout test from literature, and (b) ratio of bearing area of anchor heads to their minimum required bearing areas corresponding to concrete pressure of  $15 \cdot f_c$  under anchors head at peak load as a function of anchor embedment depth.

As the figure shows, the bearing area of the tested anchors varied significantly from  $0.7 \cdot A_{b,min}$  to  $10.9 \cdot A_{b,min}$ . For short anchors ( $h_{ef} \leq 100$  mm), the mean ratio of the bearing area to the minimum bearing area ( $A_b/A_{b,min}$ ) is 3.62, while this ratio is only 1.24 (i.e. almost three times smaller) for deep anchors ( $h_{ef} > 100$  mm). This indicates that the CC method has not been developed systematically with respect to the size of anchor head, as the bearing area of the tested short and deep headed anchors varied significantly. The results presented in Fig. 3 show that the CC method may underestimate or overestimate the failure load of headed anchors if their head sizes differ appreciably from those of previously tested short and deep anchors.

In practice, headed anchors with various head sizes are often used in unreinforced or reinforced concrete members with different geometries. However, the CC method was developed based on the simplifying assumptions that the member thickness, surface reinforcement, and the size of anchor head have negligible effects on the tensile capacity of headed anchors. In addition to the uncertainties discussed above, and despite several recent experimental and numerical investigations into the capacity of cast-in-place headed anchors [9-11], the influence of the thickness of concrete component, presence of orthogonal surface reinforcement and the size of anchor head on the failure load of headed anchors is still unknown. In the present paper, systematic numerical and experimental studies are carried out to evaluate the influence of each parameter on the anchorage capacity and performance. The result of this study can provide a basis for developing improved methods of the design and assessment of headed anchors with various head sizes in unreinforced or reinforced concrete members of different geometries.

### 3. NUMERICAL STUDIES

For the purpose of this research, extensive three-dimensional (3D) FE numerical analyses were carried out through the FE program MASA (MAcroscopic Space Analysis). This program was previously developed at the Institute of Construction Materials in University of Stuttgart, Germany. For modeling the nonlinear behavior of concrete, the employed constitutive material model was based on the microplane constitutive law in the framework of the smeared crack approach. Detailed discussions of the features and various aspects related to the Microplane model can be found in Ožbolt et al. [14]. The behavior of steel in the anchor was considered as linear

elastic. For pre- and post-processing analysis, the commercial program FEMAP® was used. In general, the classical smeared fracture analysis of quasi-brittle materials leads to mesh-dependent results. To avoid mesh size sensitivity, the total energy consumption capacity of a model due to cracking should be independent of its element size. In this study, the crack band theory proposed by Bažant and Oh [15] was employed in all analyses, in which the constitutive law was related to the element size such that the concrete fracture energy  $G_f$  was independent of the elements' sizes.

### 3.1 Matrix and geometry of numerical models

To systematically evaluate the influence of member thickness, anchor head size and orthogonal surface reinforcement on the tensile breakout capacity of headed anchors, three simulation series were carried out (see the matrix of numerical studies in Table 1). In series (a), headed anchors at various embedment depths ( $h_{ef}=50-500$  mm) were simulated in unreinforced concrete members of various thicknesses ( $H=1.5-5.0h_{ef}$ ). In series (b), headed anchors at various embedment depths ( $h_{ef}=50-500$  mm) were considered to have various head sizes (i.e., small, medium and large heads). For this simulation series, all concrete members were unreinforced, and the member thickness was ( $H=3.0h_{ef}$ ). In series (c), headed anchors at various embedment depths ( $h_{ef}=50-300$  mm) were simulated in reinforced concrete slabs of various thicknesses ( $H=1.5-3.0h_{ef}$ ). For this case, the concrete slabs were orthogonally reinforced and considered to have small and large reinforcement ratios to also evaluate the influence of reinforcement amount on the anchorage capacity and performance. The ratio of the top or bottom reinforcements in each direction for the small-content was approximately 0.3%, while for the large-content was larger than 0.5%. The total number of simulations in each series is given in Table 1. Each anchor embedment depth was simulated with each member height (in series a), with each anchor head size (in series b), and with each member height and reinforcement-content (in series c).

Table 1 – Matrix of numerical studies

Series	Total number of models	$h_{ef}$ [mm]	Head size	Member height $H$	Bar condition	
(a) Member thickness	30	50	Medium	$1.5 \cdot h_{ef}$	Un-reinforced	
		100		$2.0 \cdot h_{ef}$		
		200		$2.5 \cdot h_{ef}$		
		300		$3.0 \cdot h_{ef}$		
		500		$4.0 \cdot h_{ef}$		
(b) Anchor head size	15	50	Small Medium Large	$3.0 \cdot h_{ef}$	Un-reinforced	
		100				
		200				
		300				
		500				
(c) Reinforcement amount	24	50	Medium	$1.5 \cdot h_{ef}$	Small-reinforcement content ( $\rho \approx 0.3\%$ )	
		100				$2.0 \cdot h_{ef}$
		200			$3.0 \cdot h_{ef}$	
		300				

The typical geometry of the FE models is shown in Fig. 4. In all FE models, one single anchor was simulated in the center of a rectangular concrete member. For all simulation series, the

geometry of the concrete members was defined systematically so that the length ( $L$ ) and width ( $W$ ) of the components, for all embedment depths of anchors, are proportional to the anchor embedment depth ( $L=W=6.0 \cdot h_{ef}$ ). For simulating the anchor pullout loading, a line circular support with a span of ( $L_{sup}=4.0 \cdot h_{ef}$ ) was considered for all numerical models to permit an unrestricted formation of a concrete cone fracture.

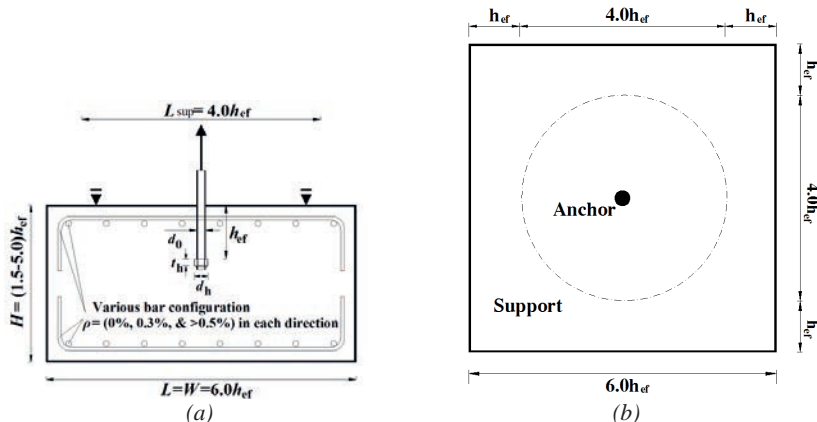


Figure 4 – Typical geometry of FE numerical models: (a) side view, and (b) top view.

The dimensions of anchors, including the embedment depth  $h_{ef}$ , shaft diameter  $d_0$ , head diameter  $d_h$ , and head thickness  $t_h$  for the studied anchors are summarized in Table 2. For series (b), the diameter of the anchors' head was set so that the concrete pressure under anchor head at anchors' peak load would be almost constant for all investigated embedment depths of anchors. The peak load for all anchors was predicted using the CC method (Eq. 3). The concrete pressure under anchor head at peak load ( $\sigma_b$ ) for the simulated small-, medium- and large-headed anchors were approximately  $20 \cdot f_c$ ,  $11 \cdot f_c$ , and  $4 \cdot f_c$ , respectively.

Table 2 – Dimensions of simulated headed anchors at various embedment depths.

$h_{ef}$ [mm]	$d_0$ [mm]	$t_h$ [mm]	$d_{h,small}$ [mm]	$d_{h,medium}$ [mm]	$d_{h,large}$ [mm]
50	10	10	13.0	16.0	21.0
100	16	15	21.4	25.0	35.0
200	30	25	38.4	45.0	62.0
300	40	35	51.5	60.0	83.0
500	60	45	76.0	85.0	122.0

### 3.2 FE discretization and simulation procedure

The typical discretized 3D FE models for headed anchors in unreinforced and reinforced concrete members are shown in Fig. 5. Due to the symmetrical geometry of the numerical models, only one-quarter of the specimens were simulated to save the CPU and computational time. This has been done by introducing double symmetry boundary conditions along the symmetrical axes. In all models, the concrete and anchor were discretized with tetrahedral and hexahedral solid finite elements, respectively. The size of FE elements was defined as approximately 30-50 mm at the concrete free edges (depending on the global size of the FE model), whereas they are refined to

approximately 5-10 mm in the vicinity of the anchor. The vertical support for anchor pullout loading was defined by constraining the support nodes in the loading direction.

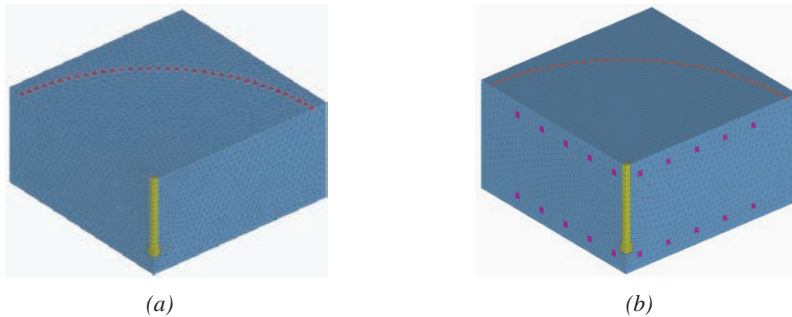


Figure 5 – Typical discretized 3D FE models for anchors cast in: (a) unreinforced concrete, and (b) reinforced concrete.

The reinforcement at the top and bottom surface of the reinforced slabs were modeled using a 3D smeared approach in a way that they were assumed to be smeared inside a row of concrete elements (see Fig. 6). The 3D smeared reinforcements were discretized using eight-node solid elements with equivalent material properties defined as weighted average of the properties of concrete and reinforcement. The equivalent properties of the 3D smeared reinforcements were defined using the expression given in Fig. 6. In simulations, the equivalent properties of smeared reinforcements were defined using the uniaxial elasto-plastic stress-strain relationship with steel strain hardening. The hardening modulus of the 3D smeared reinforcement  $E_{s,h}$  was considered as 1% of the equivalent modulus of elasticity of the 3D smeared reinforcement. The 3D von Mises yield criterion was used for analyzing the smeared reinforcement.

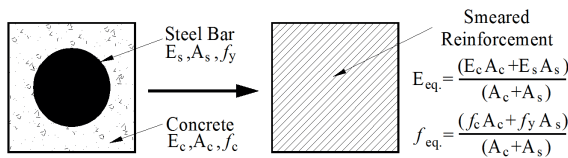


Figure 6 – Concept of 3D smeared reinforcement.

Before creating all FE models, several FE models were initially calibrated and verified against the results of a previous experimental study performed by Nilsson et al. [11]. A series of parametric studies were also carried out to evaluate the influence of concrete material properties (i.e., concrete tensile strength  $f_{ct}$  and compressive strength  $f_c$ , concrete young modulus  $E_c$ , concrete fracture energy  $G_f$ , and concrete Poisson's ratio  $\nu_c$ ), boundary conditions (i.e., full model and one-quarter model), size of mesh elements, and loading rate on the numerical results. For a complete description of the FE verification procedure and parametric studies see Nilforoush [16].

The material properties of concrete and steel in the anchor and reinforcement, in all FE analyses, were identical to the material properties of the initially calibrated and verified FE models.

The concrete properties used for all FE models were as follows: uniaxial compressive strength  $f_c=28$  [N/mm<sup>2</sup>], uniaxial tensile strength  $f_{ct}=2.2$  [N/mm<sup>2</sup>], Young's modulus  $E_c=35000$  [N/mm<sup>2</sup>], fracture energy  $G_f=70$  [N/m], and Poisson's ratio  $\nu_c=0.18$ . The mechanical properties of steel reinforcement were considered as follows: modulus of elasticity  $E_s=210\,000$  [N/mm<sup>2</sup>], Poisson's ratio  $\nu_s=0.33$ , yield strength  $f_{y,s}=500$  [N/mm<sup>2</sup>], and ultimate strength  $f_{u,s}=600$  [N/mm<sup>2</sup>]. The

behavior of steel in the anchor was assumed to be linear elastic with Young’s modulus  $E_s=210000$  [N/mm<sup>2</sup>] and Poisson’s ratio  $\nu_s=0.33$ . The anchor pullout load was simulated as displacement controlled by defining incremental deformations with a displacement-increment rate of 0.05 mm/increment on the top of anchor shaft.

Contact between the concrete and the steel anchor was assumed to exist only at the top surface of the anchor head. In addition, a very thin gap was defined between the concrete and the bottom surface of the anchor head. Moreover, a very thin interface layer which can only take up compressive stress was modeled between the anchor shaft and the concrete body, along the entire length of the anchor shaft. For the interface layer, no friction was considered between anchor shaft and concrete body as the tensile load on the anchor is mainly transferred by the anchor bearing head.

#### 4. EXPERIMENTAL STUDIES

##### 4.1 Matrix and geometry of test specimens

A supplementary experimental study was carried out to clarify the influence of member thickness, size of anchor head, and orthogonal surface reinforcement on the anchorage capacity and performance. A total of nineteen headed anchors cast-in unreinforced and reinforced concrete slabs were tested under monotonic tensile loading. Like the numerical study, three test series were considered in which the testing parameters were the same as in the numerical study (see the matrix of experiments in Table 3). Headed anchors at only one size of embedment depth were tested ( $h_{ef}=220$  mm). The number of test replicates for series (a) was three; while for series (b) and (c), they were two in each. Figure 7(a) shows the typical geometry of test specimens and tested headed anchors. In all test series, a single headed anchor was placed in the center of a rectangular concrete block. The length and width of concrete blocks for all specimens were identical ( $L=W=1300$  mm), whereas their heights varied ( $H= 330, 440$  and  $660$  mm). The member heights of 330, 440, and 660 mm correspond to  $1.5h_{ef}$ ,  $2.0h_{ef}$ , and  $3.0h_{ef}$ , respectively.

Table 3 – Matrix of experiments

Series	$h_{ef}$ [mm]	Head size	Member height [mm]	Bar configuration
a) Member thickness	220	Medium	330	Un-reinforced
			440	
			660	
(b) Anchor head size	220	Small	660	Un-reinforced
		Medium		
		Large		
(c) Surface reinforcement	220	Medium	330	8Ø12#150 mm
			440	8Ø16#150 mm
			660	8Ø20#150 mm

The headed anchors were composed of standard threaded 36-mm-diameter rods with a round bearing head at the end. To prevent the steel failure of anchors, high-strength steel rods of grade 10.9 with a yield strength of  $f_{yk}=900$  [N/mm<sup>2</sup>] and an ultimate strength of  $f_{uk}=1000$  [N/mm<sup>2</sup>] were used. To evaluate the influence of the size of anchor head, three different sizes of bearing head were tested (i.e., small, medium, and large). The geometry of headed anchors with small, medium and large heads is shown in Fig. 7(b). For the small- and medium-headed anchors, round nuts with diameters of  $d_h= 48$  and  $55$  mm, respectively, were affixed to the end of threaded rods. For large-

headed anchors, a thick circular steel plate with diameter  $d_h = 90$  mm was tapped and fastened to the end of the threaded rods. A standard hex nut was also tightened underneath of the steel plate to ensure that the plate remains in place during anchor pullout loading (see Fig. 7b). All threaded rods were covered with 2-mm-thick plastic tubes. These tubes were used to prevent friction and adhesion between the anchor shaft and concrete body, thereby ensuring the transfer of the entire load through the anchor bearing head.

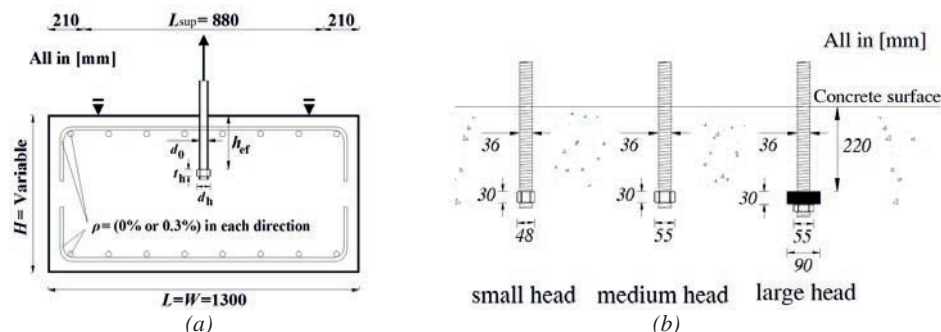


Figure 7 – Typical geometry of (a) test specimens, and (b) tested headed anchors with various head size.

The concrete blocks were cast using a ready-mix normal-weight concrete of grade C30/37 made of crushed aggregates. The mix proportion of concrete is given in Table 4. The cube compressive strength and tensile splitting strength of concrete at the time of anchor pullout loading were measured in accordance with EN 12390-3 [17] and EN 12390-6 [18], respectively. The measured cube compressive and tensile splitting strengths were  $f_{c,c} = 39.5$  [N/mm<sup>2</sup>] and  $f_{t,sp} = 3.2$  [N/mm<sup>2</sup>], respectively.

Table 4 – Mix proportion of tested concrete

Cement (kg/m <sup>3</sup> )	380
Aggregate 0–4 mm (kg/m <sup>3</sup> )	500
Aggregate 4–8 mm (kg/m <sup>3</sup> )	450
Aggregate 8–16 mm (kg/m <sup>3</sup> )	840
w/c	0.55

If the cylinder compressive strength of concrete  $f_c$  for tested specimens is equivalent to  $0.85 \cdot f_{c,c}$  and anchorage peak load is estimated using the CC method (Eq. 3), the average concrete pressure under anchor head at peak load ( $\sigma_b$ ) for the tested small-, medium- and large-headed anchors would be  $16.5 \cdot f_c$ ,  $8.3 \cdot f_c$  and  $1.8 \cdot f_c$ , respectively.

The tested reinforced concrete slabs were designed to have a small reinforcement amount: a reinforcement ratio of  $\rho \sim 0.3\%$  was applied in each surface and direction. They had orthogonal surface reinforcement at 150 mm spacing at the top and the bottom of the concrete blocks. The concrete cover was in all directions 50 mm. The reinforcing bars were of a class B500B with a yield strength of  $f_{yk}$  of 500 [N/mm<sup>2</sup>], according to the manufacturer's specifications.

## 4.2 Test setup and test procedure

The test setup and loading arrangement are shown in Fig. 8. The anchor pullout loading was carried out after the concrete had cured for  $\sim 60$  days to exclude the influence of concrete strength

growth at the time of anchor pullout testing. For anchor tension loading, the vertical reaction was taken up by a stiff circular steel ring with a width of 100 mm and an inner diameter of  $L_{sup}=880$  mm (i.e., correspond to  $4.0 \cdot h_{ef}$ ). The anchor tension loading was displacement-controlled by applying incremental deformations on the top of the anchor shaft at a constant displacement rate of 1 mm/min. The load was applied by means of a 100-ton hollow cylinder hydraulic jack. The time-deformation relation was kept approximately linear for the entire test duration. The applied load was measured by a load cell placed on the top of the jack.

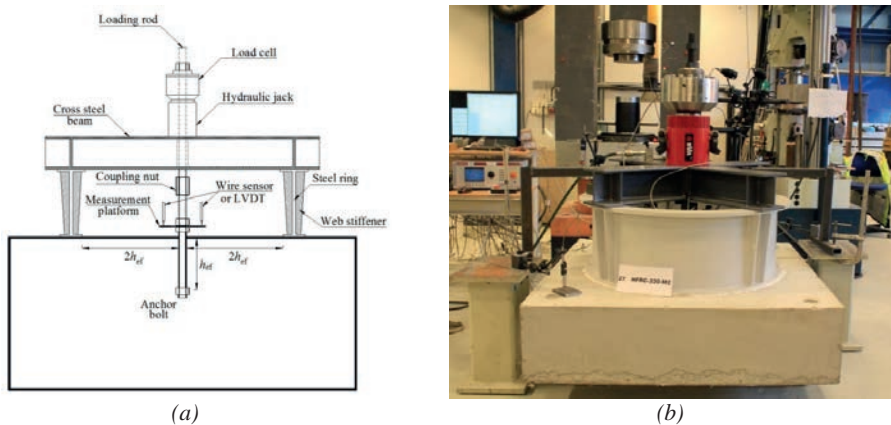


Figure 8 – (a) Schematic view of the test setup, and (b) loading arrangement

The anchor displacement was measured relative to the solid ground rather than the concrete surface to measure the anchor displacement accurately even at post-peak loads. For this reason, a measurement platform fabricated from a square steel plate ( $150 \times 150$  mm) was secured perpendicular to the testing anchor, 50 mm above the concrete surface, using a hex nut above and another below the platform (see Fig. 8a). The surface of the platform served as the reference level for measuring the vertical displacement of anchor. The vertical displacement was measured by two linear variable differential transformers (LVDTs) installed symmetrically at two side of the anchor. The LVDTs measured the displacement of the anchors relative to two rigid points outside the concrete block, on the solid ground, by means of two rigid frames (see Fig. 8b). The frames were supported from outside the blocks and contact with other structural members and testing equipment (which could have produced inaccurate displacement readings) was prevented. The anchor displacement was taken as the average of the two LVDTs. It should be noted that the measured displacement values also include the bending deformation of the tested concrete slabs.

## 5. RESULTS AND DISCUSSIONS

Due to large number of numerical results, only numerical results of headed anchors at 200 mm embedment depth, in all simulation series, are presented here. For detailed numerical results at other embedment depths see Nilforoush et al. [19,20]. In addition, the results of tested headed anchors at 220 mm embedment depth are presented in the following. In section 6, the numerical and experimental results at all embedment depths are used to evaluate the reliability of the CC method in predicting the concrete cone failure load of cast-in-place headed anchors.

### 5.1 Influence of member thickness (series a)

The numerical and experimental results of headed anchors in unreinforced concrete members of various thicknesses (i.e., series a) showed that the tensile resistance of anchors increases up to 20% with increasing the member thickness. The numerically obtained load-displacement curves and post-peak crack patterns for headed anchors at  $h_{ef}=200$  mm in unreinforced concrete members of various thicknesses are shown in Figs. 9(a) and 9(b), respectively. The anchorage is governed by concrete bending/splitting cracks in thin unreinforced concrete members ( $H < 2.0 \cdot h_{ef}$ ), while it is governed by concrete cone breakout in thicker members ( $H \geq 2.0 \cdot h_{ef}$ ). The simulation results of series (a) indicate that there is a transition zone where the failure mode changes. This transition occurs at a relative member thickness of  $H/h_{ef}=2.0$  for all anchor embedment depths investigated. The numerical findings are in very good agreement with the experimental results; see the load-displacement curves and crack patterns obtained at experiments in Figs. 10(a) and 10(b), respectively.

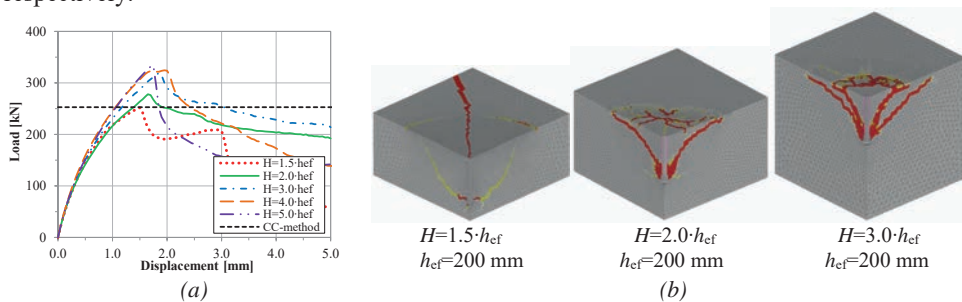


Figure 9 – (a) load-displacement curves, and (b) crack patterns obtained for the simulated anchors in unreinforced concrete members of various thicknesses,  $f_c=28$  [N/mm<sup>2</sup>] and  $f_t=2.2$  [N/mm<sup>2</sup>].

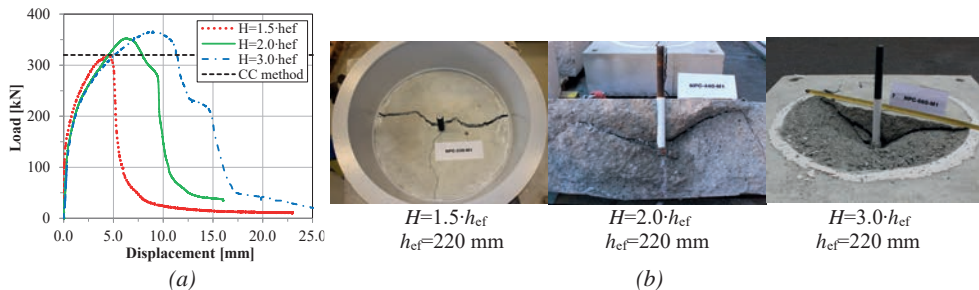


Figure 10 – (a) load-displacement curves and (b) failure patterns of the tested anchors in unreinforced concrete members of various thicknesses,  $f_c=39.5$  [N/mm<sup>2</sup>] and  $f_{t,sp}=3.2$  [N/mm<sup>2</sup>].

The concrete compressive and tensile strength at the numerical and experimental studies were different. Also note that the presented numerical results are for headed anchors with 200 mm embedment depth, while the test results are for headed anchors at 220 mm embedment depth. The load-displacement curves in Figs. 9(a) and 10(a) also show the failure load predicted by the CC method (Eq. 3) for the respective concrete strengths and embedment depths of anchors. As can be seen, the tendencies observed in the numerical analysis regarding increasing failure load and change of failure mode by increasing member thickness are fully supported by the experimental results. It should be noted that the anchor displacements, in all experiments, were generally larger than those in the simulations. This discrepancy is attributed to two reasons: (a) at experiments, the concrete in the vicinity of anchor head was locally damaged which resulted in a gradual slip

of the tested anchors and consequently an increased anchor displacement. However, this local damage of concrete cannot be accounted for in the macroscopic finite element analysis. (b) The displacements at tests were measured with respect to the solid ground rather than the concrete surface, to capture the load-displacement relationship of the tested anchors at post peak loads. Therefore, the measured displacements at tests include also the bending deformation of the tested concrete components, which is not accounted for in the simulations.

## 5.2 Influence of size of the anchor head (series b)

The numerical and experimental results of headed anchors with various head sizes (i.e., series b) showed that the anchorage capacity and stiffness increases by increasing the head size. However, the post-peak anchorage behavior became more brittle by increasing the head size. The numerically obtained load-displacement curves and the post-peak crack patterns for headed anchors at 200 mm embedment depth with various head sizes (i.e., small, medium and large) are shown in Figs. 11(a) and 11(b), respectively.

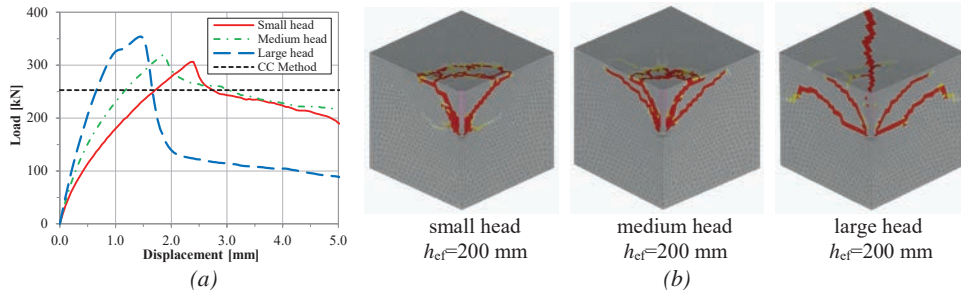


Figure 11 – (a) load-displacement curves, and (b) crack patterns obtained for the simulated anchors with various head sizes,  $f_c=28$  [ $N/mm^2$ ] and  $f_t=2.2$  [ $N/mm^2$ ].

As can be seen, irrespective of the head size, the anchorage is governed by concrete cone breakout failure as the anchors are placed in relatively thick components. However, the average concrete cone angle, with respect to the concrete surface, decreases with increase of the head size. It can also be seen that the diameter of the cone fracture at the concrete surface increases by increasing the head size. These findings are strongly supported by the experimental results: see the load-displacement curves and crack patterns obtained in tests in Figs. 12(a) and 12(b), respectively.

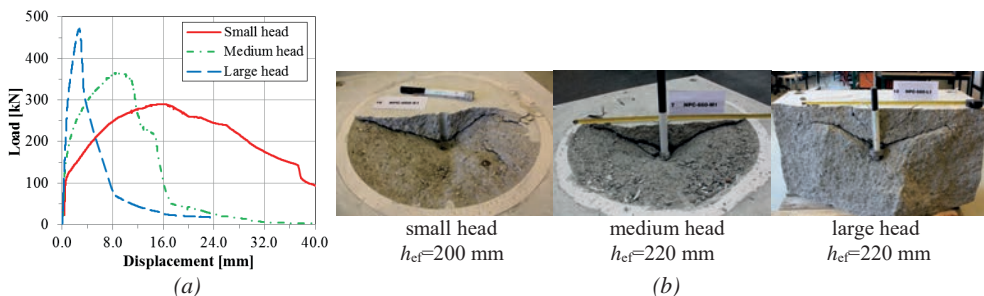


Figure 12 – (a) load-displacement curves, and (b) crack patterns obtained for the tested anchors with various head sizes,  $f_{ce}=39.5$  [ $N/mm^2$ ] and  $f_{t,sp}=3.2$  [ $N/mm^2$ ].

In all experiments, it was intended to position the anchors at an embedment depth of 220 mm; however, after casting the concrete slabs, an embedment depth of 200 mm was realized for the specimens with the small-headed anchors. Therefore, the capacity of the tested small-headed anchors would be slightly higher if they had the same embedment depth as the tested medium- and large-headed anchors. If the measured capacity of small-headed anchors at tests is normalized to the effective embedment depth of  $h_{ef}=220$  mm using a normalizing factor of  $(220/h_{ef, test})^{1.5}$ , then the experimental results show an increased rate of approximately 34% with increasing the head size. The results of simulated headed anchors at various embedment depths, however, showed a lower increase rate: the increase rate was up to 16% with increasing the head size. This discrepancy might be related to the fact that the bearing area of tested large-headed anchors was relatively larger than that of the simulated large-headed anchors. In fact, the concrete pressure under the head of the tested large-headed anchors ( $\sigma_b=1.8 \cdot f_c$ ) was less than half of the concrete pressure under the head of the simulated large-headed anchors ( $\sigma_b=4 \cdot f_c$ ).

Moreover, as figures 11(b) and 12(b) show for the simulated and tested large-headed anchors, the propagation of concrete cone cracks, at post-peak loads, is hindered by the concrete confined zone under the vertical support. This resulted in transitioning the failure mode to concrete bending cracking at post-peak loads. As this transition of failure mode happened at post-peak loads, thus it did not seem to affect the anchorage capacity, however, affected the post-peak anchorage behavior. This change of failure mode at post-peak loads can explain the brittle post-peak behavior of the large-headed anchors; see Figs. 11(a) and 12(a).

### 5.3 Influence of surface reinforcement (series c)

The numerical and experimental results of headed anchors in reinforced concrete members (i.e., series c) showed that the anchorage capacity and post-peak resistance increase if a small amount of orthogonal surface reinforcement is present (i.e.  $\rho \approx 0.3\%$  in each direction). The comparison of numerically obtained load-displacement curves of headed anchors at 200 mm embedment depth in unreinforced and reinforced concrete members of various thicknesses are shown in Fig. 13. In this figure, from the left to the right, the member thickness increases from 1.5 to 3.0 times the anchor embedment depth.

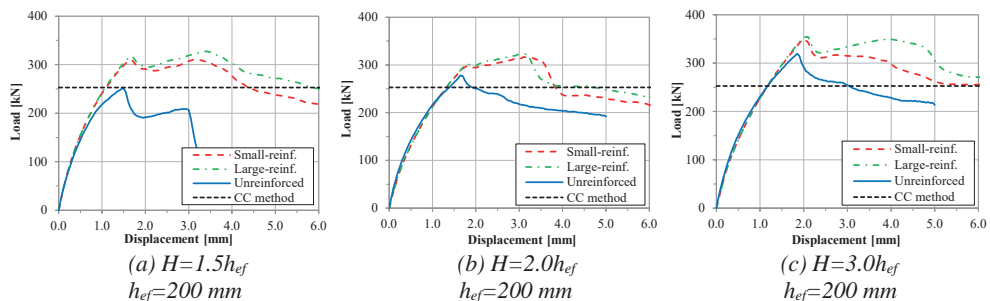


Figure 13 – Comparison of load-displacement curves of the simulated headed anchors in unreinforced and reinforced concrete members of various thicknesses,  $f_c=28$  [N/mm<sup>2</sup>] and  $f_t=2.2$  [N/mm<sup>2</sup>].

As the figure shows, the applied orthogonal surface reinforcement has a more favorable effect on the anchorage capacity of headed anchors in the thin members than those in the thick members. This is due to the fact that the global bending stiffness of concrete members increases by applying

orthogonal surface reinforcement which prevents the formation of bending/splitting cracks in thin members, thereby allowing concrete cone cracks to develop and govern the anchorage failure.

Fig. 13 further shows that the large-reinforcement content (i.e.  $\rho > 0.5\%$  in each direction) did not improve the anchorage capacity and performance any further than the small-reinforcement content ( $\rho \approx 0.3\%$ ). The same tendencies were observed for all simulated embedment depths of anchors. The load-displacement curves for the tested headed anchors in reinforced concrete slabs of various thicknesses are shown in Fig. 14. As can be seen, the experimental results confirm the tendencies observed in the numerical study.

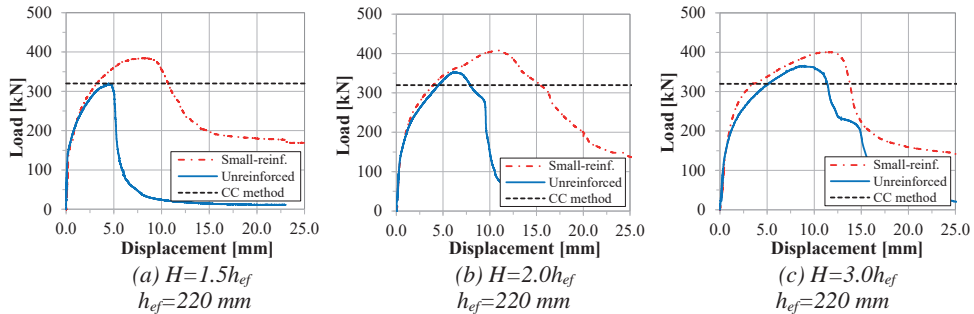


Figure 14 – Comparison of load-displacement curves of the tested anchors in unreinforced and reinforced concrete members of various thicknesses,  $f_{cc}=39.5$  [N/mm<sup>2</sup>] and  $f_{t,sp}=3.2$  [N/mm<sup>2</sup>].

The crack patterns obtained for headed anchors in reinforced concrete members of various thicknesses at simulations and tests are shown in Figs. 15 and 16, respectively. The failure of all simulated and tested headed anchors in reinforced concrete members was concrete cone breakout. In fact, the observed concrete bending/splitting failure in the thin unreinforced concrete is prevented by a small amount of orthogonal surface reinforcement.

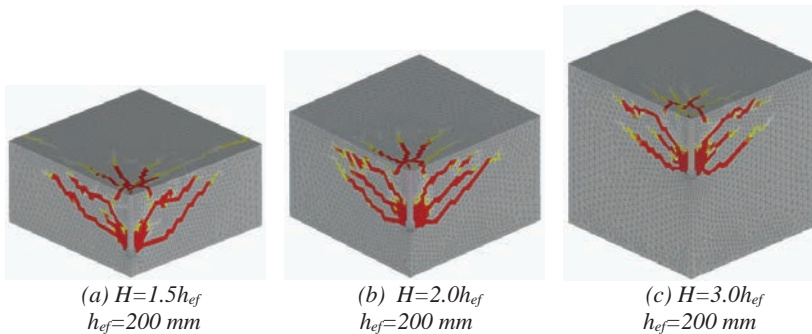


Figure 15 – Crack patterns of the simulated anchors in reinforced concrete members of various thicknesses.

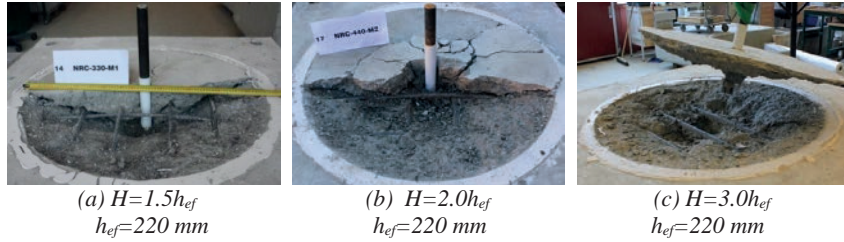


Figure 16 – Crack patterns at tests for anchors in reinforced concrete members of various thicknesses.

#### 5.4 Influence of span of vertical support

To better understand if the geometry of concrete slab and the span of vertical support has an impact on the anchorage failure load and failure mode, additional analyses were carried out. For this reason, two headed anchors at 200 mm embedment depth with a medium head size were modeled in larger concrete slabs with a length and width of ( $L=W=9.0h_{ef}$ ). In both analyses, the member height was identical ( $H=2.0h_{ef}$ ), but the span of vertical support was different ( $L_{sup}=4.0h_{ef}$  and  $8.0h_{ef}$ ). Figure 17 shows the crack patterns obtained for the simulated headed anchors with small and large supports.

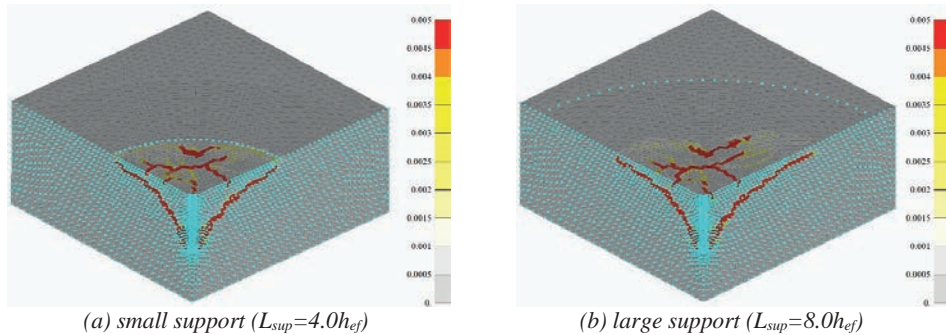


Figure 17 – Crack patterns obtained for the headed anchors loaded with small and large supports.

As can be seen, in both cases, anchors fail via concrete cone breakout. It can also be seen that the slop of concrete cone cracks is identical in both cases, albeit the horizontal extension of concrete cone at the concrete surface is slightly larger for the simulated anchor with the large support. Figure 18 also shows the load-displacement relations obtained for the two conditions. As can be seen, the stiffness and capacity of anchors change slightly if the span of vertical support is doubled. From Figs. 17 and 18, it can be concluded that the span of vertical support has negligible influence on the anchorage capacity and the horizontal extension of concrete cone at the concrete surface.

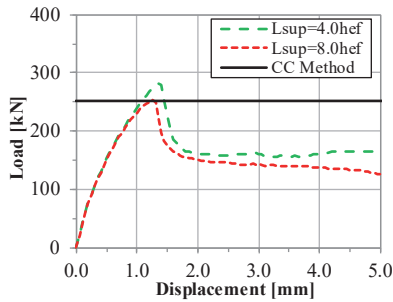


Figure 18 – Numerically obtained load-displacement curves for headed anchors loaded with small and large supports ( $h_{ef}=200$  mm,  $H=2.0h_{ef}$ )

## 6. DESIGN PROPOSALS

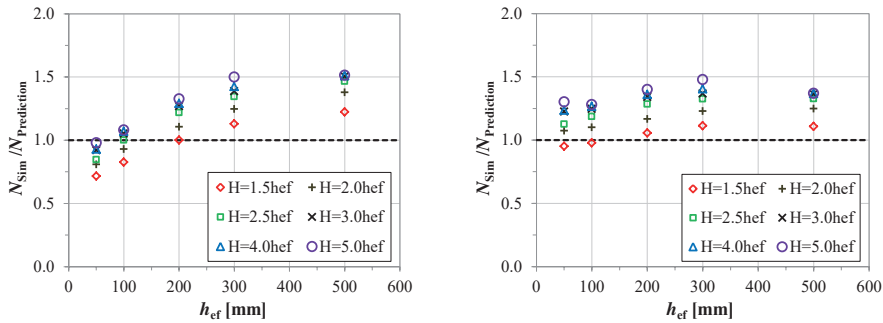
In this section, the numerical and experimental results at all embedment depths are used to evaluate the reliability of the CC method in predicting the concrete cone failure load of cast-in-place headed anchors. The numerical and experimental results of series a, b, and c showed that the anchorage capacity increases with increase of the member thickness, by enlarging the anchor head size, or if orthogonal surface reinforced is present in the concrete. Taking the influence of these parameters into account can help to improve the prediction accuracy of the failure load of headed anchors with different head sizes in unreinforced and reinforced concrete members of different geometries.

Fig. 19(a) shows ratios of calculated failure loads to the values predicted by the CC method (Eq. 3) as a function of anchor embedment depth for the simulated headed anchors of series (a). As the figure shows, the CC method overestimates the tensile breakout capacity of the short anchors ( $h_{ef} \leq 100$  mm) in thin unreinforced members, whereas it underestimates the breakout failure load of deep anchors ( $h_{ef} > 100$  mm) in thick unreinforced members. This overestimation of the failure load of short anchors is also the case for the modified CC method (Eq. 4), because both equations are identical for short embedment depths ( $h_{ef} < 280$  mm). As previously discussed, this overestimation is attributed to the fact that the tested short anchors that have been considered for the development of the CC method had relatively larger heads and consequently failed at higher loads (than the simulated failure loads in this study).

To account for the overestimation of the failure load of short headed anchors by the CC method and the modified CC method, it is recommended to use the modified CC method (Eq. 4b) regarding large embedment depths ( $h_{ef} \geq 280$  mm) also for small embedment depths as follows:

$$N_{u,m} = 6.585 \sqrt{f_c} h_{ef}^{5/3} \quad (5)$$

Equation (5) can be used for headed anchors with relatively small heads and embedment depths up to  $h_{ef}=500$  mm in unreinforced concrete members with a member thickness of  $H=2.0 \cdot h_{ef}$ . The ratios of simulated failure loads of series (a) to the values predicted by Eq. (5) are presented in Fig. 19(b) as a function of anchor embedment depth. As the figure shows, Eq. (5) predicts better the failure load of the simulated headed anchors in relatively thin members, for the entire range of the embedment depths investigated, while still underestimates the anchorage capacity in thick members.



(a) Predictions based on the CC method (Eq. 3) (b) Predictions based on proposed Eq. (5)  
 Figure 19 – Ratio of simulated failure loads to the values predicted by CC method (Eq. 3) and (Eq. 5) as a function of anchor embedment depth for headed anchors in unreinforced concrete members of various thicknesses.

As mentioned before, the failure mode of all the simulated and tested headed anchors in unreinforced concrete members of various thicknesses transitions from concrete splitting to cone breakout failure at a member thickness of  $H=2.0 \cdot h_{ef}$ . To evaluate the increase rate due to member thickness, all the measured capacities in unreinforced concrete members of various thicknesses, at both tests and simulations, are normalized to the capacity of headed anchors in concrete members with a thickness of  $(H=2.0 \cdot h_{ef})$  and plotted in Fig. 20 as a function of the relative member thickness of  $(H/2.0 \cdot h_{ef})$ . As the figure shows, the relative anchorage capacity increases up to approximately 20% with increasing the relative member thickness. To evaluate the rate of increase in the capacity of headed anchors, two power trend lines were fitted to the test and simulation results. The fitted trend lines coincide and indicate that the relative capacity ( $N_{H=1.5-5.0 \cdot hef} / N_{H=2.0 \cdot hef}$ ) at tests and simulations increases proportional to  $(H/2.0 \cdot h_{ef})^{0.24}$  and  $(H/2.0 \cdot h_{ef})^{0.25}$ , respectively.

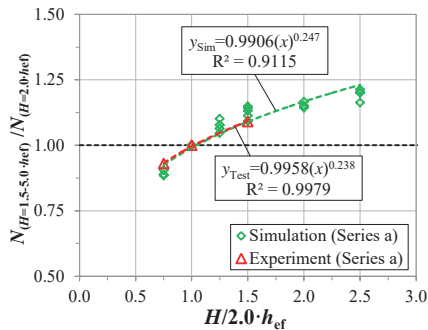


Figure 20 – Relative capacity of tested and simulated anchors in unreinforced concrete members of various thicknesses as a function of relative member thickness.

In the simulation of headed anchors with various head sizes (series b), the concrete pressure ( $\sigma_b$ ) under anchor head at peak load for the small-, medium- and large-headed anchors was approximately  $20 \cdot f_c$ ,  $11 \cdot f_c$ , and  $4 \cdot f_c$ , respectively. As mentioned before, based on ACI 349 [7] and ACI 318 [8], the mean concrete pressure ( $\sigma_b$ ) under the head of a headed anchor in an uncracked concrete member is limited to  $15 \cdot f_c$  to prevent a pullout failure. As the concrete pressure of  $15 \cdot f_c$  is between the values of concrete pressures under the head of the simulated small- and medium-headed anchors, therefore the minimum required bearing area ( $A_{b,min}$ ), at peak load, was calculated for each embedment depth of anchors using equation below:

$$A_{b,min} = \frac{N_{u,m}}{15 \cdot f_c} = \frac{16.8 \sqrt{f_c} (h_{ef})^{1.5}}{15 \cdot f_c} \quad (6)$$

In addition, the capacity of anchors with the minimum required bearing areas ( $N_{min.head}$ ) was estimated by linearly interpolating the calculated capacities of the small- and medium-headed anchors. Fig. 21 shows the relationship between the relative anchorage capacities ( $N_{various\ head} / N_{min.head}$ ) and the relative bearing areas ( $A_b / A_{b,min}$ ) for the simulated and tested headed anchors with various head sizes. As the figure shows, in both tests and simulations, the relative anchorage capacity ( $N_{various\ head} / N_{min.head}$ ) increases by increasing the relative anchor bearing area ( $A_b / A_{b,min}$ ). To evaluate the rate of increase in the capacity of headed anchors with respect to anchor bearing area, two power trend lines were fitted to the test and simulation results. The fitted trend lines indicate that the relative capacity ( $N_{various\ head} / N_{min.head}$ ) at tests and simulations increases proportional to approximately  $(A_b / A_{b,min})^{0.133}$  and  $(A_b / A_{b,min})^{0.10}$ , respectively.

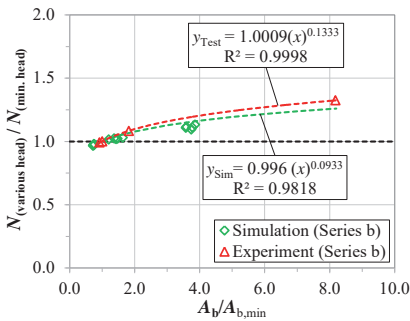


Figure 21 – Relative anchorage capacity as a function of relative anchor bearing area for the simulated and tested headed anchors with different head sizes.

To evaluate the influence of surface reinforcement on the tensile breakout resistance of headed anchors, the relative capacities of tested and simulated headed anchors in reinforced concrete members of various thicknesses (i.e., series c) to the capacity of the corresponding anchors in unreinforced concrete members ( $N_{Reinforced} / N_{Unreinforced}$ ) are plotted in Fig. 22 as a function of a relative member thickness ( $H / h_{ef}$ ).

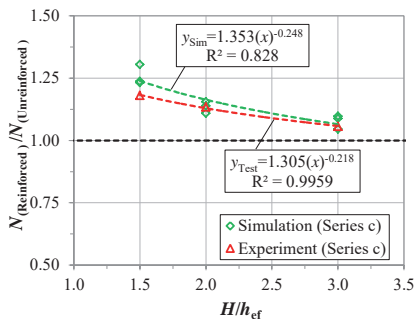


Figure 22 – Relative capacity of anchors in reinforced to unreinforced concrete slabs as a function of relative member thickness ( $H / h_{ef}$ ) for the simulated and tested headed anchors.

As the figure shows, in both the experiments and simulations, the relative anchorage capacity ( $N_{Reinforced} / N_{Unreinforced}$ ) increases with decrease of the relative member thickness ( $H / h_{ef}$ ). To evaluate the rate of increase in the capacity of headed anchors, two power trend lines were fitted

to the test and simulation results. The trend lines stipulate that the relative anchorage capacity ( $N_{\text{Reinforced}}/N_{\text{Unreinforced}}$ ) at test and simulation increases proportional to  $[1.31(H/h_{\text{ef}})^{-0.22}]$  and  $[1.35(H/h_{\text{ef}})^{-0.25}]$ , respectively.

To account for the influence of member thickness, anchor head size, and surface reinforcement on the capacity of headed anchors, the proposed Eq. (5) is here extended by incorporating three modification factors (namely  $\Psi_H$ ,  $\Psi_{\text{AH}}$ , and  $\Psi_{\text{Sr}}$  respectively for the member thickness, anchor head size, and surface reinforcement) as follows:

$$N_c = N_{\text{u,m}} \cdot \Psi_H \cdot \Psi_{\text{AH}} \cdot \Psi_{\text{Sr}} \quad (7)$$

where  $\Psi_H$ ,  $\Psi_{\text{AH}}$ , and  $\Psi_{\text{Sr}}$  can be calculated as below:

$$\Psi_H = \left( \frac{H}{2.0 \cdot h_{\text{ef}}} \right)^{0.25} \leq 1.20 \quad (8)$$

$$\Psi_{\text{AH}} = \left( \frac{A_b}{A_{b,\text{min}}} \right)^{0.1} \quad (9)$$

$$\Psi_{\text{Sr}} = \begin{cases} 1.35 \left( \frac{h_{\text{ef}}}{H} \right)^{0.25} \leq 1.20 & \text{for } H \leq 3.0 \cdot h_{\text{ef}} \\ 1.00 & \text{for } H > 3.0 \cdot h_{\text{ef}} \end{cases} \quad (10)$$

where  $H$ : member thickness [mm],  $h_{\text{ef}}$ : anchor embedment depth [mm],  $A_b$ : anchor bearing area [mm<sup>2</sup>], and  $A_{b,\text{min}}$ : the minimum required bearing area corresponding to a concrete pressure ( $\sigma_b$ ) of  $15 \cdot f_c$  under anchor head at peak load which can be determined from Eq. (6).

The proposed modification factor  $\Psi_H$  was extracted from Fig. 20.  $\Psi_H$  is limited to 1.20 as it was found that the tensile capacity of headed anchors increases up to approximately 20% with increasing the member thickness. The simulation results of series (a) revealed that, for  $\Psi_H < 1.0$ , unreinforced concrete members fail by concrete bending/splitting, whereas for  $\Psi_H \geq 1.0$  both reinforced and unreinforced concrete members fail via concrete cone breakout. The proposed Eq. (7) can predict the failure load associated with both the concrete cone and concrete splitting failure modes of headed anchors. Compared to the CC method, Eq. (7) is more conservative as it gives a lower failure load for the headed anchors in relatively thin unreinforced concrete members ( $H < 2.0 \cdot h_{\text{ef}}$ ). For design of headed anchors, one need also to calculate the bending cracking failure load of the concrete component, based on the theory of elasticity or yield line theory, and compare it with the failure load predicted by Eq. (7). It would be obvious that the lowest failure load will govern the anchorage.

The proposed modification factor  $\Psi_{\text{AH}}$  was extracted from Fig. 21.  $\Psi_{\text{AH}}$  is smaller than one for anchors with small heads (when anchor bearing area  $A_b$  is smaller than the minimum required bearing area  $A_{b,\text{min}}$ ) and thus, compared to the CC method, Eq. (7) predicts lower failure loads for headed anchors with the small heads. Based on the numerical and experimental results, it was realized that the average concrete cone angle with respect to the concrete surface decreases with increasing head size. In the case of anchors with large heads, the diameter of the concrete cone at the concrete surface is  $> 4.0 \cdot h_{\text{ef}}$ . This differs from the projected failure area of  $(3.0 \cdot h_{\text{ef}} \times 3.0 \cdot h_{\text{ef}})$  assumed by the CC method. Currently, the characteristic anchor spacing ( $s_{\text{cr}}$ ) for a group of headed

anchors and edge distance ( $c_{cr}$ ) for headed anchors close to free concrete edges is limited to  $3.0 \cdot h_{ef}$  and  $1.5 \cdot h_{ef}$ , respectively [4-8]. If the concrete cone envelope obtained for the tested and simulated large-headed anchors in this study is extended to reach the concrete surface, the diameter of the concrete cone at the concrete surface is approximately  $5.0 \cdot h_{ef}$ . Therefore, for the design of headed anchors with large heads in groups or close to concrete free edges, the characteristic anchor spacing ( $s_{cr}$ ) and the characteristic edge distance ( $c_{cr}$ ) should be increased to  $5.0 \cdot h_{ef}$  and  $2.5 \cdot h_{ef}$ , respectively.

The proposed modification factor  $\Psi_{Sr}$  was also extracted from Fig. 22.  $\Psi_{Sr}$  is also limited to 1.20 as the numerical and experimental results showed an increase of up to approximately 20% in the capacity of headed anchors if orthogonal surface reinforcement is present. It was also shown that the favorable influence of surface reinforcement on the anchorage capacity decreases by increasing the thickness of the concrete component. It should be noted that the proposed  $\Psi_{Sr}$  factor is applicable if the concrete member is orthogonally reinforced with a minimum reinforcement content of ( $\rho \approx 0.3\%$ ) in each direction.

To further evaluate the validity of the proposed model (Eq. 7) in predicting the capacity of single headed anchors with various head sizes in plain and reinforce concrete members of various thicknesses, the failure load of 124 pullout tests on single headed anchors from literature and those tests in the test series (a, b, and c) in this study are compiled in the following and compared with the corresponding values predicted by the CC method and the proposed model. The experimental data from literature were previously reported by Eligehausen et al. [10], Nilsson et al. [11], Zhao [12], and Lee et al. [13]. As in these studies, the concrete compressive strength, the thickness of concrete component, the size of anchor head, and the amount of orthogonal surface reinforcement were variable, all measured capacities were normalized and presented in Fig. 23 as a function of anchor embedment depth. In these experiments, headed anchors at various embedment depths (up to  $h_{ef}=1143$  mm) were tested in concrete slabs of different strengths. Since the concrete strength at different tests was measured on concrete cube or cylinder specimens, all the measured concrete cube compressive strengths at tests were initially converted to their equivalent cylinder compressive strengths using the following relation ( $f_c \approx 0.84 \cdot f_{cc}$ ). The measured concrete cylinder compressive strengths at tests vary from 19.1 to 45.1 [N/mm<sup>2</sup>]. All the measured failure loads at tests were then normalized to a concrete cylinder compressive strength of  $f_c=28$  [N/mm<sup>2</sup>] using a normalizing factor of  $(28/f_{c,test})^{0.5}$ .

In addition, the tested headed anchors were in concrete members of different thicknesses. The relative member thickness ( $H/2.0 \cdot h_{ef}$ ) for the tested anchors varies from 0.57 to 1.65. Therefore, all the measured failure loads at tests were further normalized to a relative member thickness of ( $H/2.0 \cdot h_{ef}=1$ ) using a normalizing factor of  $[1/(H/2.0 \cdot h_{ef})_{test}]^{0.25}$ . Moreover, the relative bearing area ( $A_b/A_{b,min}$ ) of tested headed anchors varies from approximately 0.8 to 8.1. Therefore, all failure loads at tests were further normalized to a relative bearing area of ( $A_b/A_{b,min}=4.0$ ) using a normalizing factor of  $[4/(A_b/A_{b,min})_{test}]^{0.1}$ . The applied normalizing factors are based on the proposed model (Eq. 7), as stipulates that the tensile breakout capacity is proportional to  $(f_c)^{0.5}$ ,  $(H/2.0 \cdot h_{ef})^{0.25}$ , and  $(A_b/A_{b,min})^{0.1}$ . Furthermore, the reinforcement-content of the tested concrete slabs varies from 0% to 1.16%. As the proposed model (Eq. 7) stipulates different values for the modification factor  $\Psi_{Sr}$  depending on the member thickness, therefore the value of  $\Psi_{Sr}$  was evaluated for all tested concrete slabs and then all the measured failure loads at tests were further normalized to  $\Psi_{Sr}=1.0$  using a normalizing factor of  $[1/(\Psi_{Sr})_{test}]$ .

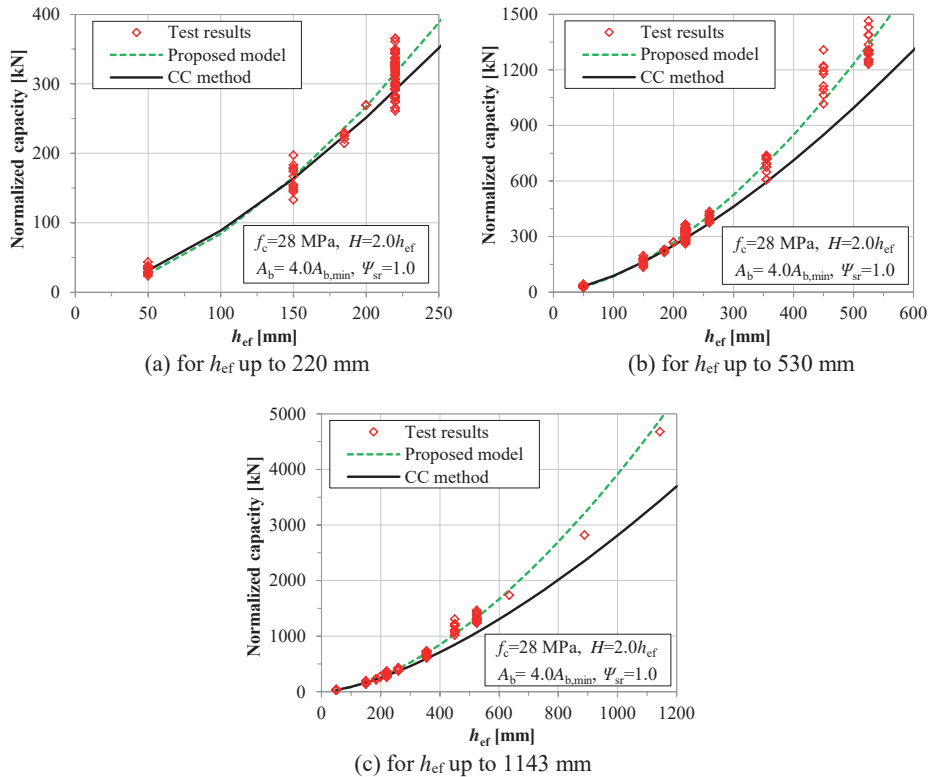


Figure 23 – Normalized concrete cone failure load of the tested anchors in this study and 124 anchors from literature [10-13] as a function of embedment depth; comparison between measured capacities at tests and predictions via the CC method (Eq. 3) and the proposed model (Eq. 7).

Figure 23 also shows the normalized failure loads predicted by the CC method and the proposed model (Eq. 7). As the figure shows, the CC method (Eq. 4) underestimates the tensile breakout capacities of deep anchors. In contrast, the proposed model (Eq. 7) better predicts the normalized capacity of the tested anchors for the embedment depths up to 635 mm. However, it seems that the proposed model (Eq. 7) overestimates slightly the anchorage capacity of anchors with embedment depths  $>635$  mm. There are two possible reasons for this overestimation: (a) the reported concrete compressive strengths for the tested deep anchors ( $h_{ef} \geq 635$  mm) were measured on small cylinder specimens, whereby the tested anchorage components were extremely large, and their mechanical properties could have been possibly reduced due to the effect of non-elastic deformations (i.e., creep, shrinkage, temperature, etc.). Therefore, the measured strengths in the experiments with  $h_{ef} \geq 635$  mm may not necessarily represent the actual strength of tested anchorage components. (b) The tests on deep headed anchors reported by Lee et al [13] were performed in concrete components with different geometrical conditions than those considered in the numerical and experimental studies presented in the current paper. Indeed, the width of concrete components in the tests with  $h_{ef} \geq 635$  mm was  $(3.6-5.0) \cdot h_{ef}$ , while it was  $6.0 \cdot h_{ef}$  in the conducted numerical and experimental studies presented in this paper. As the tested headed anchors with  $h_{ef} \geq 635$  mm had quite large heads, their failure cone fracture could have not been fully developed, due to possible truncation of the concrete cone fracture with the concrete free edges. The truncated concrete cone envelope may theoretically result in reduced capacities for

these anchors. In fact, the capacity of the tested anchors could have been higher if they had been tested in wider concrete components.

Nevertheless, to ensure the accuracy of the proposed model in predicting the capacity of headed anchors with embedment depths  $>635$  mm, further experimental and numerical evaluations of deep headed anchors are required. Until the result of these evaluations become available, it is recommended to use the proposed model (Eq. 7) for the maximum embedment depths given in ACI 349 [7] and ACI 318 [8] only (i.e.,  $h_{ef} \leq 635$  mm).

## 6. CONCLUSIONS

The influence of the thickness of concrete member, size of anchor head, and amount of orthogonal surface reinforcement on the concrete-related failure load of tension loaded headed anchors was evaluated both numerically and experimentally. Based on the experimental and numerical results, it was found that the ultimate capacity of headed anchors increases by increasing member thickness or if a small amount of orthogonal surface reinforcement ( $\rho \approx 0.3\%$  in each direction) is present at the anchoring zone. Furthermore, the anchorage post-peak resistance increases when orthogonal surface reinforcement is present. This is attributed to an increase of the global bending stiffness of the concrete members which is obtained by increasing the member thickness or adding surface reinforcement.

The anchorage fails by concrete splitting in relatively thin unreinforced concrete ( $H < 2.0h_{ef}$ ). However, a small amount of orthogonal surface reinforcement can prevent concrete splitting failure and change the failure mode to concrete cone breakout, thereby increasing the anchorage capacity. It was also found that the increase rate due to surface reinforcement is dependent on the member thickness: the thinner the concrete member the larger the favorable influence of surface reinforcement on the anchorage capacity. The numerical results further showed that a large-reinforcement ratio does not improve the tensile capacity and performance of headed anchors any further than what a small-reinforcement ratio does.

Both the tests and simulations showed that the tensile breakout capacity of headed anchors further increases by increasing the bearing area of anchors' head. However, the anchorage behavior becomes stiffer and more brittle when enlarging the head size. In the current standards, the characteristic anchor spacing ( $s_{cr}$ ) for a group of anchors and edge distance ( $c_{cr}$ ) for anchors close to concrete free edge/s are considered as  $3.0 \cdot h_{ef}$  and  $1.5 \cdot h_{ef}$ , respectively. Both the numerical and experimental results showed that the average cone angle with respect to the concrete surface decreases with increase of head size. In the case of anchors with large heads, the diameter of the concrete cone at the concrete surface was  $>4.0 \cdot h_{ef}$ . This differs from the projected concrete cone failure area of ( $3.0 \cdot h_{ef} \times 3.0 \cdot h_{ef}$ ) on the concrete surface, assumed by the CC method. Therefore, for the design of anchors with large heads in groups or close to concrete free edge/s, it is recommended to increase  $s_{cr}$  and  $c_{cr}$  to  $5.0 \cdot h_{ef}$  and  $2.5 \cdot h_{ef}$ , respectively.

It was demonstrated that the CC method overestimates the capacity of short anchors ( $h_{ef} \leq 100$  mm) if anchors have relatively small heads or positioned in relatively thin unreinforced concrete members. It was, on the other hand, realized that the CC method underestimates the tensile capacity of deep anchors if they have large heads or positioned in relatively thick members. To refine the CC method and better predict the tensile breakout capacity of cast-in-place headed anchors with various head sizes in unreinforced and reinforced uncracked concrete members of various thicknesses, the CC method (Eq. 3) was modified and further extended, see Eq. (7), by

incorporating three modification factors to take the influence of member thickness, anchor head size, and orthogonal surface reinforcement into account.

The proposed Eq. (7) should be used only for the maximum embedment depths given in ACI 349 [7] and ACI 318 [8] (i.e.,  $h_{ef} \leq 635$  mm). To extend the application of Eq. (7) to headed anchors with  $h_{ef} > 635$  mm, further numerical and experimental evaluations of headed anchors at larger embedment depths (than considered in this study) are required.

## REFERENCES

1. Eligehausen R, Mallée R & Silva J F: “Anchorage in Concrete Construction”. Ernst & Sohn, Berlin, Germany, 2006, 378 pp.
2. ACI Committee 349: “Code Requirements for Nuclear Safety-Related Concrete Structures (ACI 349-85)”. American Concrete Institute, Detroit, USA, 1985.
3. Fuchs W, Eligehausen R & Breen J E: “Concrete Capacity Design (CCD) Approach for Fastening to Concrete”. *ACI Structural Journal*, Vol. 92, No. 1, 1995, pp. 73–94.
4. CEB: “Design of Fastenings in Concrete, Comité Euro-International du Béton”. Thomas Telford, Lausanne, Switzerland, 1997, 92 pp.
5. CEN/TS 1992-4: “CEN Technical Specification (TS): Design of Fastenings for Use in Concrete, Final Draft”. European Organization for Standardization (CEN), Brussels, Belgium, 2009, 166 pp.
6. *fib* Bulletin 58. “Design of Anchorages in concrete – Guide to good practice”. International Federation for Structural Concrete, Lausanne, Switzerland, 2011, 280 pp.
7. ACI 349: “Code Requirements for Nuclear Safety-Related Concrete Structures, Appendix D”. American Concrete Institute, Farmington Hills, MI, USA, 2006.
8. ACI 318: “Building Code Requirements for Structural Concrete and Commentary”. American Concrete Institute, Farmington Hills, MI, USA, 2014, 524 pp.
9. Ožbolt J, Eligehausen R, Periškić G & Mayer U: “3D FE Analysis of Anchor Bolts with Large Embedment Depths,” *Engineering Fracture Mechanics*, Vol. 74, Nos. 1-2, 2007, pp.168-178.
10. Eligehausen R, Bouška P, Červenka V & Pukl, R: “Size Effect of the Concrete Cone Failure Load of Anchor Bolts”. *Proceedings*, 1<sup>st</sup> International Conference of Fracture Mechanics of Concrete Structures (FRAMCOS 1), Z.P. Bazant, ed., 1992, pp. 517–525.
11. Nilsson M, Ohlsson U & Elfgren L: “Effects of Surface Reinforcement on Bearing Capacity of Concrete with Anchor Bolts.” *Nordic Concrete Research*, No. 44, 2011, pp. 161–174.
12. Zhao G: “Tragverhalten von randfernen Kopfbolzenverankerungen bei Betonbruch”. *Ph.D. Dissertation*, University of Stuttgart, Stuttgart, Germany, 1993, 204 pp. (In German).
13. Lee, N. H., Kim, K. S., Bang, C. J., & Park, K. R., (2007). “Tensile-headed anchors with large diameter and deep embedment in concrete”. *ACI Structural Journal*, Vol. 104, No. 4, 2007, pp. 479-486.
14. Ožbolt J, Li Y & Kožar I: “Microplane Model for Concrete with Relaxed Kinematic Constraint,” *International Journal of Solids and Structures*, Vol. 38, No. 16, 2001, pp. 2683-2711.
15. Bažant Z P & Oh B H: “Crack Band Theory for Fracture of Concrete,” *Materials and Structures (RILEM)*, Vol. 16, No. 3, 1983, pp. 155-177.

16. Nilforoush R: “Anchorage in Concrete Structures: Numerical and Experimental Evaluations of Load-Carrying Capacity of Cast-in-Place Headed Anchors and Post-Installed Adhesive Anchors”. *Ph.D. Dissertation*, Dep. of Civil, Environment and Natural Resources Engineering, Div. of Structural and Fire Engineering, Luleå University of Technology, Luleå, Sweden, 2017, 354 pp.
17. EN 12390-3 (2009). “Testing hardened concrete. Compressive strength of test specimens”. 19 pp.
18. EN 12390-6 (2009). “Testing hardened concrete. Tensile splitting strength of test specimens”. 11 pp.
19. Nilforoush R, Nilsson M, Elfgren L, Ožbolt J, Hofmann J & Eligehausen, R: “Tensile Capacity of Anchor Bolts in Uncracked Concrete: Influence of Member Thickness and Anchor’s Head Size”. *ACI Structural Journal*, Vol. 114, No. 6, 2017, pp. 1519-1530
20. Nilforoush R, Nilsson M, Elfgren L, Ožbolt J, Hofmann J & Eligehausen R: “Influence of Surface Reinforcement, Member Thickness, and Cracked Concrete on Tensile Capacity of Anchor Bolts”. *ACI Structural Journal*, Vol. 114, No. 6, 2017, pp. 1543-1556
21. Nilforoush, R., Nilsson, M., Elfgren, L., “Experimental Evaluation of Influence of Member Thickness, Anchor-Head Size, and Reinforcement on the Tensile Capacity of Headed Anchors in Uncracked Concrete”, *Journal of Structural Engineering*, Vol. 144, No. 4, 2018, 14 pp, 04018012-1-14.



	
© Article authors. This is an open access article distributed under the Creative Commons Attribution-NonCommercial-NoDerivs licens. ( <a href="http://creativecommons.org/licenses/by-nc-nd/3.0/">http://creativecommons.org/licenses/by-nc-nd/3.0/</a> ).	ISSN online 2545-2819 ISSN print 0800-6377
DOI: 10.2478/ncr-2019-0092	Received: Sept. 7, 2018 Revision received: April 17, 2019 Accepted: June 18, 2019

## Comparison of Punching Shear Design in Finland According to the Current and the Former Method



Tuomas Lehtonen  
M.Sc.  
Specialist, Structural Analysis  
Ramboll Finland Oy  
Pakkahuoneenaukio 2, FI-33101 Tampere.  
(Corresponding author) E-mail: [tuomas.lehtonen@ramboll.fi](mailto:tuomas.lehtonen@ramboll.fi)



Matias Hirvikoski  
B.Sc.  
M.Sc. student at Tampere University of Technology  
Tieteenkatu 18 A95, FI-33720 Tampere.  
e-mail: [matias.hirvikoski@student.tut.fi](mailto:matias.hirvikoski@student.tut.fi)



Julius Rajamäki  
B.Sc.  
M.Sc. student at Tampere University of Technology  
Insinöörintie 59 B79, FI-33720 Tampere.  
e-mail: [julius.rajamaki@student.tut.fi](mailto:julius.rajamaki@student.tut.fi)

### ABSTRACT

In the beginning of 2017 the design method for punching shear in Finland was changed. The method presented in Eurocode 2 was adopted with some nationally determined parameters and rules. During 2016 and 2017 computational analyses were conducted to compare the previous national design method and the new one. Comparison setups were created in which different

parameters were varied. The results were presented as line charts. The focus was to find out how the predicted punching resistances differ between the two methods. It was discovered that the differences are significant and can be almost 60% in some cases.

**Key words:** Punching, Eurocode, comparison, national annex, structural design.

## 1. INTRODUCTION

### 1.1 General

The former national annex (NA) of Finland for Eurocode 2 (EC2) [1] stated that the punching design method in its default form was forbidden due to observed discrepancies between predicted and experimental results. Because of these discrepancies, the NA instructed that the method presented in The National Building Code of Finland (part B4) [2] was to be used instead. This changed in the beginning of 2017 when the new national annexes for Eurocodes were released and the old ones abolished. The new NA for EC2 instructed to use the punching design method of EC2 but with a couple of national rules.

Computational analyses from Ref. [3] and [4] compared these two methods: the former national one and the new EC2-based one. The study aimed to investigate how much they differ, as well as to gain information on the effect of this change on the practical design of concrete structures.

Ref. [5] refers to fib Bulletin 2, Figure 4.4-45 [6] which represents the dependency of the factor  $C_{Rc}$  and different variables when compared to test results. It discusses that the constant factor for  $C_{Rc}$  should not be used uniformly because the aforementioned figure shows nonlinear dependency of the punching resistance when the ratio  $B/d$  (the ratio between the equivalent diameter and the effective thickness of the slab), as shown in Figure 1. Thus, a revised and non-constant factor for  $C_{Rc}$  was composed and implemented in the new NA. The bulletin addresses the same issue, as it states that when  $B$  is less than about  $0.75d$ , basic punching equations should not be used. It also mentions that the CEB-FIB Model Code 90 has an upper limit equation [7] for the punching resistance which is based specifically on this matter. Eurocode 2 Commentary document [8] also discusses the constant coefficient  $C_{Rc}$  and concludes that the constant factor is correct. However, this document fails to account for the ratio  $B/d$  by dealing with the overall resistance based on experimental results rather than isolating the specific effect of this ratio. In literature, this effect is sometimes referred to as the “specific column perimeter  $u_0/d$ ”. It differs from the ratio  $B/d$  by the numerator but addresses the same effect – the ratio of the punching column dimensions and the effective thickness of the slab. The B4 method does not directly include this effect in its equations. However, the variable  $\beta_{B4}$  affects the resistance so that when there is eccentricity present, a smaller column periphery results in a smaller resistance, see Equation 11.

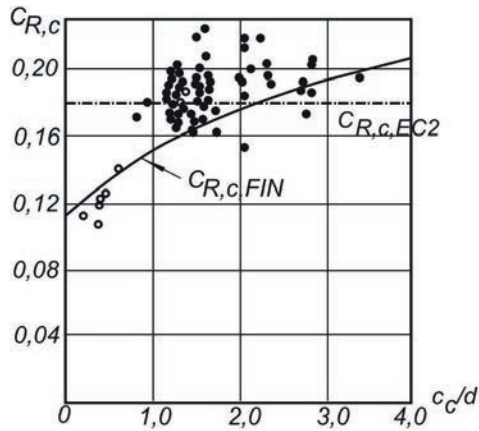


Figure 1 –  $C_{R,c}$  factor compared to experimental values [5].

Finland is not the only country to manipulate the default parameters of EC2 regarding punching shear design. The German National Annex DIN EN 1992-1-1 / NA: 2013-04 also includes a modified set of equations to account for the specific column perimeter  $u_0/d$ . The resulting values for  $C_{Rc}$  are in good agreement with the ones the Finnish NA propose.

## 1.2 Description of the design methods

This section presents the design equations for both methods. It should be emphasized that the basic control perimeters for the two methods differ substantially. In EC2 the basic control perimeter is taken at a distance of  $2.0d$  from the loaded area (edge of the column) with rounded corners and in B4 this value is  $0.5d$  and with a rectangular shape, see Figure 2.

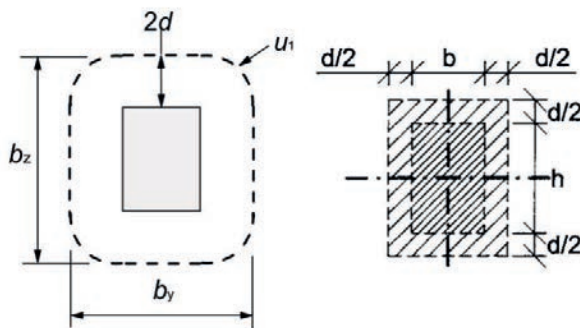


Figure 2 – Basic control perimeters according to the compared methods (EC2 left, B4 right) [1,2].

EC2 & Finnish National Annex (EC2) includes equations for punching resistance without shear reinforcement as follows in Equations 1...6.

$$V_{Rd,c,EC2} = C_{Rd,c} k_{EC2} (100 \rho_{fk})^{1/3} u_{EC} d / \beta_{EC2} \quad (1)$$

$$C_{Rd,c} = \frac{0.3(D/d+1.5)}{\gamma_c(D/d+4)} \quad (2)$$

$$D = \sqrt{c_1 c_2} \quad (3)$$

$c_1, c_2$  = side lengths of the rectangular column

$d$  = effective thickness of the slab

$$k_{EC2} = 1 + \sqrt{\frac{200}{d[\text{mm}]}} \leq 2 \quad (4)$$

$$\rho = \frac{A_s}{bd} \leq 20\% \quad (5)$$

$$u_{EC2} = 2(c_1 + c_2) + 4\pi d \quad (6)$$

$\beta_{EC2}$  = eccentricity coefficient

For the punching resistance with shear reinforcement, the equations from EC2 are as follows:

$$V_{Rd,cs,EC2} = \left[ \frac{0.75}{4.5} C_{Rd,c} k_{EC2} (100\rho f_{ck})^{\frac{1}{3}} + A_{sw,tot} f_{ywd,ef} \left( \frac{1}{u_{EC2}d} \right) \sin(\alpha) \right] u_{EC2} d / \beta_{EC2} \quad (7)$$

$A_{sw,tot}$  = total shear reinforcement inside an area of  $1.5d$  from the column side

$$f_{ywd,ef} = 250 + 0.25d \leq f_{ywd} \text{ [MPa]} \quad (8)$$

The National Building Code of Finland (B4) includes equations for the punching resistance without shear reinforcement as follows in Equations 9...14.

$$V_{Rd,c,B4} = k_{B4} \beta_{B4} (1 + 50\rho) u_{B4} d f_{ctd} \quad (9)$$

$$k_{B4} = 1.6 - d[\text{m}] \geq 1 \quad (10)$$

$$\beta_{B4} = \frac{0.40}{1 + \frac{1.5e}{\sqrt{A_u}}} \quad (11)$$

$$\rho = \frac{A_s}{bd} \leq 8\% \quad (12)$$

$e$  = eccentricity of the punching load

$A_u$  = area inside the control perimeter

$$u_{B4} = 2(c_1 + c_2) + 4d \quad (13)$$

For the punching resistance with shear reinforcement, the equations from B4 are as follows:

$$V_{Rd,cs,B4} = (0.25V_{Rd,c,B4} + A_{sw,tot} f_{yd} \sin(\alpha)) \leq 2V_{Rd,c,B4} \quad (14)$$

$f_{yd}$  = design strength of shear reinforcement  $\leq 300$  MPa

The design tensile strength of concrete  $f_{ctd}$  is needed in calculation according to B4. This is calculated as follows:

$$f_{ctd} = \alpha_{ct} f_{ctk,0,05} / \gamma_c \quad (15)$$

$$\alpha_{ct} = 1.0$$

$$f_{ctk,0,05} = 0.7f_{ctm} \quad (16)$$

$$f_{ctm} = 0.30f_{ck}^{2/3}, \text{ when concrete class } \leq \text{C50/60} \quad (17)$$

This way the design tensile strength as a factor of compressive strength can be expressed as an approximate value, for example for concrete C30/37 as follows:

$$f_{ctd} \approx 0.045f_{ck} \quad (18)$$

It should be mentioned that the Finnish National Annex declares the minimum value for shear strength  $v_{min} = 0$ . This means that if there is no tensile reinforcement, there is no punching strength either. In the default EC2, the minimum value is defined as:

$$v_{min} = 0.035k^{3/2}f_{ck}^{1/2} \quad (19)$$

Of course, one must bear in mind that situations where there is absolutely no tensile reinforcement are unrealistic because of minimum reinforcement requirements. Thus, zero punching resistances are purely theoretical when using the Finnish NA.

The maximum increase of punching resistance using shear reinforcement varies between the two methods. The EC2 method has a value of 1.6, defined by the Finnish NA, which is the maximum resistance allowed by using shear reinforcement compared to the value with no shear reinforcement. In the B4 method this value is 2.0, as can be seen from the Equation 14. These maximum resistance increase factors mean that no matter how much shear reinforcement is used, the resulting resistance cannot exceed these values. This is also clearly visible in the comparison charts in Chapter 3. This can be expressed as follows:

$$V_{Rd,cs,EC2} \leq 1.6V_{Rd,c,EC2} \quad (20)$$

$$V_{Rd,cs,B4} \leq 2.0V_{Rd,c,B4} \quad (21)$$

Both methods allow the use of a single line of bent-down bars with an angle of 30 degrees. Only EC2 gives a minimum shear reinforcement equation, which is shown below:

$$A_{sw,min} \geq \frac{0.08\sqrt{f_{ck}}/f_{yk}}{1.5\sin(\alpha)+\cos(\alpha)} S_r S_t \quad (22)$$

The Finnish NA states that when using other than radially placed shear reinforcement,  $S_r S_t$  can be replaced by the total amount of shear reinforcement inside the basic control perimeter  $u_l$ .

## 2. COMPARISON SETUPS

Different setups were chosen to compare results. The following properties apply to all:

- Reinforcement class B500B

- Square column 380 mm x 380 mm ( $c$  in Figure 3)
- Distance from reinforcement centre of gravity to the edge of concrete slab was 40 mm ( $d_s$  in Figure 3)
- Safety factor for concrete  $\gamma_c = 1.5$
- Reduction factor for compressive strength of concrete  $\alpha_{cc} = 0.85$
- Reduction factor for tensile strength of concrete  $\alpha_{ct} = 1.00$
- Safety factor for reinforcement  $\gamma_s = 1.15$

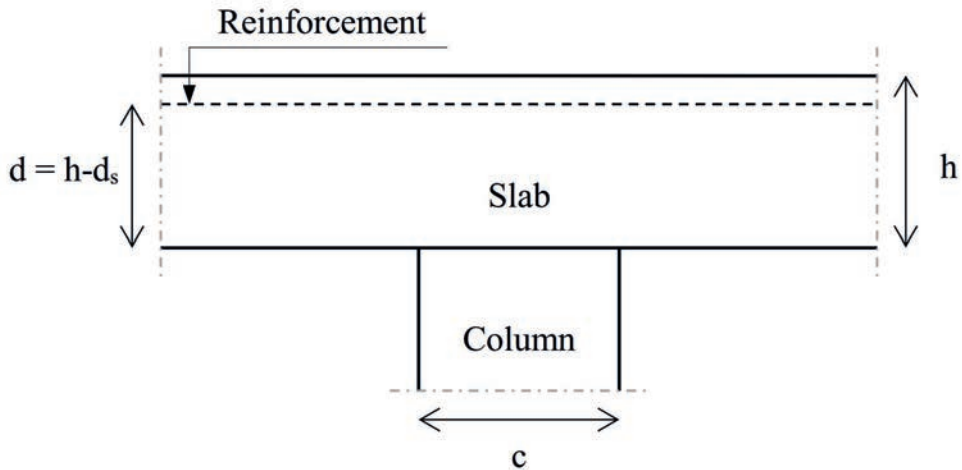


Figure 3 – Schematic representation of the structure.

Punching resistance both with and without shear reinforcement was considered. Bent-down bars with an effective angle of 30 degrees were used in all cases when shear reinforcement was applied. In addition, effect of the eccentricity factor  $\beta$  (relating to EC2) was observed as two values: 1.0 and 1.15. This factor takes non-symmetrical shear force distribution into account. The larger the eccentricity of the punching force the lower the punching resistance. Factor  $\beta$  increases as the eccentricity increases.

### **2.1 Varying reinforcement ratio (setup #1)**

The first setup was chosen to represent the effect of slab's reinforcement ratio  $\rho$  (ratio between tensile reinforcement area and the product of cross-section width and effective thickness  $d$ ) on the punching resistance. Three constant effective thicknesses  $d$  (distance from the bottom of the slab to the center-line of effective reinforcement) were adopted, and reinforcement ratio was varied between 1.51‰ and 25‰. The lower limit represents the minimum reinforcement requirement due to bending and the upper one is chosen to be a bit over the maximum reinforcement ratio of EC2 regarding punching resistance. Eurocode 2 gives a limit value of 20‰ after which an increase in reinforcement ratio is no longer effective in increasing punching resistance. Maximum reinforcement ratio in these comparisons is about 18.3‰. This represents the maximum amount of reinforcement in the cross-section and should be considered as the realistic upper limit for reinforcement ratios. In usual design situations the ratio is considerably lower than that. Thus, all the values of reinforcement ratio above the maximum are purely theoretical and represented only to show how the equations behave further on. No shear reinforcement was involved in this comparison.

### **2.2 Varying concrete strength (setup #2)**

The second setup was chosen to represent the effect of concrete strength  $f_{ck}$  on the punching shear resistance. The related design code equations [1, 2], see Equations 1-18, show the concrete strength as a variable is not in same proportion between the two codes. To clarify this notion graphs were plotted with three constant effective thicknesses  $d$  and concrete strength was varied between 12 and 50 MPa. No shear reinforcement was involved in this comparison. Reinforcement ratio was kept as a constant value of 8‰.

### **2.3 Varying amount of shear reinforcement (setup #3)**

The third setup represents how much the applied shear reinforcement affects the punching shear resistance. A single line of bent-down bars with an angle of 30 degrees were chosen as a typical form of shear reinforcement. The total amount of shear reinforcement area passing the punching cone was varied between 0 and 16000 mm<sup>2</sup>. Reinforcement ratio was kept as a constant value of 8‰.

### 3. RESULTS

Comparison line charts were chosen as the main form of displaying results due to their clarity and versatility. Abbreviations *B4* and *EC2* relate to the previous Finnish design method and the Eurocode method, respectively. The charts present the punching shear resistance as a single value in kilonewtons taking all the required verifications into account, i.e. maximum compressive stress around the column perimeter  $u_0$  (length of column periphery).

#### 3.1 Varying reinforcement ratio (setup #1)

Figure 4 illustrates the differences between the two methods. Resistances according to the EC2 method are lower than the B4 method's only with very low reinforcement ratios  $\rho$  (around 3%). The higher the reinforcement ratio the larger the difference between the two methods.

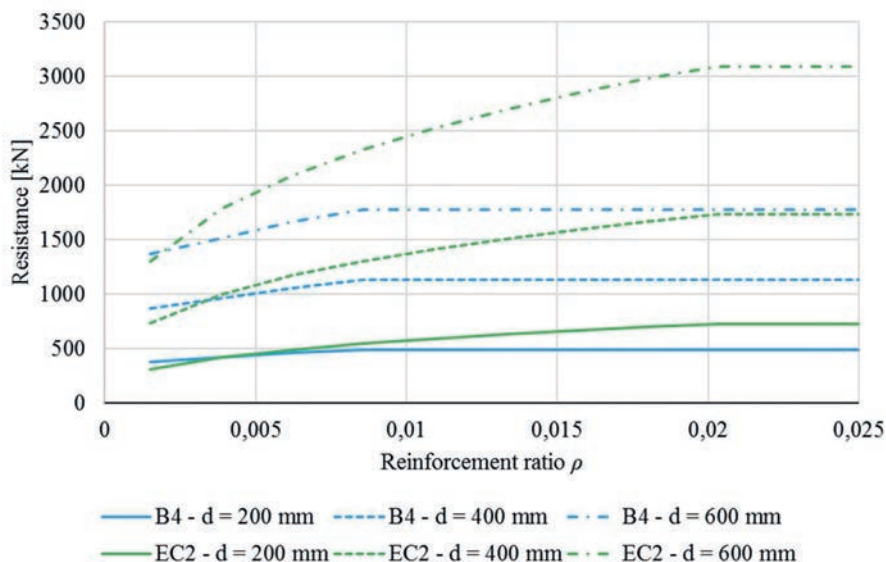


Figure 4 – Punching resistance in setup #1.

Figure 5 further clarifies how large the relative differences are. Relative difference is defined as the remainder of resistances according to EC2 method and B4 method divided by the resistance of B4 method. This results in a positive value when EC2-resistance is higher than B4-resistance, and vice versa, negative values represent situations where B4-resistance exceeds that of the EC2's.

The relative difference increases as effective thickness increases, but nonlinearly. The reason for this behaviour is explained later when dealing with effect of slab thickness on punching resistance, see Section 3.4.

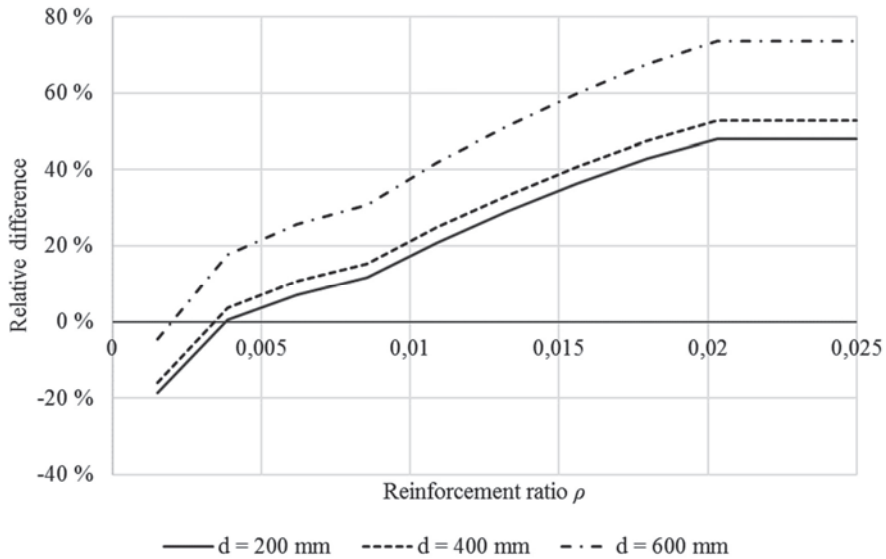


Figure 5 – Relative difference of resistances in setup #1.

### 3.2 Varying concrete strength (setup #2)

Concrete strength plays an important role in punching shear resistance, see Figure 6. It is apparent that the relative difference decreases as the concrete strength increases. In other words, influence of concrete strength seems to be higher in B4 method.

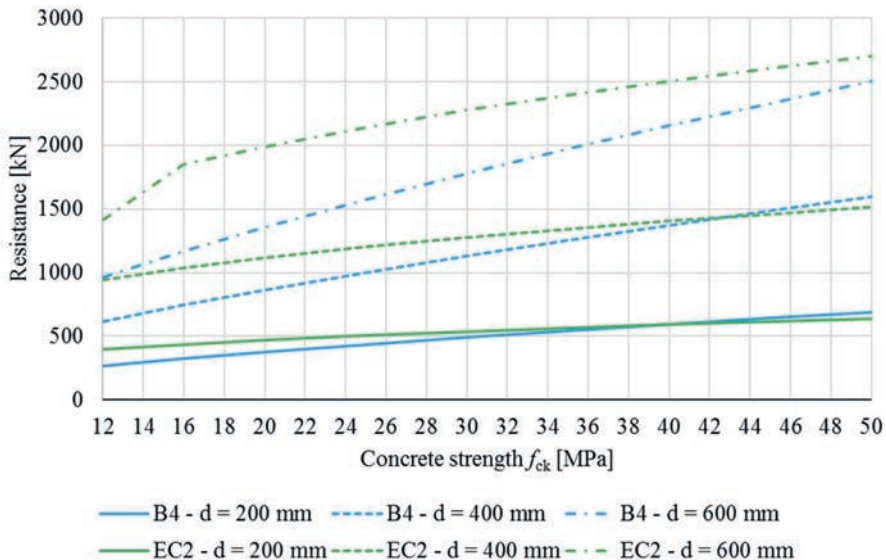


Figure 6 – Punching resistance in setup #2.

The relative difference is at its peak, almost 60%, when examining very low concrete strengths, see Figure 7. Compared to the B4 method, increasing concrete strength in the EC2 method doesn't increase punching resistance relatively as much. The reason for this is found from the design equations: the B4 method has an exponent of  $2/3$  for  $f_{ck}$  whereas EC2 has  $1/3$ . It should be emphasized that concrete strengths  $f_{ck}$  below 25 MPa are very low and not used in everyday building design. The graph is constructed to show the differences and the factors affecting the punching resistance.

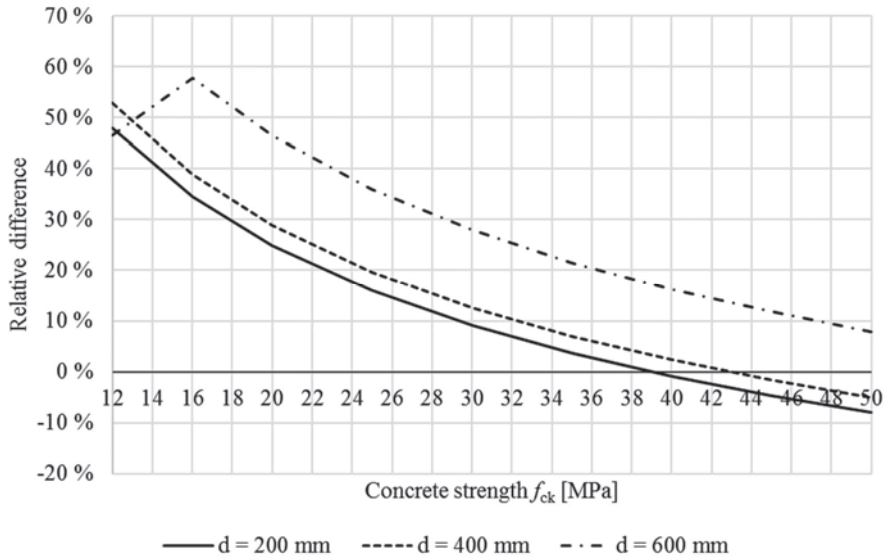


Figure 7 – Relative difference of resistances in setup #2.

### 3.3 Varying amount of shear reinforcement (setup #3)

Figure 8 shows how shear reinforcement affects punching shear resistance. The more shear reinforcement is applied, the higher the punching resistance. Although effective, shear reinforcement influence is limited to a certain amount within design codes. In the B4 method a maximum of two times the resistance of unreinforced (shear reinforced) slab is allowed, whereas the EC2 method allows only 1,6 as the maximum increase factor. Therefore, the figure below shows only partial incline portions of resistance curves: after the maximum effect is reached, curves plateau.

For all three effective depths  $d$  the curve stays horizontal until the minimum amount of shear reinforcement is reached. This is the point where resistance calculated based on shear reinforced structure is higher than that of unreinforced structure. Adding shear reinforcement increases resistance and the slope of the curve displaying this phenomenon seems similar in both methods.

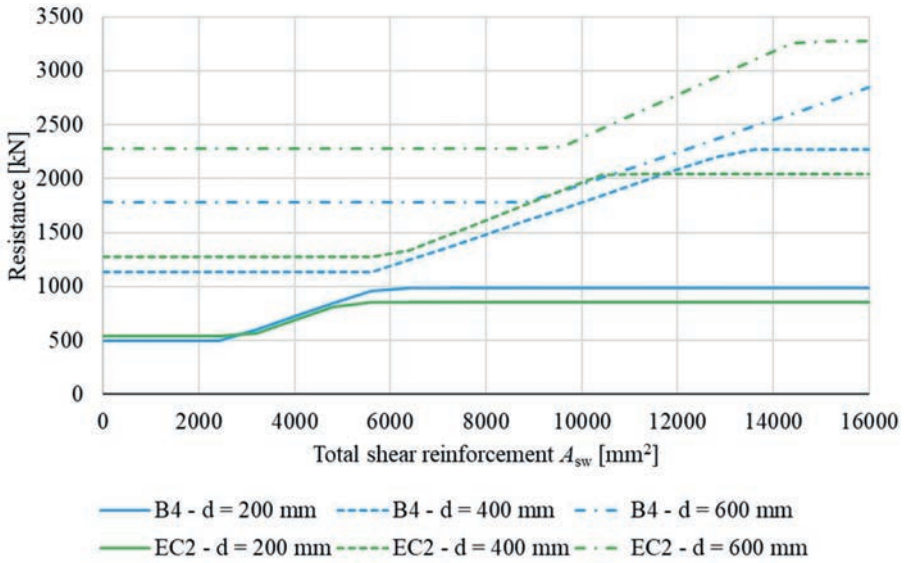


Figure 8 – Punching resistance in setup #3.

Relative differences decrease and switch signs when the area of shear reinforcement increases, see Figure 9. It can be deciphered that the maximum amount of punching shear resistance is higher with the B4 method than the EC2 method.

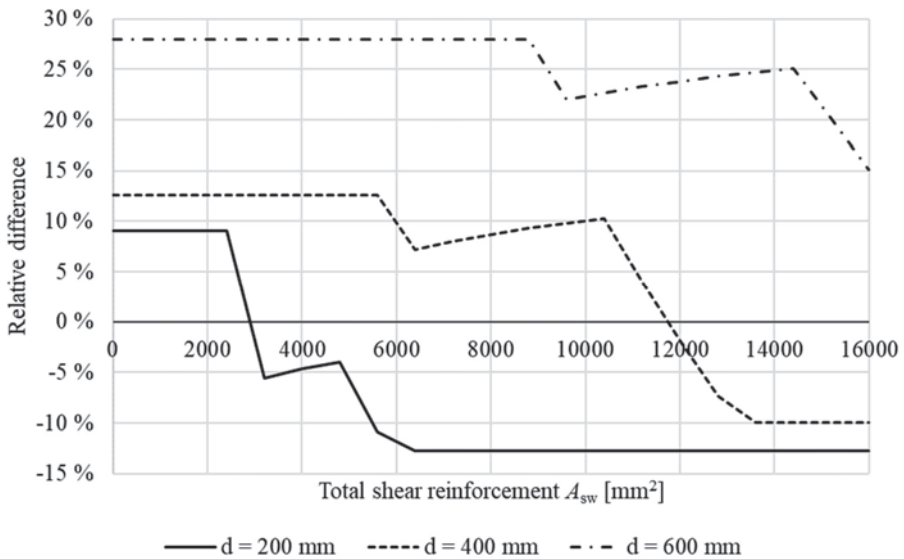


Figure 9 – Relative difference of resistances in setup #3.

### 3.4 Effect of slab thickness

The most notable change in the Finnish national annex in relation to the default Eurocode 2 is the factor  $C_{Rd,c}$  (coefficient derived from tests affecting shear resistance) which is a constant value in the default EC2 but a variable (considering the effective diameter of the column and the effective slab thickness as factors) in the Finnish NA. This is the most profound difference between the two EC2 methods and constitutes the primary reason why the default EC2 method was forbidden in Finland.

As previous graphs have shown, the EC2 method seems to result in higher resistances than the B4 method as the effective thickness increases. Figure 10 shows how the shape factors  $k$  (present in both methods but with different equations) are related to the effective depth. Also control perimeters  $u$  are plotted, defined in Equations 6 and 13.

In the absence of axial forces, the punching shear resistance (without shear reinforcement) is directly proportional to the shape factor  $k$  and control perimeters  $u$  in both. Hence, the slope of the curves in Figure 10 determines how much the punching resistances increase by the increasing effective depth  $d$ . The factor  $k'$  regarding EC2 means the product of the shape factor  $k$  and  $C_{Rd,c}$ . This gives a more accurate form of comparison to method B4.

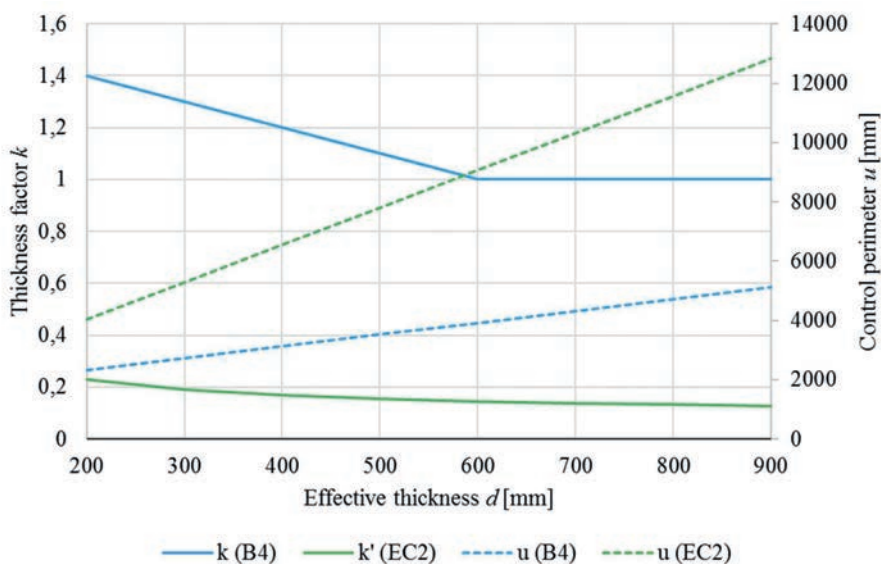


Figure 10 – Effect of thickness factors and control perimeters on punching resistance.

Increasing the effective depth  $d$  decreases the shape factor  $k'$  (EC2) less than  $k$  (B4) when  $d$  is below 600 mm, after which it remains constant for the B4 method. The control perimeters of the EC2 method increase more than in the B4 method as the effective depth  $d$  increases. This can be interpreted such that in general, punching shear resistances according to EC2 increase more than those of the B4 method. In other words, thicker slabs can be utilized more effectively in the EC2 method regarding punching.

## 4. CONCLUSIONS

The results in this study demonstrates that the new method implemented in Finland as a national annex for Eurocode 2 gives very different results in some cases compared to the former B4 method. It is worth mentioning that the previous method no longer applies to new building projects in Finland, however bridge design remains to be performed using the B4 method.

According to the new method, higher reinforcement ratios can be utilized with an upper limit of 20% whereas with the old B4 method the limit was only 8%. However, the maximum reinforcement ratio can be lower than 20%, which prohibits the use of such a high amount of reinforcement.

A general conclusion can be made that the new method gives higher punching shear resistances. Slab thicknesses compared to the past are likely to change due to this difference. Concrete compressive strength affects the results significantly: the higher the strength, the smaller the relative difference between the two methods. The two methods weight different variables in the resulting resistance. In short, B4 is more concrete tensile strength oriented whereas EC2 utilizes tensile reinforcement more than B4. It should be noted, that the absolute amount of tensile reinforcement is higher when using EC2 method because the basic control perimeter is longer, and reinforcement must be placed and anchored on a wider area than that of B4's.

The reason for such differences lies behind the complexity of the two design codes. B4 method is more straightforward than EC2 method. The latter has more design equations and is constructed to consider various scenarios and phenomena. It is understandable that simplified methods are usually more conservative than advanced ones, because they must narrow down the variables to be simple enough for everyday use. Despite this, it doesn't mean that advanced methods always produce safe results or are in any way superior to more simple ones.

### 4.1 What the future holds

The second generation of Eurocodes is currently under development and will probably be published around 2022-2024. As in the past, the fib Model Code is a major influencer for the upcoming concrete Eurocode provisions. Drafts of the new EN 1992 have already being published. According to the latest draft [9] shear design will be completely overhauled, and this also concerns punching shear design. The new approach is based on Model Code 2010 [10] and Critical Shear Crack Theory. Basic perimeter will be reduced to  $0.5d$  from the current  $2.0d$  and the whole set of equations are replaced by new ones.

The most important reasons for changing the current default EC2 method are summarized in the background documents [11] for the second generation EC2 as listed below:

- Physical inconsistency with the control perimeter at  $2.0d$  and the need for iterative calculation process when dealing with punching shear design of footings,
- The current size effect does not suitably describe the corresponding phenomenon and both underestimate and overestimate the punching resistance in different scenarios,
- The current method includes no slenderness effect,

- There is both underestimation and overestimation in punching resistance according to experimental tests when shear reinforcement is used.

In general, the background document states that there has been numerous works criticizing different aspects of the current EC2 method. From this it can be deduced that the shortcomings of the current EC2 have been recognized and due to these, the modifications provided by the Finnish National Annex are implemented.

## REFERENCES

1. EN 1992-1-1:2004: “Eurocode 2: Design of concrete structures. Part 1-1: General rules and rules for buildings”, European Committee for Standardization, Brussels, Belgium, 2004.
2. The National Building Code of Finland, Part B4: “Concrete structures, regulations and guidelines 2005”. Ministry of the Environment, Helsinki, Finland, 2005.
3. Hirvikoski, M: “The change in punching shear resistance without shear reinforcement according to the new Finnish National Annex to Eurocode 2”, *B.Sc. Thesis*, Tampere University of Technology, Faculty of Business and Built Environment, Laboratory of Civil Engineering, Tampere, Finland, 2017.
4. Rajamäki J: “The change in punching shear resistance with shear reinforcement according to Eurocode 2 with Finnish National Annex”, *B.Sc. Thesis*, Tampere University of Technology, Faculty of Business and Built Environment, Laboratory of Civil Engineering, Tampere, Finland, 2017.
5. Leskelä, M.V.: ”EN 1992-1-1: Uusi eurocode 2 standardi betonirakenteiden suunnittelua varten”, Rakentajain Kalenteri 2003, Rakennustieto Oy, 2007. (In Finnish).
6. fédération internationale du béton (fib): “Structural Concrete, Volume 2”, *fib Bulletin 2*, Lausanne, Switzerland, 1999.
7. Comité Euro-International du Béton: “CEB-FIP Model Code 1990”. Lausanne, Switzerland, 1993.
8. European Concrete Platform ASBL: “Eurocode 2 Commentary (rev A 31-03-2017)”. Brussels, Belgium, 2017.
9. CEN: “prEN1992-1-1:2018: Final Version of PT1-draft prEN 1992-1-1 2018 D3”, 2018.
10. fédération internationale du béton (fib): “Model Code 2010 – Final Draft”. *fib Bulletin 66*, Lausanne, Switzerland, 2012.
11. CEN: “Background to prEN 1992-1-1:2018: Background documents to the final PT1 draft prEN 1992-1-1:2018”, 2018.

	
© Article authors. This is an open access article distributed under the Creative Commons Attribution-NonCommercial-NoDerivs licens. ( <a href="http://creativecommons.org/licenses/by-nc-nd/3.0/">http://creativecommons.org/licenses/by-nc-nd/3.0/</a> ).	ISSN online 2545-2819 ISSN print 0800-6377
DOI: 10.2478/ncr-2019-0093	Received: Sept. 26, 2018 Revision received: Feb. 1, 2019 Accepted: June 18, 2019

## Stability of Air Content in Fresh Concretes with PCE-Based Superplasticizers



Fahim Al-Neshawy  
D.Sc. (Tech.), Staff Scientist  
Aalto University School of Engineering  
Department of Civil Engineering  
P.O.Box 12100, FIN-00076, Espoo, Finland  
[fahim.al-neshawy@aalto.fi](mailto:fahim.al-neshawy@aalto.fi)



Teemu Ojala  
M.Sc. Doctoral candidate  
Aalto University School of Engineering  
Department of Civil Engineering  
P.O.Box 12100, FIN-00076, Espoo, Finland  
[teemu.ojala@aalto.fi](mailto:teemu.ojala@aalto.fi)



Jouni Punkki  
D.Sc. (Tech.), Professor of Practice, Concrete Technology  
Aalto University School of Engineering  
Department of Civil Engineering  
P.O.Box 12100, FIN-00076, Espoo, Finland  
[jouni.punkki@aalto.fi](mailto:jouni.punkki@aalto.fi)

### ABSTRACT

Air contents of concrete are necessary for concrete durability in freeze-thaw exposure. According to the Finnish concrete code, the target value for air content varies between 4% and 5.5% for XF - exposure classes. Lately in Finland, some cases showed an elevation of air contents up to 15% in fresh air-entrained concrete at construction site and in drilled concrete samples.

The objectives of this study were to investigate the stability of air entrainment by measuring the air content elevation 30 minutes and 60 minutes after concrete mixing and investigating the concrete sensitivity to segregation. Composition of concretes used in this study include 7 different combination of PCE based superplasticizer and air-entraining agent admixtures, cement content of 425 kg/m<sup>3</sup>, two consistency classes S3 with water to cement ration of 0.33 and F5 with water

to cement ration of 0.38. One cement type was used for all concrete mixes. The concretes were mixed for 2 minutes and 5 minutes mixing times.

The results show that the elevation of the air content of fresh concrete depends on the consistency of the concrete and on the used combination of superplasticizer and air-entraining agents. The higher consistency classes concretes have more risk of air elevation with some combinations of PCE-based superplasticizers and air-entraining agents. The results also indicate that short mixing time would not be enough to achieve total effectivity of some air-entraining agents, especially for higher consistency classes concrete.

**Key words:** Air content, superplasticizer, air-entraining, admixtures, concrete.

## 1. INTRODUCTION

In Finland, elevated air contents have been reported in air entrained concrete. The highest air contents determined from samples drilled from structures have exceeded 15% and significant deficiencies in compressive strength of the concrete have been reported. Some indications of elevated air contents have been seen during the last years, for example the railroad bridge in Kemijärvi [1] and the Turku University Hospital [2]. Concrete composition and consistency have been noticed to affect the air entrainment [3]. In addition, one critical factor could be the use of combination of air entraining agent (AEA) and the third generation polycarboxylate ether (PCE)-based superplasticizers admixtures.

First-generation lignosulfonate-based superplasticizers (derived from the production of paper-making from wood) were air-entraining water-reducing agents. It was followed by the second-generation (early high-range) superplasticizers were derived from petroleum feed stocks: sulfonated naphthalene or melamine condensates with formaldehyde. The incorporation of second-generation superplasticizer lowers the viscosity of the fresh concrete mixture, thus facilitating the escape of air from it. Typically, 1% to 3% of the air is lost due to the addition of the admixture [4]. Third-generation Superplasticizers are polycarboxylates ethers (PCE), which are copolymers synthesized from carefully selected monomers.

Lazniewska (2009) reported that the air content in the presence of PCE superplasticizer increases with water to cement ratio as a sequence of the reduction of surface tension between the liquid and solid component of the paste [5]. It is complex to conclude what and how the chemical admixtures affect the air entrainment. Most organic chemical admixtures like PCE superplasticizer can increase the air entrainment since they can partly reduce the adsorbed AEA molecules on the solid surface by competing with them. Other admixtures like retards, accelerators, etc., have minor effect on the air entrainment [3].

The action of the first and second-generation superplasticizers is based on electrostatic repulsion. The mechanism of those superplasticizers and air-entraining agent (AEA) working in the same cement paste is shown in Figure 1. With the present of SP, the air content tends to be reduced. The negative charged cement particles, given by the adsorption of SP molecules, prevent or lower the adsorption of AEA molecules. As a result, there is less space for air bubbles to be entrained. Also, the negative charge keeps cement particles and air bubbles dispersing from each other and then reduces the friction of the mix [7] and [8].

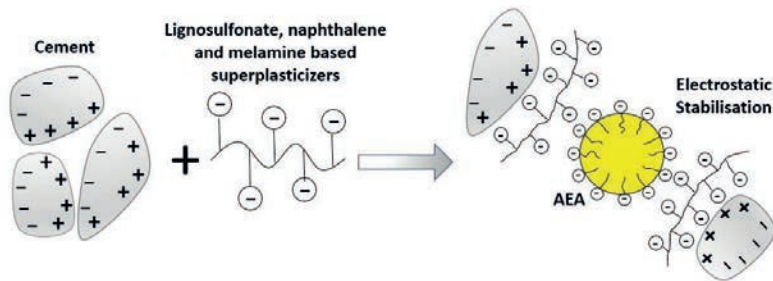


Figure 1 – Schematic draft showing electrostatic stabilization of cement and the mechanism of SP and AEA working in the same cement paste, adapted from [7] and [8].

The action of the polycarboxylate ethers (PCE) based superplasticizer cause a spatial (steric hindrance) separation of the cement particles, as shown in Figure 2. PCEs plasticizers have specific number of side chains that are distributed along a main chain. The carboxylate groups interact with the surface of the cement grain, which leads to polymer adsorption and a steric repulsion is considered as a potential mechanism of cement grains dispersion. [5], [6] and [7].

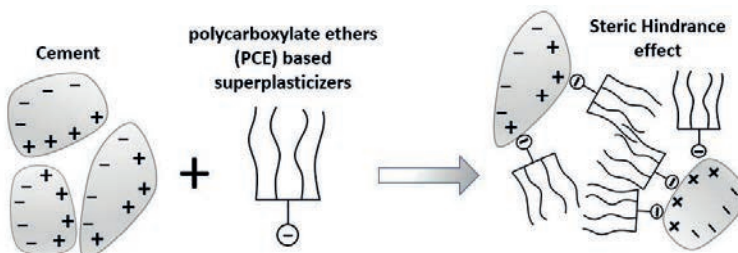


Figure 2 – Mechanism of polycarboxylate ethers (PCE) superplasticizer, adapted from [7].

Eickschen and Müller [9] investigated the action mechanisms occurring during the production of air-entrained concrete with plasticizers. Ten concretes (cement content 320 kg/m<sup>3</sup>, w/c ratio 0.50, air content of 5.5 ± 0.5% and a consistency class F4) were produced in order to investigate the action mechanisms of air void formation in fresh and hardened concrete in relation to the combination of the air-entraining agent/plasticizer/cement starting materials. The concretes were produced with CEM I 42.5 N and CEM III/A 42.5 N-LH/NA cements (see Table 1) in combination with the following admixtures:

- Two types of air-entraining agents: (i) modified wood resin and (ii) synthetic tenside 1
- Three types of plasticizer: (i) pre-cast element, (ii) ready-mixed concrete PCE superplasticizer and (iii) plasticizer based on melamine sulfonate.

Table 1. Chemical and physical properties of the cement used in the Eickschen and Müller investigation [9]

Parameter		CEM I 42.5 R	CEM III/A 42.5 N-LH/NA
K <sub>2</sub> O	mass%	0.88	0.91
Na <sub>2</sub> O	mass%	0.13	0.23
Na <sub>2</sub> O equiv.	mass%	0.71	0.83
SO <sub>3</sub>	mass%	2.96	2.90
BFS content	mass%	-	50.6
Initial setting time	min	160	220
Water demand	%	27	30
Spec. surface area	cm <sup>2</sup> /g	3250	4210
Compressive strength		2d = 25.1	2d = 17.0
		7d = 42.4	7d = 34.6
		28d = 56.5	28d = 52.1

The influence of the plasticizer on the air content of concrete with CEM I and CEM III binders is shown in Figure 3. Eickschen and Müller [9] concluded that the increase in air content was substantially greater than with the natural air-entraining agent. The increase in air content was more strongly marked when using the PCE-based plasticizers than with the conventional plasticizers (melamine sulfonate). Combinations with the synthetic air-entraining agent and a PCE-based plasticizer exhibited a greater range of fluctuation in air content than combinations with natural air-entraining agents and conventional plasticizers.

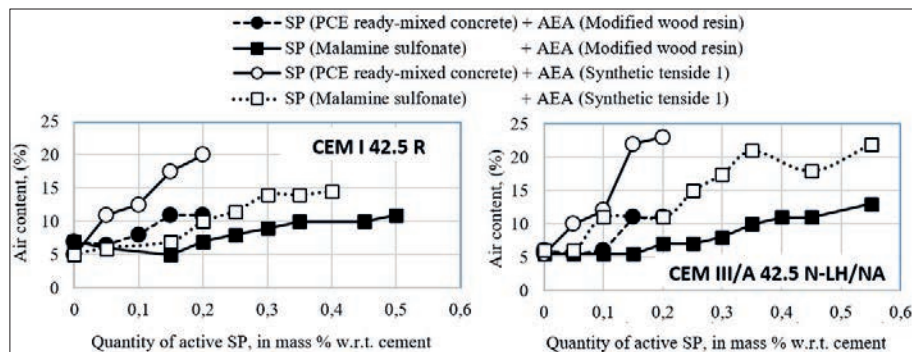


Figure 3 – The effect of the type and the quantity of superplasticizer on the air content of concrete mixtures using CEM I and CEM III cements and different types of Air-Entraining Agents. The chart data are based on Eickschen and Müller (2012) results. [9].

Based on the recent Finnish cases of Kemijärvi [1] and [2], the air content may elevate after mixing and causes strength problems. The aim of the study was to investigate and secure the stability of the protective pore system in air entrained concrete and thereby reduce the risk for elevated air contents in concrete structures.

The authors believe that the air content potential phenomenon is the reason for the elevated air content. It is explained by the maximum potential air content which depends on the admixture combination, concrete composition and the consistency of concrete. It is possible that only part of

the entrained air is formed during the normal mixing process, especially when the mixing time is short, and more air is formed in the concrete truck mixers. A relative effective mixing process is needed to achieve the air content potential during the mixing process.

The risk for elevated air contents can be reduced by using longer mixing time. Then also the dosage of air-entraining agents can be reduced.

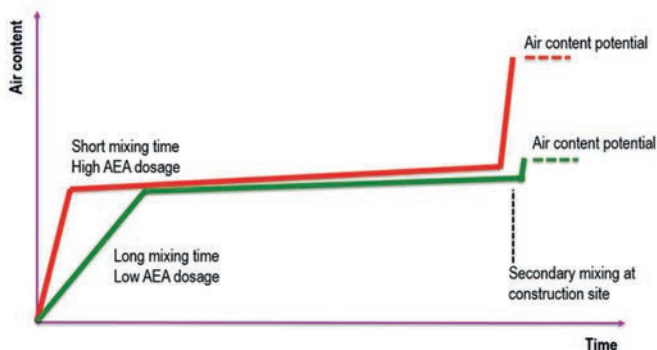


Figure 4 – Illustrated effects of the mixing time (mixing efficiency) and the AEA dosage on the increase of the air content after mixing [10].

## 2. MATERIALS AND METHODS

The aim of the investigation was to clarify the factors affecting the stability of the air entrainment in fresh concrete. The factors investigated were (i) the concrete composition and (ii) combination of different superplasticizers and air-entraining agents.

To carry out the investigation, concrete mixtures with different types of AEAs and PCE-based superplasticizers were prepared and the stability of entrained air was evaluated. The following variables were tested:

- i. Concrete composition factors: air content of concrete, consistency of concrete and mixing time.
- ii. Chemical admixture (SP + AEA) combinations from seven different admixture producers were investigated. All the superplasticizers tested were polycarboxylate ethers.

Effects of the above-mentioned variables on the air content of concrete at different times after mixing were analyzed. The air content was measured immediately after mixing, 30 minutes and 60 minutes after mixing. In addition, after 60 minutes superplasticizer was added to compensate the workability loss and air content were measured after 75 minutes after mixing. Also, the density variation of the concrete was monitored [10].

The laboratory investigations were carried out with a typical concrete composition for structural concrete. The properties of the investigated concrete were:

- Compressive strength class: C35/45-P50 (P-factor is a value used to evaluate the freeze-thaw resistance in the Finnish codes and standards) [11].

- Consistency of concrete: two classes (F5 and S3)
- Maximum aggregate size: 16 mm
- Cement type: Plus Cement (CEM II/B-M (S-LL) 42,5 N) produced by Finnsementti's cement plant at Parainen, Finland

Totally seven different SP and AEA admixture combinations were tested. The properties of the PCE superplasticizers used in the tests are presented in Table 1. The concrete mix design is presented in Table 2.

*Table 2 – Properties of the polycarboxylate ether based superplasticizers used in the tests.*

Superplasticizer	Density, (g/cm <sup>3</sup> )	pH	Chloride content, (%)	Alkali content, (%)
A	1.03 ± 0.02	5.5	< 0.02	< 2.0
B	1.03	6.0 – 8.0	< 0.1	≤ 2.0
C	1.055	4.3	< 0.1	< 1.0
D	1.07 ± 0.02	0.3	< 0.10	< 4.0
E	1.05 ± 0.02	6.0	< 0.05	< 2.0
F	1.05 ± 0.02	0.3	< 0.05	< 2.0
G	1.04 ± 0.02	7.0	< 0.0015	≥ 0.5 to < 1

*Table 3 – Mix design of concretes with different admixtures. (A to G are the combinations of chemical admixtures, S3 and F5 are the consistency classes of the concrete).*

Mix code	Cement (kg/m <sup>3</sup> )	Effect. water (kg/m <sup>3</sup> )	(w/c) <sub>eff</sub>	Aggreg. (kg/m <sup>3</sup> )	AEA, (kg/m <sup>3</sup> )	AEA w.r.t. cement (%)	SP, (kg/m <sup>3</sup> )	SP w.r.t. cement (%)	Target air content (%)
A-S3	425	140	0.33	1716	0.15	0.04	5.10	1.20	5.5
A-F5	425	160	0.38	1770	0.15	0.04	5.10	1.20	5.5
B-S3	425	140	0.33	1716	0.15	0.04	6.29	1.48	5.5
B-F5	425	160	0.38	1766	0.23	0.06	5.10	1.20	5.5
C-S3	425	140	0.33	1720	0.21	0.05	5.19	1.22	5.5
C-F5	425	160	0.38	1772	0.38	0.09	3.40	0.80	5.5
D-S3	425	140	0.33	1718	0.20	0.05	4.76	1.12	5.5
D-F5	425	160	0.38	1768	0.42	0.10	4.34	1.02	5.5
E-S3	425	140	0.33	1717	0.32	0.08	5.44	1.28	5.5
E-F5	425	160	0.38	1770	0.81	0.19	3.83	0.90	5.5
F-S3	425	140	0.33	1715	0.81	0.19	4.12	0.97	5.5
F-F5	425	160	0.38	1767	0.26	0.06	5.65	1.33	5.5
G-S3	425	140	0.33	1716	0.85	0.20	3.61	0.85	5.5
G-F5	425	160	0.38	1770	0.34	0.08	4.85	1.14	5.5

The aggregates used in these tests were granitic gravel, which were washed, dried and graded by sieving. The grading curve of the combined aggregate is presented in Figure 5.

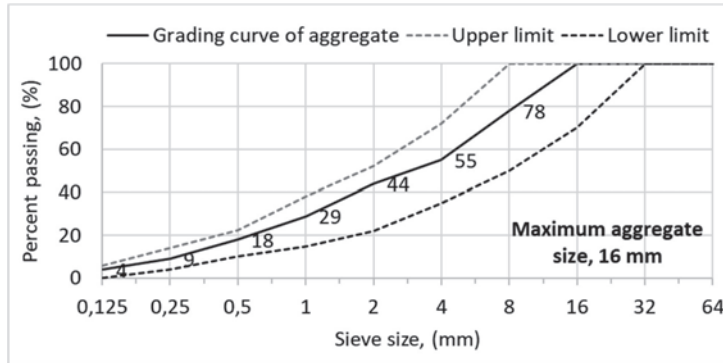


Figure 5 – Combination of aggregates used for the experimental tests.

The properties determined on fresh concrete were air content, density, temperature and consistency. Air-content of concrete was measured by the following methods: (i) pressure method according to the European standard SFS-EN 12350-7 [12] and (ii) Calculated from the fresh concrete unit weight. The air content of fresh concrete was calculated according to the ASTM C 138 - standard [13].

$$\text{Air content, } A = \frac{(T - D)}{T} \times 100 \quad (1)$$

where:

$A$  = the air content in the concrete, (%)

$D$  = the density (unit weight) of concrete, ( $\text{kg}/\text{m}^3$ )

$T$  = the theoretical density of the concrete computed on air free bases, ( $\text{kg}/\text{m}^3$ )

$$T = \frac{M}{V} = \frac{M}{1 - A_t} \quad (2)$$

where:

$M$  = the mass of all materials batched – sum of the masses of the cement, the aggregates, the mixing water and the chemical admixtures, (kg).

$V$  = the absolute volume of the component ingredients in the batch, ( $\text{m}^3$ )

$A_t$  = the target air content of the batch, (%)

Based on Equations (1) and (2), the air content is calculated as follow:

$$\text{Air content, } A = \left( 1 - \frac{D}{M} + \frac{D \times A_t}{M} \right) \times 100 \quad (3)$$

The workability of concrete was tested using two standards: (i) SFS-EN 12350-2 [14] and (ii) SFS-EN 12350-5 [15]. The measurements of fresh concrete properties took place immediately after the concrete had been mixed, after 30 minutes, after 60 minutes and after 75 minutes. The workability of concretes as function of time is presented in Table 4.

Table 4 – Workability of S3 – class and F5 concretes as function of time.

Concrete mix	Time after mixing (min)			Workability loss		Workability gain after adding extra SP dosage	
	0 min	30 min	60 min	30 min	60 min	SP dosage / cement (%)	75 min
<b>Slump test for S3 class concretes, (mm)</b>							
A-S3	130	20	10	85 %	92 %	0,018	60
B-S3	80	10	0	88 %	100 %	0,022	30
C-S3	170	40	30	76 %	82 %	0,013	130
D-S3	160	110	50	31 %	69 %	0,017	190
E-S3	110	90	60	18 %	45 %	0,019	220
F-S3	150	60	70	60 %	53 %	0,015	220
G-S3	120	80	40	33 %	67 %	0,021	180
<b>Flow table test for F5 class concretes, (mm)</b>							
A-F5	590	450	390	24 %	34 %	0,018	620
B-F5	500	490	460	2 %	8 %	0,019	500
C-F5	520	390	340	25 %	35 %	0,011	520
D-F5	660	610	510	8 %	23 %	0,018	700
E-F5	560	480	480	14 %	14 %	0,016	700
F-F5	570	500	470	12 %	18 %	0,015	700
G-F5	570	520	480	9 %	16 %	0,020	640

The following hardened concrete tests were performed: (i) 28 d compressive strength tests on three cubes (100 × 100 × 100 mm<sup>3</sup>) cast immediately after concrete mixing and three cubes cast after 75 minutes of mixing and addition of extra dosage of superplasticizer and (ii) segregation sensitivity of concrete presented by the air content and paste content difference between bottom and top parts of 150 mm diameter concrete cylinder with height of about 270–300 mm, presented in Figure 6.



Figure 6 – Example of the specimens used for sensitivity of concrete for segregation test. The same mass of concrete results different heights for the test specimens, which indicates different air contents.

### 3. EXPERIMENTAL RESULTS AND DISCUSSION

The mixing procedure of the concrete the following steps (i) dry mixing of cement and aggregates for 30 seconds, (ii) addition of 80% of the water content, (iii) after 30 seconds, addition of 10% of the water content and the AEA, (iii) after another 30 seconds, addition of 10% of the water content and the superplasticizer and continue mixing for 1 minute. The air content of fresh concretes with different chemical admixtures was measured immediately after mixing, at 30 minutes, at 60 minutes and 75 minutes after mixing. An extra dosage of superplasticizers was added and concrete was mixed for 2 min before measuring the air content at 75 minutes. The calculated air contents of all the test concretes are presented in Figure 7, Figure 8, Table 5 and Table 6.

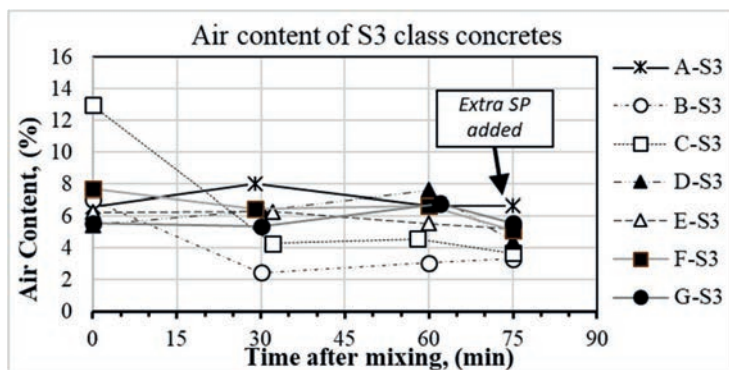


Figure 7 – Calculated air contents of the S3 consistency class concretes. The calculation is based on the fresh concrete density (unit weight)

Table 5 – Air content and air content – elevation for S3 consistency class concretes.

Concrete code	Air content, (%)							
	A-F3	B-F3	C-F3	D-F3	E-F3	F-F3	G-F3	
Time	0	6.6	7.0	13.0	5.5	6.3	7.7	5.6
after	30±2	8.0	2.5	4.3	6.4	6.3	6.5	5.4
mixing,	60±2	6.7	3.1	4.6	7.6	5.6	6.7	6.8
(min)	75±2	6.7	3.3	3.7	4.4	5.2	5.1	5.6
		<b>Air content - elevation, (%)</b>						
30 min after mixing		1.4	-4.6	-8.6	0.9	0.0	-1.2	-0.2
60 min after mixing		0.1	-4.0	-8.4	2.2	-0.7	-1.0	1.2

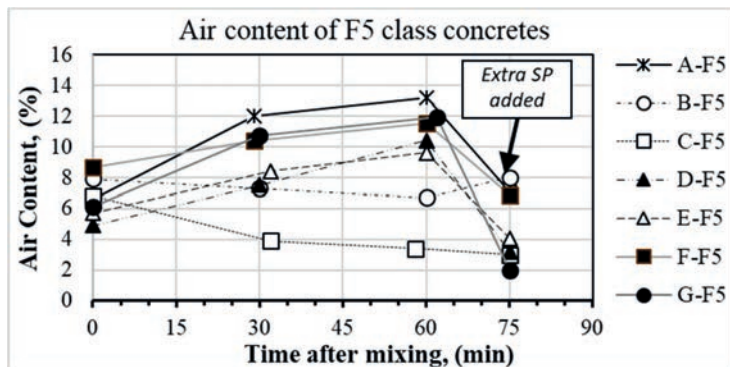


Figure 8 – Calculated air contents of the F5 consistency class concretes.

Table 6 – Air content and air content – elevation for F5 consistency class concretes.

Concrete code	Air content, (%)							
	A-F5	B-F5	C-F5	D-F5	E-F5	F-F5	G-F5	
Time	0	6.6	7.9	6.8	4.9	5.7	8.6	6,1
after	30±2	12.0	7.3	3.9	7.5	8.4	10.4	10,7
mixing,	60±2	13.2	6.7	3.4	10.4	9.6	11.5	11,9
(min)	75±2	7.1	8.0	3.0	3.2	4.1	6.9	2.0
Air content - elevation, (%)								
30 min after mixing	5.4	-0.5	-3.0	2.6	2.7	1.8	4.6	
60 min after mixing	6.6	-1.2	-3.4	5.5	3.9	2.8	5.7	

The results show that the elevation of the air content of fresh concrete depends on the consistency of the concrete and on the type of superplasticizer used. The air content-elevation was higher for the consistency class F5 concretes where the workability loss after 30 and 60 minutes was lower as presented in Table 4, except for the combination of A and B superplasticizer the air content decreases at 30 and 60 minutes after mixing. The elevation of air content in the consistency class S3 concrete was not significant as the consistency class F5 concretes. As shown in Figure 9, the consistency class plays an important role, S3 class concrete showed smaller air content elevation for some combination of AEA and superplasticizers compared to F5 class concrete.

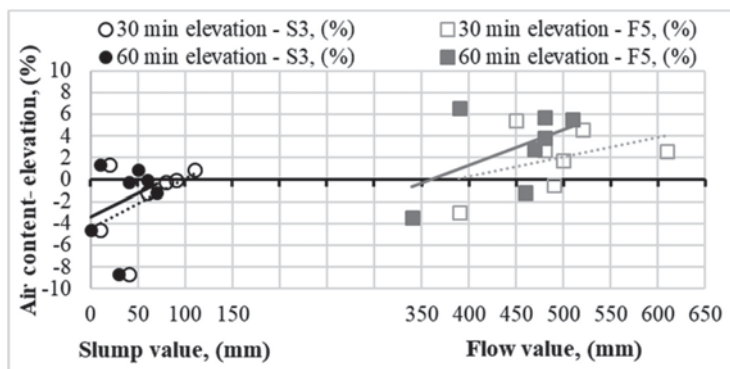


Figure 9 – The effect of the concrete consistency on the air content – elevation of concrete.

The test results indicated that the air content increases after initial mixing. A relatively high superplasticizer dosage (1.2% from weight of cement) was used. With lower dosages, the increase will probably be smaller. The consistency was determined immediately after mixing, whereas in practical applications the consistency of concrete is generally determined on construction site, it means some 15...60 min after the initial mixing. Therefore, the consistency immediately after mixing was lower compared to that found typically in the industry.

The admixtures dosages varied to some extent. It could be assumed that higher admixture dosages increase risk for the elevated air content. The effects of superplasticizers dosages on the increase of air content of concrete are presented in Figure 10. The slightly different admixture dosages used in the study did not explain the increase of air content. However, if admixture dosages would vary on the larger range, the situation could be different.

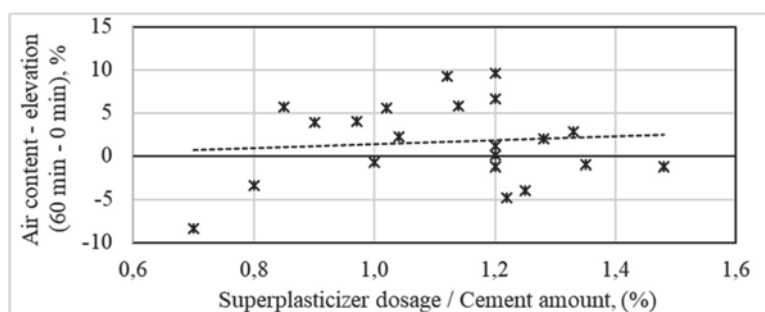


Figure 10 – Effects of superplasticizer dosage on the elevation of air content in concrete.

The sensitivity of segregation investigation were carried out on the hardened specimens that were cast immediately after mixing. The sensitivity of segregation was analyzed by comparing the densities of the bottom and top part of the cylindrical test specimens, shown in Figure 11.

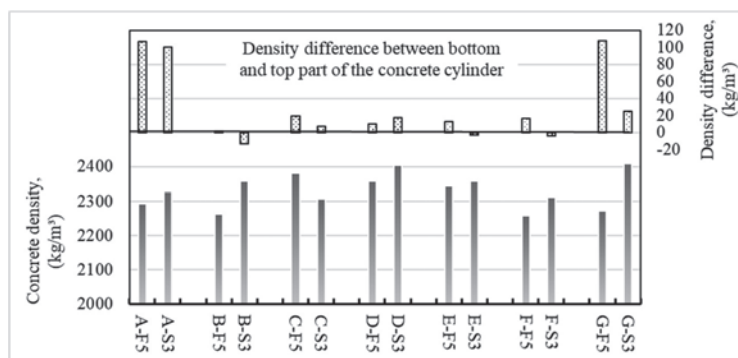


Figure 11 – Density differences of hardened concretes poured immediately after mixing for concrete mixes with different chemical admixtures combinations.

11 kg of fresh concrete was poured inside a 150mm diameter and a 300mm high cylindrical steel moulds and immediately vibration was applied using vibrating table for 30 seconds. The density differences between different parts of the hardened concrete cylinder are shown in Figure 11.

The results of the effects of air content increment on the segregation sensitivity of concrete show a slight correlation between the increase of air content and the density difference can be observed for the using of the chemical admixture combination A and G, otherwise the effect was not significant. With admixture combination A and G, a difference of about 100 kg/m<sup>3</sup> was exceeded, but other admixture combinations gave only very small difference. The results also show that the S3 consistency class concrete showed smaller segregation sensitivity compared to F5 class concrete for most types of admixtures.

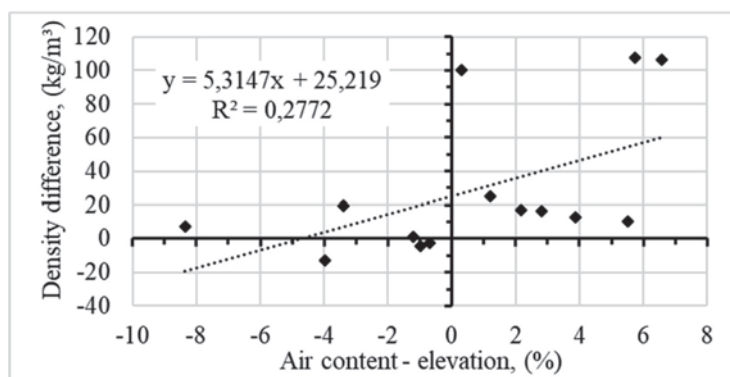


Figure 12 – The effects of air content increment of the density difference between the top and bottom parts of concrete specimens that were cast immediately after mixing and compacted for 30 sec.

As shown in Figure 12, the density difference appears to correlate with the increase of the air content after mixing. The correlation is not strong, but in most cases, the same admixtures gave both high increase of air content and high-density difference.

The effect of the mixing time on the air content of concrete with different chemical admixture combinations is presented in Table 7. The results show that 2 minute mixing time (which simulate the concrete industry practices) gives lower air content than 5 minute mixing time immediately after mixing. While, the air contents for both mixing times measured at 60 minutes after mixing were close to each other, except for the G admixture combination. The results indicate that short mixing time would not be enough to achieve total effectivity of AEA, especially for higher consistency classes concrete.

*Table 7 – The effect of mixing time on the air content potential of concrete, using pressure method.*

Concrete code	Air content, (%)		
	Time after mixing, (min)		
	0	30±2	60±2
A-F5 (mixing 2 minutes)	6.0	10.4	11.4
A-F5 (mixing 5 minutes)	10.0	11.7	11.4
B-F5 (mixing 2 minutes)	5.6	8.0	8.5
B-F5 (mixing 5 minutes)	8.1	9.0	7.6
C-F5 (mixing 2 minutes)	4.0	7.7	10.6
C-F5 (mixing 5 minutes)	8.0	10.6	12.0
D-F5 (mixing 2 minutes)	4.1	6.5	8.4
D-F5 (mixing 5 minutes)	5.6	7.6	8.8
E-F5 (mixing 2 minutes)	4.5	6.8	8.4
E-F5 (mixing 5 minutes)	4.6	7.1	9.0
F-F5 (mixing 2 minutes)	6.1	7.9	10.5
F-F5 (mixing 5 minutes)	8.2	9.8	12.0
G-F5 (mixing 2 minutes)	5.9	3.2	3.1
G-F5 (mixing 5 minutes)	8.6	3.3	3.5

#### 4. SUMMARY AND CONCLUSION

A number of concrete tests were carried out to analyze the effect of superplasticizers on the stability of the protective pore systems. Clear increase of the air content after the initial mixing of concrete was observed, the highest measured air contents were close to 13%, while the air content after mixing was 6.6%.

The increase of air content is a complex issue and several factors are affecting the phenomenon. However, based on the tests the increase of the air content after the initial mixing can be explained as follows:

1. The air content depends on the admixture combination (superplasticizer, air entraining agent and their dosage).
2. The consistency of concrete has a big role in the air content elevation of concrete in relation to different chemical admixture combination.
3. Initial mixing time also affects the air content elevation of concrete. A mixing time of 2 minutes was too short achieve the full potential air content.

The authors believe that there are probably other aspects affecting the air content elevation of fresh concrete, which could be a topic for future investigation. Occasionally air content continues increasing after initial mixing even though the initial mixing time has been rather long. In such cases, the superplasticizer is probably playing the major role, the foam killer may lose its power and air content is increasing.

#### REFERENCES

1. Mölsä S: “The reason for the Kemijärvi railroad bridge's construction defects”. 2016. (In Finnish). [Online] <https://www.rakennuslehti.fi/2016/11/kemijarven-sillan-valuvian-syyt-selvisivat-turkua-tutkitaan/> [Accessed on 29.1.2019]

2. Turunsanommat News: “The background of the concrete strength problems is the elevated air content in-site”. 2016. (In Finnish). [Online] <https://www.ts.fi/uutiset/paikalliset/3117381/Betonin+lujuusongelmien+taustalla+liialliset+ilmamaarat+Tyksin+tyomaalla> [Accessed on 29.1.2019]
3. Yang Q: “Stability of air bubbles in fresh concrete”. Master of Science Thesis. Department of Civil and Environmental Engineering, Division of Building Technology. Chalmers University of Technology, Göteborg, Sweden, 2012.
4. Zakka A, Carrasquillo R & Ramon L: “Effects of high-range water reducers on the properties of fresh and hardened concrete”. Research Report No. 1117-3F. Guidelines for Proper Use of Superplasticizers and the Effect of Retempering Practices on Performance and Durability of Concrete. Texas State Department of Highways and Public Transportation In Cooperation with the U.S. Department of Transportation Federal Highway Administration, USA, October 1989.
5. Lazniewska-Piekarczyk B: ”The effect of superplasticizers and anti-foaming agents on the air entrainment and properties of the mix of self-compacting concrete”. Article in *Cement, Wapno, Beton*. May 2009 [Online] <https://www.researchgate.net/publication/287164082> [Accessed on 29.1.2019]
6. Łazniewska-Piekarczyk B, Szwabowski J & Miera P: ”Superplasticizer compatibility problem with innovative air-entraining multicomponent Portland cement”. *Proceedings*, 14<sup>th</sup> International Congress on the Chemistry of Cement (ICCC 2015), Beijing, China, Oct. 13-16, 2015. [Online] <https://www.researchgate.net/publication/290392716> [Accessed on 3.10.2018]
7. Kubens S: “Interaction of cement and admixtures and its influence on rheological properties”. Cuvillier Verlag, Inhaberin Annette Jentzsch-Cuvillier, Nonnenstieg 8, 37075 Göttingen, Germany, 2010. [Online] <https://cuvillier.de/de/shop/publications/752> [Accessed on 29.1.2019]
8. Rath S & Ouchi M.: “Effective Mixing Method for Stability of Air Content in Fresh Mortar of Self-Compacting Concrete in Terms of Air Diameter”. *Internet Journal for Society for Social Management Systems*, Issue 10, Vol. 1. 2015, sms15-6550.
9. Eickschen E & Müller C: ”Interactions of air-entraining agents and plasticizers in concrete”. *Concrete Technology Reports 2010 – 2012*. VDZ gGmbH (Hrsg.). Düsseldorf, Germany, 2012. [Online] <https://www.vdz-online.de/en/publications/concrete-technology-reports/> [Accessed on 29.1.2019]
10. Al-Neshawy F & Punkki J: “Securing the stable protective pore system of concrete - Report for ‘Robust Air’”. Research Project, Aalto University publication series Science + Technology, No. 10, 2017, Aalto University, Helsinki, Finland. Online at: <https://aaltodoc.aalto.fi/handle/123456789/28893>
11. Finnish Transport Agency: “P-rate method for frost-resistant concrete in Finnish bridges”. (In Finnish). Report 22/2016, Helsinki, Finland, 2016. [Online] [https://julkaisut.liikennevirasto.fi/pdf8/lo\\_2016-22\\_siltabetonien\\_p-lukumenettely\\_web.pdf](https://julkaisut.liikennevirasto.fi/pdf8/lo_2016-22_siltabetonien_p-lukumenettely_web.pdf) [Accessed on 4.10.2018]
12. SFS-EN 12350-7:2009 “Testing fresh concrete. Part 7: Air content. Pressure methods”. Finnish Association of Construction Product Industries, SFS, Helsinki, Finland, 2009.
13. ASTM C138 / C138M-17a “Standard Test Method for Density (Unit Weight), Yield, and Air Content (Gravimetric) of Concrete”. ASTM International, West Conshohocken, PA, USA, 2017, [www.astm.org](http://www.astm.org)
14. SFS-EN 12350-2:2009 “Testing fresh concrete. Part 2: Slump-test”. Finnish Association of Construction Product Industries, SFS, Helsinki, Finland, 2009.
15. SFS-EN 12350-5:2009 “Testing fresh concrete. Part 5: Flow table test”. Finnish Association of Construction Product Industries, SFS, Helsinki, Finland, 2009.

## Research Council & Editorial Board of Nordic Concrete Research

Dr. Terje F. Rønning, Chairman of the Research Council		
<b>Danish Concrete Association</b>	Assoc. Prof. Marianne Tange Hasholt Technical University of Denmark Dept. of Civil Engineering Brovej, Building 118, 2800 Kgs. Lyngby, DK Tel: +45 25 17 02 <a href="mailto:matah@byg.dtu.dk">matah@byg.dtu.dk</a>	Mrs. Gitte Normann Munch-Petersen Teknologisk Institut Kongsvang Allé 29 DK - 8000 Aarhus Mobile: +45 72 20 32 45 <a href="mailto:gnmp@teknologisk.dk">gnmp@teknologisk.dk</a>
<b>Finnish Concrete Association</b>	Professor Jouni Punkki Aalto University, Dept of Civil Engineering P.O.Box 12100 FI-00076 Aalto, Finland tel. +358 50 322 4155 <a href="mailto:jouni.punkki@aalto.fi">jouni.punkki@aalto.fi</a>	Prof. Dr. Jukka Lahdensivu Tampere University of Technology P.O.Box 527 FI-33101 Tampere Mobile: +358 40 0733852 <a href="mailto:jukka.lahdensivu@tut.fi">jukka.lahdensivu@tut.fi</a>
<b>Icelandic Concrete Association</b>	Dr. Jón E. Wallevik Innovation Center Iceland IS - 112 Keldnaholti Tel: +354 522 9362 Mobile: +354 Fax: +354 522 9111 <a href="mailto:jon.w@nmi.is">jon.w@nmi.is</a>	Prof. Dr. Olafur H. Wallevik Innovation Center Iceland IS - 112 Keldnaholti Tel: +354 522 9000 Mobile: +354 860 7650 <a href="mailto:wallevik@ru.is">wallevik@ru.is</a>
<b>Norwegian Concrete Association</b>	Dr. Terje F. Rønning Heidelberg Cement NE / Cement Product development & Implementation P.O.Box 38 NO-3991 Brevik Tel.: +47 3557 2000 Mobile: +47 915 76 046 <a href="mailto:terje.ronning@heidelbergcement.com">terje.ronning@heidelbergcement.com</a>	Ola Skjølsvold SINTEF Architecture, Materials & Structures P.O. Box 4760 Torgarden NO-7465 Trondheim, Norway Tel: +47 40 00 51 00 Mobile: +47 930 58 691 <a href="mailto:ola.skjolsvold@sintef.no">ola.skjolsvold@sintef.no</a>
<b>Swedish Concrete Association</b>	Tekn. Dr. Peter Utgenannt CBI Swedish Cement and Concrete Research Institute P.O. Box 857 SE - 501 15 Borås Tel: +46 105 166 870 Mobile: +46 706 452 008 <a href="mailto:Peter.utgenannt@cbi.se">Peter.utgenannt@cbi.se</a>	Tekn. Dr. Mårten Janz ÅF, International Division Hallénborgs gata Box 585 SE-201 25 Malmö Tel: +46 10 505 7334 Mobile: + 46 70 293 6338 <a href="mailto:marten.janz@afconsult.com">marten.janz@afconsult.com</a>
<b>Editor</b>	Prof. Johan Silfwerbrand KTH Royal Institute of Technology Dept. of Civil & Architectural Engrg. Brinellvägen 23 SE-100 44 Stockholm Tel: +46 8 790 8033 Mobile: +46 70 726 4005 <a href="mailto:jsilfwer@kth.se">jsilfwer@kth.se</a>	<i>June 26, 2019</i>



## Research Council & Editorial Board of Nordic Concrete Research

Dr. Terje F. Rønning, Chairman of the Research Council		
<b>Danish Concrete Association</b>	Assoc. Prof. Marianne Tange Hasholt Technical University of Denmark Department of Civil Engineering Brovej, Building 118, 2800 Kgs. Lyngby, DK Tel: +45 25 17 02 <a href="mailto:matah@byg.dtu.dk">matah@byg.dtu.dk</a>	Mrs. Gitte Normann Munch-Petersen Teknologisk Institut Kongsvang Allé 29 DK - 8000 Aarhus Mobile: +45 72 20 32 45 <a href="mailto:gnmp@teknologisk.dk">gnmp@teknologisk.dk</a>
<b>Finnish Concrete Association</b>	Professor Jouni Punkki Aalto University, Dept of Civil Engineering P.O.Box 12100 FI-00076 Aalto, Finland tel. +358 50 322 4155 <a href="mailto:jouni.punkki@aalto.fi">jouni.punkki@aalto.fi</a>	Prof. Dr. Jukka Lahdensivu Tampere University of Technology P.O.Box 527 FI-33101 Tampere Mobile: +358 40 0733852 <a href="mailto:jukka.lahdensivu@tuni.fi">jukka.lahdensivu@tuni.fi</a>
<b>Icelandic Concrete Association</b>	Dr. Jón E. Wallevik Innovation Center Iceland IS - 112 Keldnaholti Tel: +354 522 9362 Mobile: +354 Fax: +354 522 9111 <a href="mailto:jon.w@nmi.is">jon.w@nmi.is</a>	Prof. Dr. Olafur H. Wallevik Innovation Center Iceland IS - 112 Keldnaholti Tel: +354 522 9000 Mobile: +354 860 7650 <a href="mailto:wallevik@ru.is">wallevik@ru.is</a>
<b>Norwegian Concrete Association</b>	Dr. Terje F. Rønning Heidelberg Cement NE / Cement Product development & Implementation P.O.Box 38 NO-3991 Brevik Tel.: +47 3557 2000 Mobile: +47 915 76 046 <a href="mailto:terje.ronning@heidelbergcement.com">terje.ronning@heidelbergcement.com</a>	Ola Skjølsvold SINTEF Architecture, Materials & Structures P.O. Box 4760 Torgarden NO-7465 Trondheim, Norway Tel: +47 40 00 51 00 Mobile: +47 930 58 691 <a href="mailto:ola.skjolsvold@sintef.no">ola.skjolsvold@sintef.no</a>
<b>Swedish Concrete Association</b>	Tekn. Dr. Peter Utgenannt CBI Swedish Cement and Concrete Research Institute P.O. Box 857 SE - 501 15 Borås Tel: +46 105 166 870 Mobile: +46 706 452 008 <a href="mailto:Peter.utgenannt@cbi.se">Peter.utgenannt@cbi.se</a>	Tekn. Dr. Mårten Janz ÅF, International Division Hallénborgs gata Box 585 SE-201 25 Malmö Tel: +46 10 505 7334 Mobile: + 46 70 293 6338 <a href="mailto:marten.janz@afconsult.com">marten.janz@afconsult.com</a>
<b>Editor</b>	Prof. Johan Silfwerbrand KTH Royal Institute of Technology Dept. of Civil & Architectural Engrg. Brinellvägen 23 SE-100 44 Stockholm Tel: +46 8 790 8033 Mobile: +46 70 726 4005 <a href="mailto:jsilfwer@kth.se">jsilfwer@kth.se</a>	<i>June 26, 2019</i>



